



<https://theses.gla.ac.uk/>

Theses Digitisation:

<https://www.gla.ac.uk/myglasgow/research/enlighten/theses/digitisation/>

This is a digitised version of the original print thesis.

Copyright and moral rights for this work are retained by the author

A copy can be downloaded for personal non-commercial research or study,
without prior permission or charge

This work cannot be reproduced or quoted extensively from without first
obtaining permission in writing from the author

The content must not be changed in any way or sold commercially in any
format or medium without the formal permission of the author

When referring to this work, full bibliographic details including the author,
title, awarding institution and date of the thesis must be given

Enlighten: Theses

<https://theses.gla.ac.uk/>
research-enlighten@glasgow.ac.uk

**COMPARATIVE STUDY OF PASSIVE
MODELOCKING CONFIGURATIONS
IN SEMICONDUCTOR LASERS**

by

Fernando Camacho Páez

July 1997

A thesis submitted to the Faculty of Engineering
of The University of Glasgow
for the degree of Doctor of Philosophy

© Fernando Camacho Páez, 1997

ProQuest Number: 13815341

All rights reserved

INFORMATION TO ALL USERS

The quality of this reproduction is dependent upon the quality of the copy submitted.

In the unlikely event that the author did not send a complete manuscript and there are missing pages, these will be noted. Also, if material had to be removed, a note will indicate the deletion.



ProQuest 13815341

Published by ProQuest LLC (2018). Copyright of the Dissertation is held by the Author.

All rights reserved.

This work is protected against unauthorized copying under Title 17, United States Code
Microform Edition © ProQuest LLC.

ProQuest LLC.
789 East Eisenhower Parkway
P.O. Box 1346
Ann Arbor, MI 48106 – 1346

Thesis 10953
copy 1



A Ailsa, Tom y Nico, por el tiempo que no les pude dedicar.

Abstract

This thesis is concerned with the investigation of different configurations of semiconductor lasers to generate short optical pulses through passive modelocking, and the analysis of the possible uses for these optical pulse generators.

Three different modelocking configurations have been studied to generate optical pulses at frequencies between 1 and 15 GHz; two of them monolithic configurations, namely all active cavity mode-locked lasers and extended cavity mode-locked lasers and the third one being an external cavity configuration.

The all active cavity mode-locked lasers have the advantage of having the easiest and most reliable fabrication process, but exhibited high threshold, around 100 mA for 5 mm long laser, broad pulses, around 10 ps, and high timing jitter levels, up to 22 ps (1 kHz-10MHz).

The extended cavity mode-locked lasers, which incorporate active and passive sections, are also easy to fabricate, but the reliability of the fabrication process depends on the reliability of the technique to fabricate the passive section of the device. They are excellent short pulse generators with very low threshold current, around 25 mA for a 5 mm long laser, pulses as narrow as 3.5 ps and jitter levels as low as 9 ps (1 kHz-10MHz), which indicates a high stability in the pulse generation.

With the external cavity configuration the pulse generation frequency can be reduced to values as low as hundreds of MHz. The drawback with this type of laser is their mechanical instability, which makes them a difficult device to work with.

An important application for these optical pulse generators is that of all-optical clock recovery. The locking range of the monolithic configurations, under external periodic excitation, was studied. The all active cavity lasers showed a locking range wider than 0.15% of the free running modelocking frequency, whilst the extended cavity lasers locking range was around 0.03% of the free running modelocking frequency.

Acknowledgements

Firstly, I would like to thank my supervisor Professor John Marsh for his valuable help, constant dedication and useful discussions that lead to the conclusion of this thesis.

I wish to thank Dr. Catrina Bryce, Dr. Karen McIlvaney and Dr. Steven Ayling (now in DRA) for their help and encouragement throughout the duration of this project. I am also grateful for the help I received from the technical staff, especially Jim Gray, all the members of the clean room staff, and the dry etch group.

I am very grateful to Dr. Eugene Avrutin for sharing his knowledge with me, and for allowing me to use his theoretical model to compare with my experimental results.

Also, I would like to express my gratitude to all my fellow research students and research assistants within the Optoelectronics Research Group, especially my colleagues in 70 University Avenue: Andrew, Daniel, Colin and Paulo, with whom I spent many entertaining hours.

Special thanks to all my family, principally to my parents Fernando and Mary Pura, for their support, both intellectual and financial, throughout my life.

Finally, I would like to thank my wife Ailsa, for the encouragement, long proof reading hours and hot and nice dinners given for free.

This project was supported by the Department of Electronics and Electrical Engineering of The University of Glasgow and Hamamatsu Photonics U.K.

Contents

Chapter 1 : <i>The future of digital communications: all-optical networks</i>	1
1.1 Introduction.....	1
1.2 Short optical pulse generation with semiconductor lasers.....	3
1.2.1 Gain switching	5
1.2.2 Q-switching.....	5
1.2.3 Modelocking	6
1.3 All-optical digital communications.....	8
1.3.1 Optical switching.....	8
1.3.2 Clock recovery.....	9
1.3.3 All-optical signal processing	10
1.4 Outline of the Thesis	12
Chapter 2 : <i>Semiconductor lasers; fabrication and characterisation..</i>	13
2.1 Optical modes in dielectric waveguides.....	13
2.1.1 Longitudinal modes: Fabry-Perot laser oscillation.....	13
2.1.2 Transversal modes I: dielectric slab waveguide.....	16
2.1.3 Transversal modes II: stripe geometry waveguide	19
2.2 Introduction to semiconductor lasers	20
2.2.1 Heterostructure lasers.....	21
2.2.2 Quantum-Well lasers.....	22
2.3 Semiconductor material analysis.....	25
2.3.1 Material structure.....	25
2.3.2 Material characterisation.....	26
2.4 Device fabrication and characterisation	33
2.4.1 Analysis of device structure	35
2.4.2 Device fabrication.....	36
2.4.3 Experimental set-up.....	46
2.4.4 Pulse width measurements.	49
2.5 Conclusions.	56

Chapter 3 : <i>Passive modelocking. Theoretical concepts</i>	58
3.1 Description of modelocking.....	58
3.2 Passive modelocking in semiconductor lasers.....	60
3.2.1 Pulse shortening effect: the saturable absorber.....	60
3.2.2 Pulse broadening effect.....	63
3.3 Configuration of passively mode-locked semiconductor lasers.....	65
3.4 Theory of modelocking in semiconductor lasers.....	67
3.4.1 Spectral description.....	68
3.4.2 Temporal description.....	71
3.5 Conclusions.....	74
 Chapter 4 : <i>All active cavity mode-locked lasers</i>	 76
4.1 Laser configuration.....	76
4.2 Experimental results.....	79
4.2.1 Modelocking frequency.....	80
4.2.2 Pulse width.....	85
4.2.3 Self-pulsations in mode-locked semiconductor lasers.....	87
4.2.4 Spectral analysis.....	93
4.2.5 Timing jitter.....	95
4.2.6 Development of passive modelocking.....	99
4.3 Numerical simulations.....	102
4.4 Conclusions.....	105
 Chapter 5 : <i>Extended cavity mode-locked lasers</i>	 107
5.1 Quantum well intermixing.....	107
5.1.1 IFVD by SiO ₂ / SrF ₂ dielectric encapsulation.....	111
5.1.2 IFVD by SiO ₂ / P:SiO ₂ dielectric encapsulation.....	114
5.2 Passive waveguide characterisation.....	117
5.3 Laser configuration.....	120
5.4 Experimental results.....	122
5.4.1 Modelocking frequency.....	122
5.4.2 Pulse width.....	128

5.4.3 Spectral analysis.....	129
5.4.4 Timing jitter.....	131
5.4.5 Development of passive modelocking.....	138
5.5 Numerical simulations.....	140
5.6 Conclusions.....	141
Chapter 6 : <i>External cavity mode-locked lasers</i>	143
6.1 Laser configurations.....	143
6.2 External cavities.....	144
6.2.1 Fibre gratings.....	145
6.3 Reduction of the reflectivity from a laser facet	147
6.3.1 Antireflection coatings.....	147
6.3.2 Bent waveguide lasers.....	152
6.4 Experimental results	156
6.4.1 XCL with a fibre grating.....	156
6.4.2 XCL with an external mirror.....	157
6.5 Conclusions.....	162
Chapter 7 : <i>Synchronisation of mode-locked semiconductor laser</i> <i>with external signals</i>	164
7.1 Introduction.....	164
7.2 Noise reduction in passively mode-locked semiconductor lasers	166
7.2.1 Hybrid modelocking experiments.....	168
7.2.2 Subharmonic optical locking experiments.....	175
7.3 All-optical clock recovery using semiconductor mode-locked lasers	186
7.4 Numerical simulations.....	188
7.5 Conclusions.....	189
Chapter 8 : <i>Conclusions</i>	190
Appendix I : <i>The two-photon absorption waveguide</i> <i>autocorrelator</i>	195

Appendix II: <i>Photoluminescence</i>	198
Appendix III: <i>Fourier Transform: Notations And Conventions</i>	200
Appendix IV: <i>Publications</i>	202

Chapter One THE FUTURE OF DIGITAL COMMUNICATIONS: ALL-OPTICAL NETWORKS.

As the need for ultrafast speed communications networks develops, and the possibility to interface such networks with electronic-based systems is increasingly more difficult, a new research area is opening. One solution for such networks is to use all-optical signal processing and data manipulation with a potential speed of operation beyond 100 Gbit/s. In these types of networks functions, such as multiplexing, demultiplexing, switching, routing, regenerative repeaters and synchronisation are accomplished without intermediate electrical conversion.

This thesis is concerned with the fabrication of semiconductor lasers which could be used in the implementation of such all-optical networks.

As an introduction to this chapter, the next generation of >100 Gbit/s time-division-multiplexed (TDM) optical transmission systems will be briefly analysed. Different techniques for short optical pulse generation, necessary for optical networks, will then be studied. Finally, the building blocks required for all-optical processing will be enumerated and briefly discussed.

1.1 Introduction.

Ultrafast optical TDM has the potential of providing flexible bandwidth at rates of 100 Gbit/s¹. As shown in Figure 1.1, the future ultrafast TDM local and metropolitan area networks (LAN's and MAN's) will serve high-end single users, such as high-speed video servers, terabyte media banks and super-computers that operate at speeds from 10 to 100 Gbit/s, as well as low speed users.

¹ R.A. Barry, V.W.S. Chan, K.L. Hall, E.S. Kintzer, J.D. Moores, K.A. Rauschenbach, E.A. Swanson, L.E. Adams, C.R. Doerr, S.G. Finn, H.A. Haus, E.P. Ippen, W.S. Wong and M. Haner, "All-optical network consortium—ultrafast TDM networks", *IEEE J. Selected Areas Communication*, 1996, **14**, 5, pp. 999-1013.

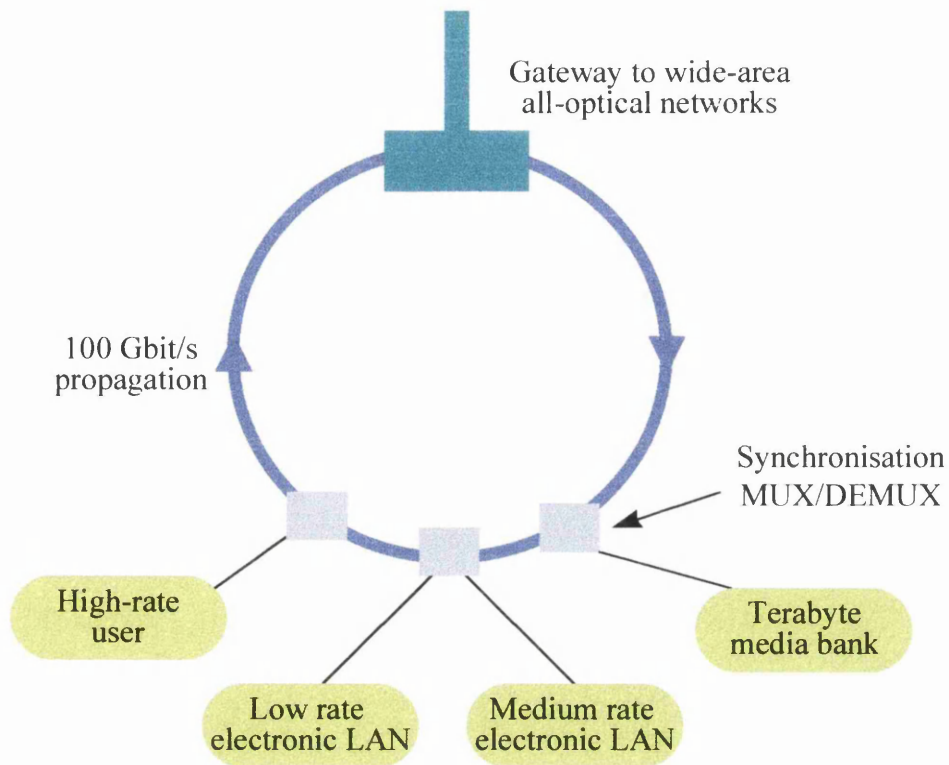


Figure 1.1: Structure for a 100 Gbit/s optical LAN/MAN after R.A. Barry *et al*¹.

The main elements required for such optical networks, related with the contents of this thesis, are:

a) Short optical pulses.

Ultrafast soliton transmission experiments have been demonstrated where a baseband data rate of 10 Gbit/s was optically multiplexed to form 40 Gbit/s² and 80 Gbit/s³ soliton streams, and where a baseband of 6.3 Gbit/s was multiplexed to form a 50 Gbit/s⁴ soliton stream. Obviously, short pulse optical sources play a main role in

² R. Ludwig, A. Ehrhardt, W. Pieper, E. Jahn, N. Agrawal, H.J. Ehrke, L. Kueller and H.G. Weber, “40 Gbit/s demultiplexing experiment with 10 GHz all-optical clock recovery using a mode-locked semiconductor laser”, *Electronics Lett.*, 1996, **32**, 4, pp. 327-329.

³ M. Nakazawa, E. Yoshida, E. Yamada, K. Suzuki, T. Kitoh and M. Kawachi, “80 Gbit/s soliton data transmission over 500 km with unequal amplitude solitons for timing clock extraction”, *Electronics Lett.*, 1994, **30**, 21, pp. 1777-1778.

⁴ O. Kamatani, S. Kawanishi and M. Saruwatari, “Prescaled 6.3 GHz clock recovery from 50 Gbit/s TDM optical signal with 50 GHz PLL using four-wave mixing in a travelling laser diode optical amplifier”, *Electronics Lett.*, 1994, **30**, 10, 807-809,

such TDM systems, as the width of the generated pulses should be short enough to allow the pulses to be multiplexed without overlapping.

b) Synchronisation.

Clock recovery is an essential element in the all-optical network to enable the receiver to be synchronised with the incoming data stream. At data rates beyond a few Gbit/s, it becomes increasingly difficult to perform the clock recovery electronically. All-optical recovery techniques are needed that can be scaled to data rates from a couple of Gbit/s⁵ to tens of Gbit/s⁶, or even 100 Gbit/s in the near future.

1.2 Short optical pulse generation with semiconductor lasers.

According to the bandwidth theorem, the minimum pulse duration of any signal is given roughly by the inverse of the spectral bandwidth as

$$\Delta t_{\min} \cong \frac{1}{\Delta f} \quad (1.1)$$

Therefore, to obtain an optical pulse as short as 1 ps the laser emission bandwidth must be at least 1 THz. When the minimum condition is fulfilled, i.e. the pulse width is close to the inverse of the bandwidth, the light pulse is said to be *transform limited*. A measure of the quality of optical pulses is the time-bandwidth product, which has a minimum when the pulses are transform limited.

From Eq.(1.1) it is obvious that to produce very short optical pulses the laser system must have a very wide spectral bandwidth. This is one of the reasons for the importance of semiconductor lasers in optical communications, as they have the potential of generating pulses as short as 50 fs⁷.

⁵ P.E. Barnsley and H.J. Wickes, "All-optical clock recovery from 2.5 Gbit/s NRZ data using self-pulsating 1.58 mm laser diode", *Electronics Lett.*, 1992, **28**, 1, pp. 4-5.

⁶ A.D. Ellis, K. Smith and D.M. Patrick, "All optical clock recovery at bit rates up to 40Gbit/s", *Electronics Lett.*, 1993, **29**, 15, pp. 1323-1324.

⁷ P.P. Vasil'ev, "Ultrashort pulse generation in diode lasers", *Optical and Quantum Electron.*, 1992, **24**, pp. 801-824.

There are various methods of generating short optical pulses in semiconductor laser diodes⁸, the most common being gain switching, Q-switching and modelocking. Figure 1.2 shows the diagram of a multi-contact semiconductor laser, which can generate short optical pulses by any of the above techniques. In this multi-contact configuration, the laser cavity is divided into a long and a short section, both formed by splitting the p-contact. The long laser section is forward biased to provide gain to the laser. By reverse biasing the short section, an intracavity saturable absorber is formed. A saturable absorber is a lossy element that becomes more transparent with increasing light intensity and will be analysed in chapter 3.

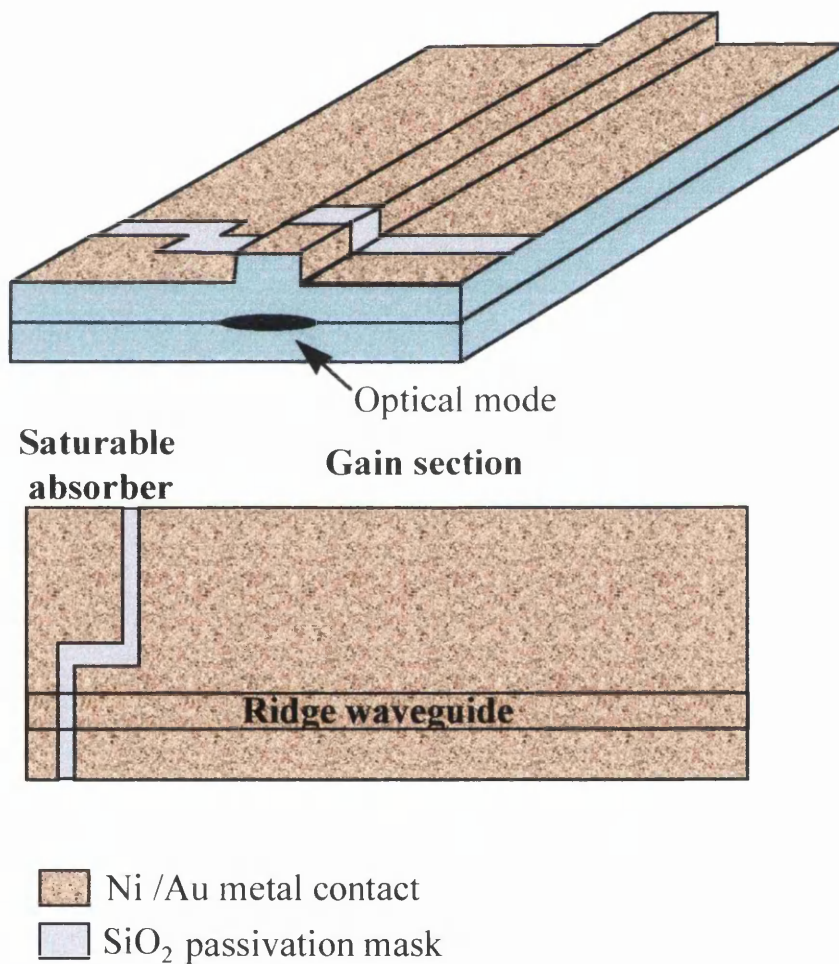


Figure 1.2: Two section laser diode incorporating a gain section and an intracavity saturable absorber.

⁸ A.E. Siegman, "Lasers", University Science Books.

1.2.1 Gain switching.

Gain switching generates optical pulses by switching the gain or loss of the laser. It can be achieved readily in a laser diode by driving the laser with pulsed or RF electrical currents, and no multi-contact configuration is required. The pulse duration, usually tens of ps, is limited by the rate of energy transfer between electron and photon populations. The amount of chirp in the gain-switched pulses is usually very large, producing a time-bandwidth product far from the theoretical limit for transform limited pulses.

1.2.2 Q-switching.

Q-switching is a widely used pulse generation technique in which the laser pumping is allowed to build up a much larger than usual population inversion inside the laser cavity, while keeping the cavity itself from oscillating by removing the cavity feedback or greatly increasing the cavity losses. After inversion has been developed, the cavity Q is switched back to its usual large value, and the stored energy is rapidly emitted in the form of an optical pulse.

This process is shown visually in Figure 1.3. Initially, the cavity losses are very high, which allows the population inversion to grow and, therefore, the optical gain which is proportional to the cavity population inversion. When the Q of the cavity is switched back to its high value, e.g. the loss in the cavity saturates, the stored energy is released as an optical pulse, the loss unsaturates and the cavity Q goes back to the low value. In Figure 1.3 the pumping interval and the pulse output interval look very similar, but in a real laser the former is typically much longer than the latter.

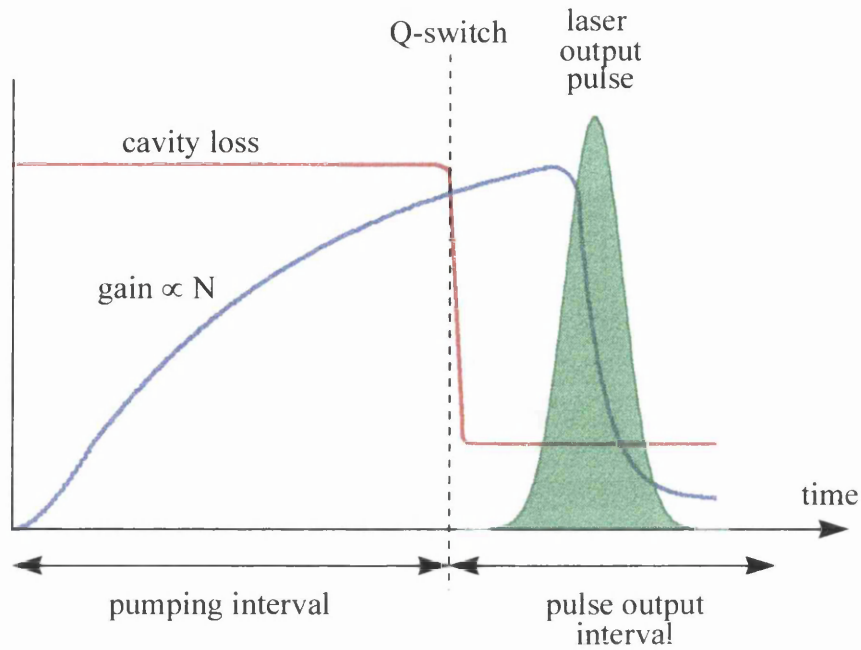


Figure 1.3: Schematic illustration of the Q-switching process.

If switching is caused by an external influence, the technique is called active Q-switching. However, there exists the possibility of self-Q-switching of a semiconductor laser by introducing a saturable absorber in the laser cavity. In the case of passive Q-switching, the pulse emission rate is governed by laser parameters and the biasing conditions, i.e. the operating frequency increases with increasing injected current and decreases with increasing saturable absorber voltage magnitude.

Pulse durations can be as short as 20 ps, and repetition frequencies are usually around a few GHz, but frequencies as high as 16 GHz have been observed⁹. As for gain-switched lasers, the Q-switched optical pulses are usually very chirped, having a large time-bandwidth product.

1.2.3 Modelocking.

The basic advantage of modelocking techniques is that of generating the shortest laser pulses. The term *modelocking* originates from the fact that, under modelocking

⁹ J.H. Marsh, D.A. Barrow, F.R. Laughton and E.L. Portnoi, "Generation and detection of Q-switched pulses from two section semiconductor lasers", *IEE Colloquium in Ultrashort optical pulses*, 1993, pp.4/1-4/6.

conditions, the different longitudinal modes in the laser optical spectrum are *locked* in phase. In the case of active modelocking, the pumping current is modulated at a frequency equal to the inverse of the round trip time of an optical pulse inside of the laser cavity. Passive modelocking, which generates the shortest optical pulses, can be achieved by introducing a saturable absorber into the laser cavity.

The way to realise passive modelocking in a semiconductor laser is the same as that of Q-switching, i.e. introducing a saturable absorber in the laser cavity, but it must be borne in mind that the optical pulse generation arises from completely different processes: in Q-switching the laser stores energy until the losses saturate and then this energy is emitted in a single pulse; in modelocking there is always a pulse (or pulses in the case of harmonic modelocking and colliding pulse modelocking) circulating inside the laser cavity and, every time the pulse is incident on one of the laser's facets, part of the pulse is emitted due to the finite reflectivity of the facets. There is also a difference in the generation rate of the optical pulses, because in Q-switching it depends on the biasing conditions whilst in modelocking it is fixed, and the time between pulses equals the time it takes the pulse to complete a cavity round trip.

Pulse widths as low as hundreds of femtoseconds¹⁰ and repetition frequencies as high as 500 GHz¹¹ have been achieved experimentally. Another advantage of modelocking techniques is that transform limited pulses can be achieved¹² without the necessity of external filters or diffractive gratings.

¹⁰ K. Tamura, E. Yoshida, E. Yamada and N. Nakazawa, "Generation of a 0.5 W average power train of femtosecond pulses at 10 GHz in the 1.55 μm region", *Electronics Lett.*, 1996, **32**, 9, pp 835-836.

¹¹ S. Arahira, S. Oshiba, Y. Matsui, T. Kunii and Y. Ogawa, "500 GHz optical short pulse generation from a monolithic passively mode-locked distributed Bragg reflector laser diode", *Appl. Phys. Lett.*, 1994, **64**, 15, pp. 1917-1919.

¹² M.C. Wu, Y.K. Chen, T. Tanbun-Ek, R.A. Logan, M.A. Chin and G. Raybon, "Transform-limited 1.4 ps optical pulses from a monolithic colliding-pulse mode-locked quantum well laser", *Appl. Phys. Lett.*, 1990, **57**, 8, pp. 759-761.

1.3 All-optical digital communications.

In order to realise ultrafast all-optical communication networks, such as the one described in section 1.1, most of the functions that in ‘today’s’ networks are implemented electronically, will have to be accomplished optically. In this section the necessary building blocks are described and the simplicity of optical processing for fulfilling some of these functions is analysed.

1.3.1 Optical switching.

All-optical switching is one of the most important functions for routing and demultiplexing data in an all-optical network.

In order to obtain optical switching, the so-called nonlinear optical loop mirror, shown in Figure 1.4, has been used³. A deep study of this all-optical AND gate is beyond the scope of this work, but it will be analysed briefly. The signal, operating at λ_s propagates both clockwise and anti-clockwise in the loop. In the absence of the control beam, operating at λ_c , the two signals interfering at the loop coupler can be adjusted with the polarisation controllers to be either fully reflected or transmitted. Optical switching is achieved by introducing the control beam, using wavelength dependent couplers, so that it travels in only one direction around the loop, clockwise in Figure 1.4. When a control pulse overlaps with a signal pulse, the phase of the clockwise signal is altered via *cross-phase modulation*¹³. The polarisation controllers are therefore adjusted so that when the clockwise and anti-clockwise signals now interfere at the loop coupler, the phase altered pulses are transmitted and the others are reflected.

All-optical switching can also be accomplished using Mach-Zehnder interferometers, as has been reported previously².

¹³ K. Smith, J.K. Lucek, R.J. Manning and K.J. Blow, “Advances in nonlinear optics for information processing and all-optical networking”, *Phil. Trans. R. Soc. London A*, 1996, **354**, pp. 707-717.

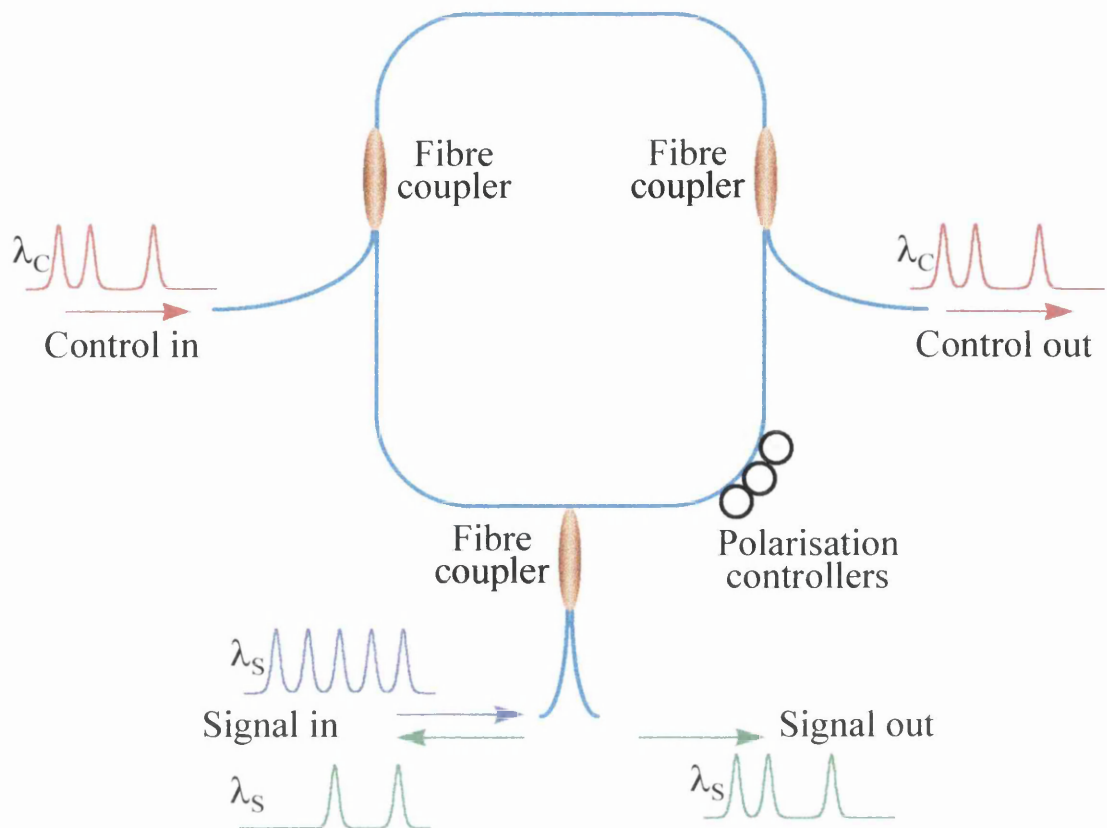


Figure 1.4: Diagram of the nonlinear optical loop mirror (NOLM).

1.3.2 Clock recovery.

It has been mentioned in section 1.1, that clock recovery is a very important issue in an all-optical network to achieve synchronisation between incoming data and control pulses in the processing centre where the data will be re-routed, demultiplexed, regenerated, etc. Different configurations have been used experimentally to obtain all-optical clock recovery, such as mode-locked optical fibre lasers¹⁴, optical tank circuits¹⁵, and self-pulsating and mode-locked semiconductor lasers^{16,6}. The operation of a clock recovery circuit, shown in Figure 1.5, is basically the same for all the above configurations: the clock recovery element, i.e. the fibre, semiconductor laser, or

¹⁴ K. Smith and J.K. Lucek, "All-optical clock recovery using a mode-locked laser", *Electronics Lett.*, 1992, **28**, 19, pp. 1814-1816.

¹⁵ M. Jinno and T. Matsumoto, "Optical tank circuits used for all-optical timing recovery", *IEEE J. Quantum Electron.*, 1992, **28**, 4, pp. 895-900.

¹⁶ U. Feiste, D.J. As and A. Ehrhardt, "18 GHz all-optical frequency locking and clock recovery using a self-pulsing two-section DFB-laser", *IEEE Photonics Technol. Lett.*, 1994, **6**, 1, pp. 106-108.

optical tank, through optical injection synchronises its own short pulse generation **in frequency and phase** with the incoming data stream and generates an optical clock pulse stream.

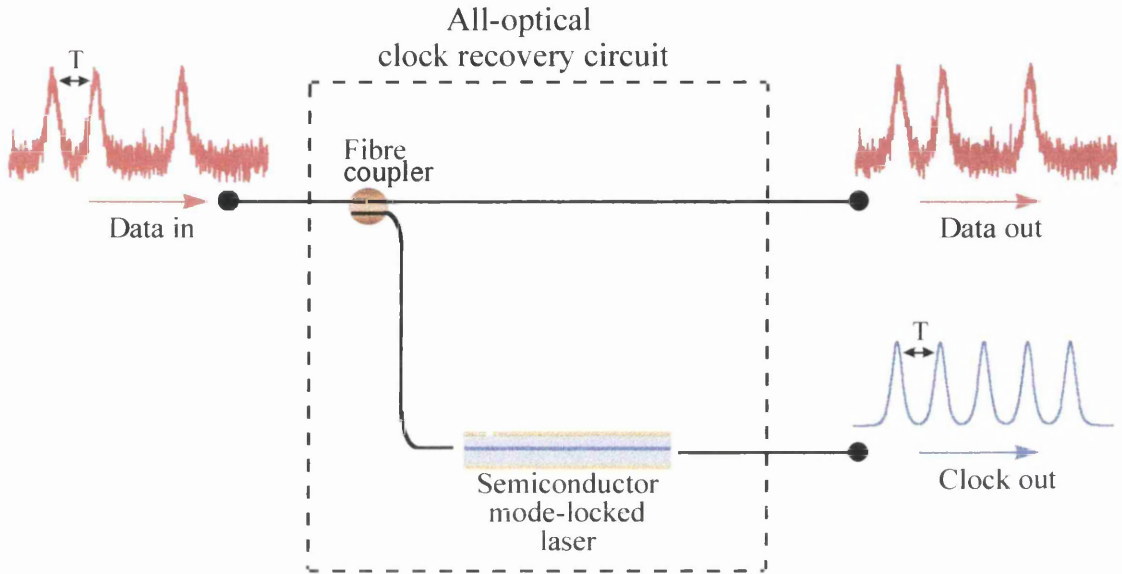


Figure 1.5: *Diagram of an all-optical clock recovery circuit using a mode-locked semiconductor laser.*

1.3.3 All-optical signal processing.

In this section we will analyse two examples of all-optical signal processing using the NOLM and the clock recovery circuit. The first one is an all-optical signal regenerator¹⁷. The regenerator consists of a clock recovery circuit connected to an NOLM, as shown in Figure 1.6. The data signal is injected into the clock recovery circuit, which produces an optical clock and the ‘old’ data signal at its output ports. The clock is then injected into the *data in* port of the NOLM and the ‘old’ data signal is injected into the *control in* port of the NOLM. In the NOLM, the clock pulses that coincide with the ‘old’ data signal pulses are transmitted out of the *data out* port, while the ones that do not coincide are reflected back to the *data in* port. Thus, an all-optical regenerated data signal is available at the *data out* port of the NOLM.

¹⁷ W.A. Pender, P.J. Watkinson, E.J. Greer and A.D. Ellis, “10 Gbit/s all-optical regenerator”, *Electronics Lett.*, 1995, **31**, 18, pp. 1587-1588.

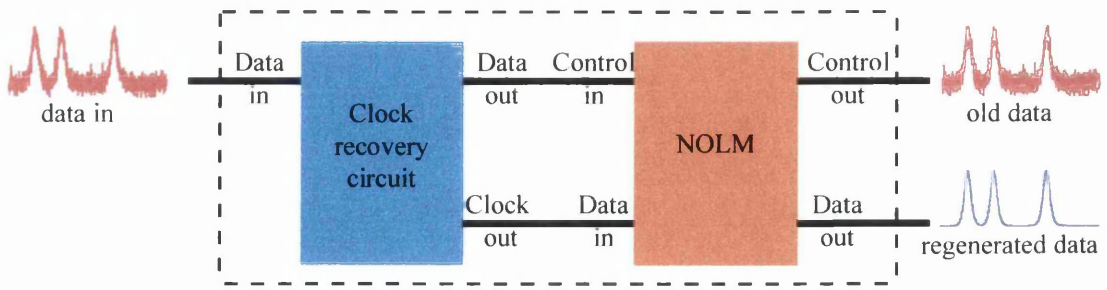


Figure 1.6: Schematic diagram of an all-optical signal regenerator.

The second example that will be analysed is that of all-optical demultiplexing. The first necessary element is a clock recovery circuit that synchronises with a sub-harmonic of the incoming data stream², instead of with the fundamental data stream frequency. This clock is then injected, through an specific delay, into an optical switch and the necessary channel can be demultiplexed, as can be seen in Figure 1.7.

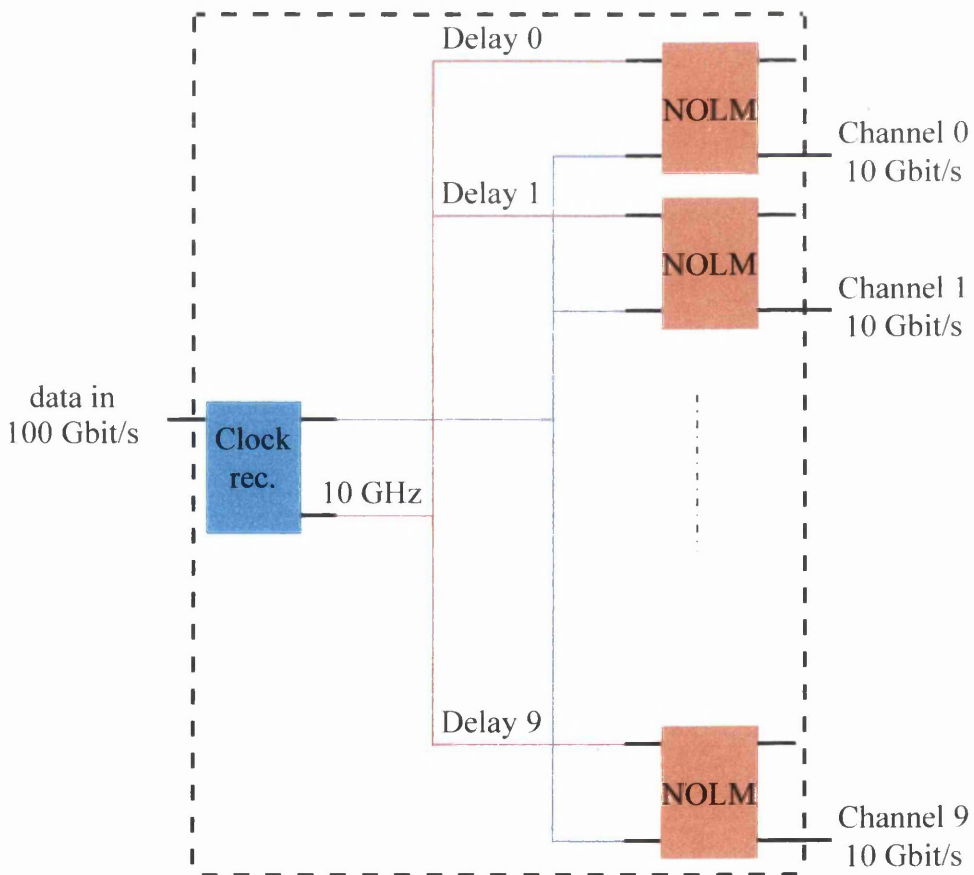


Figure 1.7: Schematic diagram of an all-optical demultiplexer.

The operation of the all-optical demultiplexer shown in Figure 1.7 is as follows; a OTM data stream at 100 Gbit/s, multiplexing ten channels at the base rate of 10 Gbit/s

is injected into the clock recovery circuit. The clock recovery circuit generates a clock at the base rate of the signal, 10 GHz, and, through different delays, is injected into the *control in* port of the NOLMs. The data stream is injected into the *data in* port of the NOLMs and thus, depending of the clock delay, the different optical channels can be selected.

1.4 Outline of the Thesis.

The main purpose of this thesis is to analyse different configurations of mode-locked semiconductor lasers and their applications as short pulse generators and clock recovery elements. It is organised as follows:

- in chapter 2, a brief study of light propagation in dielectric waveguides is given, followed by a short introduction to semiconductor lasers, both heterostructure and quantum well devices. This is followed by a deep analysis of the semiconductor laser material used for the device fabrication and the semiconductor laser fabrication procedure. This chapter finishes with a description of the experimental set-ups used for measuring the temporal and spectral behaviour of the semiconductor lasers.
- chapter 3 brings a review of modelocking in semiconductor lasers, the most widely used technique to generate short optical pulses, with special attention to passive modelocking.
- chapter 4, 5 and 6 describe the characteristics of the three different configurations of passively mode-locked semiconductor fabricated and tested, i.e. all-active cavity lasers, extended cavity lasers and external cavity lasers. They will show the advantages and drawbacks of each of them as short optical pulse generators.
- in chapter 7, the synchronisation of mode-locked semiconductor lasers with external signals is studied, and the tuneability of the modelocking frequency, under external excitation, is analysed. A theoretical analysis of the above configurations as clock recovery elements is also presented at the end of this chapter.
- chapter 8 summarises the results obtained in this thesis and presents the most important conclusions.

One of the most important characteristics of a semiconductor laser configuration is the ease and reliability of the fabrication process. Following a brief introduction about light guiding and semiconductor lasers, this chapter covers the fabrication of semiconductor mode-locked lasers, describing the material used in the fabrication, how it was characterised, structure of devices, step-by-step fabrication guide and the experimental set-up utilised to measure dynamics and spectral properties of the mode-locked lasers.

2.1 Optical modes in dielectric waveguides.

Light travelling in a dielectric waveguide, such as the semiconductor devices that will be analysed later in this chapter, travels in distinct *optical modes*, where a mode is a spatial distribution of the optical energy in one or more dimensions. In this section, an analysis of the optical modes in a dielectric waveguide, both in transversal and longitudinal directions, is performed.

2.1.1 Longitudinal modes: Fabry-Perot laser oscillation.

The Fabry-Perot laser interferometer, shown in Figure 2.1, is the most typical optical resonator, and it consists of two mirrors, to provide the necessary feedback, and a gain medium. The mirror reflectivities R_1 and R_2 are related to the electric field reflectances r_1 and r_2 through $R_1 \equiv r_1^2$ and $R_2 \equiv r_2^2$. The light electric field intensity in Figure 2.1, after one round trip, is given by

$$E_3 = E_1 r_1 r_2 e^{(g-\alpha)L - j2kL} \quad (2.1)$$

where g is the optical gain per cm in the medium, α is the optical loss per cm from processes such as free-carrier absorption, scattering and diffraction, L is the resonator length and k is the light propagation constant in the oscillator, given by $k = 2\pi n_{\text{eff}} / \lambda_0$ where n_{eff} is the effective refractive index for the wave within the

From Eq.(2.4) the optical frequencies *allowed* to resonate in the Fabry-Perot oscillator can be found. It gives

$$2kL = 2m\pi \quad (m = 1,2,3,\dots) \quad (2.6)$$

Introducing the value of the propagation constant in Eq.(2.6), the spacing of the Fabry-Perot or longitudinal modes in the oscillator is given by

$$f_m = \frac{c}{2n_{eff}L} \quad (2.7)$$

As mentioned above the output from a Fabry-Perot laser consists of a series of longitudinal modes. The frequency interval separating longitudinal modes in a semiconductor laser depends on the length of the resonator and on the refractive index and dispersion of the semiconductor material. For a typical GaAs/AlGaAs semiconductor laser 500 μm long, this separation between the longitudinal modes is around 0.2 nm. Figure 2.2 shows the optical spectrum of a 500 μm laser, just below threshold. It can be seen that the spontaneous emission is split up into peaks corresponding to modes of the Fabry-Perot cavity and, as mentioned above, with a separation around 0.2 nm.

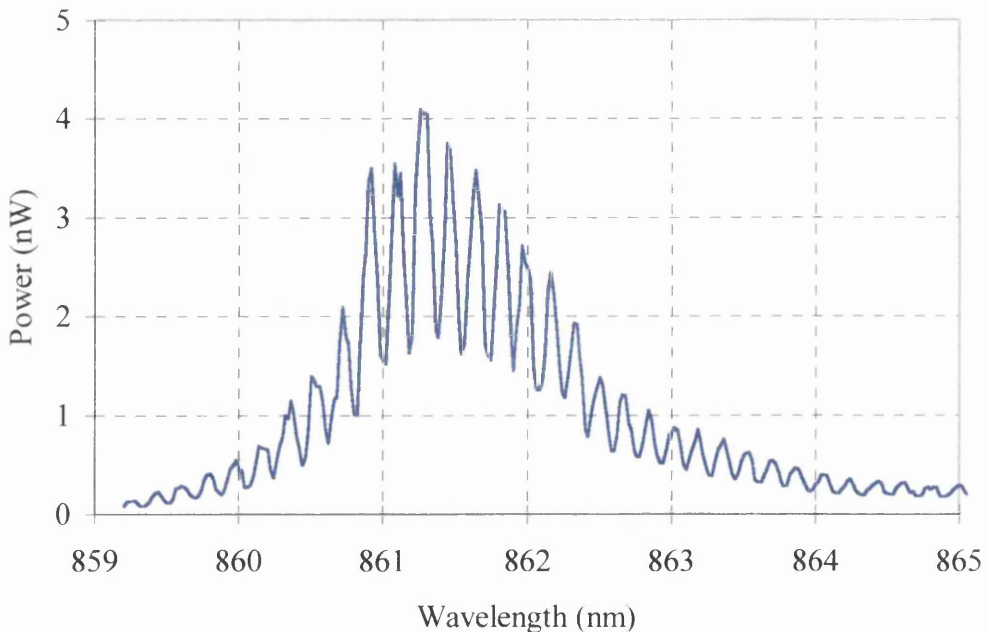


Figure 2.2: Longitudinal modes in a 500 μm long GaAs/AlGaAs laser.

2.1.2 Transversal modes I: dielectric slab waveguide.

In a three layer slab waveguide, a dielectric material with high refractive index n_2 and a thickness d is surrounded by two layers of a dielectric material with lower refractive indexes n_1 and n_3 , as shown in Figure 2.3. The effect of sandwiching the high index layer between the two low index layers is that a light beam will be confined or ‘guided’ due to total internal reflection at the layer interfaces. The bouncing beam would be expected to have a field distribution which is standing wave in the x direction within the high dielectric layer, and which is evanescent in the surrounding lower dielectric regions.

For the following analysis the refractive indexes n_1 and n_3 of the surrounding layers are considered equal, i.e. only the case of symmetric slab waveguide is analysed because it will be the case in the real structures that will be studied later in this chapter.

A formal analysis of the slab waveguide requires solving the Maxwell’s wave equation for the electric and magnetic fields. An alternative method is the so-called ray-optic approach, which will be used here¹. In this latter formulation, the light propagates in zigzag paths in the x - z plane, undergoing total internal reflection at the dielectric layer interfaces, as can be seen in Figure 2.3.

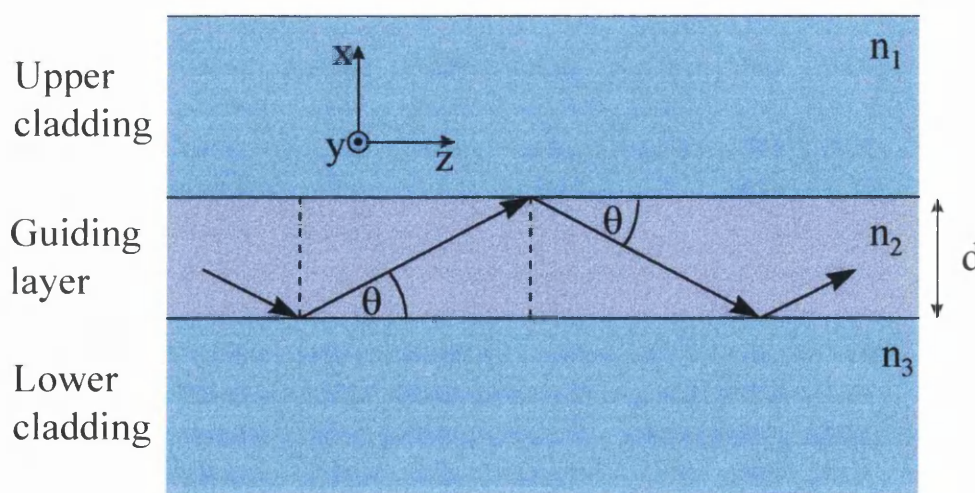


Figure 2.3: Schematic diagram of a three layer dielectric slab waveguide.

¹ R.G. Hunsperger, “Integrated optics: theory and technology”, Springer, 1995.

To avoid destructive interference of optical energy as the plane wave travels along the guiding layer, the total phase change of a point, moving in such a wavefront that travels from the interface between the layers 1 and 2 to the interface between the layers 2 and 3 and back again must be a multiple of 2π . This condition can be expressed as

$$2d k \sin(\theta_m) - 2\phi_{23} - 2\phi_{12} = 2m\pi \quad (m = 0,1,2,\dots) \quad (2.8)$$

where d is the thickness of the guiding layer, k is the propagation constant of the plane wave, given by $k = 2\pi n_2/\lambda_0$, θ_m is the angle of reflection with respect to the z direction, m is the mode number and ϕ_{23} and ϕ_{12} , the Goos-Hänchen shifts², are the phase changes suffered due to the total internal reflection at the interfaces. For the symmetric slab waveguide, $\phi = \phi_{23} = \phi_{12}$ and is given by¹

$$\tan(\phi^{TE}) = \frac{\sqrt{\cos^2(\theta) - \frac{n_1^2}{n_2^2}}}{\sin(\theta)} \quad (2.9)$$

$$\tan(\phi^{TM}) = \frac{n_2^2}{n_1^2} \frac{\sqrt{\cos^2(\theta) - \frac{n_1^2}{n_2^2}}}{\sin(\theta)} \quad (2.10)$$

where ϕ^{TE} and ϕ^{TM} are the Goos-Hänchen shifts for TE and TM polarised waves respectively.

Solving Eq.(2.8) with either Eq.(2.9) or Eq.(2.10), depending on the polarisation of the guided wave, the reflection angles θ_m corresponding to the different modes, can be obtained. It is also possible to solve Eq.(2.8) graphically, plotting $d k \sin(\theta) - m\pi$ and ϕ as functions of θ . Figure 2.4 shows the graphical solution for a typical slab waveguide propagating a TE polarised wave, with a core region of $\text{Al}_{0.2}\text{Ga}_{0.8}\text{As}$ ($n \sim 3.36$) 230 nm wide, surrounded by two layers of $\text{Al}_{0.4}\text{Ga}_{0.6}\text{As}$ ($n \sim 3.22$), an approximation of the real structure for the dielectric waveguides used in this work. It can be seen that, for these values, the waveguide is single moded in the x direction, and the angle of the internal reflections of the propagating wave is θ_0 .

² D.L. Lee, "Electromagnetic principles of integrated optics", Wiley, 1986.

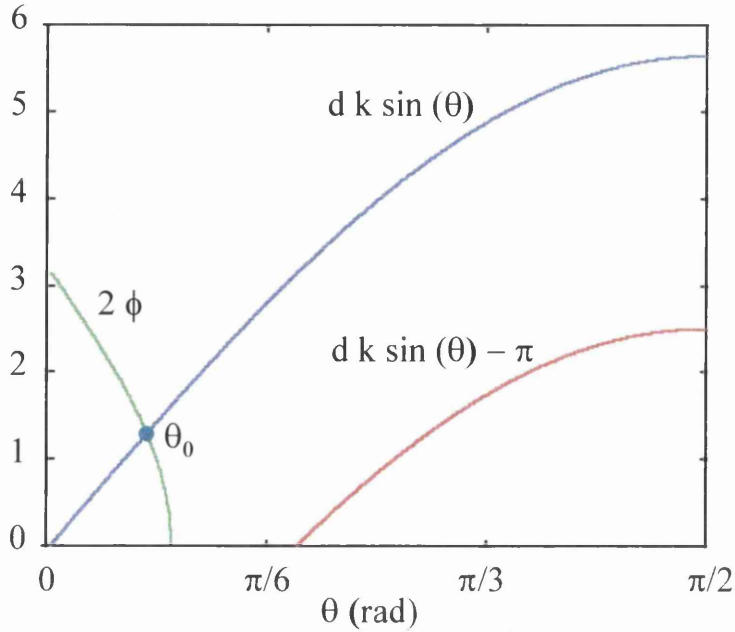


Figure 2.4: Graphical solution for the allowed modes in a symmetrical slab waveguide.

For each allowed mode, there is a corresponding propagation constant in the z direction given by

$$\beta_m = k \cos(\theta_m) \quad (2.11)$$

and an effective refractive index given by

$$n_{eff_m} = n_2 \cos(\theta_m) \quad (2.12)$$

When a mode cannot propagate in a waveguide is said to be ‘cut-off’. The ‘cut-off’ condition for the TE or TM polarised waves is found by solving Maxwell’s wave equation for the electric and magnetic fields^{1,2}. For a TE polarised wave, it is given by

$$\frac{k d}{n_2} \sqrt{n_2^2 - n_1^2} = m\pi \quad (m = 0,1,2,\dots) \quad (2.13)$$

Figure 2.5 shows the ‘cut-off’ condition for the zeroth to the third order modes, where $\Delta n = n_2 - n_1$. From this graph it is possible to calculate the maximum width of a waveguide, such as the one analysed in Figure 2.4, for it to be single mode in the x direction. With Δn equal to 0.14, as it is the case of the dielectric slab analysed above, the ‘cut-off’ condition for the first order mode is $d/\lambda_0 = 0.521$. For an operating

wavelength of 860 nm, the maximum width of the guiding layer, for the slab waveguide to be single mode, is found to be around 450 nm.

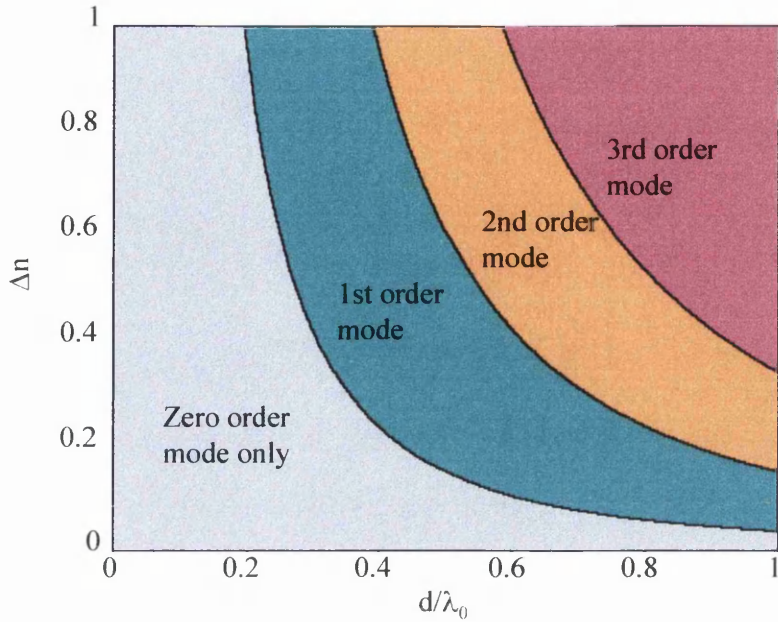


Figure 2.5: Mode cut-off conditions for a symmetric three layer slab waveguide.

2.1.3 Transversal modes II: stripe geometry waveguide.

The slab waveguide analysed above provides optical confinement in just one dimension (x dimension in Figure 2.3), but it is more usual to require confinement in both transversal dimensions. It is possible to fabricate a waveguide with confinement in both the x and y directions as depicted in Figure 2.6, named *strip-loaded waveguide*.

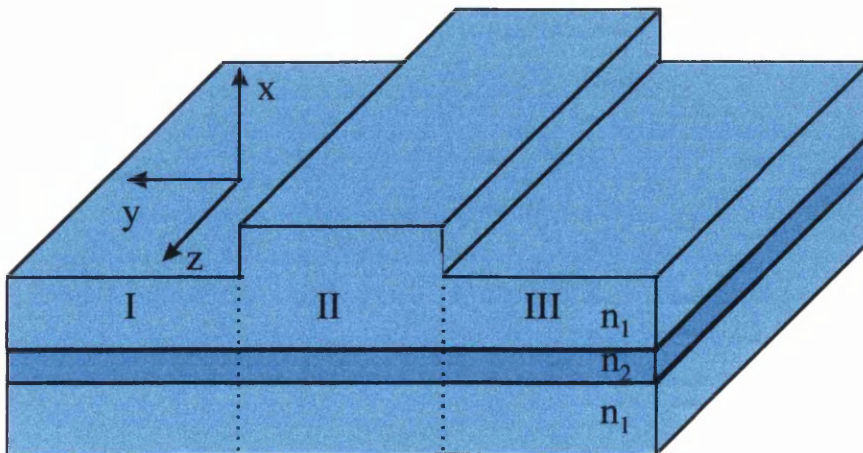


Figure 2.6: Diagram of dielectric strip-loaded waveguide.

The exact analytical solution of Maxwell's wave equations for the electric and magnetic field for this structure is not possible, but a simple approach is to use the *Effective Index Method*². The effective index method is based on calculating the effective refractive index of the regions I, II and III of the strip-loaded geometry. The presence of the strip makes the effective index of region II larger than the effective index in the adjacent regions I and III, and thus there is confinement in the y direction as well as in the x direction. The strip-loaded waveguides used in this work were simulated with Fwave IV, a program based on the effective index method which solves the vector electromagnetic wave equation using a finite difference implementation. Results are presented in section 2.4.1

2.2 Introduction to semiconductor lasers.

The semiconductor laser diode is an excellent light source for use in optoelectronic integrated circuits (OEICs) and optical fibre communications because of its small size, efficiency, simple fabrication and high reliability.

Laser operation in semiconductor devices was first demonstrated in 1962 by three different groups of workers. The laser was fabricated in GaAs, and consisted of a single p-n junction operated at cryogenic temperature. Figure 2.7 shows this basic structure of a p-n junction laser. The ohmic contacts are made to permit the flow of electrical current which is the pumping energy source of the device.

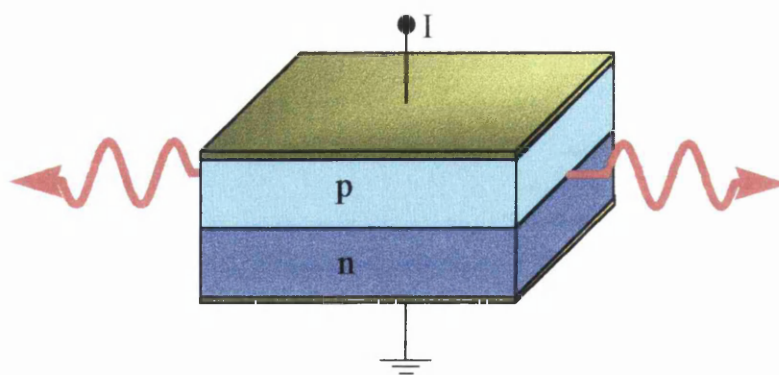


Figure 2.7: *Basic structure of a p-n junction laser.*

The basic original design formed from just a p-n junction, named a *homostructure laser*, evolved with the introduction of heterojunctions, and eventually the *double*

heterostructure laser allowed room temperature operation by confining electrons, holes and photons in the same region, *the active region*, of the device.

2.2.1 Heterostructure lasers.

Heterostructure lasers are fabricated from semiconductors with a composition in which one or two of the constituent elements can be replaced in any proportion by certain other elements, as (AlGa)As or (InGa)(AsP) where the elements in the brackets can be mutually substituted. An example of the GaAs/AlGaAs type of laser can be seen in Figure 2.8, where a thin undoped layer of GaAs, *the active layer*, is sandwiched between two layers of $\text{Al}_x\text{Ga}_{1-x}\text{As}$ of opposite doping, *the cladding layers*. This figure shows the band energy diagram, under forward bias, and the distribution of refractive index and light intensity in the double heterostructure laser.

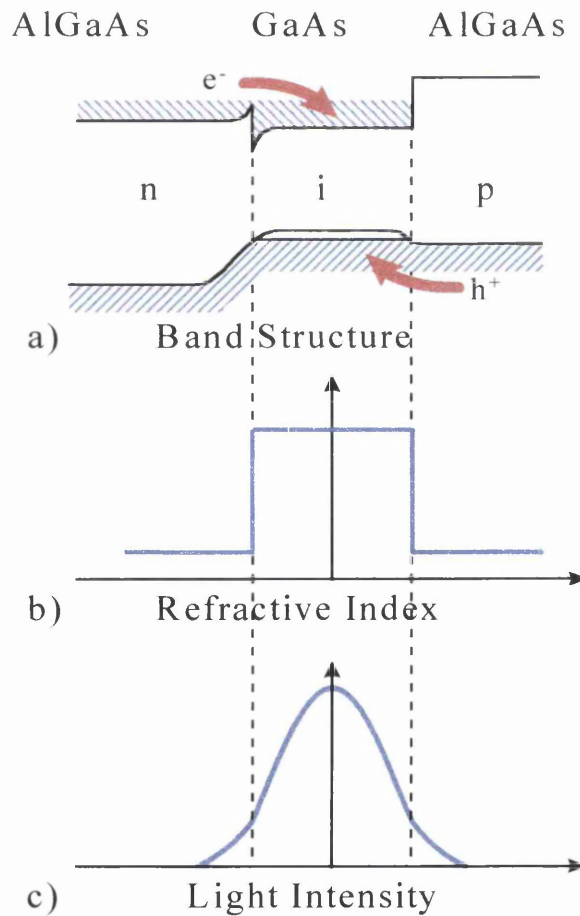


Figure 2.8: Double heterostructure device profiles of a) potential of conduction and valence bands under forward bias, b) index of refraction and c) light intensity.

The GaAs/Al_xGa_{1-x}As double heterostructure laser has two properties which distinguish it from the homostructure laser:

- The larger index of refraction of the active layer confines photons and guides the optical wave between the two cladding layers. The dependence of the index of refraction with x can be approximated³ as $\Delta n \sim -0.7x$.
- The band discontinuities in the conduction and valence bands confine the electrons and holes within the active layer. The dependence of the bandgap energy can be approximated³ for $x < 0.42$ as $\Delta E_g \sim 1.266x$ eV.

The threshold condition for a Fabry-Perot double heterostructure laser can be obtained from Eq.(2.3), by introducing the optical confinement factor Γ . The confinement factor represents the fraction of the mode power carried within the active region, according to

$$\Gamma = \frac{\int_{-d/2}^{+d/2} |E(x)|^2 dx}{\int_{-\infty}^{+\infty} |E(x)|^2 dx} \quad (2.14)$$

where d is the active layer thickness. Introducing the confinement factor in Eq.(2.3), the threshold current for the double heterostructure device can be written as

$$\Gamma g_{th} = \Gamma \alpha_A + (1 - \Gamma) \alpha_C + \frac{1}{2L} \ln \frac{1}{R_1 R_2} \quad (2.15)$$

where α_A is the internal loss coefficient of the active layer and α_C is the loss coefficient in the cladding layers.

2.2.2 Quantum-Well lasers.

When the thickness of the active layer in a double heterostructure laser is reduced to less than 200 Å, the confined electrons and holes display quantum effects⁴. These

³ A. Yariv, "Quantum Electronics", John Wiley & Sons, 1989.

⁴ N. Holonyak, R.M. Kolbas, R.D. Dupuis, P.D. Dapkus, "Quantum-well heterostructure lasers", *IEEE J. Quantum Electron.*, 1980, **QE-16**, 2, pp. 170-185.

structures will show *quasi two-dimensional* properties, with the free motion of the carriers occurring just in two dimensions, perpendicular to the growth direction.

The use of quantum wells has several effects:

- a) Energy levels in the conduction and valence bands become quantized. These confined states are found by solving Schrödinger's equation under the appropriate boundary conditions⁵, which will not be done here. Figure 2.9(a) shows the square well potential characteristics of a quantum well device. Due to the fact that the electrons and holes are confined to the quantized energy states, lasing occurs at energies determined by the bandgap and confining energies, i.e. the energy of the photons emitted by radiative recombination for $n=1$ (e1-hh1) would be given by $h\nu = E_g + E_{c1} + E_{hh1}$. Figure 2.9(b) shows the solution for Schrödinger's equation, for the first three energy levels, in the *infinite deep well* approximation.

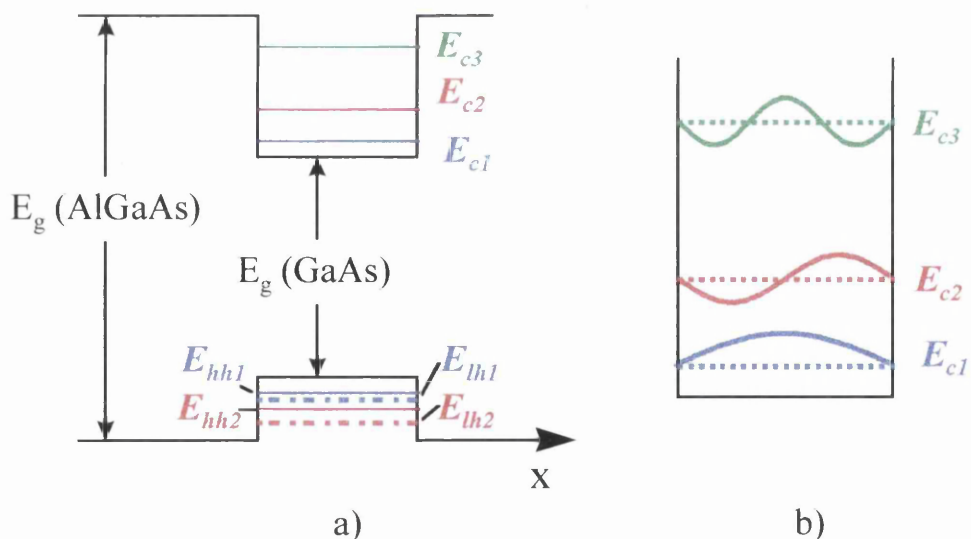


Figure 2.9: (a) Square-well potential characteristics of a GaAs/Al_xGa_{1-x}As quantum well heterostructure and (b) energy levels and wave functions of an infinite deep well after Weisbuch et al.⁶.

⁵ J. Davies, Lecture notes presented at University of Glasgow.

⁶ C. Weisbuch and B. Vinter, "Quantum Semiconductor Structures", Academic Press, 1991.

b) The density of states in a quantum well laser becomes *quasi*-two-dimensional. Figure 2.10 shows the densities for the 2D and 3D systems. One important point is that the 2D-density of states is finite, whereas the 3D one tends to zero when the energy tends to zero. This has fundamental consequences for 2D systems as all dynamic phenomena remain finite at low kinetic energies and low temperatures.

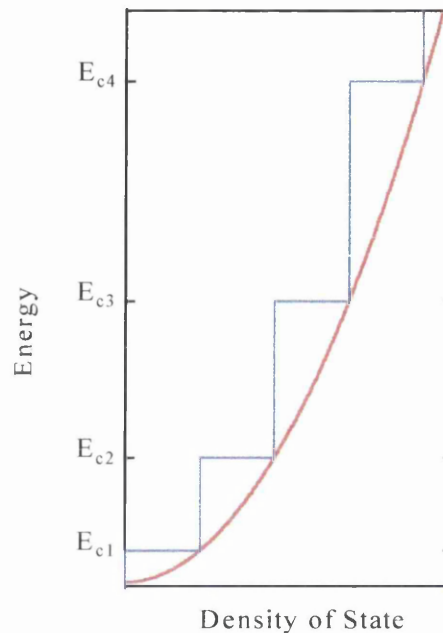


Figure 2.10: *Two-dimensional density of states (blue) and comparison with the three dimensional case (red) after Weisbuch et al⁶.*

c) For very thin layers the confinement factor Γ is very small, which means that the optical wave is not confined within the active layer and leaks into the cladding layers. To overcome this effect the *separate confinement heterostructure* is used, as shown in Figure 2.11. In the separate confinement heterostructure, the quantum wells are surrounded by two layers with lower refractive indexes (waveguide layers); all these layers form the active layer, and they are surrounded by two layers of an even lower index, the cladding layers. Therefore, the optical wave is confined within the waveguide layers and the confinement factor per quantum well is increased in comparison with the simple quantum well structure, as can be seen in Figure 2.11.

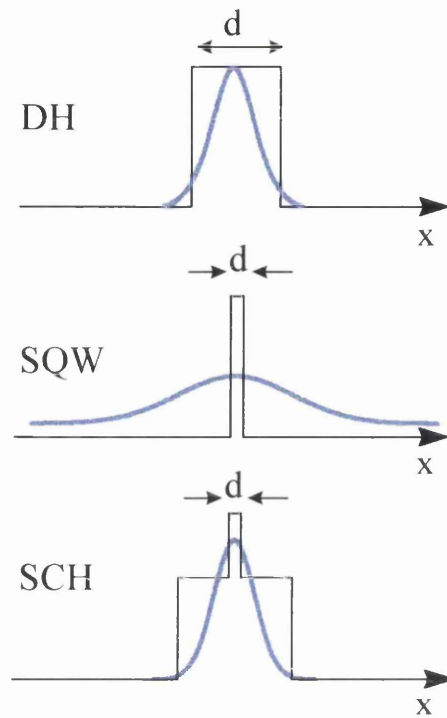


Figure 2.11: *Schematics of index of refraction (black) and the intensity of an optical guided wave (blue) for double heterostructure (DH), single quantum well (SQW) and separate confinement heterostructure (SCH) waveguides.*

2.3 Semiconductor material analysis.

Before fabricating devices, it is very important to assess the quality of the semiconductor material. The material should have low internal optical losses and high efficiency. For GaAs material, the internal optical losses are expected³ to be less than 10 cm^{-1} , while the internal quantum efficiency should be close to 1. In this section, a semiconductor material analysis technique is described and results for different wafers of semiconductor material are presented.

2.3.1 Material structure.

The semiconductor material was grown by metal organic vapour phase epitaxy (MOVPE) at Sheffield University. The structure, shown in Figure 2.12, was grown on a GaAs substrate, doped to $1.5 \cdot 10^{18} \text{ cm}^{-3}$ with silicon. This was followed by a $0.1 \mu\text{m}$ GaAs buffer layer doped to 10^{18} cm^{-3} with silicon and a $1.5 \mu\text{m}$ $\text{Al}_{0.4}\text{Ga}_{0.6}\text{As}$ cladding

layer also doped with silicon to $8 \cdot 10^{17} \text{ cm}^{-3}$. The active layer consisted of two 10nm GaAs wells separated by a 10nm $\text{Al}_{0.2}\text{Ga}_{0.8}\text{As}$ barrier and they were surrounded by two 0.1 μm $\text{Al}_{0.2}\text{Ga}_{0.8}\text{As}$ waveguide layers. All these guiding layers were undoped. The upper cladding layer was a 0.9 μm $\text{Al}_{0.4}\text{Ga}_{0.6}\text{As}$ layer doped to $5 \cdot 10^{17} \text{ cm}^{-3}$ with carbon. The contact layer was a 0.1 μm GaAs layer heavily doped with zinc ($8 \cdot 10^{18} \text{ cm}^{-3}$). This type of structure with two waveguide layers sandwiching the quantum wells is called a *separate confinement heterostructure*, section 2.2.2, and is used to overcome the effect of the poor optical confinement in standard quantum well structures. With this structure the optical confinement is provided by the two guiding layers surrounding the quantum wells, while the carrier confinement occurs in the quantum wells.

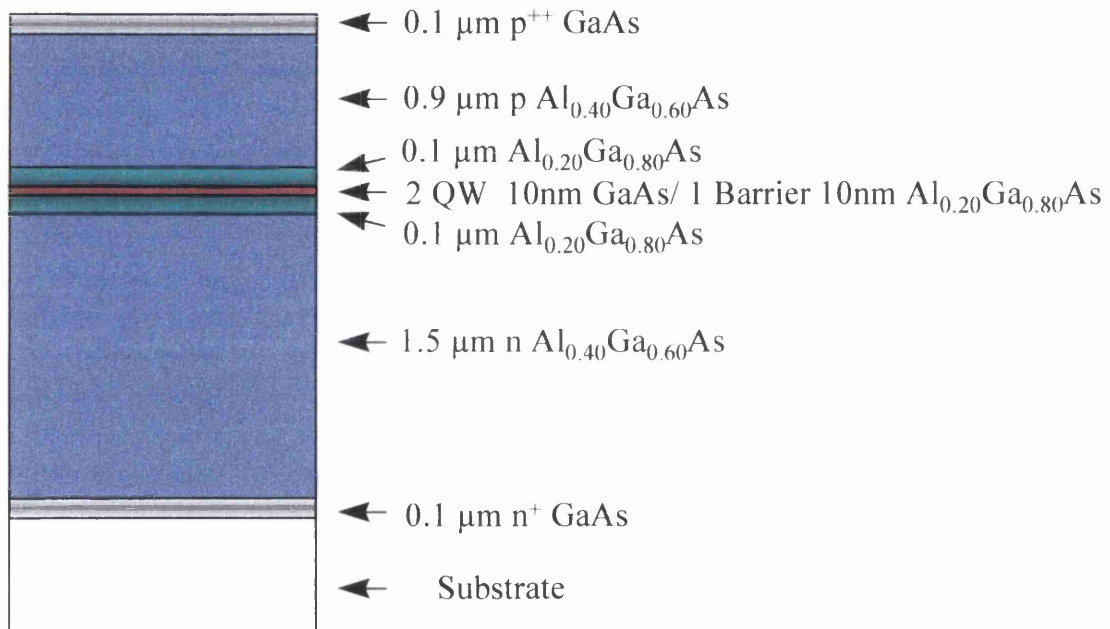


Figure 2.12: *Material structure of semiconductor laser.*

2.3.2 Material characterisation.

To define the quality of a semiconductor laser material the following characteristics must be obtained:

- * Internal optical losses α_i , losses per cm in the active layer, mainly due to free carrier absorption.
- * Internal quantum efficiency η_i , representing the fraction of carrier recombination that is radiative and therefore participates in gain.

- * Infinity threshold current density J_{∞} in A/cm^2 , defined as the threshold current density for a infinitely long laser.
- * Transparency current density J_T in A/cm^2 , defined as the current needed per well to obtain an stimulated emission rate of photons equal to the absorption rate.
- * Gain parameter g_0 in cm^{-1} per well, which is the maximum gain coefficient as defined by McIlroy *et al*⁷.
- * Optical confinement factor Γ_w per well, defined as the ratio of the light intensity within a quantum well to the sum of light intensity both within and outside the quantum well. The optical confinement factor, for the structure used in this work and depicted in Figure 2.12 is 2.75%.

Characterisation of the semiconductor material is performed by fabricating SiO_2 insulated stripe lasers, or oxide stripe lasers (OSL), with 75 μm wide stripes and different lengths, and measuring the light-current (L-I) curves. From these L-I curves all the above material characteristics can be found, as will be shown. The OSL is good for such characterisation because the gain guiding structure of the OSL is free from the scattering losses present in index guided structures such as ridge waveguide lasers. The wide stripe also reduces the error in determining current densities due to the reduction of current spreading in the upper cladding layer⁸.

Two important relationships will be used to characterise the material. The first relates the optical gain in the laser cavity at threshold to the loss. Threshold is defined as the condition when the net gain in the laser cavity first becomes unity, as analysed in section 2.1.1. Eq.(2.15) shows the gain threshold for double heterostructure lasers, which can be written as follows for a quantum well laser

⁷ P.W.A. McIlroy, A. Kurobe and Y. Uematsu, "Analysis and application of theoretical gain curves to the design of multi-quantum-well lasers", *IEEE J. Quantum Electron.*, 1985, **QE-21**, 12, pp.1958-1963.

⁸ G.H.B. Thompson, "Physics of Semiconductor Laser Devices", *John Wiley & Sons*, 1980.

$$n\Gamma_w g_{th} = \alpha_i + \frac{1}{L} Ln \left[\frac{1}{R} \right] \quad (2.16)$$

where the optical gain is considered constant over the entire length of the laser cavity, n is the number of quantum wells, α_i is the internal modal loss coefficient, L is the laser length and R is the facet reflectivity, considered equal for both facets.

Eq.(2.16) shows that, at threshold, the optical gain must be equal to the optical losses in the cavity plus the losses due to the finite reflectivity of the facets. The internal losses are due mainly to free carrier absorption and can be expressed as⁹

$$\alpha_i = \Gamma \alpha_A + (1 - \Gamma) \alpha_C \quad (2.17)$$

where α_A and α_C are losses coefficients for the active and cladding layers respectively, and Γ is the optical confinement factor for the active region, i.e. quantum wells, barrier and waveguide layers.

The second equation gives the external slope efficiency above threshold η_{ext} , i.e. the conversion of the injected electrons into optical output power in photons as follows⁸

$$\eta_{ext} = \eta_i \left[1 - \frac{\alpha_i}{n\Gamma_w g_{th}} \right] \quad (2.18)$$

Combining both Eq.(2.16) and Eq.(2.18) the relation between the external slope efficiency and the laser length is found as

$$\frac{1}{\eta_{ext}} = \frac{1}{\eta_i} - \left(\frac{\alpha_i}{\eta_i Ln[R]} \right) L \quad (2.19)$$

From the above equation, it can be seen that, by plotting the reciprocal of the external efficiency, measured in photons per electron, against the laser length, and assuming a value for the facets' reflectivity, the internal losses and the internal quantum efficiency can be found.

⁹A. Sugimura, "Threshold currents for AlGaAs quantum well lasers", *IEEE J. Quantum Electron.*, 1984, **QE-20**, 4, 336-343.

The optical gain for multiple quantum well lasers, up to threshold, can be approximately related to the current density in the laser cavity as

$$\frac{g}{g_0} = \text{Ln} \left[\frac{J \eta_i}{J_T n} \right] \quad (2.20)$$

where J and g are the total injected current density and gain respectively and n is the number of quantum wells^{7,10}.

Figure 2.13 shows a typical gain curve for a quantum well laser, with the modal gain being equal to $n\Gamma_w g$. It was calculated for a device with two quantum wells, with $g_0=1000 \text{ cm}^{-1}$, $\Gamma_w=2.75\%$, $\eta_{\text{int}}=75\%$ and $J_T=90 \text{ A/cm}^2$, realistic parameters for semiconductor laser material, as will be shown.

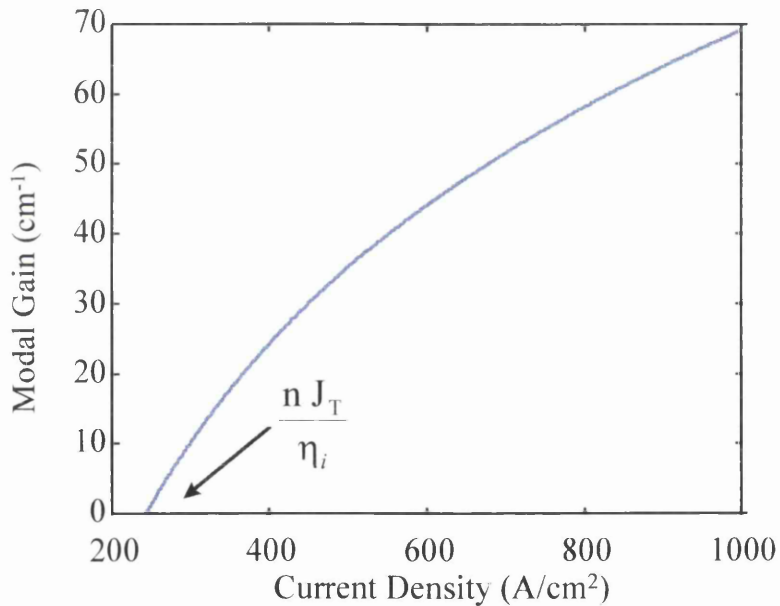


Figure 2.13: Gain curve for a SCH-DQW laser.

Combining Eq.(2.16) and Eq.(2.20), at threshold it is found that

¹⁰ A. Kurobe, H. Furuyama, S. Naritsuka, N. Sugiyama, Y. Kokubun and M. Nakamura, "Effects of well number, cavity length, and facet reflectivity on the reduction of threshold current of GaAs/AlGaAs multi-quantum well lasers", *IEEE J. Quantum Electron.*, 1988, **24**, 4, pp. 635-640.

$$\text{Ln}(J_{th}) = \left[\frac{\alpha_i}{n\Gamma_w g_0} + \text{Ln}\left(\frac{nJ_T}{\eta_i}\right) \right] - \left(\frac{\text{Ln}[R]}{n\Gamma_w g_0} \right) \frac{1}{L} \quad (2.21)$$

By plotting the natural log of the threshold current density versus the reciprocal of the cavity length, the factor $n\Gamma_w g_0$ can be found from the slope of the graph by assuming a value for the reflectivity R , and J_∞ is the intercepting point where $1/L$ is 0. Hence, using the value for the internal losses and the internal quantum efficiency calculated from the plot of the reciprocal of the external efficiency versus the laser length, the transparency current density and the gain parameter of the wells can be found.

Three different semiconductor wafers have been used for device fabrication, QT753, QT757 and QT855, all of them grown by MOVPE at Sheffield University. A detailed analysis for the first wafer is performed, and the results obtained for all of them are presented.

To perform the characterisation of the semiconductor material, OSL lasers were cleaved with different lengths: 200, 300, 500, 600, 700, 900, 1000 and 1200 μm . Light-current (L-I) curves were measured under pulsed excitation, using 400 ns long pulses at 1 kHz, which gave a duty cycle of 0.04%. A 1 cm^2 area silicon photodiode was used to measure the optical power from the laser. The detector was connected to a boxcar integrator, which averaged over the gated input signal. From the L-I curves, the threshold current in A and external efficiencies in W/A were measured.

Figure 2.14 shows the L-I curves for two devices, 200 and 500 μm long, fabricated from the wafer QT753, and both of them from the same batch of lasers. From this figure the threshold current for both devices can be measured, being 85 mA and 155 mA for the 200 and 500 μm long device respectively, which corresponded to threshold density currents of 567 A/cm^2 and 413 A/cm^2 respectively.

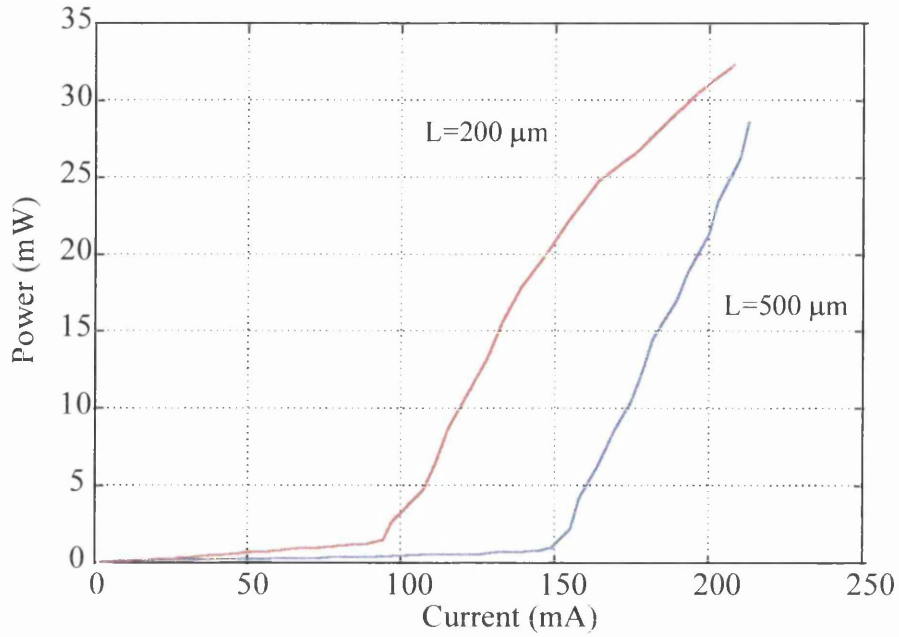


Figure 2.14: *L-I curve from two OSL laser, 200 μm long (red) and 500 μm long (blue).*

To introduce the external efficiency in Eq.(2.19) it must be converted into photons per electron. Thus, the quantum efficiency is found from

$$\eta_{ext}(\text{Photon} / \text{Electron}) = \frac{\lambda(\text{nm})}{1240} \eta_{ext}(\text{W} / \text{A}) \quad (2.22)$$

where λ is the lasing wavelength. For the L-I curve shown in Figure 2.14, the external efficiency is around 0.28 photon per electron per facet for the 200 μm long device and 0.3 photon per electron per facet for the 500 μm long one.

Including the external efficiencies of the three lasers with the lowest threshold currents, for each cavity length, Figure 2.15 is obtained. The interception at $L=0$ gives the internal quantum efficiency, around 74 %. From Eq.(2.19), and assuming a facet reflectivity of 0.32, the internal losses are found to be around 3.1 cm^{-1} .

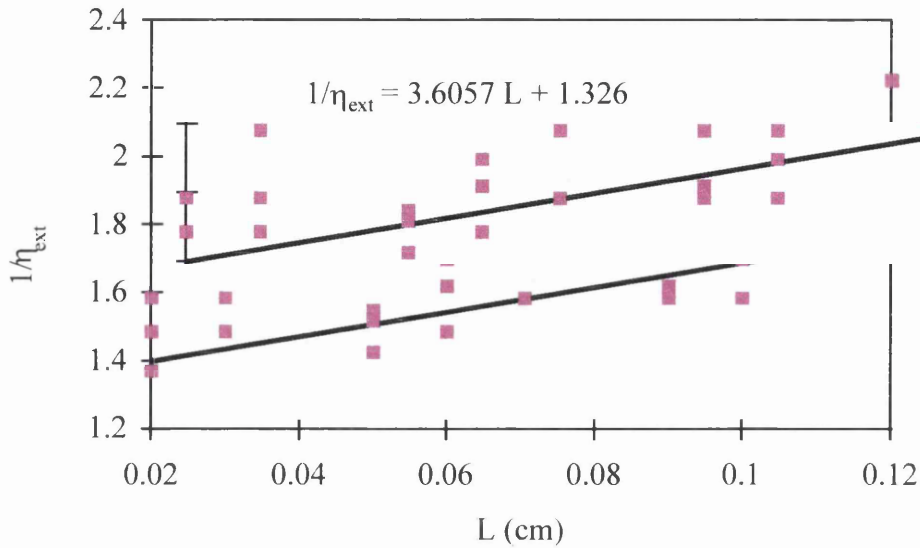


Figure 2.15: *Reciprocal of the external efficiency versus the laser length.*

Again using results from the lasers with the three lowest threshold currents, Figure 2.16 is obtained, in which the natural log of the threshold current density is plotted versus the reciprocal of the cavity length. From Eq.(2.21), and again assuming a facet reflectivity of 0.32, the quality of the active layer, and therefore the quantum wells can be assessed obtaining the transparency current density and the gain parameter. For this material, $J_t=90 \text{ A/cm}^2$ and $g_0=1035 \text{ cm}^{-1}$.

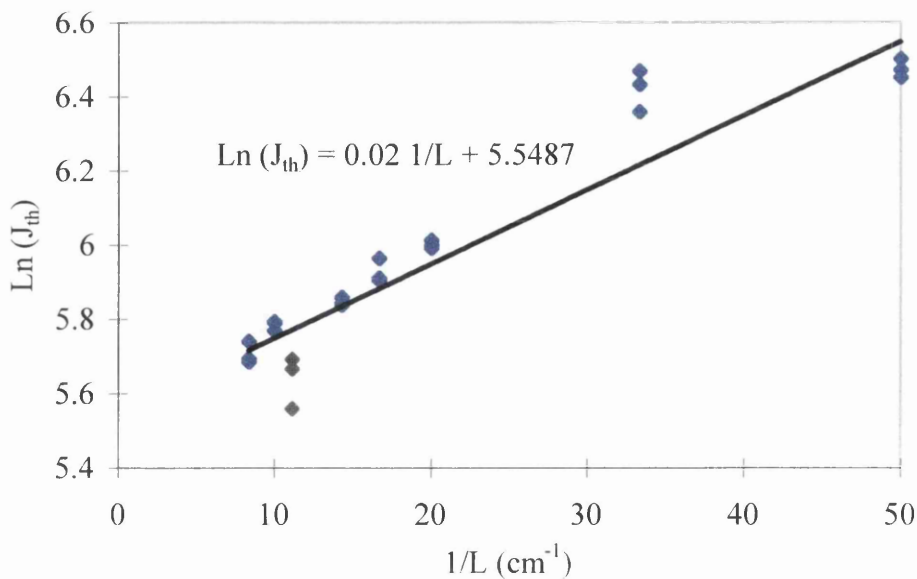


Figure 2.16: *Natural log of the threshold current density versus the reciprocal of the cavity length.*

Table 2.1 shows the results for all the semiconductor material wafers used for device fabrication. It is important to notice that, even if the internal losses are very low indicating high quality material, the internal efficiency values are lower than expected. This is most probably due to slightly inaccurate external efficiency measurements, i.e. due to the light from the laser not being completely coupled into the detector or if the detector is out of calibration, etc.

	QT 753	QT 757	QT 855
η_{int} (%)	74	70	70
α_i (cm^{-1})	3.1	5.2	4.8
J_{∞} (A/cm^2)	256	216	256
J_T (A/cm^2)	90	68	80
g_0 (cm^{-1})	1035	865	770

Table 2.1: *Material characteristics of the wafers used for device fabrication.*

2.4 Device fabrication and characterisation.

The main interest of this work is to analyse the generation of short optical pulses at rates around 10-20 GHz, because they are essential for future high speed optical communications systems. Mode-locked semiconductor lasers are chosen for this purpose because they are compact and reliable pulse sources but, due to the fact that the repetition rate of the mode-locked pulse train is inversely proportional to the cavity length, very long cavity lengths, usually an order of magnitude longer than more common semiconductor lasers, must be fabricated.

The three different semiconductor mode-locked laser configurations that have been fabricated and tested are depicted in Figure 2.17. They are:

- a) *All active cavity semiconductor mode-locked laser.* This configuration, with the laser cavity divided into two sections, is the easiest to fabricate, but it has the drawback of having the highest threshold current, due to the fact that the whole laser cavity is pumped.

- b) *Extended cavity semiconductor mode-locked laser.* This configuration, with three sections, has very low threshold currents because the integrated passive waveguide is not pumped, but it requires extra-fabrication stages to form the low-loss waveguide.
- c) *External cavity semiconductor mode-locked laser.* This configuration does not have any of the previous drawbacks, but it has mechanical instability problems. Both the above configurations are monolithic cavity devices, which are small in size and do not have the mechanical instabilities associated with the optical elements in an external cavity.

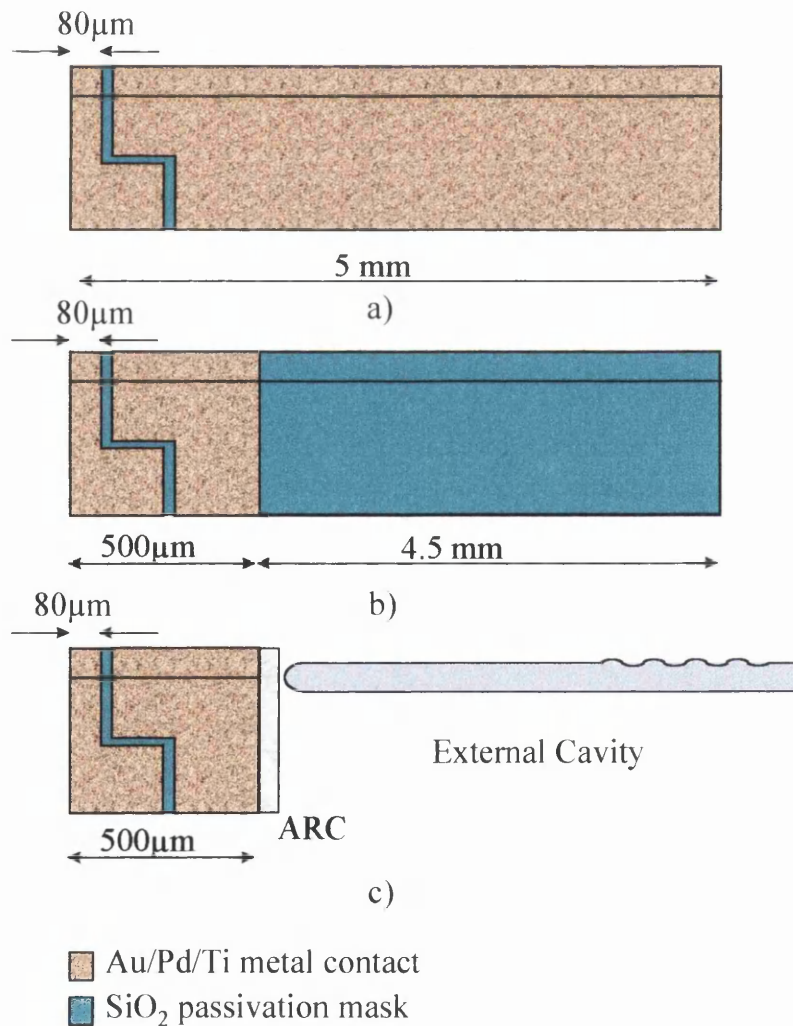


Figure 2.17: *Semiconductor mode-locked laser configurations: a) All active cavity, b) Extended cavity and c) External cavity.*

2.4.1 Analysis of device structure.

The heterostructure layers in a semiconductor laser confine the light and the injected carriers in the direction perpendicular to the layers due to the difference in refractive index and bandgap energy of the layers, as mentioned in section 2.2.1. In most laser applications, lateral confinement of both carriers and light is also needed, which provides advantages, such as reduction of the threshold current and fundamental transversal mode operation in comparison with broad area lasers without lateral confinement. These types of lasers with confinement of both carriers and light in the junction plane are called “stripe lasers”. There are different structures for stripe lasers, such as oxide stripe lasers, buried heterostructure stripe lasers and ridge waveguide lasers. This last configuration is the one used in this work. Figure 2.18 shows the cross section of the ridge waveguide laser structure. In this type of laser, the main design variables are the ridge width and the distance a between the centre of the active layer and the etched upper cladding layer. This distance determines the strength of the guiding and, combined with the ridge width, determines the propagation of higher transverse modes accompanying the fundamental mode. To achieve single transverse mode operation⁸, ridges 3 μm wide and 0.75 μm deep were fabricated, which gave a distance a of around 0.25 μm .

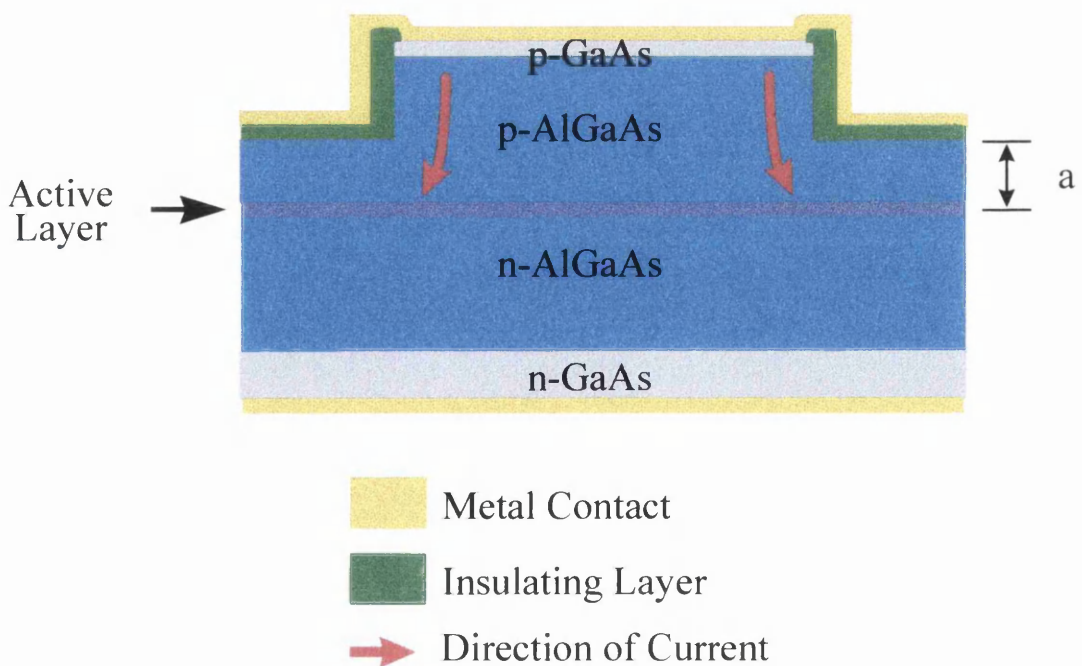


Figure 2.18: Ridge waveguide stripe laser structure.

Numerical calculations of the modal distribution of the light in the laser cavity were performed with Fwave IV, as mentioned in section 2.1.3. Figure 2.19 depicts the electric field profile of the fundamental TE mode propagating along the ridge waveguide. The magnitude of the field components are shown, with the outermost contour being the 1% of the peak field value, and the others are at 10% increments from 10 to 90%.

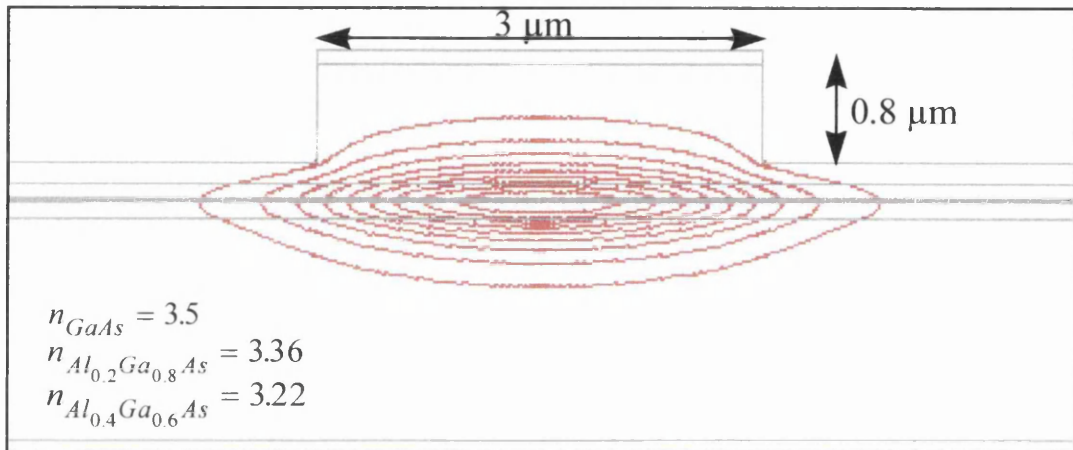


Figure 2.19: *Fwave IV simulation of the electric field of the fundamental TE mode propagating along the ridge waveguide. Material structure equal to that shown in Figure 2.12.*

2.4.2 Device fabrication.

In this section the detailed fabrication process of the semiconductor lasers is described. The fabrication technique is a self-alignment process developed by Dr. P. Cusumano in the Department of Electronics and Electrical Engineering of the University of Glasgow. The fabrication technique of the ridge waveguide mode-locked laser is as follows:

a) Material Preparation.

The material is cleaved into $8 \times 8 \text{ mm}^2$ pieces using the wafer scribe. The scribing must follow the crystal orientation of the semiconductor material (Figure 2.20(a)).

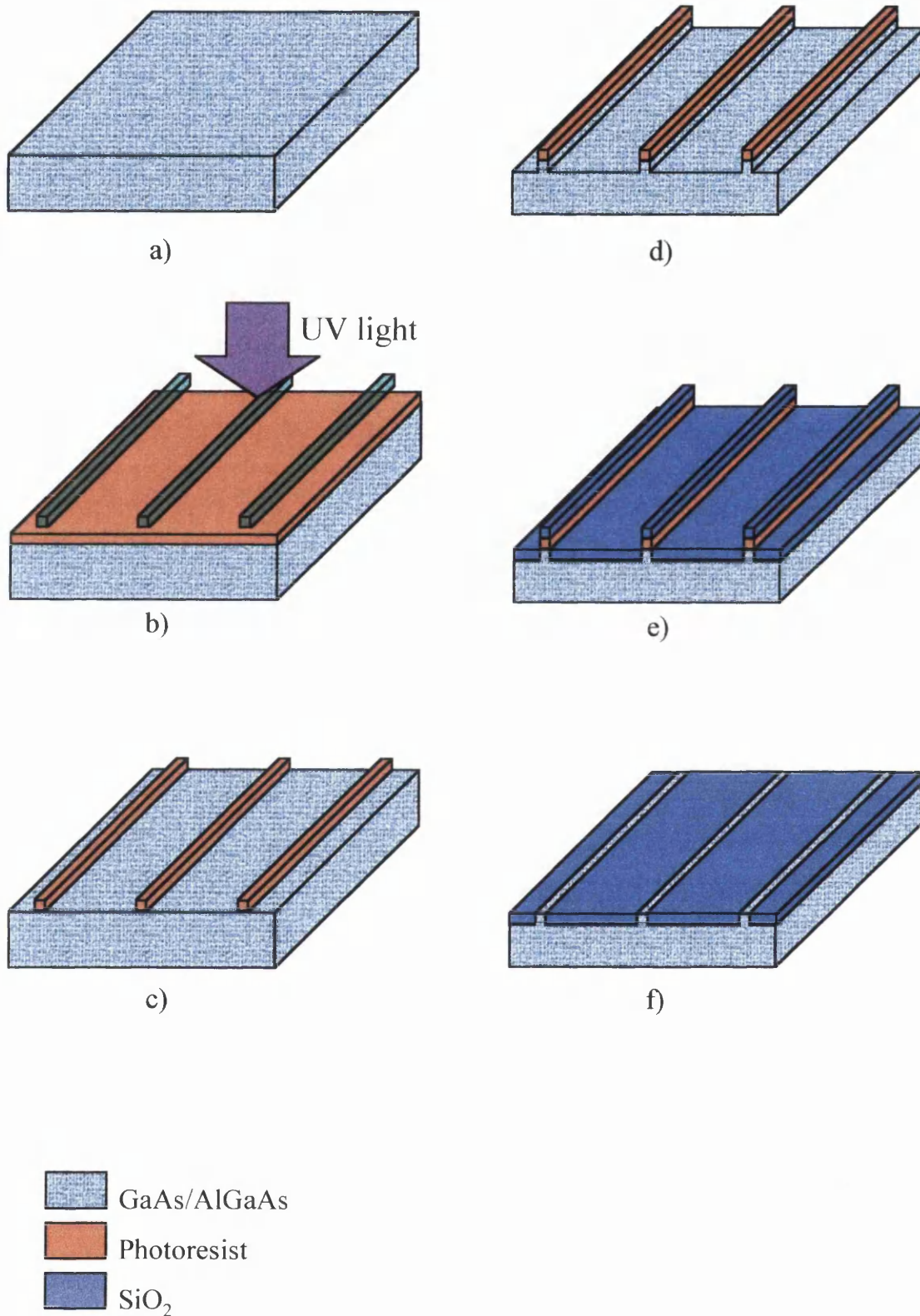
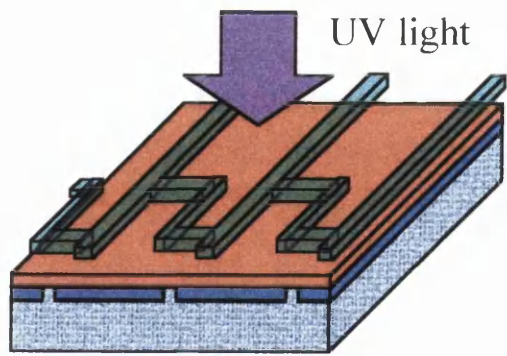
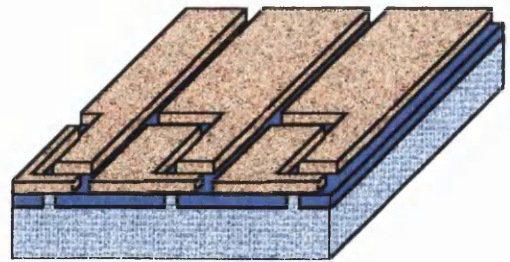


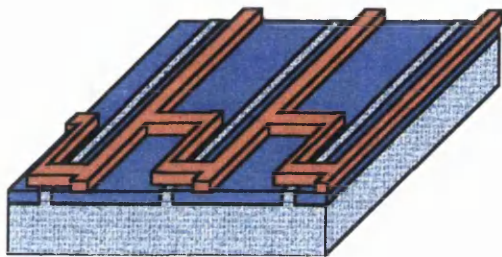
Figure 2.20: *Fabrication stages: a) sample cleaving, b) waveguide patterning, c) waveguide developing, d) waveguide etching, e) silica deposition, f) silica lift off.*



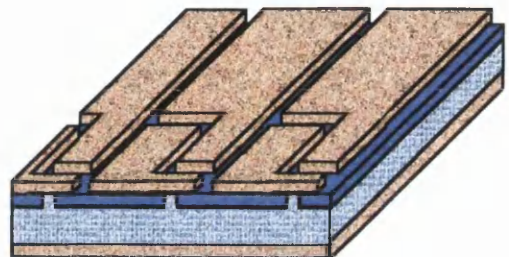
g)



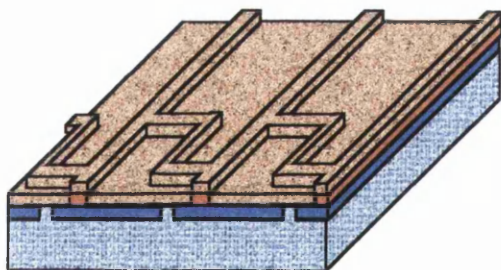
j)



h)



k)



i)

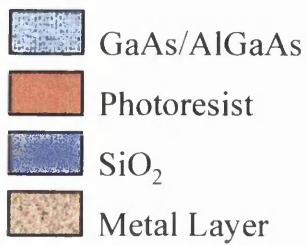


Figure 2.20: *Fabrication stages: g) contact patterning, h) contact developing, i) p-contact deposition, j) p-contact lift off, k) n-contact deposition.*

The sample was cleaned by immersion in organic solvents using the *standard cleaning procedure* which is as follows: the sample was cleaned first in acetone (C₃H₆O) and then in methanol (CH₃OH), in an ultrasonic bath for five minutes for each solvent. After flushing and rinsing in deionised water (RO water) the sample was blown dry and left to dry in an oven at 90°C for five minutes. For more dirty samples an initial cleaning stage of five minutes in opticlear in an ultrasonic bath was necessary.

b) First photolithography stage.

Photoresist Shipley S1818 was now put down onto the sample to transfer the ridge pattern to the substrate. The photoresist was spun at 4000 rpm for 30 seconds, and its thickness at this speed was 1.8 µm. A thick resist was used for the waveguide definition because it subsequently was used to lift off a silica layer that was deposited over them, as will be shown in the following sections. The sample was now baked at 90°C for 30 minutes. The ridge waveguides' pattern was then transferred to the photoresist, perpendicular to the sample cleavage planes, using the mask aligner and exposing the resist to UV light for 10 s (Figure 2.20(b)).

The resist pattern was developed in a 50:50 mix of Microposit developer and RO water. The sample was immersed in the developer for 75 seconds and then rinsed in RO water and blown dry (Figure 2.20(c)).

c) Waveguide definition.

The waveguides were defined by etching the material, with the photoresist acting as an etching mask. For the GaAs/AlGaAs system, a Reactive Ion Etch (RIE) machine using SiCl₄ plasma was used. “Dry” etching was chosen, instead of “wet” etching, because it produced much cleaner and more vertical waveguide sidewalls. Wet etching has no preferential etching direction, which leads to isotropic circular profiles and undercuts the etching mask¹¹, as it can be seen in Figure 2.21. Ideal dry etching produces an anisotropic profile because the electric field in the etching chamber makes ions strike horizontal surfaces almost exclusively at normal incidence.

¹¹ D. M. Manos and D. L. Flamm, “Plasma Etching”, *Academic Press* 1989.

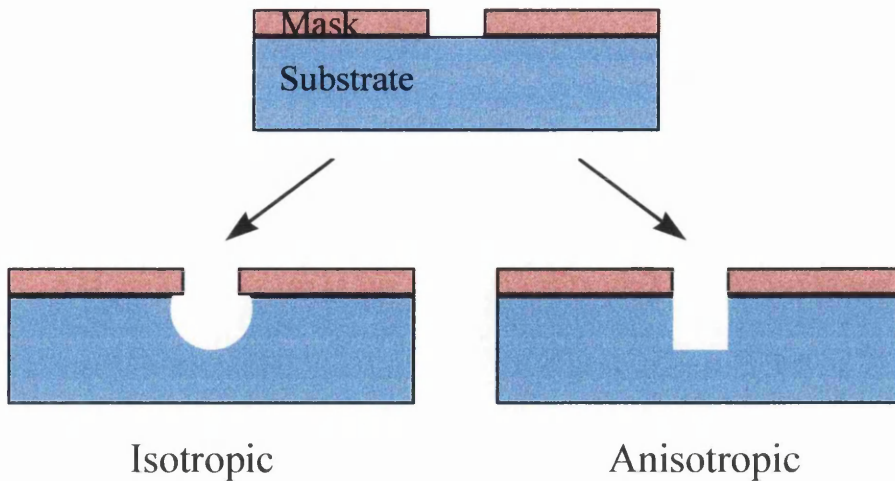


Figure 2.21: *Left: Isotropic etching; the horizontal and vertical etch rates are equal, right: anisotropic etching; the horizontal etch component is very insignificant.*

The sample was etched to leave a thickness of 250 nm above the active layer to form the ridge waveguides, i.e. an etching depth of 750 nm. The etching depth was *in-situ* monitored by laser reflectance measurements, which gave a very accurate waveguide depth (Figure 2.20(d))

d) Silica deposition and lift off.

A 200 nm thick layer of SiO_2 was now deposited by electron-beam evaporation at room temperature over the whole sample surface (Figure 2.20(e)). It was very important to deposit this silica layer at room temperature because, if the photoresist was exposed to very high temperatures (e.g. PECVD silica is deposited heating up the sample at 300°C) it was not possible to remove it from the sample. By placing the sample in acetone in an ultrasonic bath for 20-30 seconds, the silica on top of the ridges was lifted off (Figure 2.20(f)).

e) Second photolithography stage.

Before metallisation, it was necessary to perform another photolithography stage to pattern the two contacts of the p-side metal layer. A new layer of photoresist S1818 was spun, and baked at 90°C for fifteen minutes. The sample was then soaked in chlorobenzene ($\text{C}_6\text{H}_5\text{Cl}$) for 15 minutes, which improved the metal layer lift off

process. The sample was baked for another 15 minutes at 90°C, and was then patterned to define the metallised section of the laser using the mask aligner and exposing the resist to UV light for 10 s (Figure 2.20(g)).

As before, the photoresist was developed using Microposit developer and RO water (Figure 2.20(h)).

f) p-Side metallisation.

A Ti/Pd/Au p-side metal layer was evaporated onto the sample, forming an Schottky contact¹² with the sample GaAs contact layer (Figure 2.20(i)). The sample was then immersed in acetone until all the metal on top of the photoresist lifted off (Figure 2.20(j)).

g) Two-sections isolation.

To improve the electrical isolation between both sections, the highly doped GaAs contact layer was removed. This contact layer was wet etched by immersing the sample in ammonia diluted in peroxide (NH₃-1, H₂O₂-20) for 6 seconds. This etching solution has a high selectivity between GaAs and AlGaAs, which makes it very suitable for this purpose.

To measure the resistance between both sections, a HP semiconductor parameter analyser was used. Probing both contacts of the semiconductor laser, a voltage was applied between both sections and the injected current was measured. Figure 2.22 shows the two section voltage-current curve (left axis) and the dynamic resistance-voltage curve (right axis), the former being measured using the HP semiconductor parameter analyser and the latter being the derivative of the voltage-current curve. The typical resistance between both sections was around 5 to 6 kΩ. As mentioned above, the p-metal contact formed a Schottky contact with the semiconductor, giving a noticeable nonlinearity to the voltage-current curve, and therefore to the dynamic resistance curve.

¹² D. K. Schroder, "Semiconductor material and device characterisation", *John Wiley & Sons*, 1990.

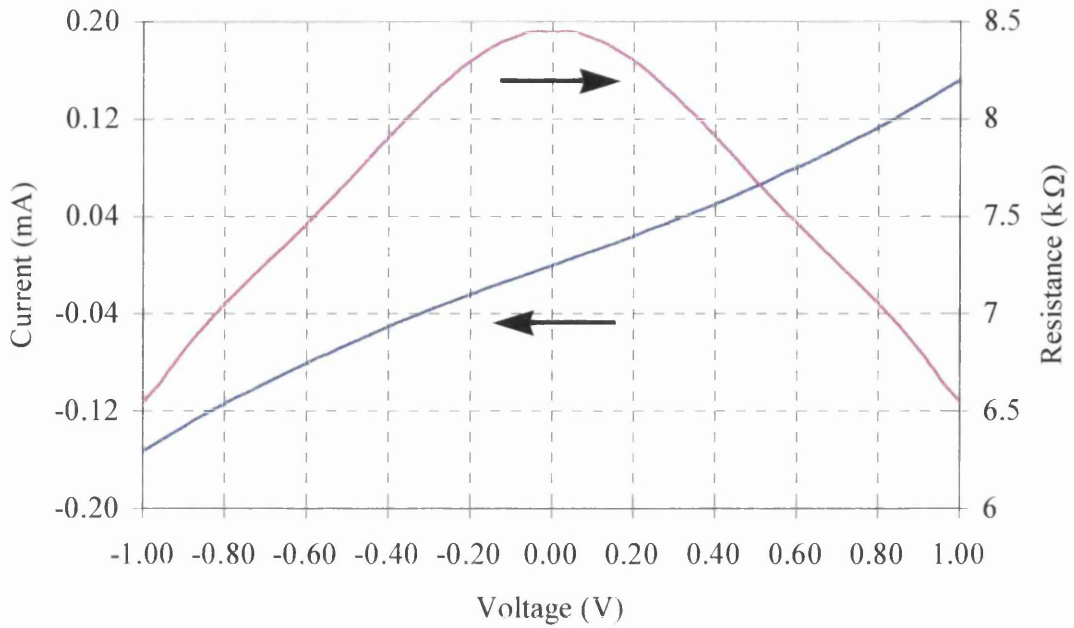


Figure 2.22: *Voltage-current curve and dynamic resistance-voltage curve for the two sections.*

h) n-Side metallisation.

Before the evaporation of the n-side metal layer, the sample was thinned to reduce the substrate thickness to around 160-180 μm . This was achieved by mechanically polishing the substrate with 9 μm and 3 μm Al_2O_3 powder. The sample was then cleaned in a refluxing condenser with boiling solvents to ensure the removal of the wax used during the substrate thinning. This cleaning stage consisted of immersion in opticlear for 30 minutes, followed by 20 minutes in acetone.

The sample was now ready for the n-metal evaporation. An ohmic contact was formed with the evaporation of Au/Ge/Au/Ni/Au (Figure 2.20(k))¹².

The contacts were now annealed at 360°C for 60 seconds, which reduced the resistance of the contacts. The performance of semiconductor lasers is generally degraded by series resistance, which arises from the semiconductor resistivity, the contact resistance and sometimes depends on geometrical factors. The diode current

as a function of the applied voltage is given by¹³

$$I = I_0(e^{qV/nkT} - 1) \quad (2.23)$$

where V is the applied voltage and n is the ideality factor. When series resistance contributes to device behaviour the current-voltage expression becomes

$$I = I_0(e^{q(V-Ir_s)/nkT} - 1) \quad (2.24)$$

where r_s is the series resistance. Obviously, the bigger the series resistance the poorer the laser diode efficiency becomes in converting injected power into optical output power. High series resistance also has the problem of heat effects as the power dissipated in the series resistance will generate heat which will degrade the overall operation of the laser diode.

Figure 2.23 depicts a typical current-voltage curve for a ridge laser, also measured with an HP parameter analyser, showing a turn-on voltage of around 1.3 V and a dynamic resistance of 20 Ω .

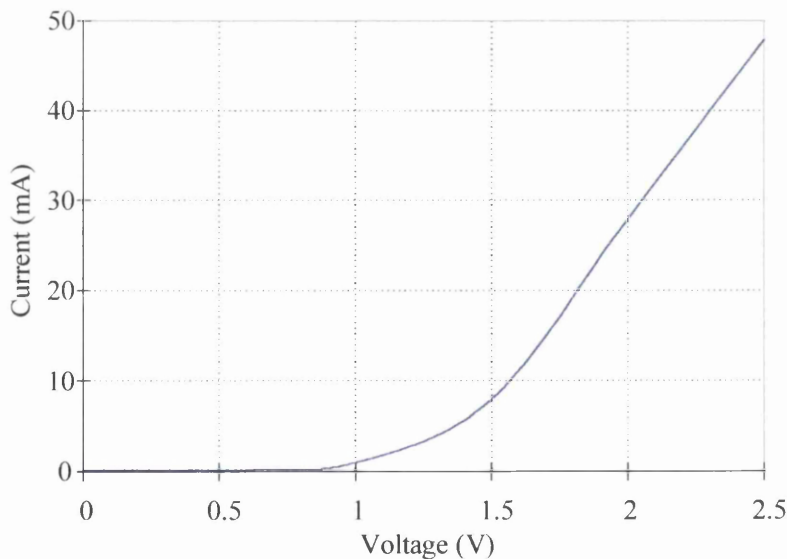
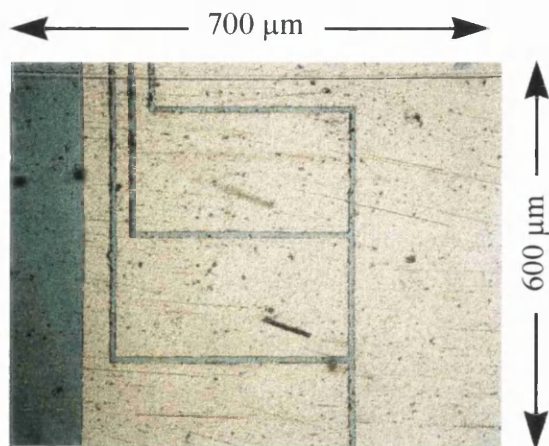


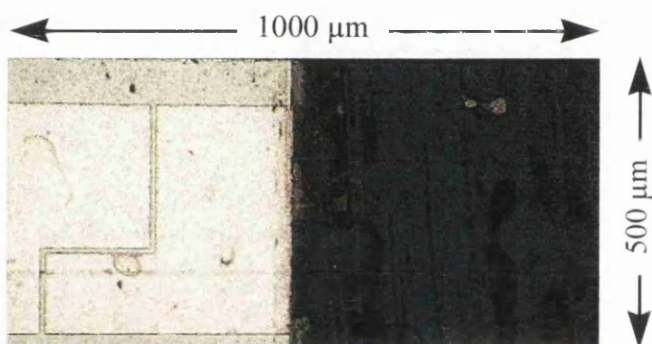
Figure 2.23: *Voltage-current curve of a laser diode.*

The lasers were now ready for cleaving and testing. Accurate cleavage was one of the most important and difficult issues of the laser fabrication because the “health” of a semiconductor laser depended greatly on the cleaved facets.

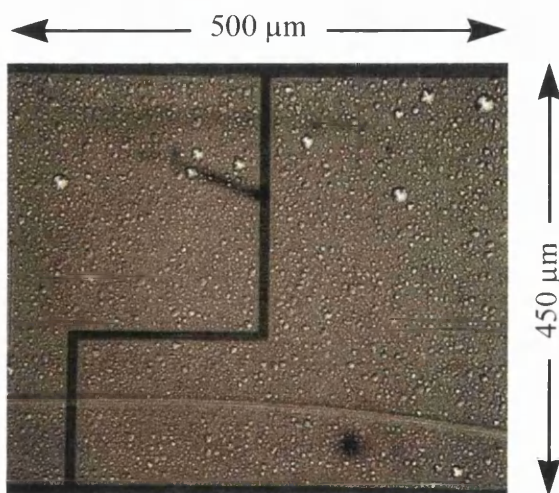
¹³ S.M. Sze, “Physics of semiconductor devices”, *John Wiley and Sons*, 1981.



a) All-active cavity mode-locked laser



b) Extended cavity mode-locked laser



c) Bent waveguide laser.

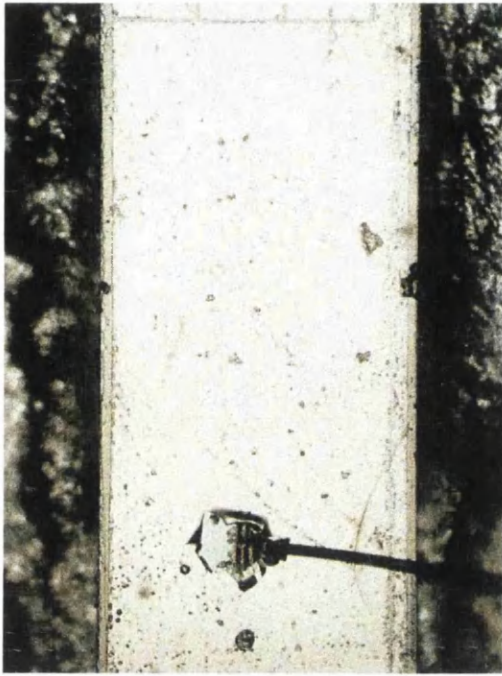
Figure 2.24: Photograph of fabricated devices: a) all-active cavity laser, b) extended cavity laser and c) bent waveguide laser.

Figure 2.24 shows photographs of fabricated semiconductor lasers which were ready to cleave (these configurations will be analysed in following chapters). Figure 2.24(a) shows a close-up of a 5 mm long all-active cavity laser. It can be seen that the saturable absorber was divided into three sections, the one closest to the facet being 40 μm long and the other two 20 μm . The ridge waveguide was 3 μm wide. Figure 2.24(b) shows part of a 4 mm long extended cavity laser, with a saturable absorber 50 μm long and a gain section 450 μm long. The ridge waveguide also was 3 μm wide. Figure 2.24(c) shows a 500 μm long bent waveguide laser, with a waveguide bending angle of 8° , a saturable absorber 50 μm long and a gain section 450 μm long. In this case the ridge waveguide was 5 μm wide

Once the lasers were cleaved, they were tested and the L-I characteristics were obtained, measured under pulsed excitation. The lasers with the lowest threshold currents were soldered with indium to a copper heatsink coated with gold. The process was accomplished using a die bonder. Both laser contacts were now wire bonded, using 25 μm gold wire, to contact pads glued to the copper heatsink from which the electrical connections to the powers supplies were made. This ultrasonic bonding was performed with a wire bonder. After wire bonding, the lasers were ready for experimental research.

Figure 2.25 shows photographs of two devices that were soldered to copper heatsinks and wire bonded. Figure 2.25(a) shows part of a 5 mm long all-active cavity laser and Figure 2.25(b) shows a 500 μm long two-section laser. The main difficulties when soldering the devices and when wire bonding them can be seen in this figure:

- a) the problem when soldering the device is that the indium or the flux used for the soldering process can overflow under the device. If this overflowing happens at the side of the devices, as in Figure 2.25(a), it is not a problem, but if flux or indium goes to the facet of the devices they will be ruined.
- b) the problem when wire bonding is that it is a 'violent' process. That is the reason why sometimes the bonded contact is damaged, as in Figure 2.25(a) and Figure 2.25(b).



a)



b)

Figure 2.25: *Photograph of mounted and bonded devices: a) 5 mm long all-active cavity laser and b) 500 μm two-section laser.*

2.4.3 Experimental set-up.

Figure 2.26 shows the experimental set-up used in most of the mode-locked laser characterisation research carried out in this work. First of all, the use of lensed fibres is noticeable, instead of the more usual arrangement where the light from the laser diode is collimated or focused through external lenses. The coupling of radiation from a diode laser into a single-mode optical fibre represents a significant source of inefficiency in many optoelectronics applications. The difficulties of designing a high coupling efficiency element include the very high angular divergence of the radiation from a semiconductor laser, the divergence difference in the two orthogonal directions and the small dimensions of emitting area and fibre core. An attractive approach to this problem was to form the required lens surface directly on the end of the optical fibre. There are various techniques for producing a variety of lens profiles on a single-

mode fibre end¹⁴, however the lensed fibres used in this work were made by fusing the cleaved end of a single mode fibre using an optical fibre fusion splicer. This technique produced lensed fibre with measured coupling losses of around 6 dB, results not far from the optimum of around 3 dB obtained with tapered lensed fibres¹⁵, and much better than the 10 dB losses obtained using external lenses.

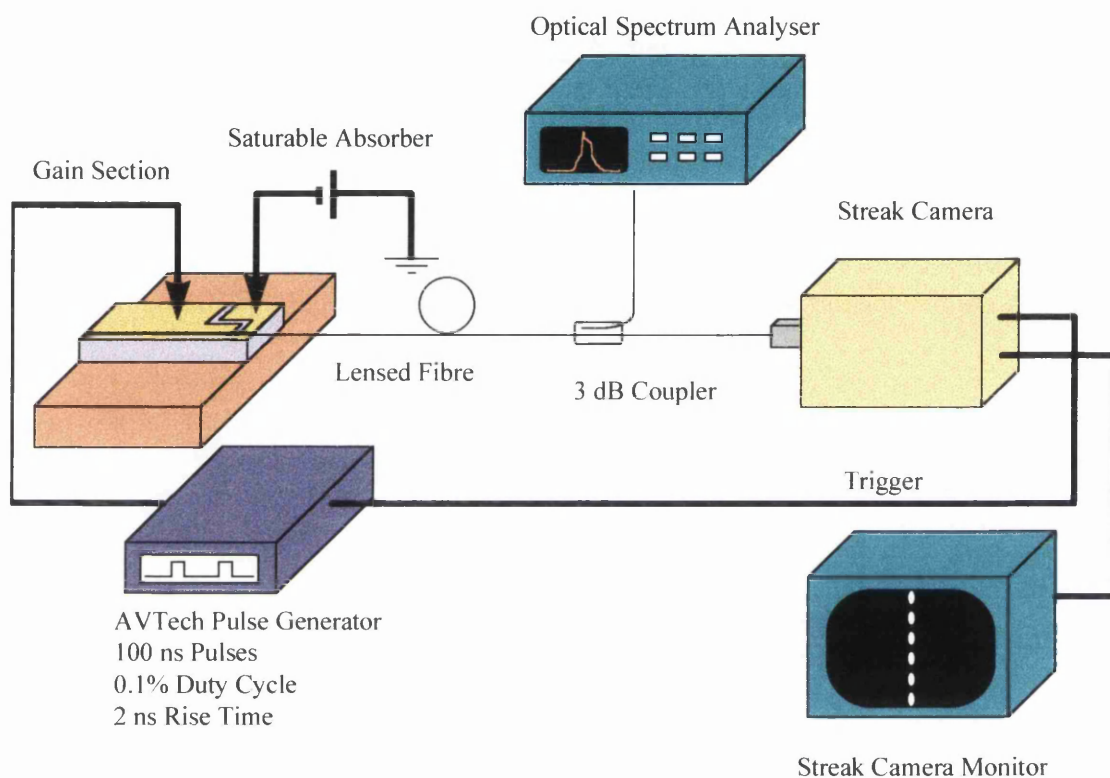


Figure 2.26: *Diagram of the experimental set-up.*

By means of a 3 dB fibre coupler, the output light from the laser was divided into two signals, which allows simultaneous monitoring of dynamics and spectral properties of the mode-locked laser.

¹⁴ L. Forrest, M.A. O'Key, M.R. Osborne, R.W. Musk and P. Spicer, "Laser machining of fibre lenses", *Proc. 4th IEEE International Workshop on high-performance devices for microwave and optoelectronic applications, Leeds*, 1996, pp. 68-69.

¹⁵ Z. Wang, B. Mikkelsen, B. Pedersen, K.E. Stubkjaer and D.S. Olesen, "Coupling between angled-facet amplifiers and tapered lens-ended fibers", *IEEE J. Quantum Electron.*, 1991, **9**, 1, pp. 49-55.

The spectral measurements were taken with an Advantest optical spectrum analyser with a wavelength resolution of 0.1 nm.

The temporal measurements were taken with a Hamamatsu C5680 universal streak camera. A streak camera is a high-speed light detector which enables direct temporal measurements. The streak camera converts incident light into electrons and performs a high-speed sweep (deflecting electrons from top to bottom), enabling detection of the time variation of the incident light intensity by converting these into different positions on the screen. Figure 2.27 shows the operating principle¹⁶ of the streak tube, the heart of the streak camera. The light to be measured is projected onto the slit and focused onto the photocathode, where the photons are converted into a number of electrons proportional to the incident light intensity. These electrons, accelerated and conducted towards the phosphor screen, are swept from top to bottom by means of a high-speed voltage synchronised to the incident light. Then, they are multiplied in the micro-channel plate (MCP), after which they are bombarded against the phosphor screen of the streak tube and converted into an optical image.

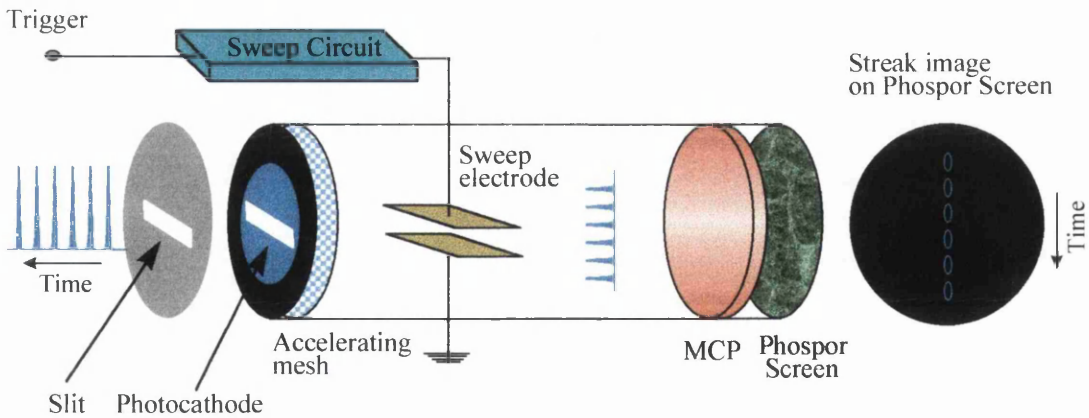


Figure 2.27: Operating principle of the streak tube.

Most of the experimental results obtained in this work were acquired while operating the semiconductor lasers under pulsed excitation. The advantage of this method is that

¹⁶ "Instruction manual for universal streak camera C5680", Hamamatsu Photonics Ltd., 1994.

the devices do not heat as much as under CW operation and temporal measurements are much easier to obtain due to the fact that the streak camera can be triggered directly from the pulse generator. The injected current pulses were produced by an ‘AVTech’ generator. The pulse width could be varied from 100 ns to 5 μ s, the repetition frequency from 10 Hz to 10 kHz, and the maximum current was 5 A. Figure 2.28 shows a current pulse from the AVTech generator injected into a sampling oscilloscope, with a input impedance of 50 Ω . In this figure, the pulse width was 100 ns and the peak current was around 200 mA. The inset shows the rise time, around 2 ns.

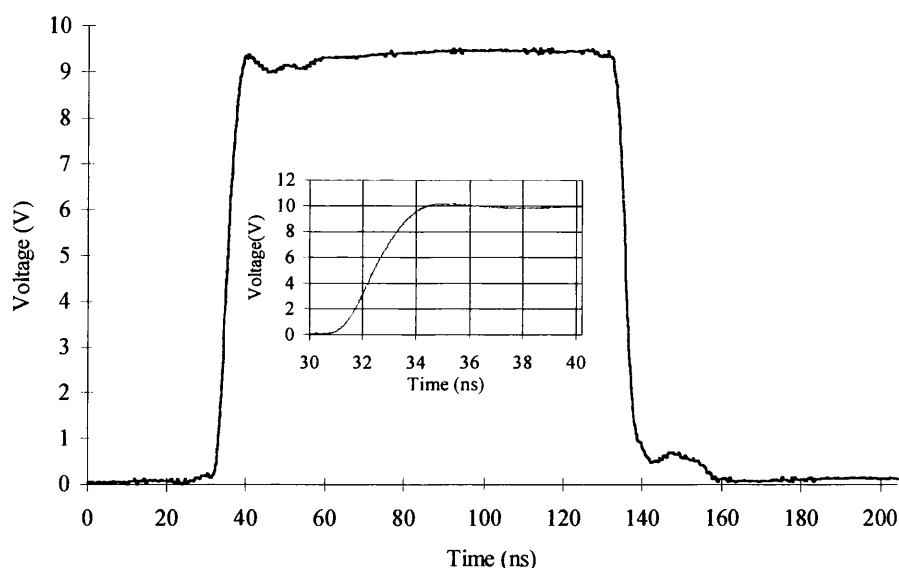


Figure 2.28: *AVTech current pulse (inset shows the rise time of around 2 ns).*

2.4.4 Pulse width measurements.

The problem of measuring short optical pulses (<10 ps) is of great practical and theoretical interest. It is impossible to use the fastest conventional photodetectors because of their response times of around 20 ps, and the streak camera used for the temporal experiments did not resolve short pulse widths accurately, probably due to the finite spot size of the focused light beam.

By measuring the autocorrelation function of an optical pulse, the pulse duration can be obtained accurately. The most common way of measuring the autocorrelation

function is using second-harmonic generation (SHG)¹⁷. The incident train of pulses is divided into two orthogonally polarised beams, which are incident onto a SHG crystal, and the pulse width is obtained by measuring the intensity of the second-harmonic light as a function of the time delay between the two beams.

In our case two-photon absorption (TPA) had been used to perform autocorrelation measurements¹⁸. TPA, briefly described in Appendix I, is a nonresonant, nonlinear optical process which occurs for photons with energy $h\nu$ less than the semiconductor energy gap E_g , but greater than $E_g/2$. When a semiconductor is irradiated by an intense beam of light, an electron can be excited from the valence band to the conduction band by the absorption of two photons.

Figure 2.29 shows the experimental set-up used for the autocorrelation measurements. The light beam from the laser under test, which was operated under pulsed excitation, was divided into two by means of a 3 dB fibre coupler. Both arms of the autocorrelator were made of 25 m of single mode optical fibre at 860 nm, but in one of them a fibre stretcher was introduced to provide the delay between both beams necessary to effectuate the autocorrelation measurements. A polarisation controller was also included in both arms of the autocorrelator to adjust the polarisation in each arm to any desired state. Both beams were then combined, again by means of a 3 dB coupler. One of the outputs of the 3 dB coupler was monitored through a polariser with a camera, to check the polarisation state in each arm. The other output from the 3 dB coupler was injected into the TPA waveguide and the output mode from the waveguide was monitored with another camera. The TPA photocurrent was measured using a boxcar integrator, instead of the more usual lock-in amplifier, which was more adequate for detecting pulsed signals.

¹⁷ H.P. Weber, "Method for pulsewidth measurement of ultrashort light pulses generated by phase-locked lasers using nonlinear optics", *J. Appl. Phys.*, 1967, **38**, pp.2231-2234.

¹⁸ F.R. Laughton, J.H. Marsh, D.A. Barrow and E.L. Portnoi, "The two-photon absorption semiconductor waveguide autocorrelator", *IEEE J. Quantum Electron.*, 1994, **30**, 3, 838-845.

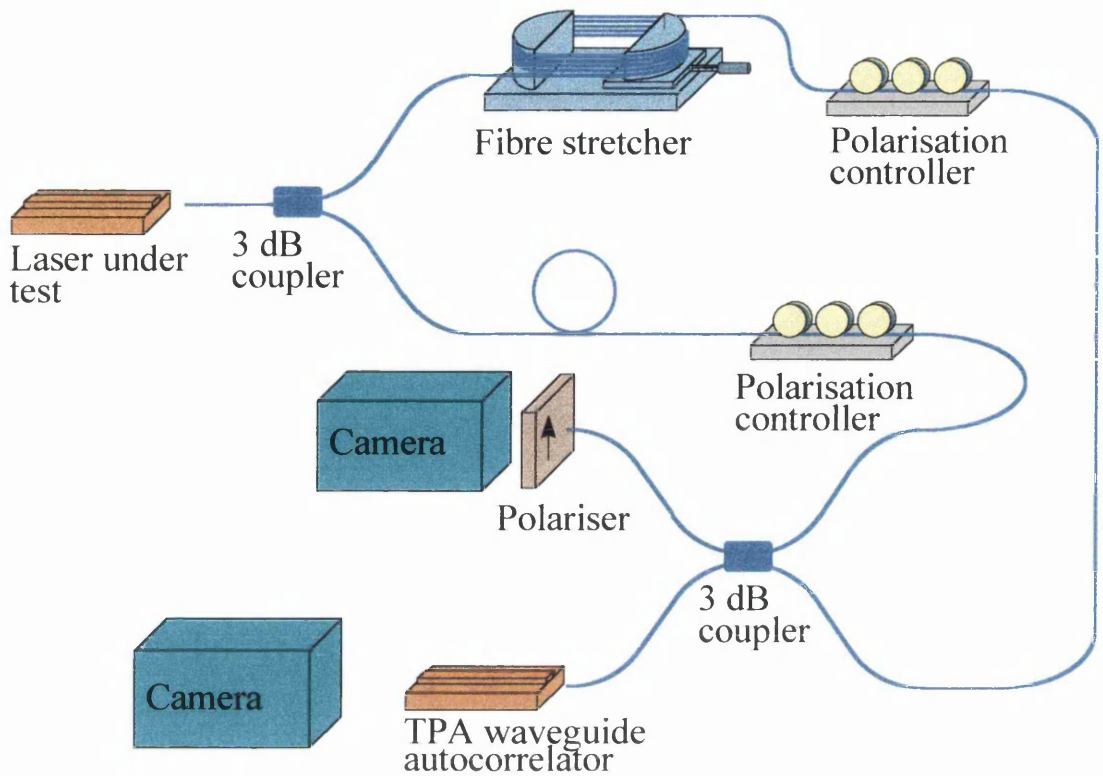


Figure 2.29: *Diagram of the 'in-fibre' autocorrelation measurements set-up.*

Due to the chromatic dispersion in the optical fibre, the optical pulses travelling through it are broadened. The fibre has an estimated dispersion at 850 nm of 80 ps/nm·km, which gives a total dispersion of 2 ps/nm for the total length of the autocorrelator fibre. The initial pulse width is calculated from the measured pulse width as¹⁹

$$\tau_i = \sqrt{\tau_f^2 - \tau_d^2} \tag{2.25}$$

where τ_i , and τ_f are the initial and final pulse width respectively, and τ_d is the estimated dispersion.

A detailed description of every part of the autocorrelator is now given;

¹⁹ A.E. Siegman, "Lasers", *University Science Books*.

Fibre stretcher

Figure 2.30 shows a detailed diagram of the fibre stretcher. By stretching the optical fibre in the fibre stretcher, the total optical length of one of the arms was changed, and therefore the time delay between both beams. The stretcher was made of a fixed part and a moving part, with the moving part calibrated in 10 μm steps. Taking into account that the optical fibre was wound around the stretcher 10 times, every time the stretcher was opened one step, the fibre was extended by around 200 μm .

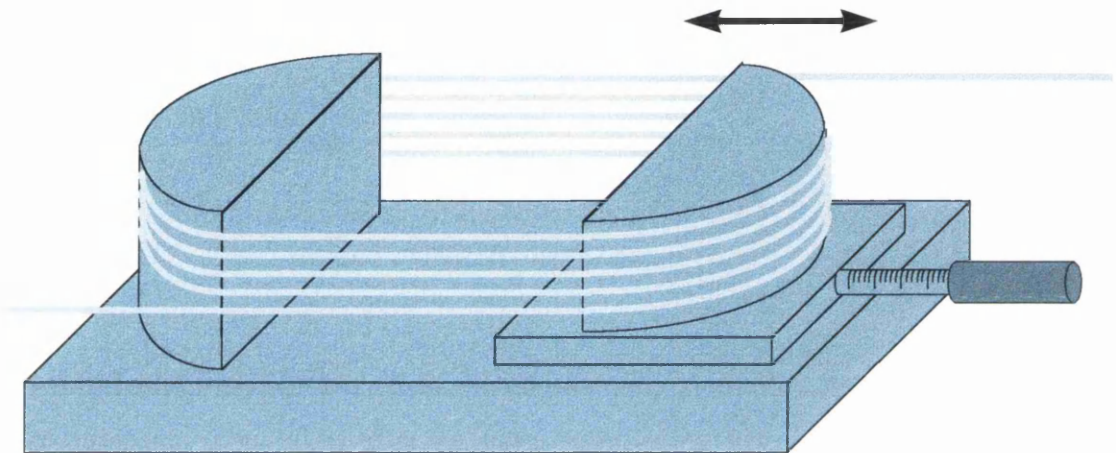


Figure 2.30: *Detailed diagram of the fibre stretcher.*

Figure 2.31 shows the streak profile of an optical pulse travelling through both arms, for different delays, combined before the detection with the streak camera. In Figure 2.31(a) the fibre was not stretched and the difference between the optical path of the autocorrelator arms was around -120 ps. In Figure 2.31(b) the fibre stretcher was opened 100 steps, i.e. the fibre was stretched around 2 cm, 0.1% of the total length of the fibre, and the delay between both pulses was approximately zero, which is the reason why it is not possible to distinguish them. In Figure 2.31(c) the fibre stretcher was opened another 100 steps and the delay between the pulses increases to around +120 ps.

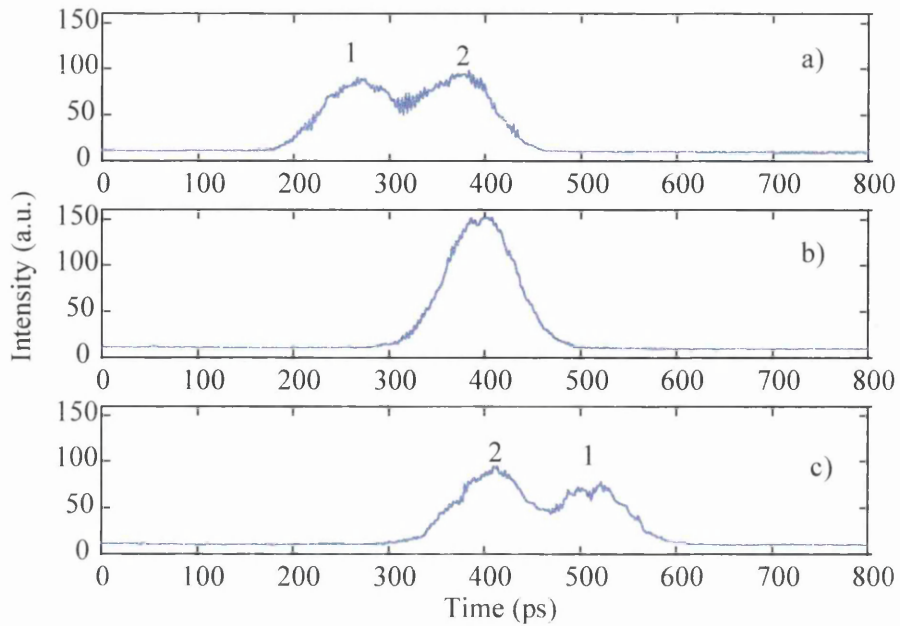


Figure 2.31: *Measurements of the autocorrelator arms' delay.*

Two different methods were used to calibrate the fibre stretcher *in time*. First of all, measurements were taken from the pulse to pulse delay increase when the stretcher was extended, but this pulse to pulse delay was impossible to measure when the distance between the pulses made them indistinguishable. Secondly, measurements of the combined pulse width were taken, which had a minimum when the delay between both pulses was zero, and increased monotonically with increasing delay magnitude. Figure 2.32 shows these measurements, where the squares are the measurements of the pulse to pulse distance and the circles the measurements of the combined pulse width minus the minimum width. In both cases the linear regression is also shown, and the slope in both cases is 1.1 ps per step, the calibration *in time* of the stretcher.

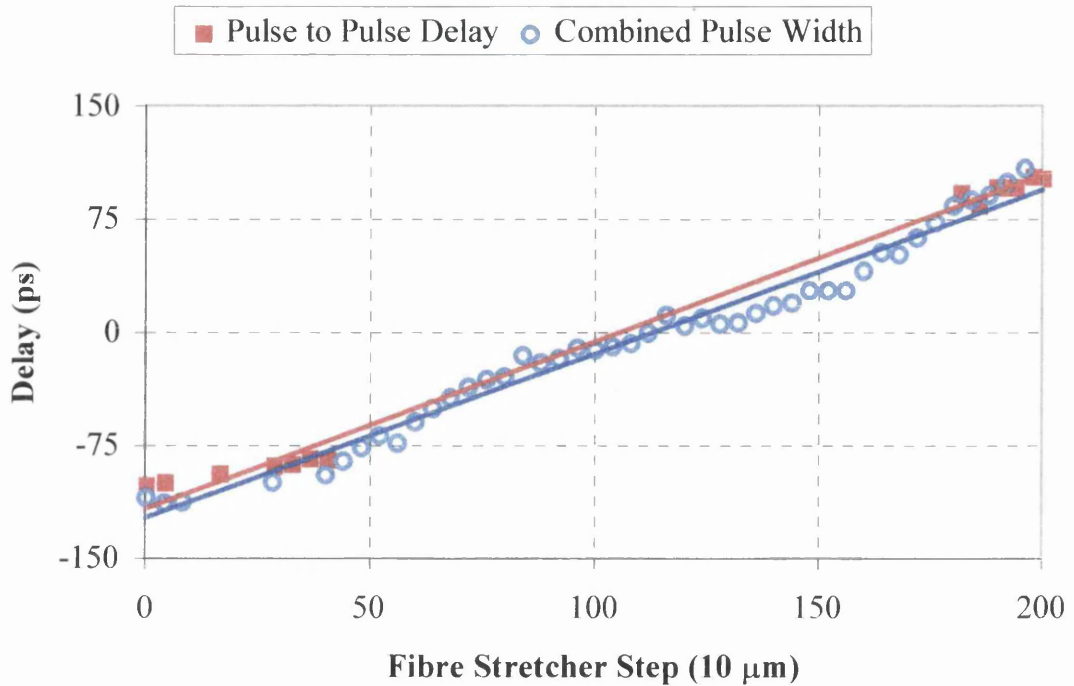


Figure 2.32: *Fibre stretcher ‘in time’ calibration.*

Polariser controller

The polarisation controller utilises stress induced birefringence to create three independent fractional “wave plates” to alter the polarisation in a single mode fibre. The single mode fibre is looped into three independent spools to create these independent fractional “wave plates”. The amount of birefringence induced in the fibre is a function of the fibre cladding diameter, the spool diameter, the number of fibre loops per spool and the wavelength of the light. To transform an arbitrary input polarisation state into an arbitrary output polarisation state, a combination of three paddles is required, and a ‘quarter wave plate’, a ‘half wave plate’ and a ‘quarter wave plate’ is the desired configuration. The first ‘quarter wave plate’ transforms the input polarisation state into a linear polarisation state, the ‘half wave plate’ rotates the linear polarisation state and the last ‘quarter wave plate’ transforms the linear state into an arbitrary polarisation state. Therefore, adjusting each of the three paddles allows complete control of the output polarisation state.

TPA waveguide

The TPA waveguide material was grown by molecular beam epitaxy (MBE), and the structure is shown in Figure 2.33. Ridge waveguides 3 μm wide and 1 mm long were fabricated and wet etching was used to isolate individual devices. The energy bandgap of the active layer was around 1.68 eV³, while the energy bandgap for the material used in the fabrication of the semiconductor lasers was around 1.42 eV. Obviously, this material can perform TPA, as the energy of the photons to be detected is lower than the energy bandgap of the waveguide material, but is higher than half of the energy bandgap.

p ⁺ GaAs	50 Å
p Al _{0.3} Ga _{0.7} As	0.6 μm
i Al _{0.3} Ga _{0.7} As	0.4 μm
i Al _{0.2} Ga _{0.8} As	0.6 μm
i Al _{0.3} Ga _{0.7} As	0.4 μm
n Al _{0.3} Ga _{0.7} As	4 μm
n ⁺ GaAs	substrate

Figure 2.33: *Material structure for the TPA waveguide autocorrelator.*

The experimental set-up for the TPA waveguide detection is shown in Figure 2.34. The two beams were orthogonally polarised to reduce interference effects within the waveguide, as detailed in Appendix I. When the time delay t_d between the beams was altered, the photocurrent generated by TPA also changed. By measuring this photocurrent as a function of t_d , the pulse width could be measured.

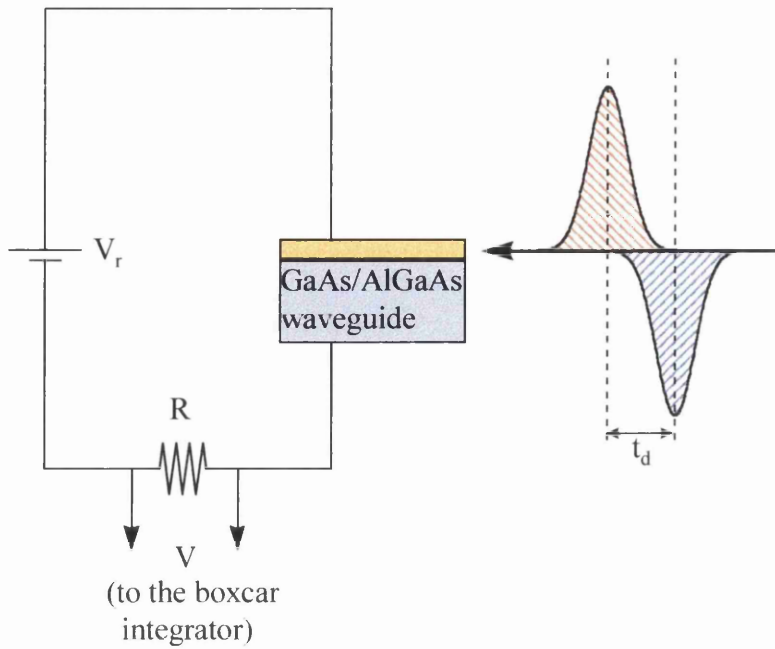


Figure 2.34: *Experimental set-up for the TPA photocurrent detection.*

2.5 Conclusions.

The fabrication technique described in this chapter is simpler than the more usual technique using silica as an etching mask for the waveguide definition. The results are also better because the contact window is self-aligned to the ridge. When silica is used as an etching mask, the contact window must be perfectly aligned to the ridge using the mask aligner; a very difficult step that usually gives problems with small misalignments. This latter technique also gives problems with over-etching the silica passivation mask, which results in lasers with poorer performances and higher threshold currents.

One of the main problems still to be solved is to improve the adherence of the p-contact layer to the silica layer used as a passivation mask. This poor adherence makes the process of wire bonding the devices very difficult. Some techniques have been used to improve this adherence, for example deoxidising the sample with HCl, which does help, but makes lift-off of the metal layer much more difficult to achieve. Also the contact annealing stage plays an important role, because the p-contact adherence is usually worse after annealing, most probably due to the evaporation of water absorbed by the silica, but the contact resistance is much lower once the metal is annealed. The

best compromise solution is to evaporate the n-metal layer first, anneal it and then evaporate the p-contact.

The ease of experimental measurements using the set-up described above is also noticeable. The utilisation of single mode lensed fibre makes the alignment between the laser and the fibre very simple. The use of the 3 dB fibre coupler is also very important because it allows simultaneous monitoring of the dynamics and optical spectra of the laser.

Chapter Three **PASSIVE MODELOCKING.**
THEORETICAL CONCEPTS.

With the development of digital optical networks, so far being standardised for data rates up to 10 Gbit/s, a need arises for sources of high bit rate, short optical pulses. Obviously, semiconductor lasers have very good characteristics for this purpose, as modelocking in semiconductor lasers can generate short optical pulses (<1 ps) at a very high bit rate (>100 GHz). They also have the advantage of ease of fabrication, small size, long lifetime, etc. This chapter covers a theoretical study of modelocking in semiconductor lasers, describing the process of modelocking itself and analysing the methods of modelocking in semiconductor lasers.

3.1 Description of modelocking.

Modelocking, from the frequency domain point of view, implies that the relative phases of the existing longitudinal modes in the laser cavity are held fixed with respect to each other. With proper relative phases between the longitudinal modes, the resulting periodic temporal output is a train of optical pulses. To produce short pulses, modes over a wide frequency range must be locked. Therefore, the minimum pulse width is ultimately limited by the overall semiconductor laser bandwidth. There are three different forms of modelocking, which are:

1. *Active modelocking*: where the gain or loss of the laser is modulated at a frequency equal to the longitudinal modes spacing.
2. *Passive modelocking*: where modelocking is achieved by placing a saturable absorber in the laser cavity.
3. *Hybrid modelocking*: which is a combination of both previous techniques.

Modelocking, from the time domain point of view, is a dynamic regime in which an optical pulse circulates in a laser cavity. When this optical pulse travels around the mode-locked laser cavity, there are mechanisms that broaden, shorten and reshape the

optical pulse. The final pulse width and shape results from a balance between these mechanisms, which include¹

a) pulse shortening:

- Saturable absorption and gain (passive or hybrid modelocking).
- Active gain or loss modulation (active or hybrid modelocking).

b) pulse broadening:

- Gain saturation.
- Gain and group velocity dispersion.
- Self-phase modulation due to changes in refractive index as a consequence of saturable absorption, saturable gain and active gain or loss modulation (interacting with gain or group velocity dispersion).

Pulse narrowing by active gain modulation is not as effective as pulse narrowing due to saturable gain and absorption because, when the optical pulse width becomes narrow in comparison with the active gain modulation electrical pulse width, the optical pulse is not shortened any further. That is the reason the shortest pulses generated to date using semiconductor lasers were achieved using either passive or hybrid modelocking².

As mentioned, passively mode-locked lasers generate the shortest optical pulses, and they do not depend on an injected electrical signal which would limit the maximum operating frequency of the devices. Thus, the following analysis will only cover passive modelocking, the modelocking technique which offers the best results in terms of short pulse generation.

¹ D.J. Derickson, R.J. Helkey, A. Mar, J.R. Karin, J.G. Wasserbauer and J.E. Bowers, "Short pulse generation using multisegment mode-locked semiconductor lasers", *IEEE J. Quantum Electron.*, 1992, **28**, 10, pp. 2186-2202.

² K.Y. Lau, "Short-pulse and high-frequency signal generation in semiconductor lasers", *IEEE J. Lightwave Technol.*, 1989, **7**, 2, pp. 400-419.

3.2 Passive modelocking in semiconductor lasers.

Passive modelocking in semiconductor lasers is induced by inserting a saturable absorber in the optical path, as shown in Figure 3.1 which represents the conventional passive modelocking configuration. A saturable absorber is a lossy element that becomes more transparent with increasing light intensity.

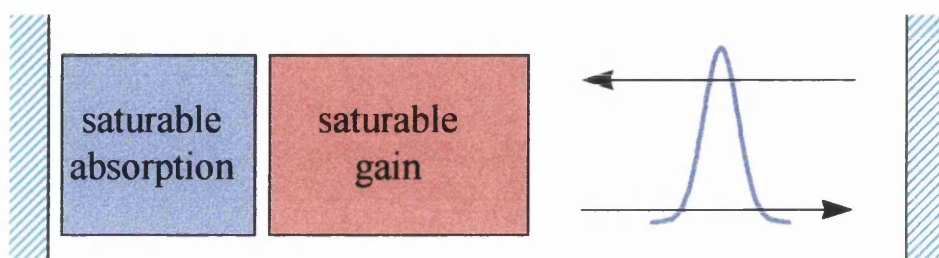


Figure 3.1: Typical geometry of a passively mode-locked laser.

3.2.1 Pulse shortening effect: the saturable absorber.

Figure 3.2 shows the time-dependent gain and loss in a passively mode-locked laser system³. Before the arrival of the pulse, the loss and gain are approaching their steady-state values, with the loss being larger than the gain. The leading edge of the optical pulse is absorbed during the passage of the optical pulse through the saturable absorber. As the intensity of the pulse increases, the loss saturates and the central part of the optical pulse is amplified. When the gain saturates below the unsaturable loss (due to mirror transmission, waveguide losses, etc.) the trailing edge of the optical pulse suffers loss again. The conjunction of these loss and gain mechanisms leads to a net pulse narrowing on each transit around the mode-locked laser cavity, until a steady-state is reached between the shortening effects and the broadening effects due to gain and group velocity dispersion that will be described in a following section.

³ P.W. Smith, Y. Silberberg and D.A.B. Miller, "Modelocking of semiconductor diode lasers using saturable exciton nonlinearities", *J. Opt. Soc. Am. B*, 1985, **2**, 7, pp. 1228-1236.

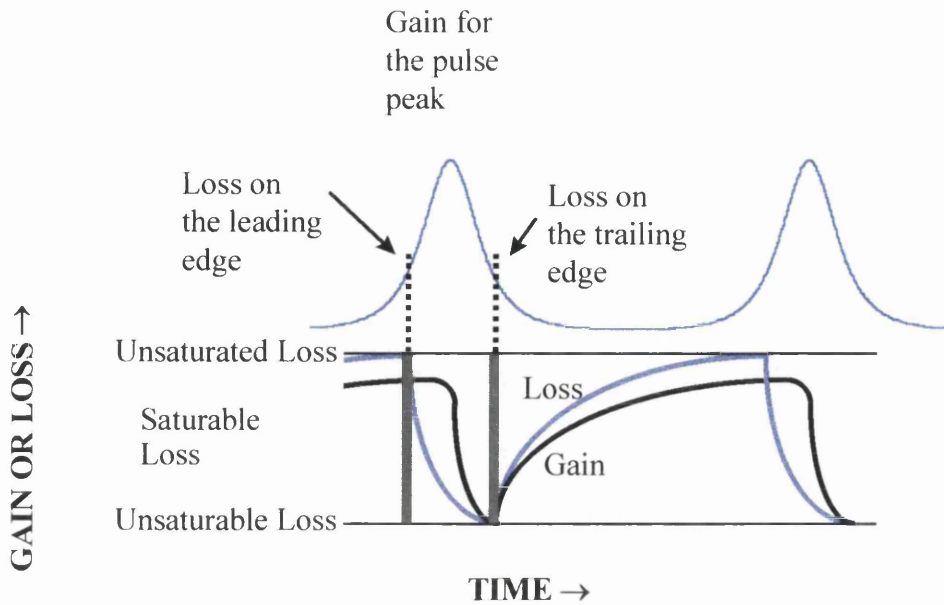


Figure 3.2: *Gain and loss dynamics for ideal mode locking with a slow saturable absorber.*

This type of saturable absorber, with a recovery time being long compared with the mode-locked optical pulse duration, is named a *slow saturable absorber*^{4,5}.

The saturable absorber/gain medium must fulfil two conditions³: a) the loss must saturate faster than the gain, and b) the recovery time of the loss must be faster than that of the gain. With these two conditions the loss will remain greater than the gain all the time, except near the peak of the optical pulse and therefore spontaneous emission will not be able to build up between pulses, which would create a chaotic and random pulse train.

GaAs/AlGaAs MQW material, as in this work, can easily satisfy the first condition mentioned above^{3,6}. The second condition depends on the fabrication method used for

⁴ H.A. Haus, "Theory of mode locking with a slow saturable absorber", *IEEE J. Quantum Electron.*, 1975, **11**, 9, pp. 736-746.

⁵ H.A. Haus, "Theory of mode locking with a fast saturable absorber", *J. Appl. Phys.*, 1975, **46**, 7, pp. 3049-3058.

⁶ H.A. Haus and Y. Silberberg, "Theory of modelocking of a laser diode with a multiple-quantum-well structure", *J. Opt. Soc. Am. B*, 1985, **2**, 7, pp. 1237-1243.

the saturable absorber. The intrinsic recovery time of the absorption is dictated by carrier recombination, around 30 ns for an undoped multiple-quantum well structure⁶. In order to satisfy the second condition, a way to reduce this absorption recovery time must be found. There are several techniques to fabricate an integrated slow saturable absorber within the cavity of a semiconductor laser, the most important being proton bombardment and ion implantation⁷ and non-uniform current injection in split contacts⁸.

a) Proton bombardment and ion implantation.

The bombardment of semiconductor with high-energy ions increases the recombination rate by generating damage centres which serve as recombination sites. Smith *et al*³ demonstrated that this carrier recombination time can be reduced down to 10 ps. Thus, to fabricate the saturable absorber one or both of the lasers' facets is proton bombarded or ion implanted.

b) Split contacts.

This technique uses a short section of the laser cavity, formed by splitting the p-contact of the semiconductor laser, as a saturable absorber. The long laser section is forward biased to provide gain to the laser. By reverse biasing the short section, an intracavity saturable absorber is formed. The incoming optical pulse saturates the absorption of this short section but, after the passage of the pulse, the carriers are swept away, as the saturable absorber is reverse biased, and the absorption returns to its high loss (unsaturated loss) state.

The absorption recovery time of waveguide saturable absorbers with GaAs quantum well active regions was measured by Derickson *et al*¹. The absorption recovers back to its maximum value in a time of less than 15 ps, for a four quantum well, 80 μm long

⁷ A.G. Deryagin, D.V. Kuksenkov, V.I. Kuchinskii, E.L. Portnoi and I.Y. Khrushchev, "Generation of 110GHz train of subpicosecond pulses in 1.535 μm spectral region by passively mode-locked InGaAsP/InP laser diodes", *Electronics Lett.*, 1994, **30**, 4, pp. 309-311.

⁸ S. Sanders, L. Eng and A. Yariv, "Passive mode-locking of monolithic InGaAs/AlGaAs double quantum well lasers at 42 GHz repetition rate", *Electronics Lett.*, 1990, **26**, 14, pp 1087-1089.

reverse biased saturable absorber. Since the absorption recovery time sets an upper limit on the achievable repetition rate in a passively mode-locked semiconductor laser, the measured recovery time implies that very high mode locking frequencies are possible^{9,10}.

3.2.2 Pulse broadening effect.

The main cause of pulse broadening in semiconductor lasers is self-phase modulation (SPM) of the optical pulses interacting with gain dispersion and group velocity dispersion. In semiconductor lasers, changes in the carrier density occurring as a result of gain and loss saturation lead to relatively large changes in the refractive index¹¹. These changes in the index of refraction are related to gain changes through the *linewidth enhancement factor* α ¹², which is defined as

$$\alpha = \frac{\partial \chi_r / \partial N}{\partial \chi_i / \partial N} \quad (3.1)$$

where N is the carrier density and $\chi = \chi_r + j\chi_i$ is the optical complex susceptibility of the gain medium.

The effect of SPM is better understood with Figure 3.3. When an optical pulse travels through a semiconductor amplifier with an energy approaching the saturation energy of the amplifier, the gain saturates and the carrier density is depleted. This reduction in the carrier density causes an increase of the refractive index, and thus a reduction of the instantaneous optical frequency over the duration of the pulse. When an optical pulse saturates the loss of a saturable absorber, the carrier density increases, which

⁹ Y.K. Chen and M.C. Wu, "Monolithic colliding-pulse mode-locked quantum-well lasers", *IEEE J. Quantum Electron.*, 1992, **28**, 10, pp. 2176-2185.

¹⁰ S. Arahira, S. Oshiba, Y. Matsui, T. Kunii and Y. Ogawa, "500 GHz optical short pulse generation from a monolithic passively mode-locked distributed Bragg reflector laser diode", *Appl. Phys. Lett.*, 1994, **64**, 15, pp. 1917-1919.

¹¹ G. P. Agrawal and N. A. Olsson, "Self-phase modulation and spectral broadening of optical pulses in semiconductor laser amplifiers", *IEEE J. Quantum Electron.*, 1989, **25**, 11, pp. 2297-2306.

¹² M. Osinski and J. Buus, "Linewidth broadening factor in semiconductor lasers—An overview", *IEEE J. Quantum Electron.*, 1987, **QE-23**, pp. 9-29.

causes a decrease in the refractive index and therefore an increase of the instantaneous optical frequency in the leading edge of the optical pulse¹.

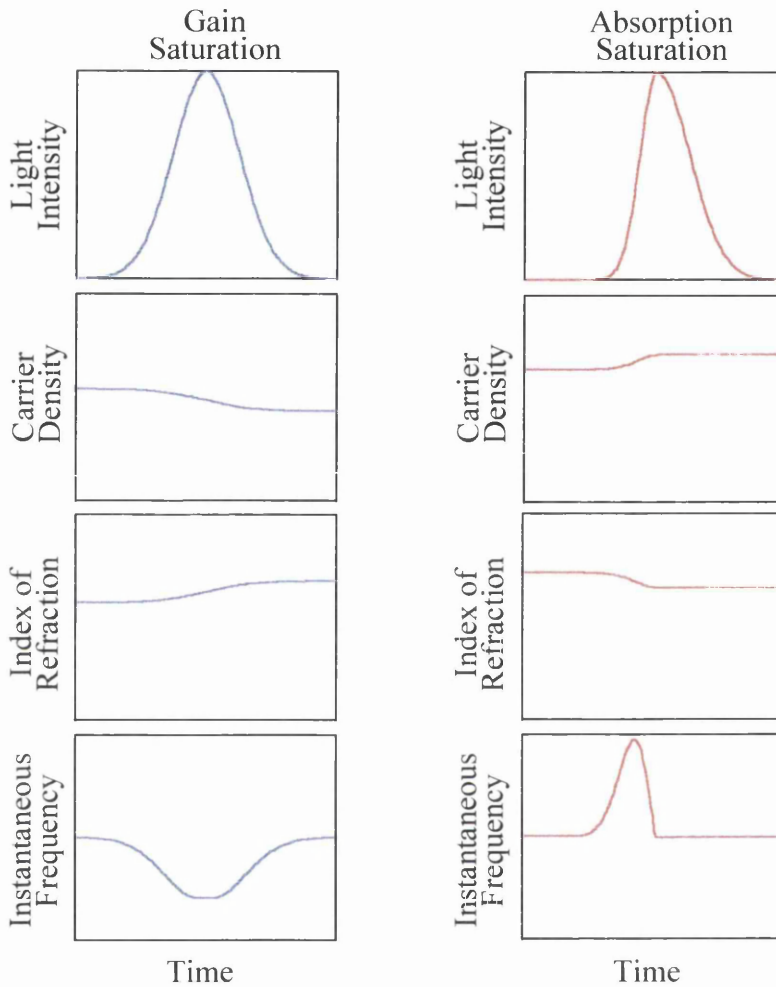


Figure 3.3: *SPM effects in mode-locked semiconductor lasers due to gain saturation (left) and absorption saturation (right) after Derickson et al¹.*

These spectral changes due to the SPM-induced frequency chirp cause an excess spectral bandwidth beyond the pulse transform limit, but do not broaden the pulse itself. Pulse width broadening is caused by group velocity dispersion (GVD) in the laser cavity, which can be enhanced by the spectral broadening caused by SPM. In semiconductor lasers, the GVD parameter is caused by material dispersion and also by gain-dispersion-induced GVD. The spectral width of a short pulse is sufficiently wide that it becomes comparable to the gain bandwidth leading to a physical phenomenon

known as *gain dispersion*¹³. The effect of gain dispersion is to reduce the gain for spectral components far away from the optical carrier frequency. This gain dispersion leads to GVD, which generally causes temporal broadening of the optical pulse since each wavelength component of the pulse travels at a different velocity in the laser cavity.

The interaction between gain and loss saturation induced SPM and gain dispersion induced GVD is, therefore, as follows; gain and loss saturation induce SPM that imposes chirp on the optical pulse such that the wavelength of its leading edge is shifted to shorter wavelengths, while the centre and trailing edge wavelengths are shifted to longer wavelengths. On the other hand, gain dispersion induces normal GVD such that the shorter wavelengths of the optical pulse, i.e. the leading edge of the pulse, travel faster along the laser cavity than the longer wavelengths, i.e. the trailing edge. Clearly, with the leading edge travelling faster than the trailing edge, the pulse will be broadened in time.

3.3 Configuration of passively mode-locked semiconductor lasers.

Figure 3.4 shows typical configuration that have been implemented in semiconductor laser to obtain passive modelocking. These configurations are:

*a) External cavity lasers*¹.

The first demonstration of passive modelocking was achieved using this type of configuration. One of the semiconductor laser's facets is coupled to an external cavity, which can be either air or an optical fibre, and therefore it requires a reduction in the reflectivity of this facet (e.g. an anti-reflection coating). This configuration suffers from mechanical instabilities and secondary pulse formation due to reflections at the facet coupled to the external cavity.

*b) All-active cavity lasers*¹.

Easy to fabricate and functional configuration. When a long cavity is required to reduce the operating frequency, this configuration suffers from high threshold current and over-heating effects as the whole cavity is pumped.

¹³ G. P. Agrawal, "Effect of gain dispersion on ultrashort pulse amplification in semiconductor laser amplifiers", *IEEE J. Quantum Electron.*, 1991, **27**, 6, pp. 1843-1849.

c) *Extended cavity lasers*¹⁴.

A integrated low-loss passive waveguide is incorporated in the laser cavity, which means that the cavity length can be extended without having high threshold currents. The reliability of this configuration depends on the reliability of the process used to fabricate the passive waveguide.

d) *Distributed Bragg reflector (DBR) lasers*¹⁵.

This configuration is required when an exact control of the centre wavelength and bandwidth of the pulse source is required. Usually, the timing jitter in this configuration, i.e. the noise related to pulse period variations, is much higher than that of Fabry-Perot configurations.

e) *Colliding pulse modelocking lasers*⁹.

The saturable absorber is placed in the centre of the laser cavity and, thus, there are two pulses circulating in the cavity which collide in the absorber. Very accurate cleavage of the device is required to place the saturable absorber exactly in the middle of the cavity.

f) *Multiple colliding pulse modelocking lasers*¹⁶.

There are as many pulses circulating in the cavity as gain sections, colliding among themselves in the saturable absorbers. Very high repetition frequencies can be achieved.

g) *Ring lasers*¹⁷.

Colliding pulse modelocking is realised in ring geometries easily, without the need to place the saturable absorber exactly in the middle of the cavity. Suffers from

¹⁴ P.B. Hansen, G. Raybon, U. Koren, P.P. Iannone, B.I. Miller, G.M. Young, M.A. Newkirk and C.A. Burrus, "InGaAsP monolithic extended-cavity lasers with integrated saturable absorbers for active, passive and hybrid mode locking at 8.6 GHz", *Appl. Phys. Lett.*, 1993, **62**, 13, pp. 1445-1447.

¹⁵ S. Arahira and Y. Ogawa, "Passive and hybrid modelocking in a multi-electrode DBR laser with two gain sections", *Electronics Lett.*, 1995, **31**, 10, pp. 808-809.

¹⁶ J.F. Martins-Filho, E.A. Avrutin, C.N. Ironside and J.S. Roberts, "Monolithic multiple colliding pulse mode-locked quantum-well lasers: experiment and theory", *IEEE J. Selected Topics in Quantum Electron.*, 1995, **1**, 2, pp. 539-551.

¹⁷ T.F. Krauss, R.M. De La Rue, P.J.R. Laybourn, B. Vogege, C.R. Stanley, "Efficient semiconductor ring lasers made by a simple self-aligned fabrication process", *IEEE J. Selected Topics in Quantum Electron.*, 1995, **1**, 2, pp. 757-761.

radiation losses in the bend waveguides and undesired reflections at the output couplers.

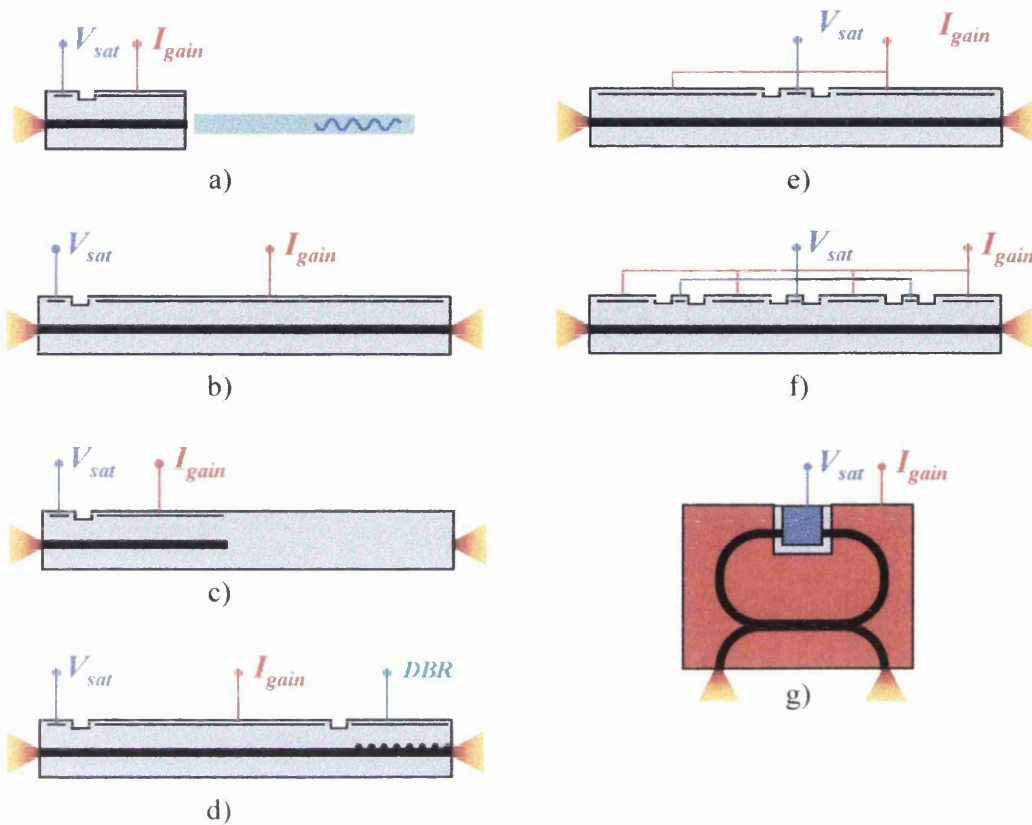


Figure 3.4: *Diagrams of passively mode-locked semiconductor laser configurations: a) external cavity, b) two sections, all-active cavity, c) three sections, passive waveguide cavity, d) DBR, all-active cavity, e) colliding pulse configuration, f) multiple colliding pulse configuration and g) ring laser.*

3.4 Theory of modelocking in semiconductor lasers.

Passive modelocking, the type of modelocking analysed in this chapter, is a very complex nonlinear process, and is even more difficult to model analytically^{18,19,20}. In

¹⁸ H.A. Haus, "Parameter ranges for CW passive mode locking", *IEEE J. Quantum Electron.*, 1976, **12**, 3, pp. 169-176.

¹⁹ E.P. Ippen, "Principles of passive mode locking", *Appl. Phys. B*, 1994, **58**, pp. 159-170.

²⁰ R.G.M.P. Koumans and R. van Roijen, "Theory for passive mode-locking in semiconductor laser structures including the effects of self-phase modulation, dispersion, and pulse collisions", *IEEE J. Quantum Electron.*, 1996, **32**, 3, pp. 478-492.

this section simplified analytical solutions for CW mode-locked pulses will be obtained. A much more detailed analysis of the different approaches to the theory and physical mechanisms of modelocking in semiconductor lasers can be found in the work of Avrutin *et al*²¹.

3.4.1 Spectral description.

Although a rigorous analysis of the electric field in the laser cavity must be based on Maxwell's equations, the simplified analysis that follows shows some of the general properties of mode-locked lasers. Using complex notation the total optical electric field in the laser cavity can be written as

$$E(t) = \sum_n E_n \cdot e^{j[(\omega_0+n\omega)t+\phi_n]} \quad (3.2)$$

where the summation is extended over the oscillating modes, ω_0 is an arbitrary central frequency, ω is the separation between the longitudinal modes, which is equal to $\pi c/L$, where L is the cavity length, and ϕ_n is the phase of the n^{th} mode.

One property of the electric field $E(t)$ is that it is periodic in $T \equiv 2\pi/\omega = 2L/c$, which is the round-trip time inside the resonator, if the phases ϕ_n of the different longitudinal modes are fixed.

Modelocking implies that the relative phases of the modes are held fixed with respect to each other, which means that the resulting periodic temporal output is a train of pulses with a period of T . One of the most useful forms of modelocking is when the relative phases are equal to zero. If it is assumed that there are N oscillating modes with equal amplitudes E_0 , Eq.(3.2) can be written as

$$E(t) = E_0 \sum_{-(N-1)/2}^{(N-1)/2} e^{j(\omega_0+n\omega)t} = E_0 e^{j\omega_0 t} \frac{\sin(N\omega t / 2)}{\sin(\omega t / 2)} \quad (3.3)$$

²¹ E.A. Avrutin, J.H. Marsh and E.L. Portnoi, "Mode-locked diode lasers for microwave optoelectronics applications", to be published in *International J. High Speed Electronics & Systems*.

The average optical intensity of the laser, which is proportional to $E(t)E^*(t)$, where $*$ denotes complex conjugate, is given by

$$P(t) = P_0 \frac{\sin^2(N\omega t / 2)}{\sin^2(\omega t / 2)} \quad (3.4)$$

Figure 3.5 shows an example of the different optical intensity patterns that can be obtained by having fixed or random longitudinal modes amplitude and phase. In Figure 3.5 (a), (b) and (c) the amplitude of the longitudinal modes are constant and the phase difference between them is zero. These graphs represent Eq.(3.4) for $N=3, 5$ and 8 longitudinal modes. From these three graphs, some properties of the output power of a mode-locked laser can be observed:

- The power is emitted in a form of a train of pulses with frequency inversely proportional to the laser cavity length. Thus, for typical cavity lengths in semiconductor lasers of $500 \mu\text{m}$, the repetition rate of the pulse train will be in the order of 100 GHz .
- The larger the number of modes locked together, the higher the energy of the pulse, as it is roughly proportional to the number of modes squared. This can be seen in Figure 3.5 (a), (b) and (c) where the amplitude of the pulses increases from 9 to 64 a.u.
- In each situation there is one primary mode-locked pulse per period, with a FWHM pulse width given roughly by T/N , plus $N-2$ much weaker peaks.

Figure 3.5.d shows the time output assuming a gaussian optical spectrum (gaussian amplitude of the longitudinal modes, with a spectral width corresponding to four longitudinal mode spacings) and with all the modes in phase. Again the result is a train of periodically spaced short pulses, but these pulses now have gaussian shapes in time, with essentially no secondary pulses. Figure 3.5.e shows an example of the pulses obtained from an spectrum with all the modes in phase, but with random amplitudes over the N modes. Periodic pulses are still obtained in this case, but there is an irregular background of sub-pulses between the main pulses. Figure 3.5.f shows the case of uniform amplitudes of the longitudinal modes but with random relative phases among them. This signal consists of a random set of peaks, essentially a noise-like

signal. The signal is still periodic in T because the random relative phase between the modes was held fixed for the calculations. This would not be the real case of a semiconductor laser operating with multiple longitudinal modes, as the relative phases would change with time.

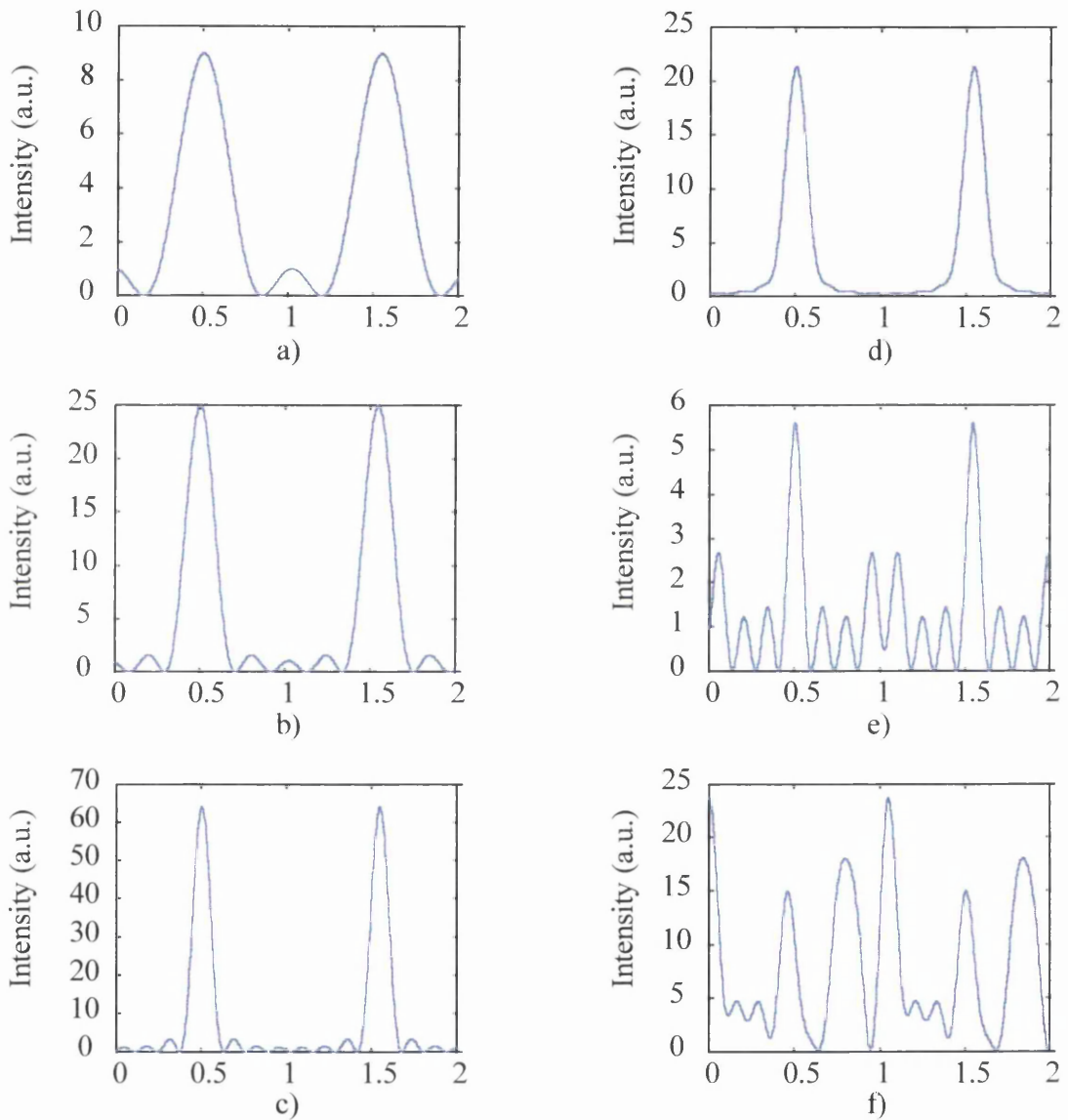


Figure 3.5: *Different intensity patterns in time synthesised using : a) 3 modes, equal amplitudes, all in phase, b) 5 modes, equal amplitudes, all in phase, c) 8 modes, equal amplitudes, all in phase, d) 8 modes, gaussian variation of their amplitudes, all in phase, e) 8 modes, random amplitudes, all in phase, f) 8 modes, equal amplitudes, random phases.*

From these properties, and due to the wide gain-bandwidth of the semiconductor lasers (order of THz), optical pulses can in principle be generated with pulse widths down to tens of femtoseconds. Obviously, to produce such short pulses, modes should be locked over a very wide frequency range.

3.4.2 Temporal description.

As mentioned, modelocking is described as the propagation of an optical pulse within a laser cavity. A simplified analytical solution for the mode-locked optical pulse²² is obtained in this section. First of all, it is considered that the pulse inside the cavity can be described by

$$E(t) = \text{Re} \left[\hat{E}(t) e^{j\omega_0 t} \right] \quad (3.5)$$

so that $\hat{E}(t)$ is the complex envelope of the pulse, with a Fourier transform $\hat{E}(\omega)$. The instantaneous intensity of the pulse is

$$I(t) = |\hat{E}(t)|^2 \quad (3.6)$$

The laser cavity consists of a laser medium or amplifier, with a gain coefficient $g(t)$, a saturable absorber, with a loss coefficient $l(t)$ and a dispersive and bandwidth-limiting element, as shown in Figure 3.6.

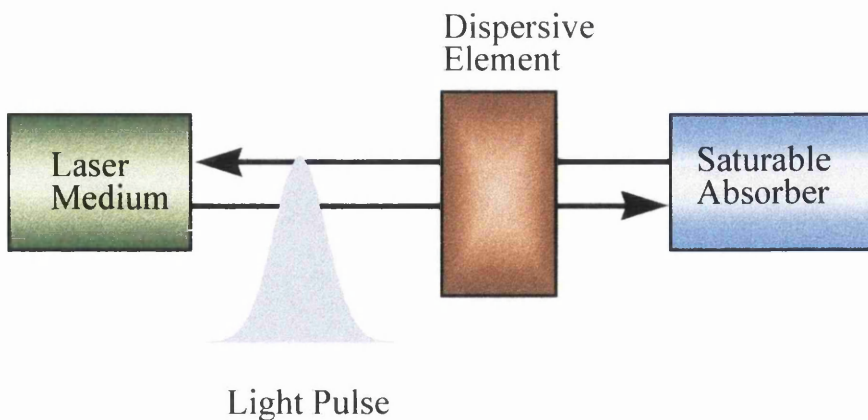


Figure 3.6: Diagram of the proposed model for the mode-locked laser.

The optical cavity, represented by the dispersive element in the model, has an approximate round-trip transfer function

²² A.E. Siegman, "Lasers", *University Science Books*.

$$\hat{E}'(\omega) = \hat{E}(\omega) \exp \left[-a_0 - j \frac{a_1}{\omega_c} (\omega - \omega_0) - \frac{1}{\omega_c^2} (\omega - \omega_0)^2 \right] \quad (3.7)$$

where $\hat{E}'(\omega)$ is the pulse envelope Fourier transform after one round trip, a_0 is the round trip loss, $-ja_1(\omega-\omega_0)/\omega_c$ represents any linear dispersion or time-delay effects and $(\omega-\omega_0)^2/\omega_c^2$ is the quadratic approximation for the bandwidth-limiting effect. If it is now assumed that those effects on the pulse, in one round trip, are small, Eq.(3.7) can be approximated, using the Taylor approximation to the exponential function, to

$$\hat{E}'(\omega) \approx \left[1 - a_0 - j \frac{a_1}{\omega_c} (\omega - \omega_0) - \frac{1}{\omega_c^2} (\omega - \omega_0)^2 \right] \hat{E}(\omega) \quad (3.8)$$

Calculating the inverse Fourier transform for the transfer function in Eq.(3.8), the net change in the envelope of the optical pulse is given by

$$\hat{E}'(t) \approx \left[1 - a_0 - \frac{a_1}{\omega_c} \frac{d}{dt} + \frac{1}{\omega_c^2} \frac{d^2}{dt^2} \right] \hat{E}(t) \quad (3.9)$$

where $\hat{E}'(t)$ is the pulse envelope after one round trip. It can be seen that dispersion appears as a first derivative and bandwidth-limiting as second derivative of the optical pulse envelope. If again it is assumed that a pulse passing through the gain medium or saturable absorber is modified only slightly on one single pass we can simply add the gain and loss effects in Eq.(3.9) to give

$$\hat{E}'(t) \approx \left[1 + g(t) - l(t) - a_0 - \frac{a_1}{\omega_c} \frac{d}{dt} + \frac{1}{\omega_c^2} \frac{d^2}{dt^2} \right] \hat{E}(t) \quad (3.10)$$

To find a self-consistent solution for Eq.(3.10) the net change of the pulse envelope, after one round trip, can be at most a small time shift δT , i.e. the shape of the pulse is conserved over the repetition period. This can be written as

$$\hat{E}'(t) = \hat{E}(t + \delta T) \quad (3.11)$$

and as δT is a time shift, small compared with the pulsewidth itself. Eq.(3.11) can be written as

$$\hat{E}'(t) \approx \hat{E}(t) + \frac{d\hat{E}(t)}{dt} \delta T \quad (3.12)$$

From Eq.(3.10) and Eq.(3.12), the steady-state pulse shape must be a solution of the differential equation

$$\frac{1}{\omega_c^2} \frac{d^2 \hat{E}(t)}{dt^2} - \left(\frac{a_1}{\omega_c} + \delta T \right) \frac{d\hat{E}(t)}{dt} + (g(t) - l(t) - a_0) \hat{E}(t) = 0 \quad (3.13)$$

A further analysis for the time-dependent loss $l(t)$, and gain $g(t)$ is now necessary, but we are just going to point out that when the pulse is shorter than the recovery time of $l(t)$ and $g(t)$ they are of the form¹⁹

$$l(t) = l_i \exp\left(\frac{1}{E_A} \int^t |\hat{E}(t)|^2 dt\right) \quad (3.14)$$

$$g(t) = g_i \exp\left(\frac{1}{E_L} \int^t |\hat{E}(t)|^2 dt\right) \quad (3.15)$$

where $1/E_A$ and $1/E_L$ are the inverse saturation energy of the absorber and laser medium respectively, and l_i and g_i are the values of the loss and gain just before the arrival of the pulse. Introducing Eq.(3.14) and Eq.(3.15) in Eq.(3.13) quite a complicated nonlinear integro-differential equation is obtained. A solution for that equation is a *hyperbolic secant* in the form^{20,23}

$$\hat{E}(t) = E_0 \operatorname{sech}\left(\frac{t}{\tau_p}\right) \quad (3.16)$$

and the optical intensity can be written as

$$I(t) = I_0 \operatorname{sech}^2\left(\frac{t}{\tau_p}\right) \quad (3.17)$$

²³ J.A. Leegwater. "Theory of mode-locked semiconductor lasers", *IEEE J. Quantum Electron.*, 1996, **32**, 10, pp.1782-1790.

where E_0 , I_0 and τ_p are constants to be determined. Note that the parameter τ_p in this function is not the FWHM pulse width, but is related to the intensity FWHM pulse width as $\tau_{\text{FWHM}} = 2 \cosh^{-1}(\sqrt{2}) \tau_p \approx 1.76 \tau_p$.

An attempt to find out the value or set of values for the previous constants, which gives stable and self-starting solutions will not be carried out here, but it will be pointed out that solutions are only found for a limited range of laser parameters, which seem to be available in only a limited set of types of laser. This set, fortunately, includes semiconductor laser diodes²².

Figure 3.7 shows a comparison between the hyperbolic secant square pulse shape (sech^2) and the better known gaussian pulse shape. It can be seen that both shapes are very similar, except in the pulse wings where the sech^2 pulse shape has higher values than the gaussian.

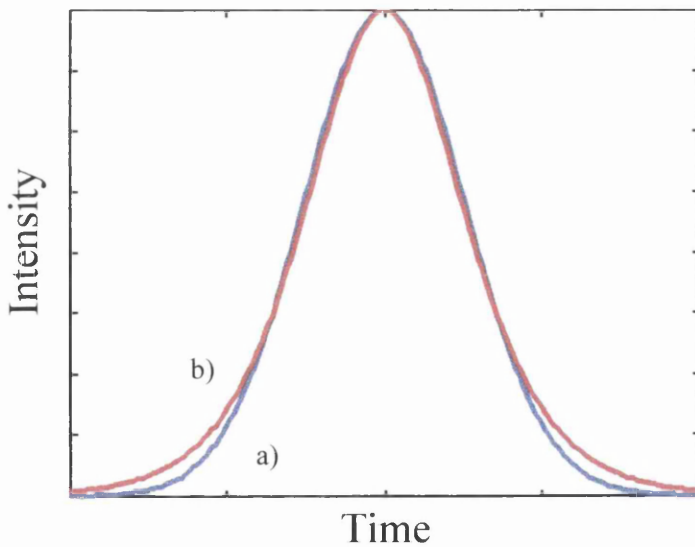


Figure 3.7: Comparison between (a) gaussian pulse (blue line) and (b) hyperbolic secant square pulse (red line).

3.5 Conclusions.

A review of the physics involved in modelocking was carried out in this chapter. An study of the physical mechanisms that shorten and broaden a optical pulse within a semiconductor laser cavity was made, and different configurations for achieving

passive modelocking in semiconductor lasers were summarised. An analysis of modelocking, from the frequency and time domain points of view, was also made and an analytical solution for the mode-locked pulse shape was obtained.

Chapter Four *ALL ACTIVE CAVITY MODE-LOCKED LASERS.*

The all active cavity laser (AAL) is the first of three different kinds of passive modelocking semiconductor lasers that will be analysed. This chapter documents the experimental results of the AAL configuration as a modelocking device. Modelocking characteristics including operating frequency, pulse width, spectral width, noise and development time are studied. The self-pulsations accompanying the modelocking operation are investigated in both the time and spectral domains. A numerical model is used to analyse the experimental results.

4.1 Laser configuration.

The AAL configuration is shown in Figure 4.1. The laser is divided into two different sections: the gain section and the saturable absorber section. The gain section has a maximum length of 5 mm, while the saturable absorber maximum length is 100 μm . After some unsuccessful attempts with different saturable absorber length to gain section length ratios, it was determined that this ratio must exceed 1% for mode-locked operation to be observed.

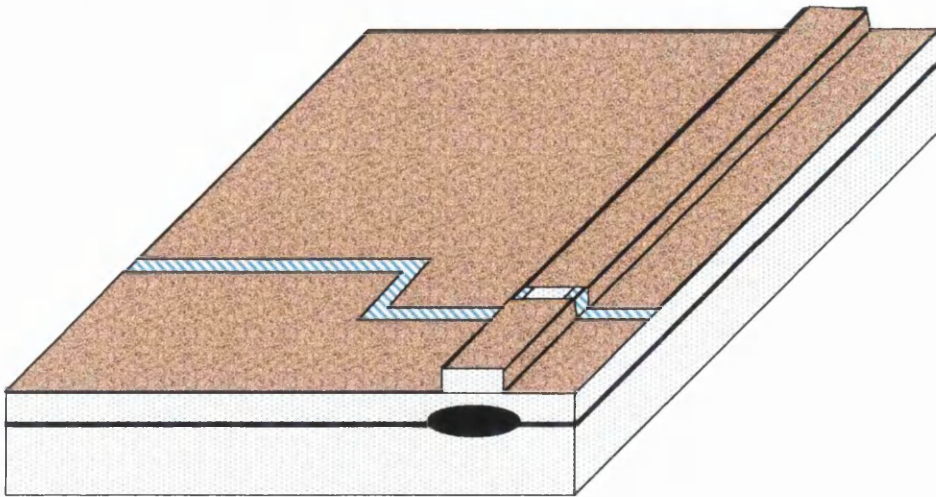


Figure 4.1: *All active cavity semiconductor laser design.*

The devices used in the experiments reported in this chapter had a total length of either 2.5 or 5 mm, with the saturable absorber length being 60 μm and 80 μm respectively. The ridge waveguide was 3 μm wide and 0.8 μm deep, to secure single transverse

mode operation. The two contacts were made by lifting off the metal layer, and the contact isolation resistance was around 5-6 k Ω after the highly doped p-GaAs contact layer was removed from the ridge between the contacts.

With both sections forward biased, the AAL configuration had threshold currents between 50-70 mA for the 2.5 mm long devices, and between 90-120 mA for the 5 mm long devices. Figure 4.2 shows the difference in light-current (I-L) curves, from a 5 mm long AAL, when both sections were connected together and when just the gain section was forward biased, leaving the saturable absorber floating.

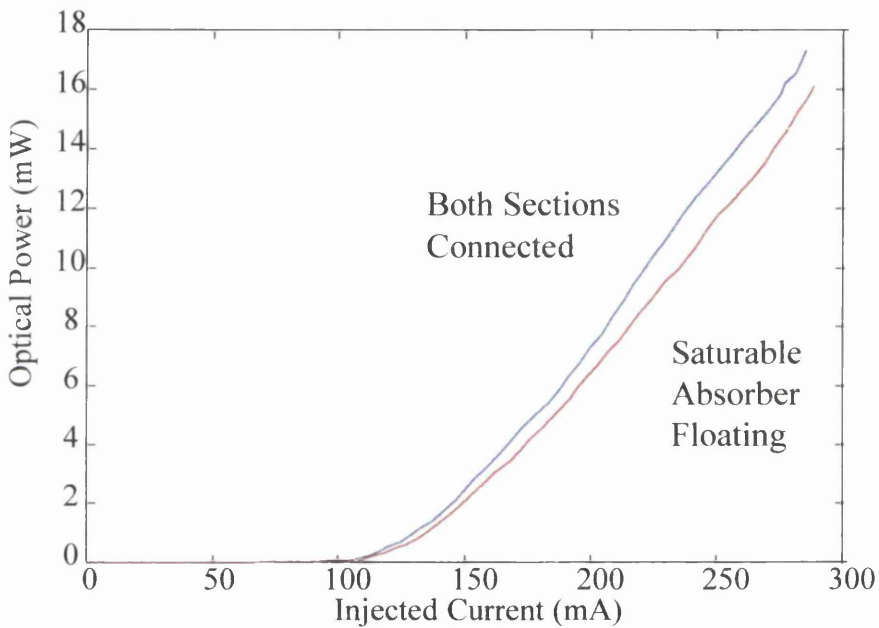


Figure 4.2: *I-L curves of a 5 mm long AAL when both sections were connected together (blue) and when the saturable absorber was floating (red).*

It can be seen that the threshold current slightly increased from around 110 mA to 115 mA when the saturable absorber was floating, due to the losses introduced in the laser cavity. The external quantum efficiency decreased, from 0.10 W/A to 0.09 W/A, also due to this increase in internal loss. Both effects can be explained using Eq.(2.16) and Eq.(2.18) from the previous chapter. From the former, the threshold gain when the saturable absorber is biased and when it is left floating can be expressed, respectively, as

$$g_{th}^{Bias} \Gamma = \alpha_i + \frac{1}{L_G + L_S} \text{Ln} \left[\frac{1}{R} \right] \quad (4.1)$$

$$g_{th}^{Float} \Gamma = \alpha_i + \alpha_S \frac{L_S}{L_G} + \frac{1}{L_G} \text{Ln} \left[\frac{1}{R} \right] \quad (4.2)$$

where L_G and L_S are the gain section and saturable absorber lengths respectively, and α_S , approximately equal¹ to 57 cm^{-1} , corresponds to the propagation loss through the saturable absorber when it is not pumped. Obviously, the required gain at threshold is higher when the saturable absorber is not pumped than when the saturable absorber is forward biased, and therefore the required current to achieved this gain is also higher. Assuming a logarithmic dependence of the gain with the current density² as in Eq.(2.20), and taking into account that L_S is much smaller than L_G , the relation between the threshold currents for the cases when the saturable absorber is pumped and when it is not is

$$\frac{I_{th}^{Float}}{I_{th}^{Bias}} = \exp \left[\frac{\left(\alpha_S + \frac{1}{L_G} \text{Ln} \left[\frac{1}{R} \right] \right) L_S}{n g_0 \Gamma_w L_G} \right] \quad (4.3)$$

where I_{th}^{Bias} and I_{th}^{Float} are the threshold currents when the saturable absorber is forward biased and when it is floating, respectively. Taking values from the previous chapter for the material used for the fabrication of these devices, QT757, and assuming a mirror reflectivity of 0.32, an increase of 2.1% was expected in the threshold current when the saturable absorber was floating. This compares with a value of 4% estimated from Figure 4.2, the difference being so large because of the difficulty of determining I_{th} accurately from this figure.

¹ P. Cusumano, T. Krauss and J.H. Marsh, "High extinction ratio GaAs/AlGaAs electroabsorption modulator integrated with passive waveguides using impurity-free vacancy diffusion", *Electronics Lett.*, 1995, **31**, 4, pp. 315-317.

² P.W.A. McIlroy, A. Kurobe and Y. Uematsu, "Analysis and application of theoretical gain curves to the design of multi-quantum-well lasers", *IEEE J. Quantum Electron.*, 1985, **QE-21**, 12, pp.1958-1963.

From Eq.(2.18) the external quantum efficiency slope, when the saturable absorber is not biased, is found to be

$$\eta_{Ext}^{Float} = \eta_i \left[\frac{\frac{1}{L_G} \text{Ln} \left[\frac{1}{R} \right]}{\alpha_i + \alpha_S \frac{L_S}{L_G} + \frac{1}{L_G} \text{Ln} \left[\frac{1}{R} \right]} \right] \quad (4.4)$$

while, for the case when the saturable absorber is forward biased, the quantum efficiency is as follows

$$\eta_{Ext}^{Bias} = \eta_i \left[\frac{\frac{1}{L_G + L_S} \text{Ln} \left[\frac{1}{R} \right]}{\alpha_i + \frac{1}{L_G + L_S} \text{Ln} \left[\frac{1}{R} \right]} \right] \quad (4.5)$$

The ratio of the quantum efficiencies, measured from the I-L curves, is then found to be

$$\frac{\eta_{Ext}^{Float}}{\eta_{Ext}^{Bias}} = \frac{\alpha_i (L_S + L_G) + \text{Ln} \left[\frac{1}{R} \right]}{\alpha_i L_G + \alpha_S L_S + \text{Ln} \left[\frac{1}{R} \right]} \quad (4.6)$$

where η_{Ext}^{Bias} and η_{Ext}^{Float} are the external quantum efficiencies when the saturable is forward biased and when it is floating, respectively. Again taking values for the material QT757, and assuming a mirror reflectivity of 0.32 a decrease of 12% is calculated, in very good agreement with the measured value of 11%.

4.2 Experimental results.

Due to the high threshold current for this configuration and the difficulty of providing efficient heat sinking to the devices, it was not possible to drive the AAL configuration under continuous-wave (CW) operation. The experimental results obtained in this section were therefore acquired under pulsed excitation. The gain section was driven with 100 ns wide pulses, at a duty cycle of 0.1%, and a DC reverse voltage was applied to the saturable absorber.

4.2.1 Modelocking frequency.

As mentioned previously, the frequency of a mode-locked pulse train is inversely proportional to the cavity length, according to the equation

$$f = \frac{c}{2 L n_g} \quad (4.7)$$

where n_g is the group refractive index of the semiconductor material, c/n_g is the local speed of the light and L is the laser length.

The group refractive index takes account of dispersion in the semiconductor material. The effective refractive index n_{eff} for a guided wave within a laser resonator depends on the wavelength λ because the semiconductor and the waveguide are dispersive. This dispersion is dominated by the material dispersion, but other factors, such as gain dispersion, also affect the variation of the effective refractive index with the wavelength. The group refractive index is then given by³

$$n_g = n_{eff} - \lambda \frac{dn_{eff}}{d\lambda} \quad (4.8)$$

For GaAs the group refractive index is approximately 3.75-4, which gives operating frequencies between 7.5 and 8 GHz for 5 mm long devices and between 15 and 16 GHz for 2.5 mm long lasers.

Time domain measurements:

Figure 4.3 is a three dimensional intensity representation of a streak camera image of the output from a 5 mm long AAL, with an injected current of 250 mA and a reverse voltage of -4 V. It shows a well-developed mode-locked pulse train with a pulse separation around 130 ps, giving a mode-locked frequency close to 7.8 GHz.

³ G.H.B. Thompson, "Physics of Semiconductor Laser Devices", *John Wiley & Sons*, 1980.

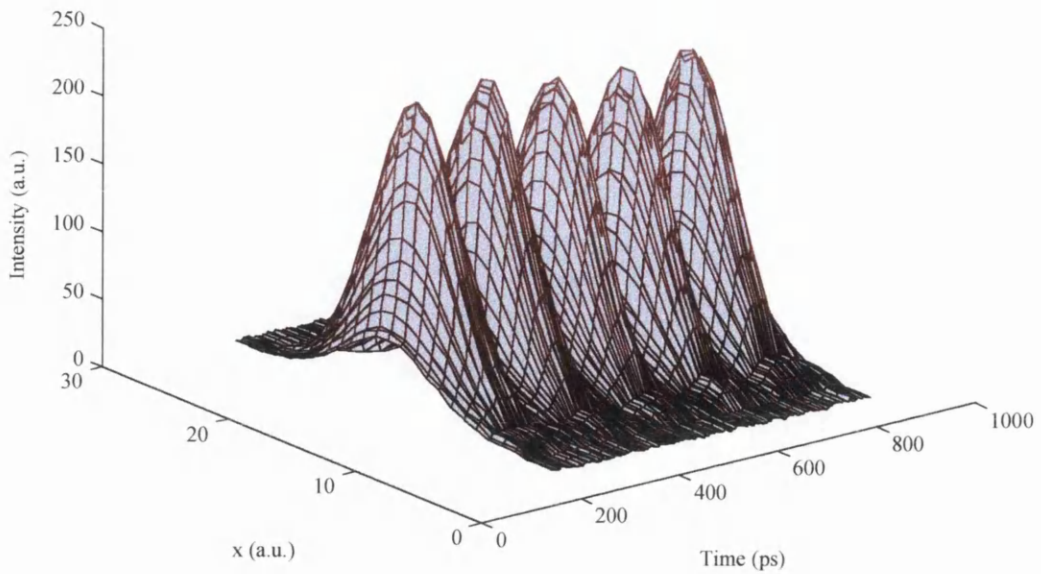


Figure 4.3: *Mode-locked pulse train from a 5 mm long AAL.*

Figure 4.4 shows the Fourier transform (FFT) of a 20 ns long streak profile with 16384 data points, which gives a resolution bandwidth of around 50 MHz. The main peaks are at the modelocking frequency, around 7.8 GHz, and the second harmonic, around 15.6 GHz. It is noticeable that the sidebands around the oscillating frequency were relatively large, in both the fundamental and the second harmonic, meaning that the mode-locked pulse train was very noisy, both in amplitude and phase. The phase noise is the source of the timing jitter, which will be analysed later in this chapter.

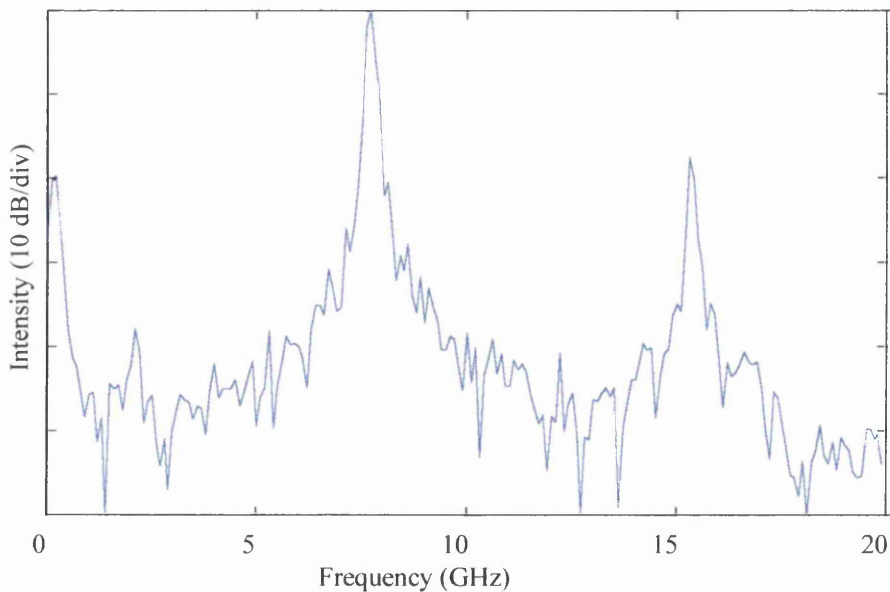


Figure 4.4: *FFT of the mode-locked pulse train data.*

Figure 4.5 shows a streak camera profile taken from a 2.5 mm long AAL working with an injected current of 150 mA, and a reverse voltage of -6 V. The pulse separation is around 65 ps, which gives an approximate operating frequency of 15.4 GHz.

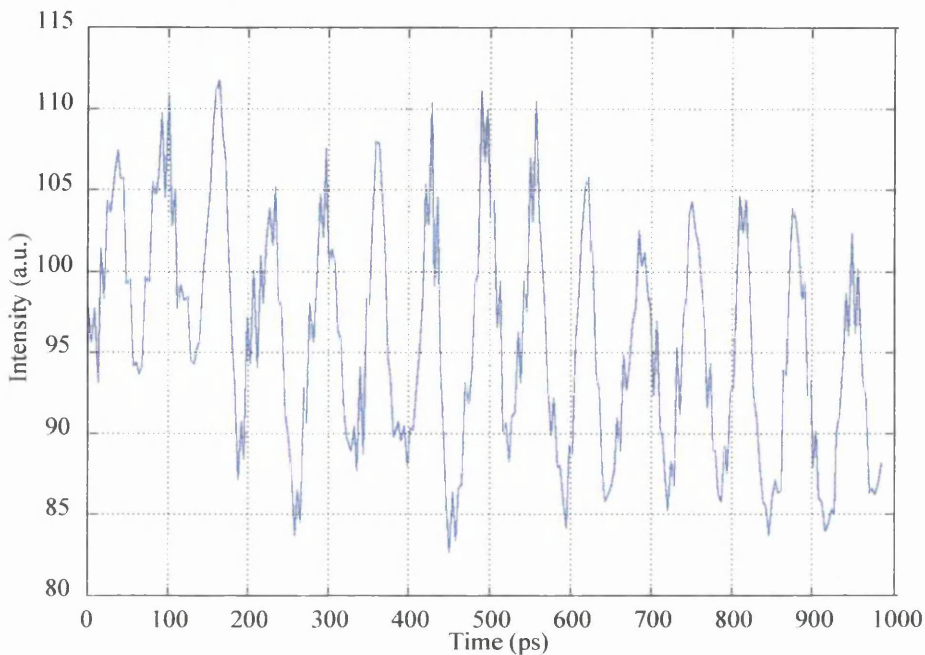


Figure 4.5: *Mode-locked pulse train from a 2.5 mm long AAL.*

Frequency domain measurements:

A microwave spectrum analyser with a spectral bandwidth of 40 GHz was used to measure the modelocking frequency of the AAL. The AAL output power was coupled into a lensed fibre which was connected to a pig-tailed GEC-Marconi GaAs photodetector with a 3 dB bandwidth of 18 GHz.

Due to the fact that the mode-locked AAL was operating under pulsed excitation, the frequency spectrum of the mode-locked signal was the convolution of two different signals⁴:

- a) The spectrum of a mode-locked pulse train operating at around 7.7 GHz. This frequency spectrum is the Fourier transform of a mode-locked pulse at the modelocking frequency and successive harmonics.

⁴ F.G. Stremler, "Introduction to communication systems", Addison-Wesley, 1992.

- b) The spectrum of the injected current pulses, which are approximately square pulses 100 ns long at a frequency of 10 kHz.

To measure the frequency spectrum of the second signal some considerations must be examined. The resolution bandwidth used to measure a pulsed signal greatly affects the measurement. When the resolution bandwidth is narrow compared to the current pulse repetition frequency, say 10 kHz, the display will show the individual frequency components making up the pulsed signal, as can be seen in Figure 4.6. This is called the *narrow band mode*. The separation between the different peaks is equal to the repetition frequency of the current pulses, i.e. 10 kHz.

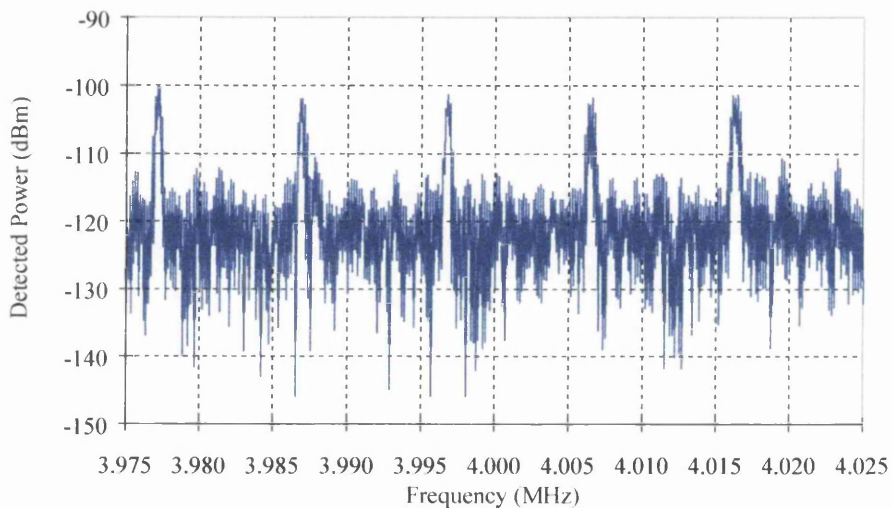


Figure 4.6: *Narrow band mode for measuring current pulse repetition frequency.*

When the resolution bandwidth is wide compared to the pulse repetition frequency the *broadband mode* is seen, as in Figure 4.7. The envelope of the spectrum is traced out by pulse lines which are separated by the current pulse repetition frequency. From this envelope the current pulse width can be easily identified, as the reciprocal of the frequency difference between the main lobe peak and the first envelope null, or between every successive two envelope nulls.

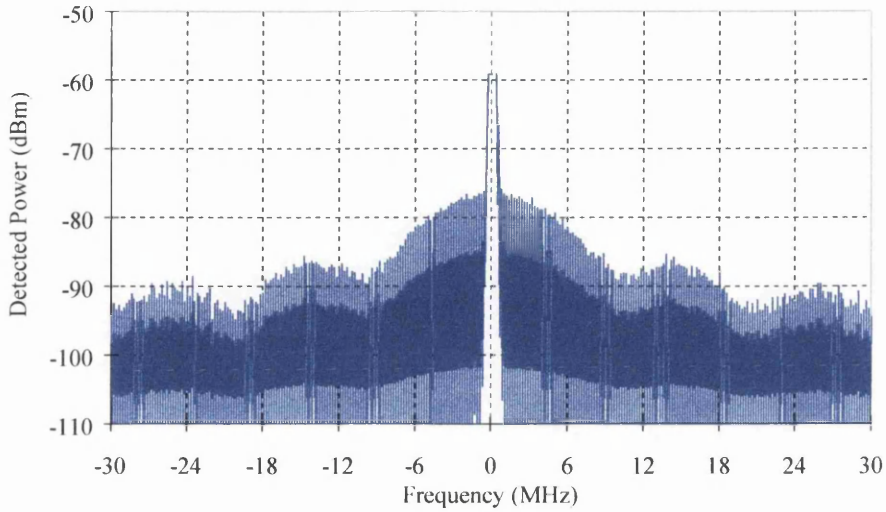


Figure 4.7: *Broadband mode for measuring current pulse width.*

Figure 4.8 shows the envelope of the measured microwave spectrum (broadband mode) from the same 5 mm long AAL used above, around the fundamental modelocking frequency.

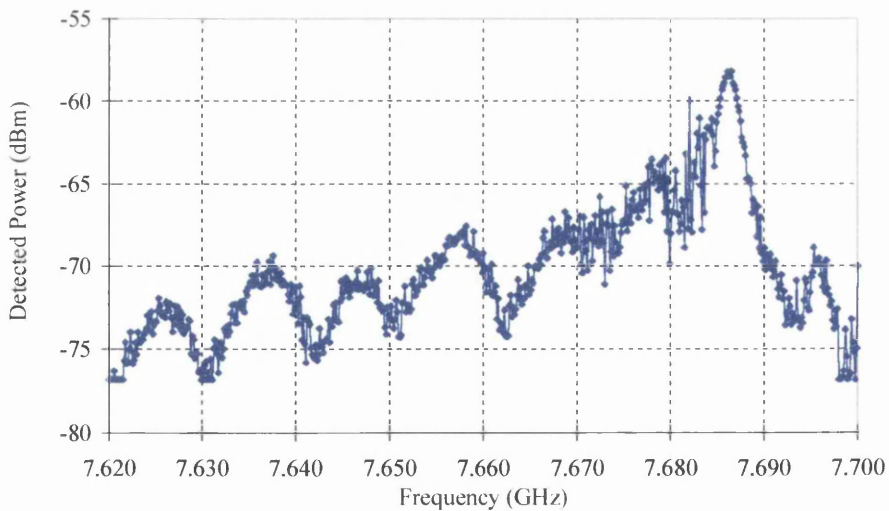


Figure 4.8: *Microwave spectrum of a mode-locked AAL operating under pulse excitation.*

The reason why a exact replica of the injected current pulse spectrum was not shown at the modelocking frequency was probably due to the non-perfect square shape of the injected current pulse. In any case, the current pulse width could be obtained perfectly

by measuring the reciprocal frequency between two nulls in the spectrum envelope, and the modelocking frequency was at the centre of the main lobe, around 7.685 GHz.

4.2.2 Pulse width.

The pulse width from a mode-locked AAL was analysed using the TPA autocorrelator described in chapter 2. The pulse width was measured for two different saturable absorber voltages, -3 and -4 V, and the autocorrelation traces and fitting curves are depicted in Figure 4.9.

The determination of the original pulse width from the width of the TPA correlation trace is somewhat ambiguous. The relation between the FWHM of the measured autocorrelation t_0 and the FWHM of the pulse τ_0 depends on the assumed shaped of the mode-locked pulse. In our case, the mode-locked pulse shape is assumed to be hyperbolic secant square^{5,6} (sech^2), and so $t_0/\tau_0 = 1.55$. The fitting curve in Figure 4.9 was calculated using a Simplex method, assuming a sech^2 shape.

In can be seen in Figure 4.9 that the FWHM of the fitting curve, for the autocorrelation with $V_{\text{sat}} = -3$ V, was 22.5 ps. The FWHM of mode-locked pulses was 14.5 ps, equal to the measured autocorrelation FWHM divided by the factor 1.55. The FWHM of mode-locked pulses when the saturable absorber voltage was -4 V was 11.1 ps.

⁵ H.A. Haus, "Theory of mode locking with a slow saturable absorber", *IEEE J. Quantum Electron.*, 1975, **QE-11**, 9, pp. 736-746.

⁶ J.A. Leegwater, "Theory of mode-locked semiconductor lasers", *IEEE J. Quantum Electron.*, 1996, **32**, 10, pp. 1782-1790.

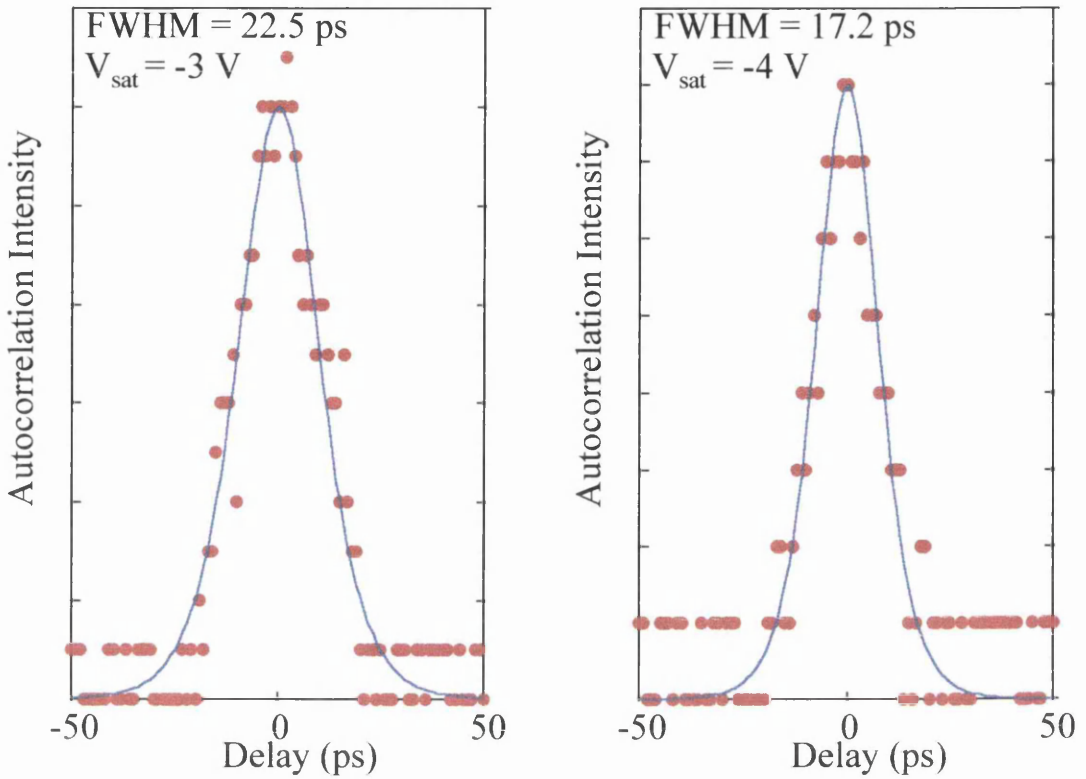


Figure 4.9: *TPA autocorrelation measurements (dots) and fitting curve assuming hyperbolic secant square shape of the modelocking pulse (line) for $V_{\text{sat}} = -3 \text{ V}$ (left) and $V_{\text{sat}} = -4 \text{ V}$ (right).*

To obtain the true FWHM of mode-locked pulses, the dispersion in the fibre autocorrelator must also be taken into account. The dispersion in the autocorrelator, obtained in chapter 2, was estimated to be 2 ps/nm, the spectral width of the modelocking pulses, as will be shown in a following section, was 2 nm, and therefore the total dispersion suffered by mode-locked pulses in the autocorrelator was 4 ps. From Eq.(2.25) the true FWHM of the modelocking pulses was estimated to be 13.9 and 10.3 ps for the cases when the saturable absorber voltage was -3 and -4 V respectively. Table 4.1 resumes the above calculations.

V_{sat} (V)	Autocorrelation FWHM (ps)	Sech ² FWHM (ps)	True FWHM (ps)
-3	22.5	14.5	13.9
-4	17.2	11.1	10.3

Table 4.1: *Calculation of the true pulse width from the autocorrelation trace.*

The poor performance in respect of the pulse width of the AAL may be a result of gain dispersion effects^{7,8}, which tend to broaden the pulses more effectively when the optical pulse propagates through long sections of active waveguide. The enhanced broadening of the optical pulse can be attributed to group velocity dispersion (GVD) induced by gain dispersion. Gain dispersion occurs for optical pulses whose width is short enough that their spectral width becomes comparable to the gain bandwidth. The effect of gain dispersion is to reduce the gain from spectral components far away from the carrier frequency. Gain saturation imposes a chirp on the amplified pulse such that its leading edge is red shifted while the trailing edge is blue shifted⁹. Gain dispersion, on the other hand, induces normal GVD such that red shifted components of the pulse travel faster than the blue shifted components. Clearly, the leading edge would arrive earlier while the trailing edge is delayed, causing pulse broadening. The longer the active cavity, the broader the optical pulses. Pulse width performance is improved, as it will be shown in a later chapter, with the incorporation of low-loss passive waveguides which act as a more ideal medium for short pulse propagation.

4.2.3 Self-pulsations in mode-locked semiconductor lasers.

Passive modelocking can be adversely affected, or even suppressed, by the occurrence of self-pulsations. A mode-locked pulse train modulated by a deep self-pulsing envelope has been reported in many cases^{10,11,12}, as well as being predicted by

⁷G. P. Agrawal, "Effect of gain dispersion on ultrashort pulse amplification in semiconductor laser amplifiers", *IEEE J. Quantum Electron.*, 1991, **27**, 6, pp. 1843-1849.

⁸ D.J. Derickson, R.J. Helkey, A. Mar, J.R. Karin, J.G. Wasserbauer and J.E. Bowers, "Short pulse generation using multisegment mode-locked semiconductor lasers", *IEEE J. Quantum Electron.*, 1992, **28**, 10, pp. 2186-2202.

⁹ G. P. Agrawal and N. A. Olsson, "Self-phase modulation and spectral broadening of optical pulses in semiconductor laser amplifiers", *IEEE J. Quantum Electron.*, 1989, **25**, 11, pp. 2297-2306.

¹⁰ J. Palaski and K. Y. Lau, "Parameter ranges for ultrahigh frequency mode locking of semiconductor lasers", *IEEE Photonics Technol. Lett.*, 1991, **59**, 1, pp. 7-9.

¹¹ K. Y. Lau and J. Palaski, "Condition for short pulse generation in ultrahigh frequency mode-locking of semiconductor lasers", *Appl. Phys. Lett.*, 1991, **3**, 11, pp. 974-976.

¹² J. Yu and D. Bimberg, "Suppression of self-pulsation for tens of gigahertz optical pulses from passively mode-locked semiconductor lasers", *Appl. Phys. Lett.*, 1995, **67**, 22, pp. 3245-3247.

numerical simulations^{13,14}. The simultaneous presence of a saturable absorber and a gain section, required for passive modelocking to take place, can also cause these self-pulsations. Depending on the biasing conditions, a self-pulsing envelope was also observed in the temporal output of the AAL.

Figure 4.10 shows a streak image and profile of a mode-locked pulse train deeply modulated by a self-pulsing envelope.

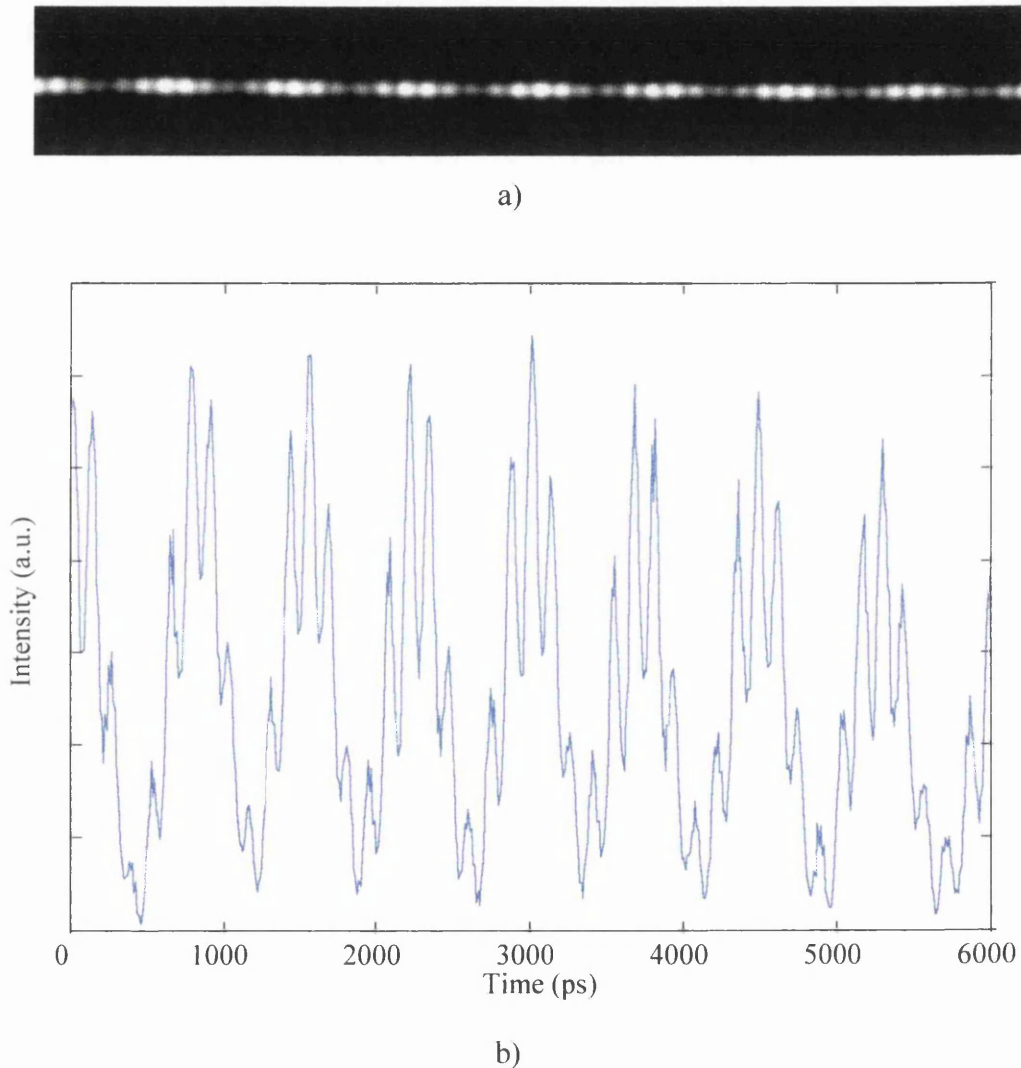


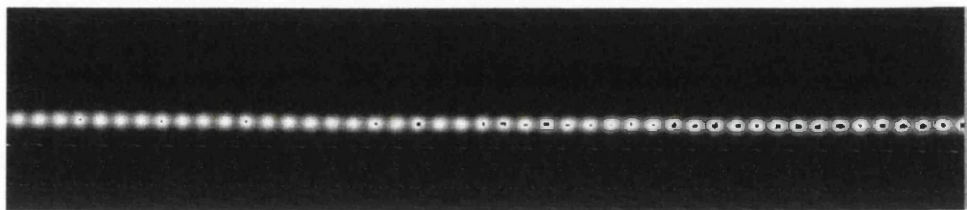
Figure 4.10: *Streak image (a) and profile (b) of a mode-locked pulse train modulated by self-pulsing envelope.*

¹³ W. Yang and A. Gopinath, "Study of passive mode locking of semiconductor lasers using time-domain modelling", *Appl. Phys. Lett.*, 1993, **63**, 20, pp. 2717-2719.

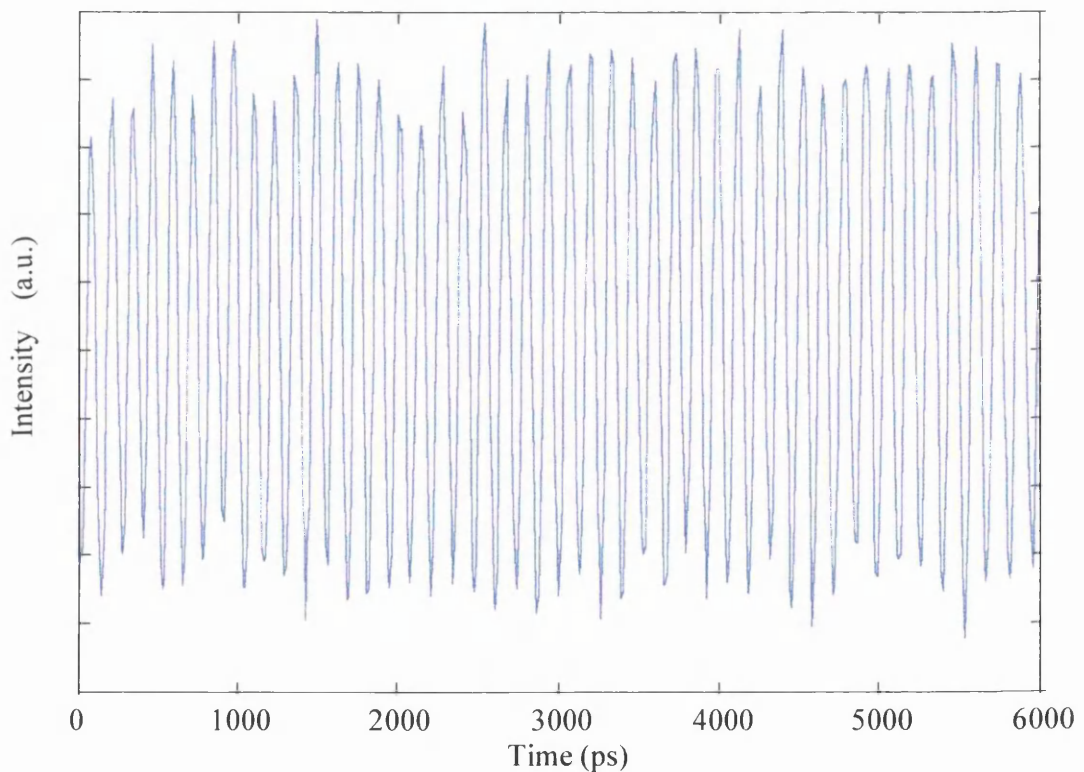
¹⁴ D.J. Jones, L.M. Zhang, J.E. Carrol and D.D. Marcenac, "Dynamics of monolithic passively mode-locked semiconductor lasers", *IEEE J. Quantum Electron.*, 1995, **31**, 6, pp. 1051-1058.

For this case, the injected current peak was 250 mA and the saturable absorber voltage was -3.9V. The frequency of the self-pulsing changed from 1.6 to 1.2 GHz as the saturable absorber voltage was changed from -2 V to -3.9 V, and also increased monotonically with the gain section current.

By increasing the gain section current, a more regular pulse train was obtained, as in Figure 4.11, which shows possibly a slight trace of the pulsing envelope. This modelocking streak image and profile was obtained with an injected current of 290 mA and a reverse voltage of -3.6V.



a)



b)

Figure 4.11: *Streak image (a) and profile (b) of a regular mode-locked pulse train.*

Obviously, the self-pulsing envelope accompanying the optical pulse train has to be taken into account in practical applications. For this reason, further analysis of the laser operating regions was undertaken to establish the biasing conditions where self-pulsations were not present.

Depending on the injected current and the saturable absorber reverse voltage, different operating regions could be obtained: self-pulsation and modelocking, regular modelocking and regular self-pulsation. There are some differences between the results presented here from those reported earlier, which mostly deal with shorter lasers^{10,11}. The main difference from the reported behaviour of most of the shorter devices is that in our case, for some parameter values, an upper, as well as a lower, limit to pure modelocking was observed; above this limit, the envelope modulation reappears and becomes more irregular. This type of instability is probably due to fast nonlinearities.

Figure 4.12 shows a map of the operating regions for a AAL with a threshold current of 140 mA.

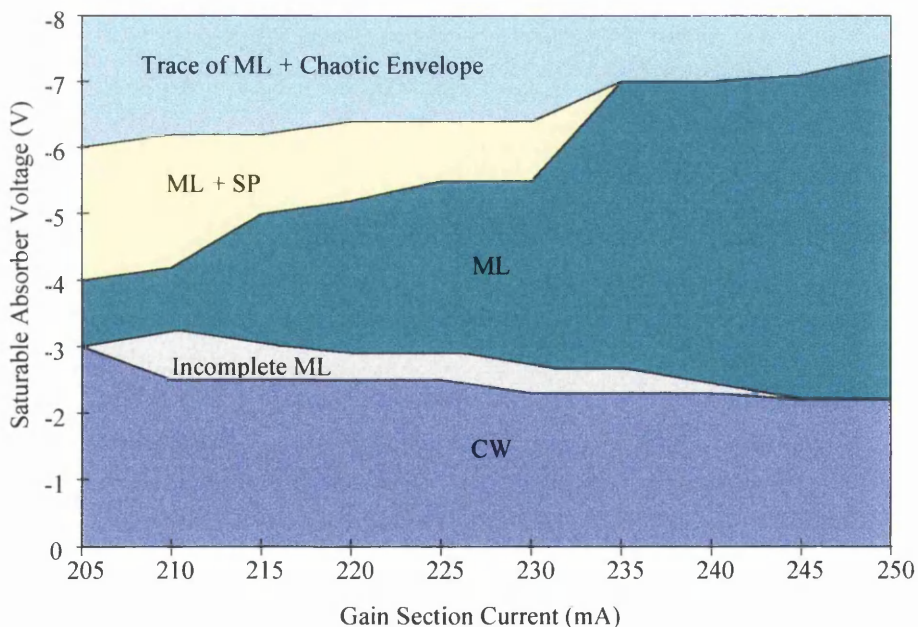


Figure 4.12: Working area map of an AAL.

When zero or a very low reverse bias was applied to the saturable absorber, or when the injected current was lower than 200 mA (~ 1.4 times the threshold current) the

laser did not show any modelocking or self-pulsations. With an increase of both the magnitude of the saturable absorber voltage and the gain section current, the laser operates in several dynamics regimes which are (in the order of increasing current and voltage magnitude) incomplete modelocking, regular modelocking and modelocking with a deep self-pulsing envelope. Further increases in the injected current caused the pulsing envelope to reappear but it was less regular, an upper limit for pure mode-locked operation.

These results agree completely with the theoretical model used to analyse our experimental work, which will be described in a following section. However, the above working area map was not followed for all devices. Figure 4.13 was measured with a different device, from the same semiconductor wafer, but from a different laser fabrication batch. Basically, this working area map is very similar to that analysed in Figure 4.12, except for the case when a very high voltage was applied to the saturable absorber, when pure Q-switching with no modelocking appears. This effect of Q-switching above modelocking in the working area was not predicted by the theoretical model, but has been observed by other workers¹⁰.

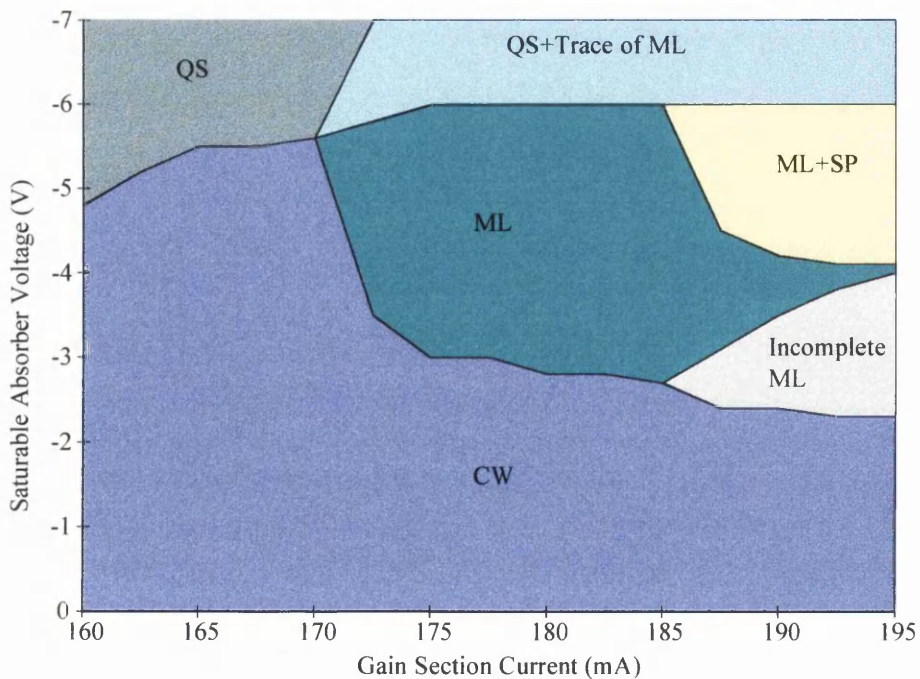


Figure 4.13: Working area map from a different AAL. No agreement with theoretical model.

This sequence of events is best visualised with the aid of the streak camera profiles shown in Figure 4.14, which were taken from the same device used to obtain the map in Figure 4.12. A constant injected current of around 220 mA was used. When the reverse voltage magnitude was very low, as in Figure 4.14 (a), the laser output was a single optical pulse exhibiting relaxation oscillations. When the magnitude of the saturable absorber reverse bias was slowly increased, modelocking began to take place, first as a sinusoidal modulation of the optical power at the modelocking frequency of around 8 GHz, Figure 4.14 (b), and then as distinct short pulses as the reverse voltage magnitude was further increased, Figure 4.14 (c),(d) and (e). When the reverse voltage was -2 V, the modelocking was still incomplete and the pulse train was not well developed. The quality of the mode-locked pulse train increased as the saturable absorber voltage was decreased to -3 V, but a deep self-pulsing envelope arose at around 2 GHz when the saturable absorber voltage was -5 V.

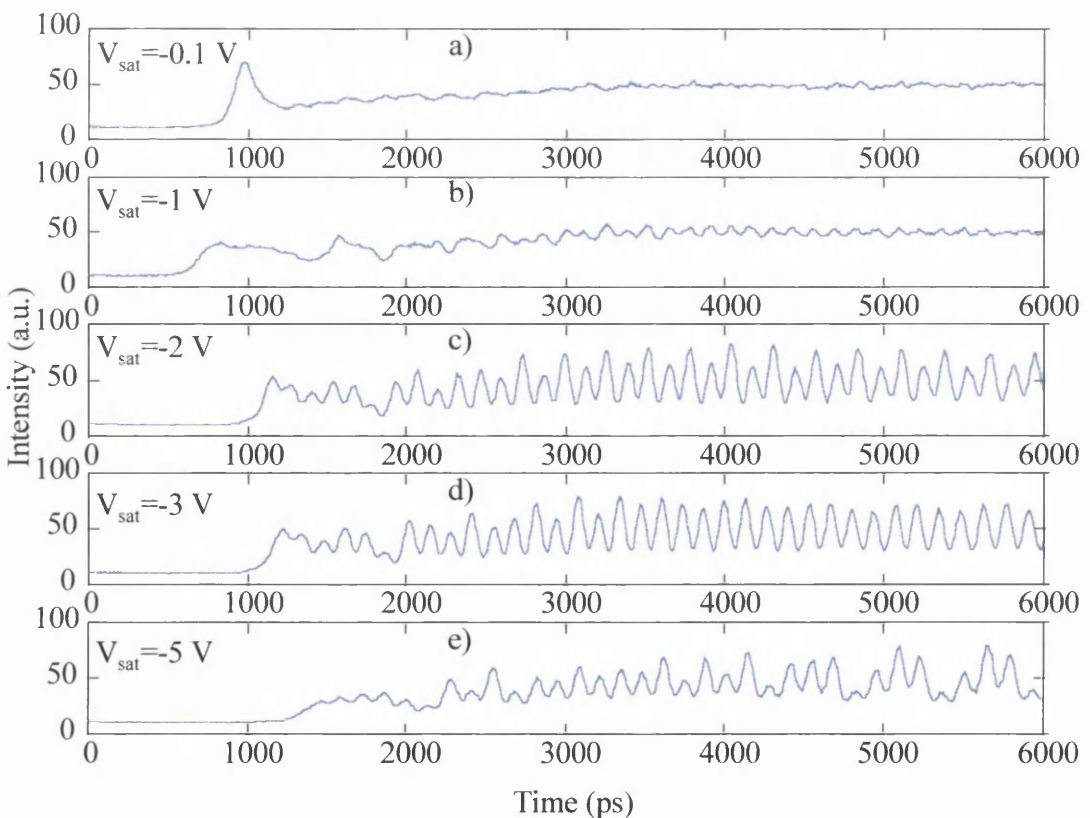


Figure 4.14: Streak camera profiles of an AAL optical output for increasing negative bias on the saturable absorber.

4.2.4 Spectral analysis.

The optical spectrum of light pulses travelling in the laser cavity can be distorted considerably during the amplification process if the refractive index becomes nonlinear, even when the pulse shape remains unchanged. When a semiconductor laser produces an optical pulse with an energy approaching the saturation energy of the laser, gain saturation leads to a depletion in the carrier density, which causes an increase in the refractive index that shifts the spectrum to longer wavelengths. When the pulse propagates through the saturable absorber, loss saturation leads to an increase in the carrier density producing the opposite effect. Therefore, gain and absorption saturation produce a shift and distortion in the optical spectrum. The physical mechanism behind this shift and distortion, is self-phase modulation (SPM)⁹. The time dependence of the saturated gain leads to a temporal modulation of the phase, i.e., the pulse modulates its own phase as a result of gain saturation.

Optical spectra were acquired with an Advantest optical spectrum analyser with a resolution of 0.1 nm. The longitudinal intermode spacing is given by

$$\delta\lambda = \frac{\lambda^2}{2 L n_g} \quad (4.9)$$

where n_g is the group refractive index of the semiconductor material, λ is the free space wavelength and L the laser cavity length. For GaAs, and a cavity length of 5 mm, the intermode spacing is around 0.018 nm. The optical spectrum analyser therefore measures the envelope of the longitudinal modes due the fact that it cannot resolve the intermode wavelength spacing.

Figure 4.15 shows spectral measurements taken from a 5 mm long laser for the cases of: (a) no modelocking (zero saturable absorber bias), (b) modelocking modulated by a deep self-pulsing envelope and (c) regular modelocking. The FWHM of the optical spectrum changed from 0.4 nm at zero absorber bias (no modelocking) to almost 2 nm when the saturable absorber was reverse biased between 3.6 and 5 V (self-pulsing envelope or regular modelocking). The optical spectra for both these cases were shifted to longer wavelengths compared to the lasing wavelength at zero saturable absorber bias. For pure modelocking, case (c), the shift was more pronounced, the

spectrum was very asymmetric with a long tail on the blue side and it had a distinct superstructure. The spectrum for modelocking combined with a self-pulsing envelope, case (b), was more narrow, more symmetric and had just one side shoulder at the red side (*opposite* from the modelocking case).

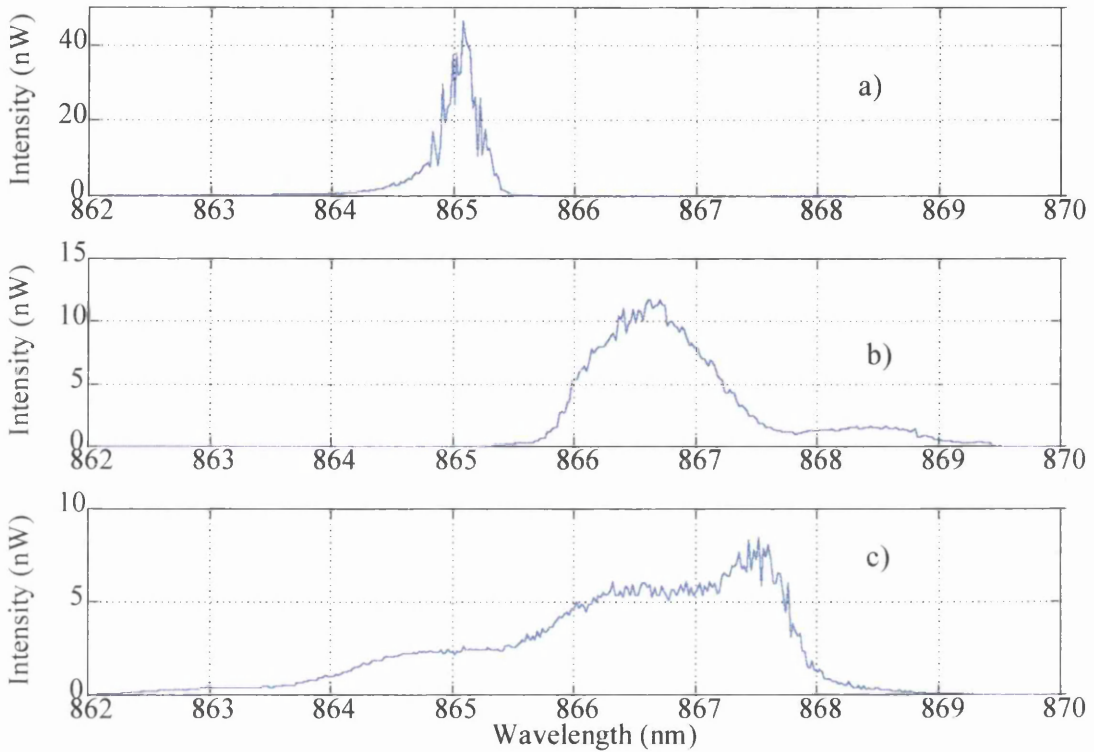


Figure 4.15: *Optical spectra for a) no modelocking, b) modelocking with self-pulsing envelope, c) pure modelocking.*

The spectrum for the mode-locked case shows a feature that is unique to semiconductor lasers and amplifiers, which is that the spectrum develops a multi-peak or multi-shouldered structure due to the SPM. Physically, the instantaneous frequency is the same at two distinct points within the pulse profile. Depending on the relative phases of the optical fields at those two points, the fields can interfere constructively or destructively. This interference leads to an oscillatory structure in the pulse spectrum.

The optical spectrum FWHM, measured in Hz, is defined as the signal bandwidth. The *time-bandwidth product* is then defined as the pulse width times the spectral bandwidth. This time-bandwidth product is a measure of the chirp present in a pulse

train, as it will increase with the amount of chirp. The theoretical time-bandwidth product value for an sech^2 pulse shape is 0.314⁸.

The time-bandwidth product for the AAL configuration can be obtained transforming the spectral width from wavelength to frequency using the identity

$$\frac{\delta f}{f} = \frac{\delta \lambda}{\lambda} \quad (4.10)$$

and is calculated to be around 7. This value, more than 20 times the theoretical one, indicates that the mode-locked pulses were highly chirped, due to the gain dispersion and gain saturation effects described in a section 4.2.2.

In external cavity lasers it is possible to obtain near transform-limited pulses by using a bandwidth limiting element such as a diffraction grating in the external cavity. This bandwidth limiting element filters out the excess bandwidth created by the SPM. Monolithic cavity structures can also have bandwidth limiting elements in the form of Bragg reflectors to reduce the optical bandwidth and therefore the time-bandwidth product¹⁵.

4.2.5 Timing jitter.

Fluctuations in mode-locked lasers include variations in both pulse intensity and pulse timing^{16,17,18,19}. Pulse to pulse timing variations give rise to a very important noise parameter that contributes directly to the time resolution in most applications of mode-

¹⁵ S. Arahira and Y. Ogawa, "Passive and hybrid modelocking in a multi-electrode DBR laser with two gain sections", *Electronics Lett.*, 1995, **31**, 10, pp. 808-809.

¹⁶ K. Petermann, "Laser diode modulation and noise", *Kluwer Academic Publishers*, 1986.

¹⁷ M.J.W. Rodwell, D.M. Bloom and K.J. Weingarten, "Subpicosecond laser timing stabilization", *IEEE J. Quantum Electron.*, 1989, **25**, 4, pp. 817-827.

¹⁸ D.J. Derickson, P.A. Morton, J.E. Bowers and R.L. Thornton, "Comparison of timing jitter in external and monolithic cavity mode-locked semiconductor lasers", *Appl. Phys. Lett.*, 1991, **59**, 26, pp. 3372-3374.

¹⁹ D.J. Derickson, A. Mar and J.E. Bowers, "Residual and absolute timing jitter in actively mode-locked semiconductor lasers", *Electronics Lett.*, 1990, **26**, 24, pp. 2026-2028.

locked lasers. Carrier density fluctuations modulate the round trip time for the optical pulses inside the laser cavity, and cause timing jitter in mode-locked devices.

Considering the timing jitter of a mode-locked pulse train described by the random variable $J(t)$, the amount of random fluctuations is characterised by the root-mean-square (rms) deviation of the noisy quantity. The rms timing jitter, a measure of how widely values are dispersed from the average pulse period, is defined as the standard deviation σ_J of $J(t)$ as

$$\sigma_J^2 = \langle J^2(t) \rangle = \lim_{\Delta \rightarrow \infty} \frac{1}{\Delta} \int_{-\Delta/2}^{\Delta/2} J^2(t) dt \quad (4.11)$$

where the operator $\langle \rangle$ denotes time average, as explained in appendix III, and Δ is the observation period. Obviously, in practical measurements, σ_J is determined over a finite time period, and the integration in Eq.(4.11) runs only over this time range.

Using Parseval's theorem, analysed in appendix III, the rms timing jitter can also be calculated as

$$\sigma_J^2 = \langle J^2(t) \rangle = \frac{1}{2\pi} \int_{-\infty}^{+\infty} S_J(\omega) d\omega \quad (4.12)$$

where $S_J(\omega)$ is the power spectrum of the noise variable $J(t)$, the Fourier transform of the autocorrelation function of $J(t)$. This relation is very important because it allows the characterisation of the rms timing jitter using power spectrum techniques²⁰ (a much more detailed analysis of jitter characterisation using power spectrum techniques is given in the next chapter).

Figure 4.16 shows a comparison of the single-sideband phase noise level, $L(f)$, between our monolithic GaAs/ AlGaAs device and an external cavity laser after Derickson *et al*¹⁸. $L(f)$ is defined¹⁷ as the ratio of the power in one phase modulation sideband, in a 1 Hz measurement bandwidth, to the total spectral power, at an offset f Hz away from the modelocking frequency. The single-sideband phase noise spectrum of the

²⁰ D. von der Linde, "Characterisation of the noise in continuously operating mode-locked lasers", *Appl. Phys. B*, 1986, **39**, pp. 201-217.

modelocking laser, at the n th harmonic, is related to the single-sideband power spectrum of the timing jitter $S_J(\omega)$ as

$$L_n(\omega) = n^2 \omega_{ML}^2 S_J(\omega) \quad (4.13)$$

where n is the harmonic number and ω_{ML} is the modelocking angular frequency.

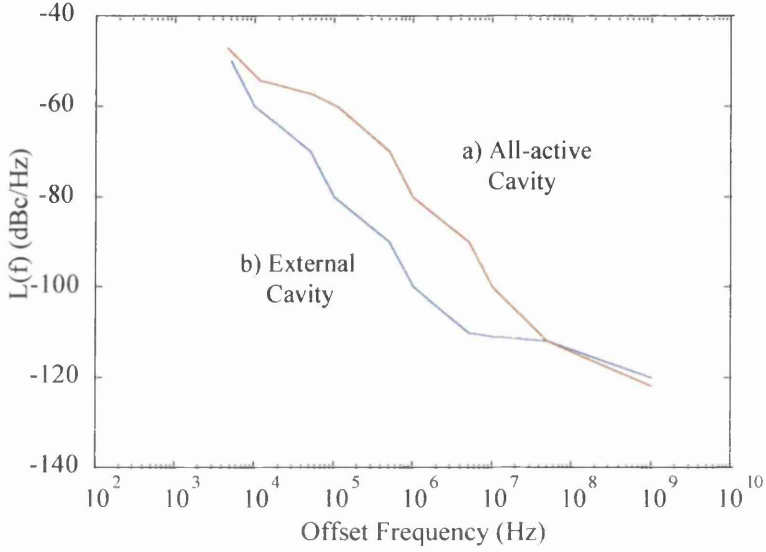


Figure 4.16: *Single side-band phase noise $L(f)$ comparison for monolithic and external cavity devices.*

The phase noise levels are larger for monolithic all-active cavity configurations than for external cavity configurations due to the fact that, for similar carrier density levels in each active waveguide, the phase modulation level will be proportional to the active waveguide lengths, and these are longer in monolithic than in external cavity devices.

Extended cavity lasers with long sections of low-loss passive waveguide should give comparable phase noise levels to external cavity devices, and they will be analysed in the following chapter.

Using Eq.(4.12) and Eq.(4.13), the phase noise level $L(f)$ can be converted to the rms timing jitter in the frequency range (f_{low}, f_{high}) by

$$\sigma_{rms} = \frac{1}{2\pi n f_{ML}} \sqrt{2 \int_{f_{low}}^{f_{high}} L_n(f) df} \quad (4.14)$$

where the factor of 2 before the integral is to take account of both sidebands, n is the harmonic number, f_{ML} is the oscillating frequency and f_{high} and f_{low} are the limits to the integration with respect to the offset frequency. The rms timing jitter levels calculated using Figure 4.16, are around 22.5 ps (1 kHz-10 MHz) for the all active cavity monolithic configuration and 12.2 ps (1.5 kHz-50 MHz) for the external cavity configuration .

Pulse to pulse timing measurements were taken in order to assess the jitter levels of the AAL pulse train, and are shown in Figure 4.17. The distances between pulses were measured from a 5 ns long streak camera profile, containing 38 pulses. From Eq.(4.11); a measure of the rms timing jitter level is obtained by averaging the pulse to pulse distances and calculating the standard deviation over the 5 ns period. From these measurements, the pulse to pulse timing standard deviation was found to be around 3 ps. The difference between the measured value of 3 ps and the estimated value of 22.5 ps is due to the fact that jitter components with frequencies under 50 MHz are not measured using a 5 ns long streak camera profile. The measurement of pulse to pulse timing over a period Δt only accounts for jitter components with frequencies above $f_{low}=1/4\Delta t$ ¹⁷. To obtain pulse timing variations for frequencies above 1 kHz, as does the estimated value, the rms timing jitter would have to be integrated over a period longer than 250 μ s.

In any case, it has been shown that the timing jitter in passively mode-locked lasers is very high, higher than 10% of the total pulse period, and a stabilising mechanism is necessary if a very stable pulse train is needed^{21,22}.

²¹ R.J. Helkey, D.J. Derickson, A. Mar, J.G. Wasserbauer, J.E. Bowers and R.L. Thornton, "Repetition frequency stabilisation of passively mode-locked semiconductor lasers", *Electronics Lett.*, 1992, **28**, 20, pp. 1920-1922.

²² M. Margalit, M. Orenstein and H.A. Haus, "Noise in pulsed injection locking of a passively mode-locked laser", *IEEE J. Quantum Electron.*, 1996, **32**, 5, pp.796-801.

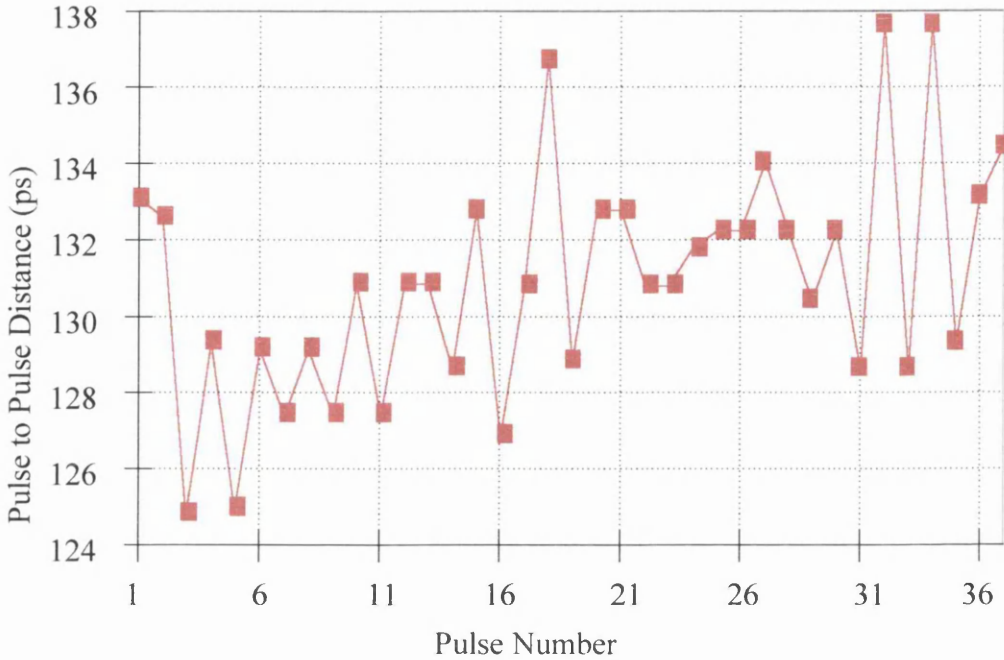


Figure 4.17: *Pulse to pulse distance measurements from a 5 ns long streak camera profile.*

4.2.6 Development of passive modelocking.

To analyse the time taken for passive modelocking to develop in the AAL configuration, a 5 mm long device was used. The development of laser oscillations and modelocking does not happen instantly, but takes a finite time, as shown in Figure 4.18. The upper graph (a) corresponds to the case when the saturable absorber was left floating with no reverse voltage, and, therefore, no modelocking appeared. The lower graph (b) corresponds to the case when a voltage of -3 V was applied to the saturable absorber, and modelocking developed. We can consider the following stages of pulse build-up in the modelocking case:

- a) When the laser pumping is turned on, carrier concentrations build up at a comparatively slow rate, until the laser gain first equals the total losses in the cavity, comprising the unsaturated absorber loss and all other internal cavity losses. At this point the circulating energy in the cavity begins to build up from a very weak noise spike from spontaneous emission. This initial noise distribution will continue to build up for some time, while simultaneously,

individual noise spikes will begin to broaden and to smooth out. This stage can be seen from 0 to around 1100 ps in Figure 4.18(b).

b) At some point, a single preferred noise spike becomes powerful enough to burn its way through the saturable absorber on succeeding round trips. This pulse will then grow more rapidly than the surrounding noise spikes. In Figure 4.18(b) this stage lasts approximately from 1100 to 2200 ps. The average of the output energy clearly shows relaxation oscillations, as expected.

c) Finally, this preferred pulse will continue to build up in intensity on succeeding round trips, until saturation occurs.

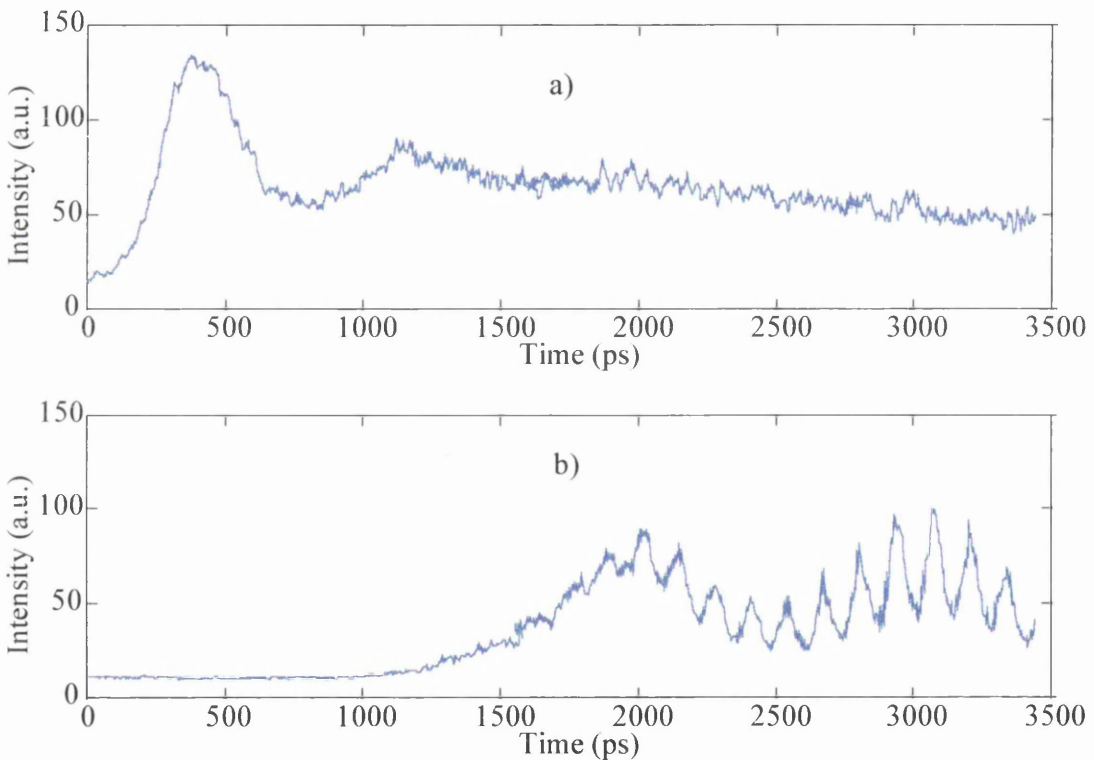


Figure 4.18: *Development of passive modelocking in an AAL.*

The optical power at the modelocking frequency increases in a simple exponential fashion^{23,24} of the form $1 - e^{-t/\tau}$. To quantify the time constant, a short-term Fourier transform of the optical output power was performed, with window lengths of 1 ns.

²³ O. Solgaard, M. H. Kiang and K. Y. Lau, "Pulse buildup in passively mode-locked monolithic quantum well semiconductor lasers", *Appl. Phys. Lett.*, 1993, **63**, 11, pp. 2021-2023.

²⁴ J. C. AuYeung, L. A. Bergman and A. R. Johnston, "Transient behaviour of an actively mode-locked semiconductor laser diode", *Appl. Phys. Lett.*, 1982, **41**, 2, pp. 124-126.

This was done by monitoring the output from the laser, and adjusting the trigger delay time by a variable time delay with a minimum delay step of 100 ps, as shown in Figure 4.19.

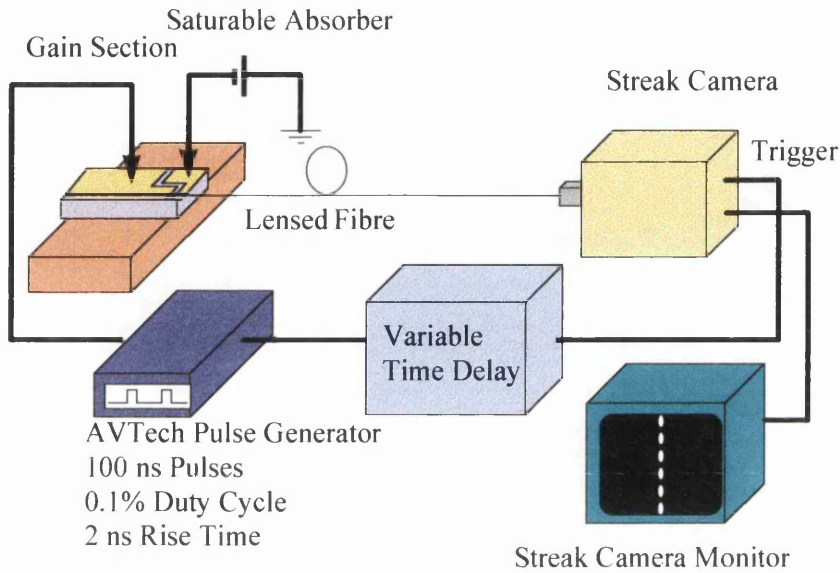


Figure 4.19: Schematic of the pulse build up measurements set-up.

Figure 4.20 shows the time evolution of the optical power at the fundamental modelocking frequency of 7.8 GHz fitted approximately to an exponential function of the form mentioned above with a time constant of 1.1 ns. The reason why the x-axis of this figure begins at 1.5 ns is because there is a further delay from the moment the current pulse reaches the gain section and when the modelocking pulse train begins to build up. This delay can be seen in Figure 4.18 by comparing the output from the laser when the saturable absorber is not connected (a) and when it is reverse biased (b).

Therefore, the mode-locked pulse train build up time is estimated to be around 2.6 ns, that is around 20 round trips, which is in good agreement with the results of AuYeung *et al.*²⁴.

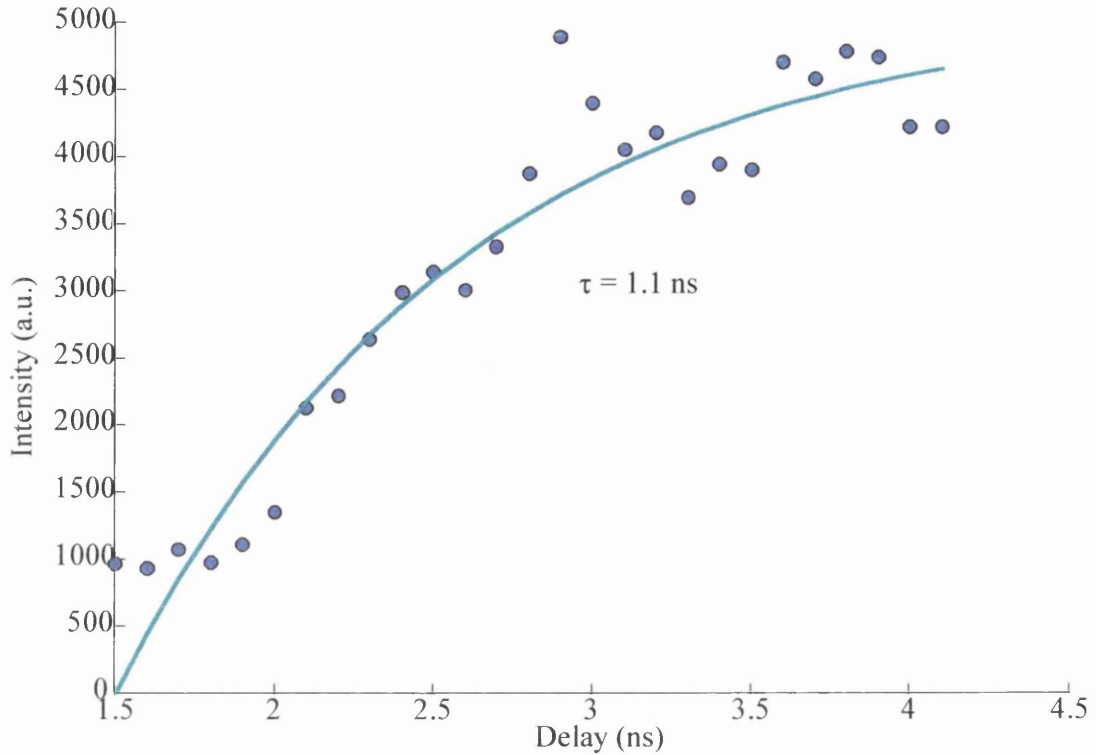


Figure 4.20: *Time evolution of the power at the fundamental modelocking frequency.*

4.3 Numerical simulations.

To include semiconductor laser peculiarities such as self-phase modulation and gain nonlinearities, not included in the simple model of chapter 3, a numerical model developed by Dr. E. A. Avrutin was used to analyse our experimental results and also to simulate all dynamical regimes. The model²⁵ consists of solving the travelling-wave equation for laser light:

²⁵ E.A. Avrutin, J.M. Arnold and J.H. Marsh, "Analysis of dynamics of monolithic passively modelocked laser diodes under external periodic excitation", *IEE Proc. Pt.J Optoelectronics*, 1996, **143**, pp. 81-88.

$$\pm \frac{\partial E_{R,L}}{\partial z} + \frac{1}{v_g} \frac{\partial E_{R,L}}{\partial t} = \Gamma \left(\hat{g} E_{R,L} + j\alpha(g - g_{th}) E_{R,L} \right) - j \frac{1}{2v_g^2} \frac{dv_g}{d\omega} \frac{\partial^2 E_{R,L}}{\partial t^2} + F_{rand} \quad (4.15)$$

where $E_{R,L}(z,t)$ are complex amplitudes of the light propagating to the right and left respectively (normalised so that $E_R^2 + E_L^2 = S(z,t)$, the local intensity in units of photon density). The operator \hat{g} includes a filter simulating gain dispersion

$$\hat{g} E = g \Delta\Omega_g \int_0^\infty E(t - \tau) \exp(-\Delta\Omega_g \tau) d\tau \quad (4.16)$$

where $\Delta\Omega_g$ is a measure of the gain linewidth and g is the usual gain value. The last term in Eq.(4.15) represents a random noise source essential for the self-starting of the model; the preceding term represents group-velocity dispersion. Eq.(4.15) is solved together with co-ordinate dependent rate equations for the carrier densities in gain and absorber sections.

$$\frac{\partial N(z,t)}{\partial t} = \frac{J(z,t)}{ed} - \frac{N}{\tau_N(z)} - v_g g S(z,t) \quad (4.17)$$

In both Eq.(4.15) and Eq.(4.17), for values of the longitudinal co-ordinate z corresponding to points in the saturable absorber section, the gain g is changed to $-a$, a being the (saturable) absorption coefficient. The recombination time τ_N is also different for gain and saturable absorber sections. For the carrier and photon density dependence of g and a , standard approximations are used:

$$g = \frac{A_g(N_g - N_{0g})}{1 + \varepsilon_g S}; \quad a = \frac{A_a(N_{0a} - N_a)}{1 + \varepsilon_a S} \quad (4.18)$$

with the values of gain and absorber cross-section being $A_g = 6 \cdot 10^{-15} \text{ cm}^{-2}$; $A_a = 6 \cdot 10^{-15} \text{ cm}^{-2}$ and nonlinearity coefficients $\varepsilon_g = 5 \cdot 10^{-18} \text{ cm}^3$ and $\varepsilon_a = 1.25 \cdot 10^{-17} \text{ cm}^3$.

Transparency carrier densities are assumed equal for both sections: $N_{0,g,a} = 1.2 \cdot 10^{18} \text{ cm}^{-3}$.

The laser length is taken to be 5 mm with the absorber occupying 80 μm . Group-velocity dispersion $dn_g/d\omega = 2 \cdot 10^{-16} \text{ s}$. The optical confinement and the effective

refractive index have been adjusted to be close to the values for the realistic structure: $\Gamma=0.07$; $n_g=3.75$. Other parameters and their values are as in²⁵.

Figure 4.21 represents the simulated temporal behaviour of the laser at two currents. At the lower current ($J/J_{th}=1.4$), Figure 4.21(a), a pulse train was observed at the round-trip period modulated by deep self-pulsing envelope, as seen in the experimental results. The modulation was also seen in the duration of individual pulses in the stream which range within approx. 2.6 to 2.8 ps. As the current was increased to $J/J_{th}=2.2$, Figure 4.21(b), the pulse train assumed features of regular modelocking. Pulse durations also became more constant, ranging only within approximately 2.67-2.73 ps. With further increase in current, however, the envelope modulation reappeared and became increasingly more irregular.

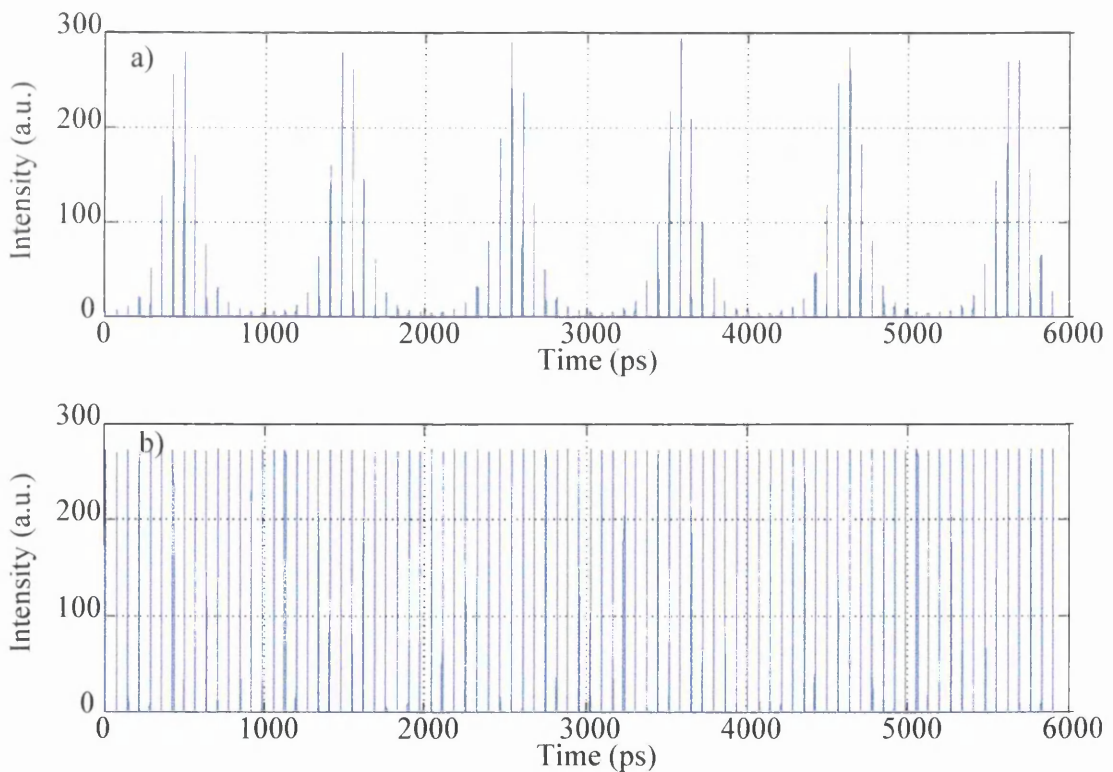


Figure 4.21: Calculated temporal profile of the laser emission at (a) $J/J_{th}=1.4$ and (b) $J/J_{th}=2.2$.

Figure 4.22 shows optical spectra corresponding to the two types of dynamical behaviour. As in the experiment, both spectra were shifted towards longer wavelengths

from the gain maximum (point of CW lasing) with the pure modelocking spectrum being shifted further, presumably due to more pronounced SPM in this case. The same SPM also led⁹, in agreement with experiment, to a pronounced asymmetry of the spectrum and its periodic multi-peak structure. The spectrum for the combined regime was more symmetric, with a trace of mode locking in the form of a side maximum at the red side, as in the experiment.

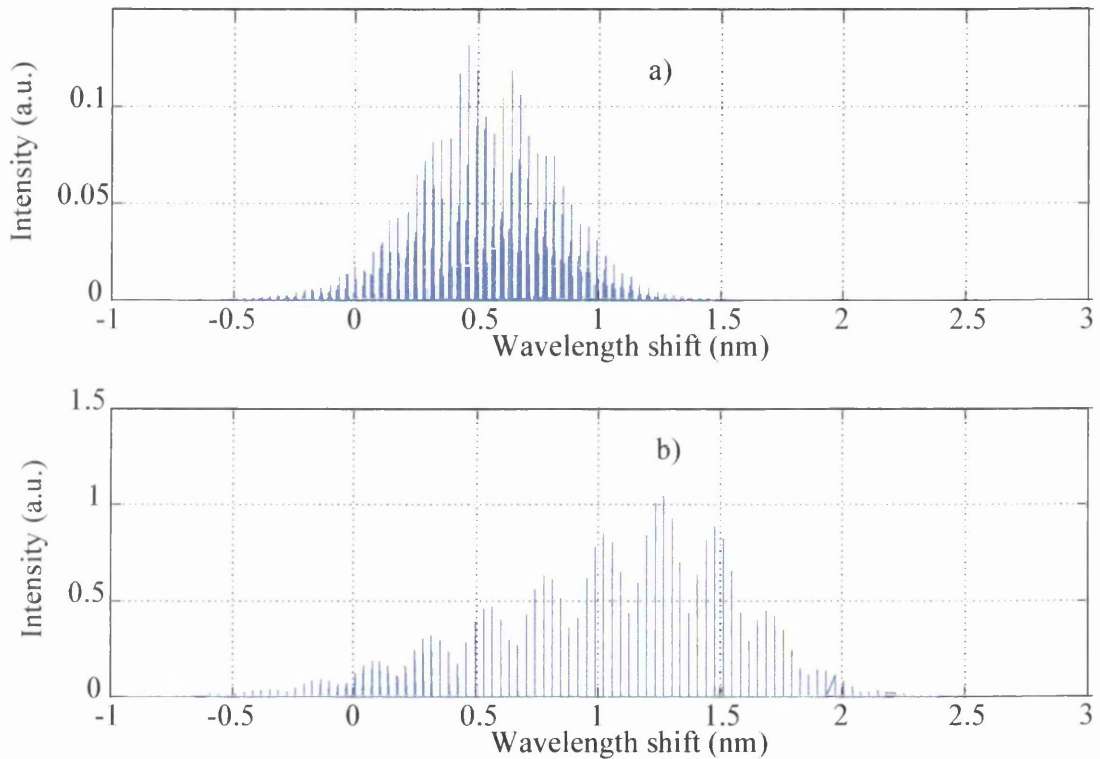


Figure 4.22: *Calculated light emission spectra at (a) $J/J_{th}=1.4$ and (b) $J/J_{th}=2.2$.*

4.4 Conclusions.

Although the modelocking performance of the AAL as a short pulse generator was not the best in terms of pulse width, spectral width and other important characteristics, its fabrication was very easy and reliable, which makes this laser configuration very good as a cheap and reliable short pulse generator, assuming that a pulse timing stabilisation mechanism is provided.

However, for any practical use, it is very important that the biasing conditions are very carefully chosen to avoid the self-pulsations that could modulate the modelocking pulse train.

It has been shown that results from the numerical simulations are in very good agreement with the experimental observations, which can obviously help in the design and development of any particular application using this type of laser.

Chapter Five *EXTENDED CAVITY MODE-LOCKED LASERS.*

As has been shown in the previous chapter, an active waveguide is not the optimum medium in which to propagate short pulses because the pulses are broadened by the group velocity dispersion induced by the gain dispersion, such that the broadening depends on the active cavity length. The jitter is also very high due to carrier concentration variations in the active waveguide, which lead to refractive index variations and therefore to optical cavity length variations.

A more natural medium in which to propagate the pulses is a passive waveguide. The next kind of mode-locked semiconductor lasers that is going to be analysed incorporates a low-loss passive waveguide in addition to the gain section and the saturable absorber. This type of laser that incorporates an integrated passive waveguide is known as an extended cavity laser (ECL). Designing the laser structure using an integrated passive waveguide enables the laser operating frequency to be reduced to a relatively low frequency, as low as 2 GHz has been reported¹, by extending the passive waveguide length, without any significant increase in the threshold current. This structure also reduces the phase noise and, consequently, the timing jitter by the ratio of active section reduction.

In this chapter the passive waveguide fabrication technique, namely impurity free vacancy disordering is analysed, and the results obtained from the mode-locked ECL are documented. Similar modelocking characteristics to those analysed for the AAL will be studied, and the same numerical model will be used to compare the experimental and theoretical results.

5.1 Quantum well intermixing (QWI).

Several techniques have been used to integrate active and passive regions in

¹ P.B. Hansen, G. Raybon, U. Koren, B.I. Miller, M.G. Young, M.A. Newkirk, M.D. Chien, B. Tell and C.A. Burrus, "2 cm long monolithic multisection laser for active modelocking at 2.2 GHz", *Electronics Lett.*, 1993, **29**, 9, pp. 739-741.

semiconductor lasers, the most important being:

- * Regrowth^{1,2,3}: which involves growing the structure, removing the upper cladding and active layer from the passive regions and regrowing the core and upper cladding layer of the passive sections.
- * Patterned substrates^{4,5,6}: where the growth of the material uses patterned substrates and the width of the QW depends on the relative area of the mask coating the substrate.
- * QWI⁷: where the bandgap of the passive regions is modified by intermixing the wells and barriers of the active layer and forming an alloy semiconductor. The bandgap of the intermixed alloy is larger than that of the original structure and can, therefore, form a low-loss passive waveguide.

QWI has the advantage, compared to the other two mentioned techniques, of forming a continuous waveguide, from the active to the transparent passive section, allowing efficient coupling and virtually no optical reflections at the interface between the active and passive regions.

A variety of QWI techniques has been demonstrated including impurity induced disordering (IID), photon-absorption induced disordering (PAID) and impurity-free

² G. Raybon, P.B. Hansen, U. Koren, B.I. Miller, M.G. Young, M. Newkirk, P.P. Iannone, C.A. Burrus, J.C. Centanni and M. Zirngibl, "Two contact, 1cm long, monolithic extended cavity laser actively modelocked at 4.4 GHz", *Electronics Lett.*, 1992, **28**, 24, pp. 2220-2221.

³ P.B. Hansen, G. Raybon, U. Koren, P.P. Iannone, B.I. Miller, G.M. Young, M.A. Newkirk and C.A. Burrus, "InGaAsP monolithic extended-cavity lasers with integrated saturable absorbers for active, passive and hybrid mode locking at 8.6 GHz", *Appl. Phys. Lett.*, 1993, **62**, 13, pp. 1445-1447.

⁴ P. Demeester, L. Buydens and P. Van Daele, "Growth velocity variations during metalorganic vapor phase epitaxy through an epitaxial shadow mask", *Appl. Phys. Lett.*, 1990, **57**, 2, pp. 168-170.

⁵ E. Colas, C. Caneau, M. Frei, E.M. Clausen, W.E. Quinn and M.S. Kim, "In situ definition of semiconductor structures by selective area growth and etching", *Appl. Phys. Lett.*, 1991, **59**, 16, pp. 2019-2021.

⁶ M. Aoki, M. Takahashi, M. Suzuki, H. Sano, K. Uomi, T. Kawano and A. Takai, "High-extinction-ratio MQW electroabsorption-modulator integrated DFB laser fabricated by in-plane bandgap energy control technique", *IEEE Photonics Technol. Lett.*, 1992, **4**, 6, pp. 580-582.

⁷ J.H. Marsh, "Quantum well intermixing", *Semiconductor Science Technol.*, 1993, **8**, pp. 1136-1155.

vacancy disordering (IFVD), the last one being used in the fabrication of the ECL used in this work.

IID^{8,9}:

In IID processes, impurities are introduced in the semiconductor material which is then annealed. Different impurities have been demonstrated to disorder GaAs/AlGaAs material similar to that used in this work, the most important being Zn or Si as p or n impurities and F or B as neutral impurities.

PAID^{10,11}:

PAID processes rely on bandgap dependent absorption of light from a powerful laser in the active layer of a multilayer structure. Heat is generated due to carrier cooling non-radiative recombination, and has the effect of increasing the interdiffusion rate between wells and barriers leading to quantum well disordering.

IFVD^{12,13}:

The passive waveguides fabricated for this work were made using IFVD by dielectric encapsulation, and the intermixing mechanism is shown in Figure 5.1. An SiO₂ cap

⁸ S.R. Andrew, J.H. Marsh, M.C. Holland and A.H. Kean, "Quantum well laser with integrated passive waveguide by neutral impurity disordering", *IEEE Photon. Technol. Lett.*, 1992, **4**, 5, pp. 426-428.

⁹ M. O'Neill, J.H. Marsh, R. M. De la Rue, J.S. Roberts, C. Button and R. Gwilliam, "Reduction of the propagation losses in impurity disordered quantum well waveguides", *Electronics Lett.*, 1990, **26**, 19, pp. 1613-1614.

¹⁰ C.J. McLean, A. McKee, J.H. Marsh and R.M. De la Rue, "Lateral control of the bandgap in GaInAs/GaInAsP MQW structures using photoabsorption-induced disordering", *Electronics Lett.*, 1993, **29**, pp. 1657-1659.

¹¹ A. McKee, C.J. McLean, A.C. Bryce, R.M. De la Rue, J.H. Marsh and C. Button, "High quality wavelength tuned multiquantum well GaInAs/GaInAsP lasers fabricated using PAID", *Appl. Phys. Lett.*, 1994, **65**, pp. 2263-2265.

¹² J. Beauvais, S.G. Ayling and J.H. marsh, "Low-loss extended cavity lasers by dielectric cap disordering with a novel masking technique.", *IEEE Photonics Technol. Lett.*, 1993, **4**, 4, pp. 372-373.

¹³ I. Gontijo, T. Krauss, R.M. De la Rue, J.S. Roberts and J.H. Marsh, "Very low loss extended cavity GaAs/AlGaAs lasers made by impurity-free vacancy diffusion", *Electronics Lett.*, 1994, **30**, 2, pp. 145-146.

layer is deposited on top of the areas to be disordered as it favours group III vacancy generation. As shown in Figure 5.1, when the sample is annealed at high temperatures, above 900° C, Ga atoms out-diffuse and dissolve in the SiO₂ layer. This process generates a substantial number of group III vacancies which diffuse through the active region into the substrate. The creation of Ga vacancies causes Al diffusion from the barrier to the well, an increase of the Al concentration within the well itself and, therefore, a widening in the bandgap of the resulting semiconductor alloy.

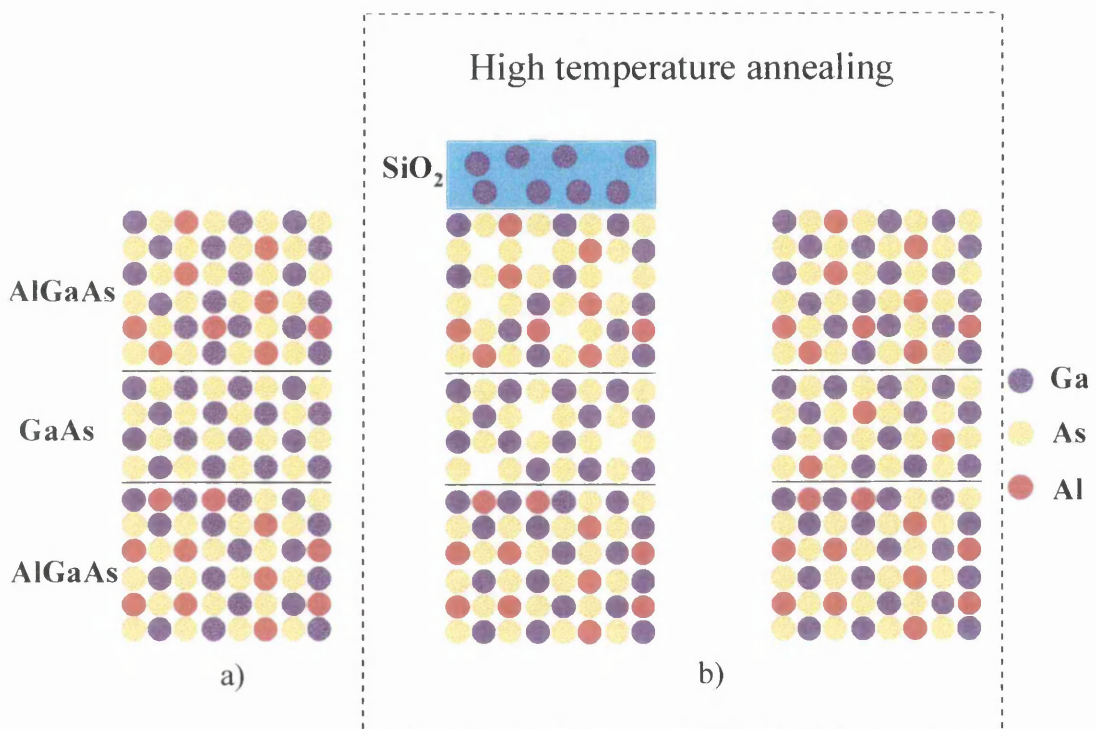


Figure 5.1: IFVD process: a) original sample, b) during high temperature annealing Ga vacancies are generated by out-diffusion of Ga atoms into the silica layer (left) and Al atoms are diffused into the active layer (right).

The shapes of the QWs after the disordering process were studied by Gontijo *et al.*¹⁴ Figure 5.2 shows the effect of the QWI on the QW shapes. Compared to the as-grown

¹⁴ I. Gontijo, T. Krauss, J.H. Marsh and R.M. De la Rue, "Postgrowth control of GaAs/AlGaAs quantum well shapes by impurity-free vacancy diffusion", *IEEE J. Quantum Electron.*, 1994, **30**, 5, pp. 1189-1195.

material, the QWs are broadened at the top and narrowed at the bottom due to the Al-Ga diffusion. These modifications shift the $n=1$ ($e1$ - $hh1$) exciton transition energy to higher energies.

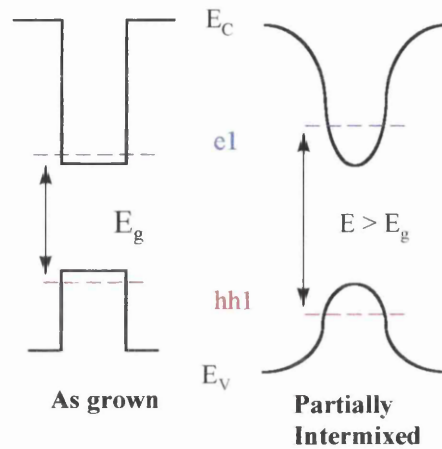


Figure 5.2: *QW shapes before and after annealing.*

As has been shown, SiO_2 enhances QWI because it is porous to Ga out-diffusion and thus group III vacancies are generated. The problem now is to find a material that can be used to prevent intermixing in areas where it is not required. Two different dielectric materials were used to prevent QWI; strontium fluoride (SrF_2) and phosphorus doped silicon oxide ($\text{P}:\text{SiO}_2$). The IFVD technique using each of them is now described.

5.1.1 IFVD by SiO_2 / SrF_2 dielectric encapsulation.

The fabrication of extended cavity mode-locked lasers followed the fabrication procedure explained in chapter 2, but a initial fabrication stage was required to disorder the QWs of the passive sections.

A 200 nm thick layer of SrF_2 was thermally evaporated over the entire surface of the sample and was then removed by chemical etching using HCl from the passive sections where the intermixing was required. A 200 nm thick layer of SiO_2 was then deposited by PECVD over the whole sample, giving the passive sections, where QWI was required, an SiO_2 cap and the active sections, where QWI was not required, an SrF_2 and SiO_2 cap. The sample was then annealed at 925°C for 40 seconds in a rapid thermal annealer (RTA), using a proximity cap of GaAs over the sample to provide a

group V over-pressure to improve the group III vacancy generation¹⁵. As described above, QWI took place under the SiO₂ cap, but was suppressed under the SrF₂ layer. The reason for this is that the SrF₂ encapsulant effectively seals the crystal surface and, consequently, is a poor source of vacancies.

Measuring the photoluminescence (PL) at 77 K, using the set-up analysed in appendix II, the exciton energy shifts were calculated. The observed PL spectra, which were taken on different areas of an GaAs/AlGaAs sample, are presented in Figure 5.3. The PL peak wavelength of the passive regions, capped with SiO₂, exhibited a blue shift of 25 nm, compared with the PL peak wavelength of the as-grown material, while the PL peak wavelength of the active regions, under the SrF₂ layer, had shifted by just 4 nm. The differential shift between the passive and active areas was 21 nm, which was sufficient for the fabrication of extended cavity lasers¹³.

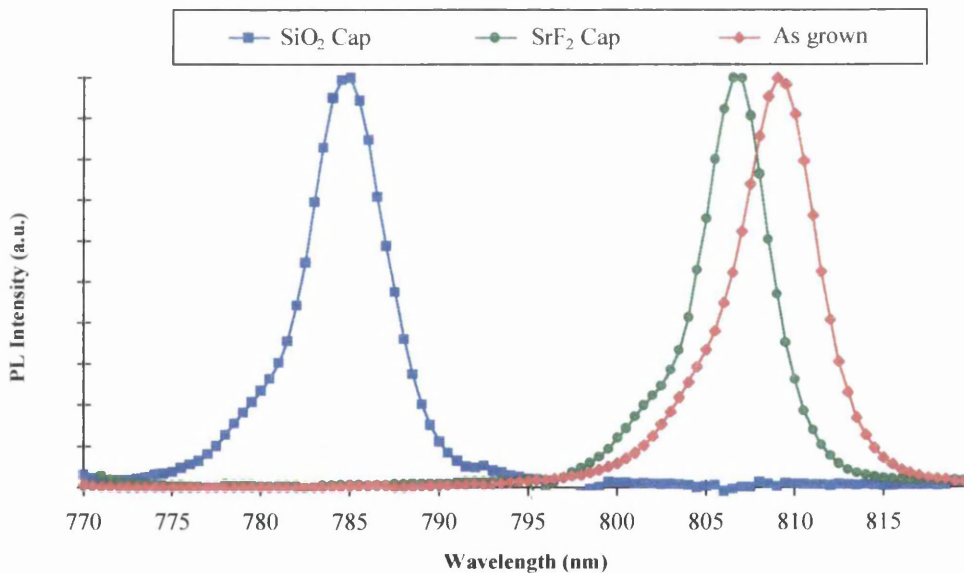


Figure 5.3: 77 K PL spectra after IFVD with SiO₂ / SrF₂.

Unfortunately, there were some problems which caused the fabrication of ECLs using IFVD with SrF₂ and SiO₂ to have poor reproducibility. First of all, the process produced some sample damage under the SrF₂ cap, principally at the interface between

¹⁵ L.J. Guido, N. Holonyak, K.C. Hsieh, R.W. Kalinski and W.E. Plano, "Effects of dielectric encapsulation and As overpressure on Al-Ga interdiffusion in Al_xGa_{1-x}As-GaAs quantum-well heterostructures", *J. Appl. Phys.*, 1987, **61**, 4, pp. 1372-1379.

the active and passive regions, mainly due to the differences in thermal expansion coefficients between SrF_2 , SiO_2 and GaAs. Secondly, there was a problem of cap removal after annealing. For temperatures over 925°C the removal of the SrF_2 cap by chemical etching with HCl was very difficult to accomplish, leaving residues which caused many problems during the following fabrication of ridge waveguide lasers. Among these was the problem of poor homogeneity in the QWI, which could be seen when measuring the PL spectra at different places in the passive and active regions. This problem is shown in Figure 5.4, which depicts the PL peak wavelength for 13 different places over a 1 cm^2 GaAs/AlGaAs sample after the IFVD process.

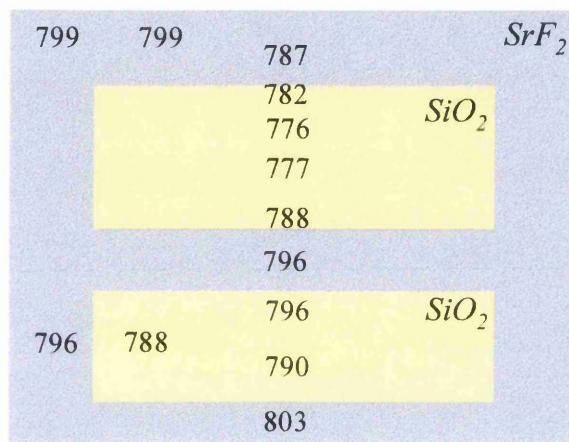


Figure 5.4: *QWI non-homogeneity after IFVD with SiO_2 / SrF_2 as dielectric caps.*

The PL peak wavelength of the as-grown material was 808 ± 2 nm over the sample. The above figure shows that neither in the active nor in the passive sections was the PL peak wavelength shift constant, or close to constant, with respect to the as-grown material. It can be seen that the PL peak wavelength, for the upper region covered with SiO_2 , had a minimum of 776 nm, a blue shift of 32 nm with respect to the as-grown material, but closer to the interface $\text{SiO}_2/\text{SrF}_2$ region the PL peak wavelength was 788 nm, a shift of just 20 nm in comparison to the as-grown material. This problem was even worse in the lower region covered with SiO_2 , because the value of the PL peak wavelength was 790 nm in the middle of the region. The same problem of non-homogeneity can be seen in the active regions covered with SrF_2 . The PL peak wavelength had a maximum of 803 nm at the lowest part of the sample, but the closer to the passive regions the lower this PL peak wavelength, down to 787 nm near to the

upper passive region. Due to these problems, the fabrication of mode-locked ECLs using IFVD with SrF₂/SiO₂ as dielectric caps was unsuccessful.

5.1.2 IFVD by SiO₂ / P:SiO₂ dielectric encapsulation.

The fabrication of integrated passive and active areas using IFVD can also be achieved by using phosphorus doped SiO₂ (P:SiO₂) instead of SrF₂ to prevent QWI. P:SiO₂ is able to prevent Ga out-diffusion and hence prevent the bandgap widening of active areas in an ECL. One possible explanation is that P:SiO₂ is more dense and void-free than SiO₂¹⁶.

A very big improvement was achieved in the fabrication of integrated passive and active areas using P:SiO₂. The main reason was that the sample surface did not suffer any damage at all, which meant that alignment marks were needed to locate the disordered and non-disordered areas. Another reason was that cap removal after the IFVD technique was accomplished very easily.

The fabrication of ECLs using P:SiO₂ and SiO₂ followed the procedure described previously in chapter 2, but again a pre-fabrication stage was needed to disorder the QWs of the passive regions.

The QWI procedure used in this case was very similar to the technique explained in the section above, but used a layer of P:SiO₂ instead of the SrF₂ layer. A 200 nm thick layer of P:SiO₂ containing 5% wt of phosphorus was deposited by PECVD over the whole sample. It was chemically removed from the passive regions by photolithography followed by wet etching in buffered HF solution. The sample was then covered with a 200 nm thick layer of SiO₂ deposited by PECVD and was rapid thermal annealed for 60 seconds at high temperature (over 900° C).

Temperatures of 910, 925 and 940° C were used to analyse the effect of temperature

¹⁶ P. Cusumano, B.S. Ooi, A. Saher Helmy, S.G. Ayling, A.C. Bryce, J.H. Marsh, B. Voegelé and M.J. Rose, "Suppression of QWI in doped GaAs/AlGaAs laser structures using phosphorus-doped SiO₂ encapsulant layer", *J. Appl. Phys.*, 1997, **81**, 5, pp. 2445-2447.

on the QWI of the active and passive regions. Figure 5.5 shows the PL peak wavelength shift of the active and passive regions versus the annealing temperature, with respect to the as-grown material PL peak wavelength which was 807 nm at 77 K. From this graph, it is obvious that very high differential shifts between the active and passive sections could be achieved using this method, but it is important to note that, to make modelocking lasers with good characteristics, the amount of QWI in the active regions must be as small as possible, to ensure that the quality of the QWs is as good as the as-grown material. This was the reason the temperature chosen for the fabrication of the ECL was 925° C, because a) the differential shift between the active and passive areas (27 nm) was high enough for the losses in the passive waveguide, at the lasing wavelength, to be very small and b) the shift in the PL peak wavelength of the active areas was sufficient small that the QW profiles were very similar to those of the as-grown material.

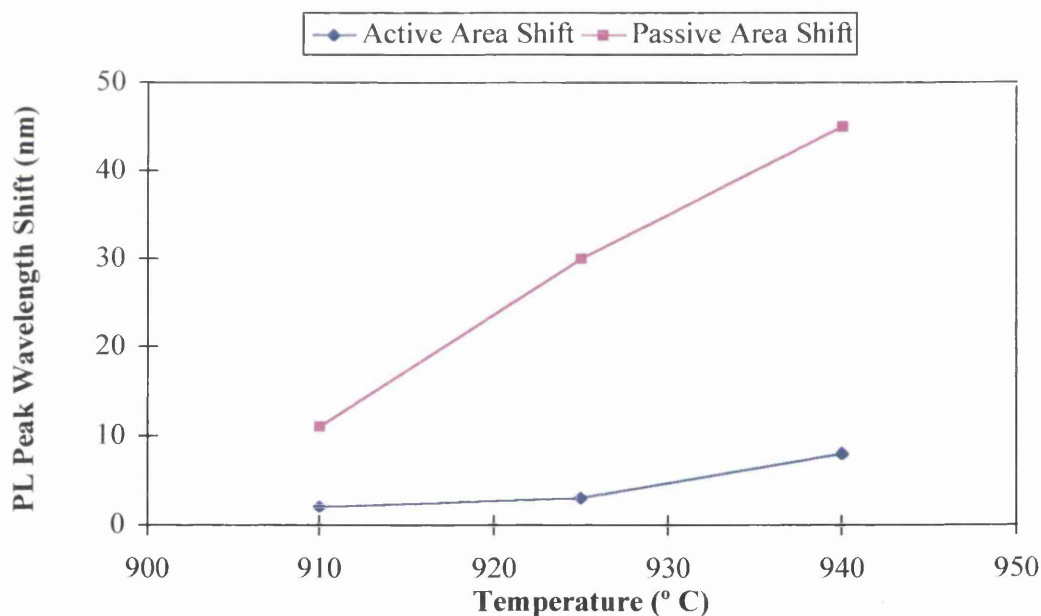


Figure 5.5: *PL peak wavelength shift versus annealing temperature after IFVD with SiO₂ / P:SiO₂.*

Figure 5.6 shows PL spectra after annealing a GaAs/AlGaAs sample at 925° C for 60 seconds, measured for different areas of the processed sample. Compared with the as-grown material, the PL peak wavelength of the area capped with SiO₂ had a blue shift of 30 nm, while the area capped with P:SiO₂ suffered a blue shift of just 3 nm. It can

also be seen that the PL spectrum of the area capped with SiO₂ exhibited some broadening compared with the area covered with P:SiO₂ and the as-grown material, probably due to non-perfect disordering in the passive area.

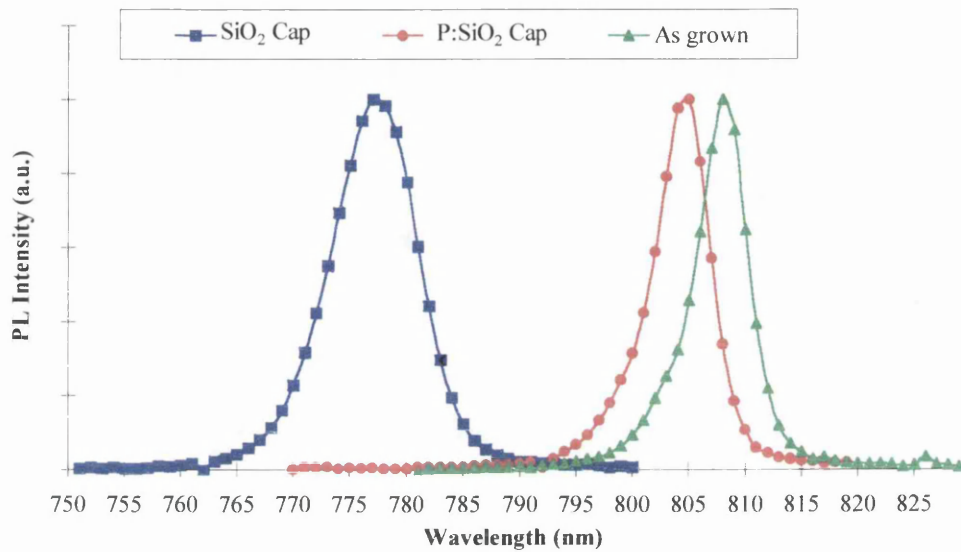


Figure 5.6: 77 K PL spectra after IFVD with SiO₂ / P:SiO₂.

One of the advantages of using P:SiO₂ and SiO₂ as dielectric encapsulants was the uniformity of the disordering and non-disordering of the passive and active regions respectively, quantified by measuring the PL peak wavelengths for different areas of the passive and active regions. Three different measurements were taken on the processed sample to analyse the homogeneity of the PL spectra over the whole sample. It was found that, for the active areas covered with P:SiO₂, the PL peak wavelength blue shift was between 3 and 4 nm with respect to the as-grown material for the three measurements, and between 28 and 35 nm with respect to the as-grown material for the passive area covered with SiO₂.

The main drawback of using P:SiO₂ as an encapsulant to prevent QWI is its sensitivity to water vapour¹⁷. P:SiO₂ seems to absorb water vapour which appears to inhibit its quality as an encapsulant to prevent QWI. This problem is shown in Figure 5.7. It depicts the PL spectra of a sample from the same wafer as that analysed above in

¹⁷ E.V.K. Rao, A. Hamoudi, Ph. Krauz, M. Juhel and H. Thibierge, “New encapsulant source for III-quantum well disordering”, *Appl. Phys. Lett.*, 1995, **66**, 4, pp. 472-474.

Figure 5.6, and the P:SiO₂ was deposited at the same time. The only difference between the IFVD processing rounds was that the sample whose PL spectra are shown in Figure 5.6 was processed and annealed within a week of the deposition of P:SiO₂, while the sample whose PL spectra are shown in Figure 5.7 was processed three weeks afterwards. In this Figure 5.7 it can be seen that, even though the area covered with SiO₂ was blue shifted by 27 nm in comparison with the as-grown material, a shift very similar to that seen in Figure 5.6, the area covered with P:SiO₂ suffered a shift of 20 nm, seven times bigger than that of the sample processed three weeks before. This effect has also been observed by other workers in our group.

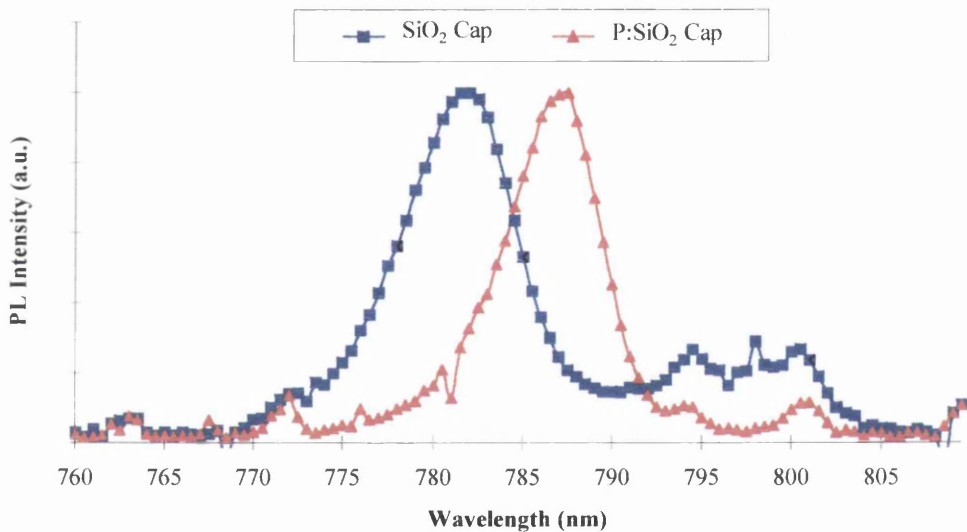


Figure 5.7: *P:SiO₂ degradation as a QWI inhibitor.*

5.2 Passive waveguides characterisation.

To analyse the operation of the lasers with integrated passive waveguides, oxide stripe lasers (OSL), with stripes 75 μm wide, were fabricated. The OSLs were cleaved into devices with different active to passive section ratios and with different cavity lengths. Figure 5.8 shows the I-L curves, measured from the active and the passive side, for an OSL with a gain section 500 μm long and a passive waveguide 1.2 mm long. These are compared with the I-L curve of the same laser after the extended cavity was cleaved off. It can be seen that the threshold current increased from around 165 mA for the laser without extended cavity to around 200 mA for the laser with passive waveguide. The external efficiency was also very different, decreasing from around

0.22 W/A for the solitary laser to 0.14 for the ECL.

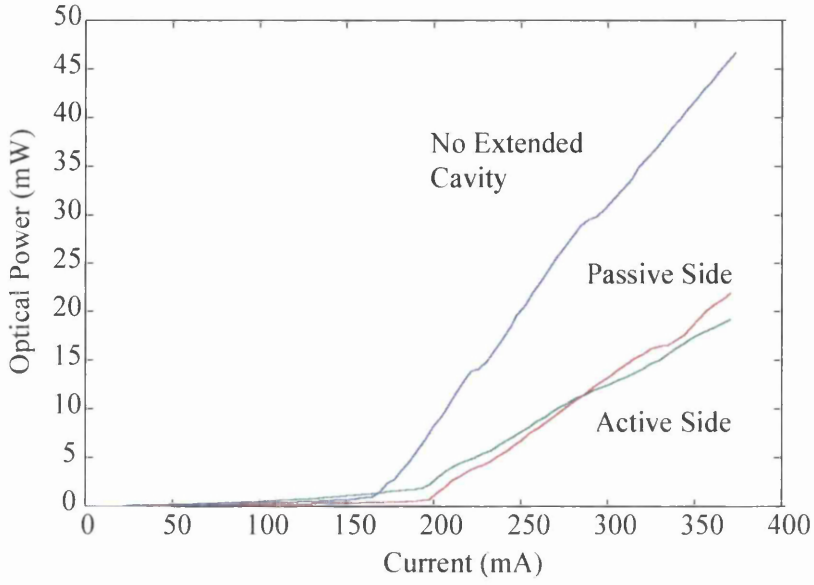


Figure 5.8: *I-L curves from the ECL-OSL.*

Both effects are explained using Eq.(2.16) and Eq.(2.18) from chapter 2. The threshold gain for the solitary laser and for the ECL respectively are

$$g_{th}^{Sol} \Gamma = \alpha_i + \frac{1}{L_G} \text{Ln} \left[\frac{1}{R} \right] \quad (5.1)$$

$$g_{th}^{Ext} \Gamma = \alpha_i + \alpha_p \frac{L_P}{L_G} + \frac{1}{L_G} \text{Ln} \left[\frac{1}{R} \right] \quad (5.2)$$

where L_G and L_P are the gain section extended cavity lengths respectively and α_p is the passive waveguide loss at the lasing wavelength. Performing an analysis similar to that in chapter 4 we obtain,

$$\frac{I_{th}^{Ext}}{I_{th}^{Sol}} = \exp \left[\frac{\alpha_p L_P}{n g_0 \Gamma_w L_G} \right] \quad (5.3)$$

In deriving Eq.(5.3), the coupling losses between the active and passive sections have been assumed to be zero because no mode mismatch due to refractive index change is introduced by the IFVD process.

Substituting the values for the material used in the fabrication of the devices (QT855), the loss of the passive waveguide at the lasing wavelength is calculated to be 3.4 cm^{-1} .

From Eq.(2.18) the relation of the quantum efficiencies, measured from the I-L curves, is then found to be

$$\frac{\eta_{Ext}^{Ext}}{\eta_{Ext}^{Sol}} = \frac{g_{th}^{Sol}}{g_{th}^{Ext}} \frac{\alpha_i + \frac{1}{L_G} \ln\left[\frac{1}{R}\right]}{\alpha_i + \frac{\alpha_p L_P}{L_G} + \frac{1}{L_G} \ln\left[\frac{1}{R}\right]} \quad (5.4)$$

where η_{Ext}^{Ext} and η_{Ext}^{Sol} are the external quantum efficiencies for the ECL and for the solitary laser respectively. Substituting the material values in Eq.(5.4), the decrease in the external efficiency of the OSL-ECL is calculated to be 30%, instead of the measured 56%. This difference is probably due to inaccurate external efficiency measurements, as has been remarked in a previous chapter.

Cusumano *et al*¹⁸ measured the losses of a ridge passive waveguide fabricated with the same material structure used for this work and using IFVD with SiO₂/P:SiO₂. They measured the losses for the TE polarisation, using the Fabry-Perot resonance method and their results are shown in Figure 5.9. It can be seen that the passive waveguide losses exhibit a minimum of about 3 cm⁻¹, a similar value to that calculated above.

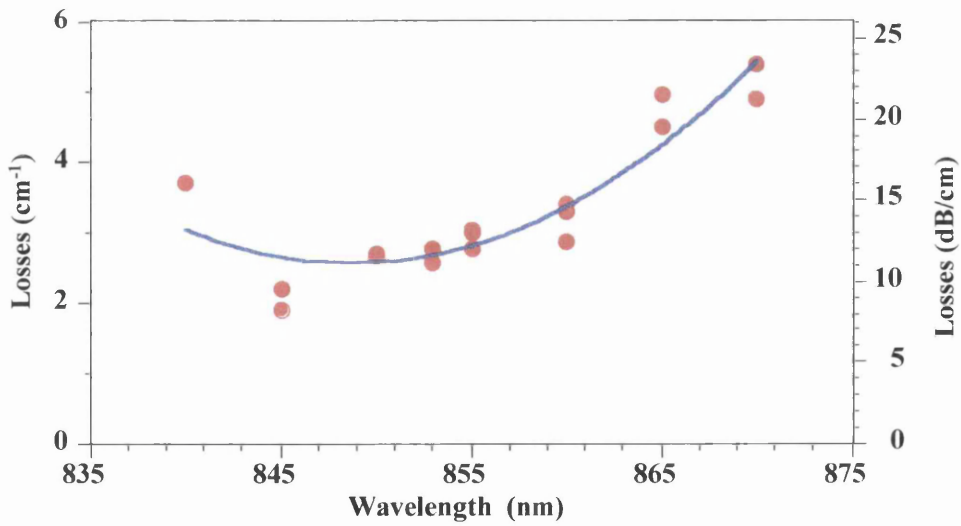


Figure 5.9: Losses in the integrated passive waveguides, measured using the Fabry-Perot resonance method, after Cusumano *et al*¹⁸.

¹⁸ P. Cusumano, J.H. Marsh, M.J. Rose, J.S. Roberts, "High quality extended cavity ridge lasers fabricated by impurity-free vacancy diffusion with a novel masking technique", *IEEE Photonics Technol. Lett.*, 1997, 9, 3, pp. 282-284.

5.3 Laser configuration.

The ECL configuration is shown in Figure 5.10. As for the AAL configuration, the laser has two different contacts, but in this case there are three sections: the saturable absorber section close to one of the facets, the gain section in the middle and the passive waveguide or extended cavity section at the other facet. The saturable absorber has a maximum length of $80\ \mu\text{m}$, the gain section has a constant length equal to $440\ \mu\text{m}$ and the extended cavity has a maximum length of $5\ \text{mm}$. As in the AAL configuration, the ridge waveguide was $3\ \mu\text{m}$ wide and $0.8\ \mu\text{m}$ deep to secure single transverse mode operation. The two contacts were also made by lifting off the metal layer, and the contact isolation resistance was again around $5\text{-}6\ \text{k}\Omega$ after the highly doped p-GaAs contact layer was removed from the ridge between the contacts.

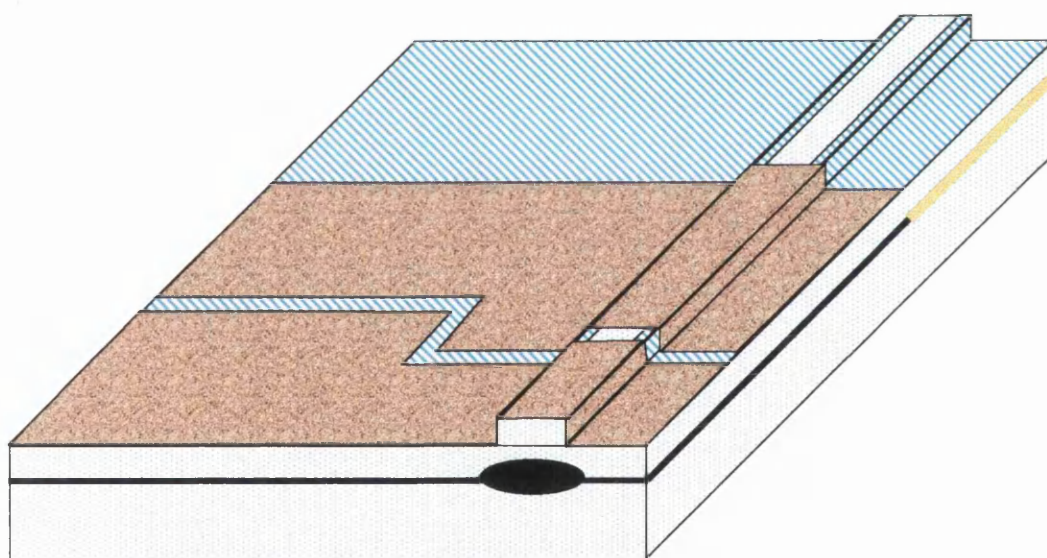


Figure 5.10: *Extended cavity semiconductor laser design.*

The threshold current for the ECL configuration, when both contacts were connected together varied between 15 and $20\ \text{mA}$, around five times lower than that of the AAL configuration. When the saturable absorber was left floating, the threshold current doubled due to the increased losses.

Figure 5.11 shows the I-L curves for a $4\ \text{mm}$ long ECL, with a saturable absorber $80\ \mu\text{m}$ long, a gain section $440\ \mu\text{m}$ long and a passive waveguide $3480\ \mu\text{m}$ long. These I-L

curves were measured from the active side, when both contacts were connected together, and from the passive and active side, when the saturable absorber was left floating. The big improvement with respect to the threshold current that this configuration offers over the AAL configuration is obvious, because for lasers with the same cavity length the ECL could have a threshold current an order of magnitude lower than the AAL threshold current.

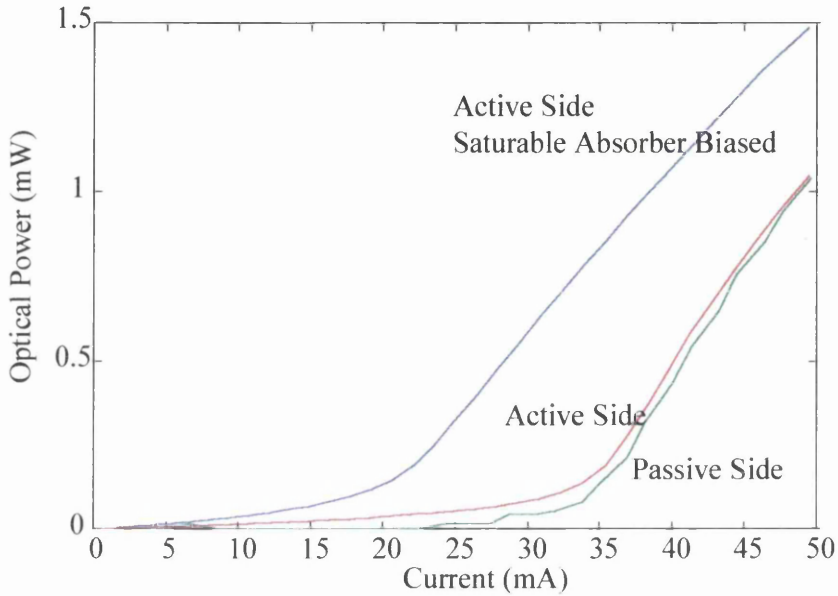


Figure 5.11: *I-L curves of a 4 mm long ECL from the active and passive side with the saturable absorber floating (red and green) and from the active side when both contacts were connected together (blue).*

The threshold current for this ECL, with both sections forward biased, was around 20 mA, but increased to 32 mA when the saturable absorber was floating. It can be seen that the I-L characteristics of the ECL were very similar when measured from the active or from the passive end of the laser, which indicates very low losses in the passive waveguide. To analyse this increase in the threshold current, Eq.(2.16) from chapter 2 was used. The threshold gain, when the saturable absorber was biased and when it was left floating can be expressed, respectively, as

$$g_{th}^{Bias} \Gamma = \alpha_i + \alpha_P \frac{L_P}{L_G + L_S} + \frac{1}{L_G + L_S} \text{Ln} \left[\frac{1}{R} \right] \quad (5.5)$$

$$g_{th}^{Float} \Gamma = \alpha_i + \alpha_S \frac{L_S}{L_G} + \alpha_P \frac{L_P}{L_G} + \frac{1}{L_G} \text{Ln} \left[\frac{1}{R} \right] \quad (5.6)$$

where L_G , L_S and L_P are the gain section, saturable absorber and extended cavity lengths respectively, α_S corresponds to the propagation loss through the saturable absorber when it was not pumped and α_P is the passive waveguide loss at the lasing wavelength. The next expression was obtained by the same analysis performed in chapter 4 to obtain Eq.(4.3), but taking into account that in this case L_S was not much smaller than L_G .

$$\frac{I_{th}^{Float}}{I_{th}^{Bias}} = \exp \left[\frac{\left(\alpha_S + \frac{\alpha_P L_P}{L_G + L_S} + \frac{1}{L_G + L_S} \text{Ln} \left[\frac{1}{R} \right] \right) L_S}{n g_0 \Gamma_w L_G} \right] \quad (5.7)$$

where I_{th}^{Bias} and I_{th}^{Sat} are the threshold currents when the saturable was forward biased and when it was floating, respectively. Taking values from chapter 2 for the material used for the fabrication of these devices, QT855, from section 5.2 for the passive waveguide loss, and assuming a mirror reflectivity of 0.32, an increase of 55% in the threshold current is calculated when the saturable absorber is left floating, again in good agreement with the measured value of 60% from Figure 5.11, taking into account the difficulty of estimating I_{th} from this figure.

5.4 Experimental results.

As in the previous chapter, the experimental results shown in this section were acquired under pulsed excitation, with 100 ns long pulses and 0.1% duty cycle, except for the modelocking frequency measurements and timing jitter calculations performed under CW operation.

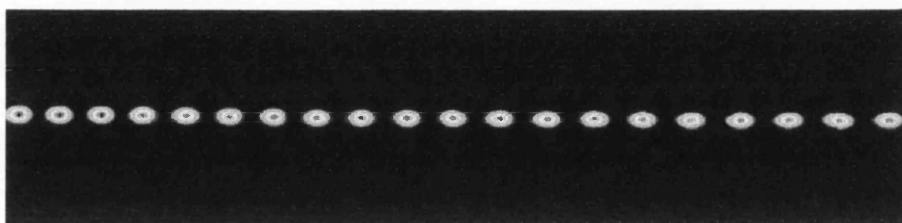
5.4.1 Modelocking frequency.

From Eq.(4.7) a modelocking frequency between 9.3 and 10 GHz is expected for a 4 mm long GaAs/AlGaAs laser.

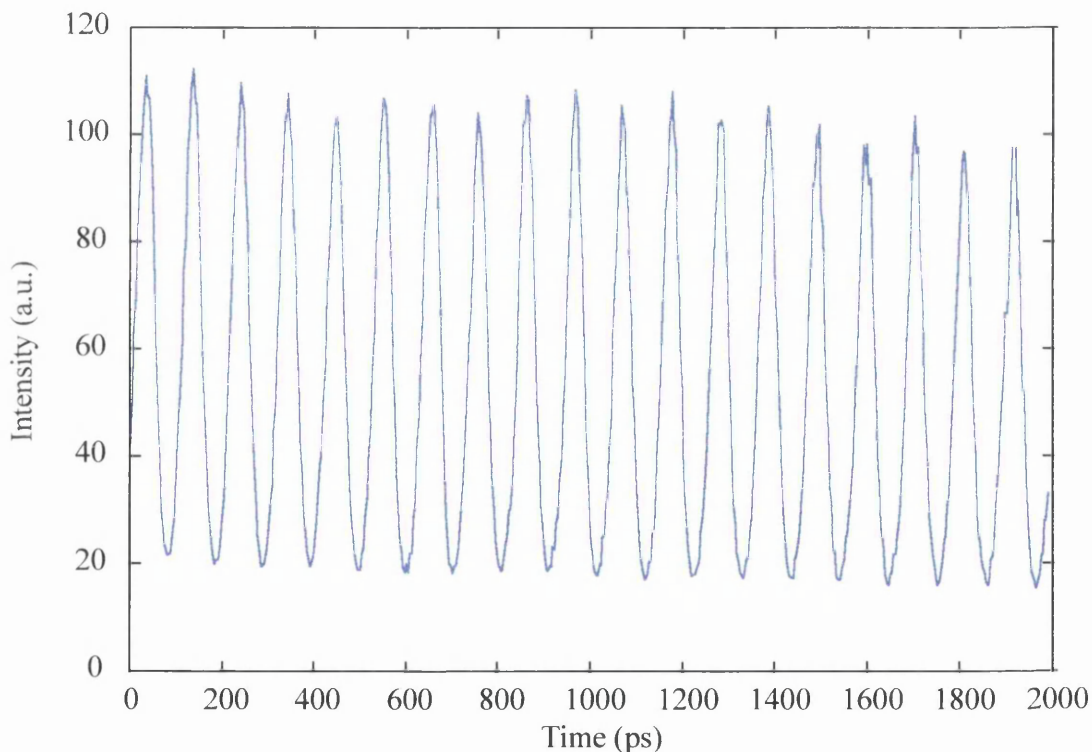
Time domain measurements:

Figure 5.12 shows a streak image and a streak profile of pulses from a 4 mm long

ECL, injected with a gain section current of 80 mA and a saturable absorber reverse voltage of -2 V. Although this will be examined more fully in a following section, it can already be observed that the pulses are narrower than for the AAL configuration.



a)



b)

Figure 5.12: *Streak image (a) and profile (b) of a mode-locked pulse train from an ECL.*

Besides the improvement in threshold current, the ECL also has a major advantage compared to the AAL, in the absence of self-pulsation regimes accompanying modelocking. Depending on the negative bias on the saturable absorber and the pumping current in the gain section, the AAL could operate in several distinct dynamical regimes, as

commented in section 4.2.3. For all device conditions investigated, the ECL showed no self-pulsing modulation of the modelocking pulse train. Figure 5.13 shows the map of the operating regions for an ECL with a threshold current of 32 mA operating under pulsed excitation. First of all, it must be mentioned that although there are no regimes of combined modelocking with self-pulsation, some devices exhibited self-pulsation at low currents ($<1.4 I_{th}$) and very high saturable absorber reverse voltages (> 5 V). It is also noticeable that modelocking can be achieved without reverse biasing the saturable absorber: for currents higher than twice the threshold current simply by grounding the saturable absorber is sufficient.

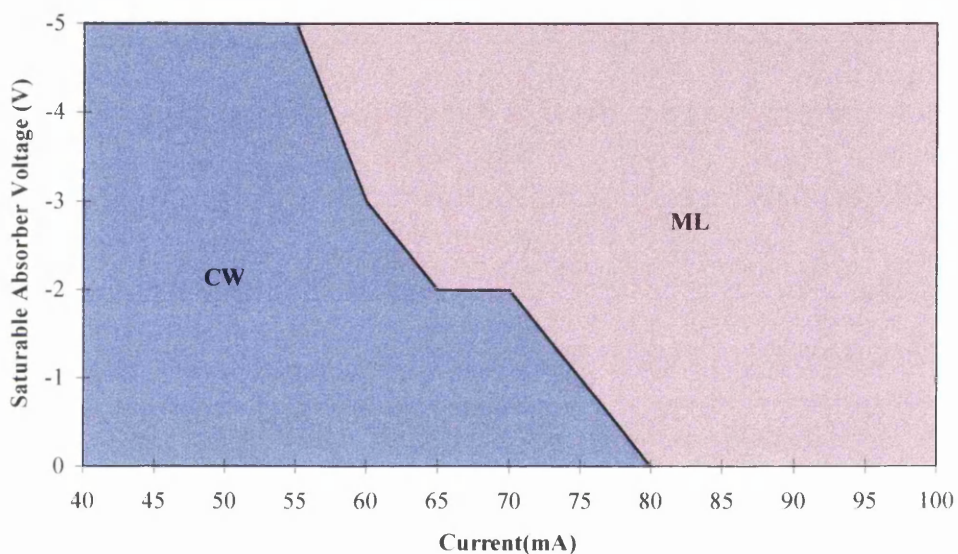
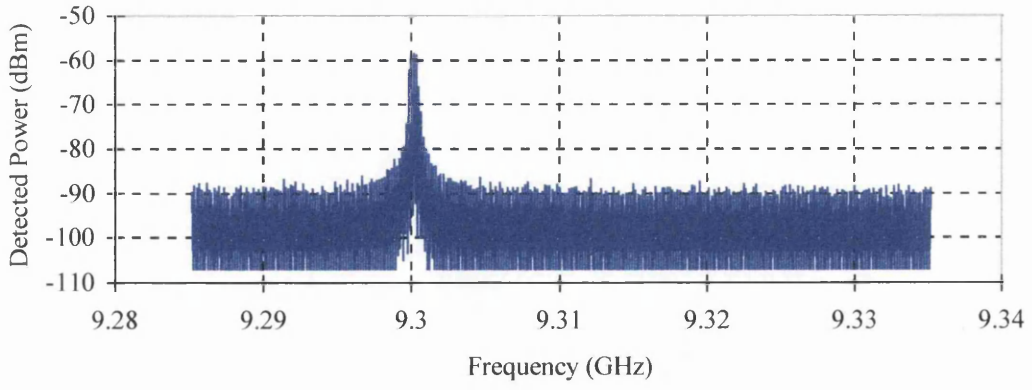


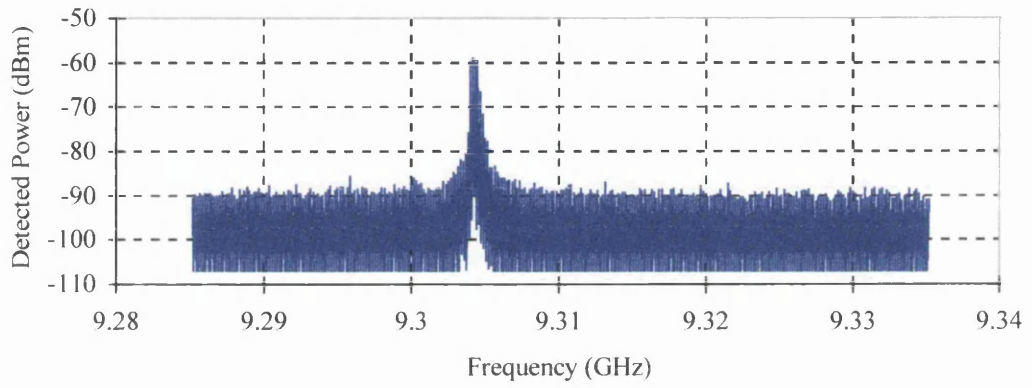
Figure 5.13: Working area map of an ECL.

Frequency domain measurements:

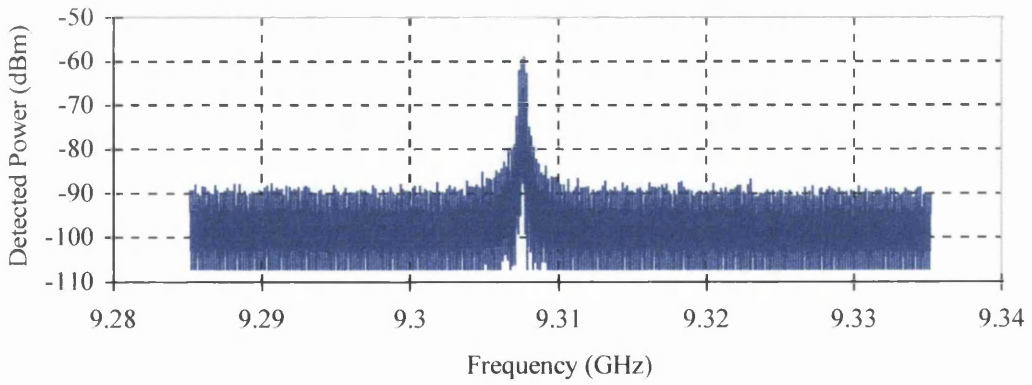
The same set-up described in chapter 4 for microwave spectral measurements was employed, but in this case the frequency measurements were performed under CW operation, instead of under pulsed excitation



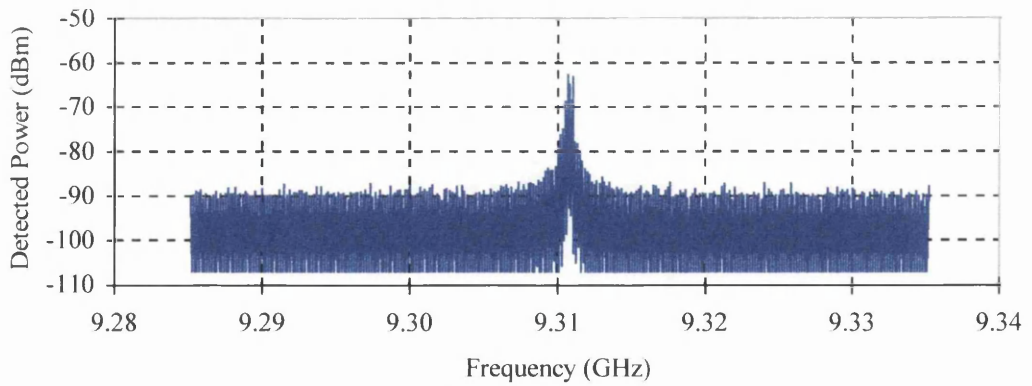
a) $V_{\text{Sat}} = -1 \text{ V}$



b) $V_{\text{Sat}} = -1.5 \text{ V}$



c) $V_{\text{Sat}} = -2 \text{ V}$



d) $V_{\text{Sat}} = -2.5 \text{ V}$

Figure 5.14: CW modelocking frequency variation with the absorber voltage.

Even though the operating frequency of a passively mode-locked laser is determined by its cavity length, so it is essentially fixed once the cavity is cleaved, it can be tuned typically over a few tens of MHz by adjusting the biasing conditions^{19,20}. Figure 5.14 shows the evolution of the modelocking frequency as the magnitude of the saturable absorber voltage was increased, keeping the injected current at 35 mA. The modelocking frequency increased with the increasing magnitude of the saturable absorber voltage, changing from 9.3 GHz, when the saturable absorber voltage was -1 V to 9.311 GHz when the saturable absorber voltage was -2.5 V, an increase of around 0.12% of the modelocking frequency. This result is very interesting because one of the main applications for a passively mode-locked semiconductor lasers is as a clock recovery element, where a variation of the modelocking frequency will be required for the laser to synchronise to an incoming signal, as will be explained in chapter 7.

A further analysis of the dependence of the modelocking frequency with the saturable absorber voltage was performed, with a different device from that used to obtain Figure 5.14 and the results are shown in Figure 5.15. The modelocking frequency had a minimum equal to 9.313 GHz when the saturable absorber voltage was -0.6 V. The modelocking frequency monotonically increased up to 9.326 GHz when the saturable absorber voltage was reduced to -2.5 V, remaining unchanged for any further increase of the saturable absorber voltage magnitude. It also increased when the saturable absorber voltage was increased to +0.2 V, but passive modelocking was not achieved with any further increase in the saturable absorber voltage. This variations of the modelocking frequency are the result of changes in the group refractive index in the laser cavity due to carrier density alterations when the saturable absorber is biased.

¹⁹ M.H. Kiang and K.Y. Lau, "Frequency and tuning characteristics of passively mode-locked semiconductor lasers operated at 77 K", *Electronics Lett.*, 1995, **31**, 11, pp. 880-882.

²⁰ K.Y. Lau, I. Kim and J. Paslaski, "Frequency stability in ultrahigh frequency mode locking of quantum-well lasers at >60 GHz", *Appl. Phys. Lett.*, 1992, **61**, 2, pp. 133-135.

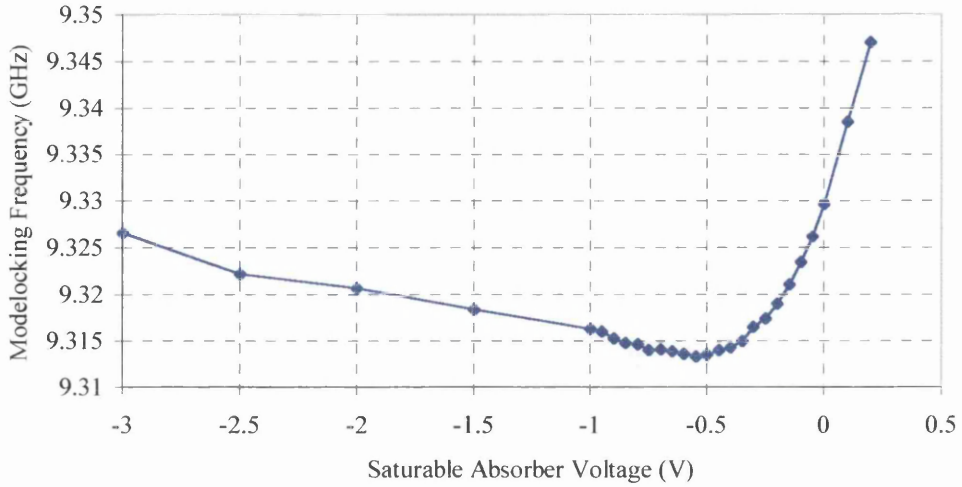


Figure 5.15: *Modelocking frequency variation with the saturable absorber voltage.*

Obviously, a change in the modelocking frequency is also expected when the current injected in the gain section is altered. Figure 5.16 shows the evolution of the modelocking frequency with the injected current keeping the saturable absorber voltage at -2 V. It can be seen that the modelocking frequency increased with increasing injected current, varying from 9.304 GHz when the current was 35 mA to 9.312 GHz when the current was increased to 40 mA.

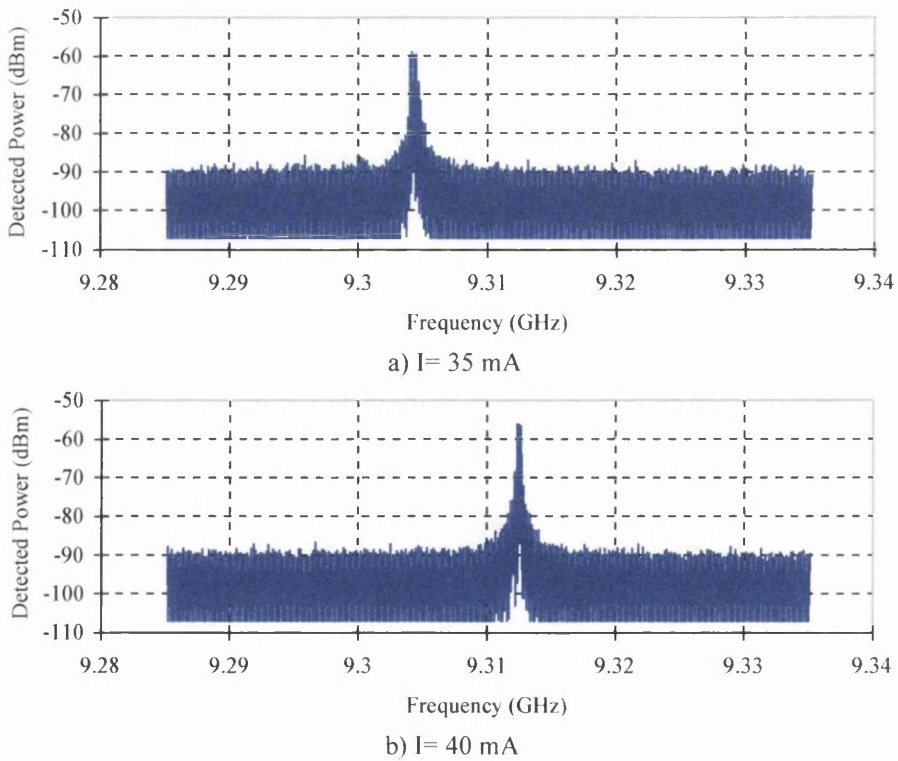


Figure 5.16: *CW modelocking frequency variation with the gain section current.*

5.4.2 Pulse width.

A laser configuration that consists of a gain section and a saturable absorber section to generate passively mode-locked pulses and a passive waveguide to give the desired cavity length is a more ideal configuration for short pulse generation than that of the AAL, where the whole laser cavity is pumped and therefore the modelocking pulses suffer high dispersion²¹ through the whole cavity length.

The pulse width of a mode-locked pulse train from an ECL was measured using the TPA autocorrelator described in chapter 2. As for the AAL configuration, the pulse width was studied for two different saturable absorber voltages, -2 and -4 V. Figure 5.17 shows the TPA autocorrelation traces and fitting curves assuming a sech^2 shape.

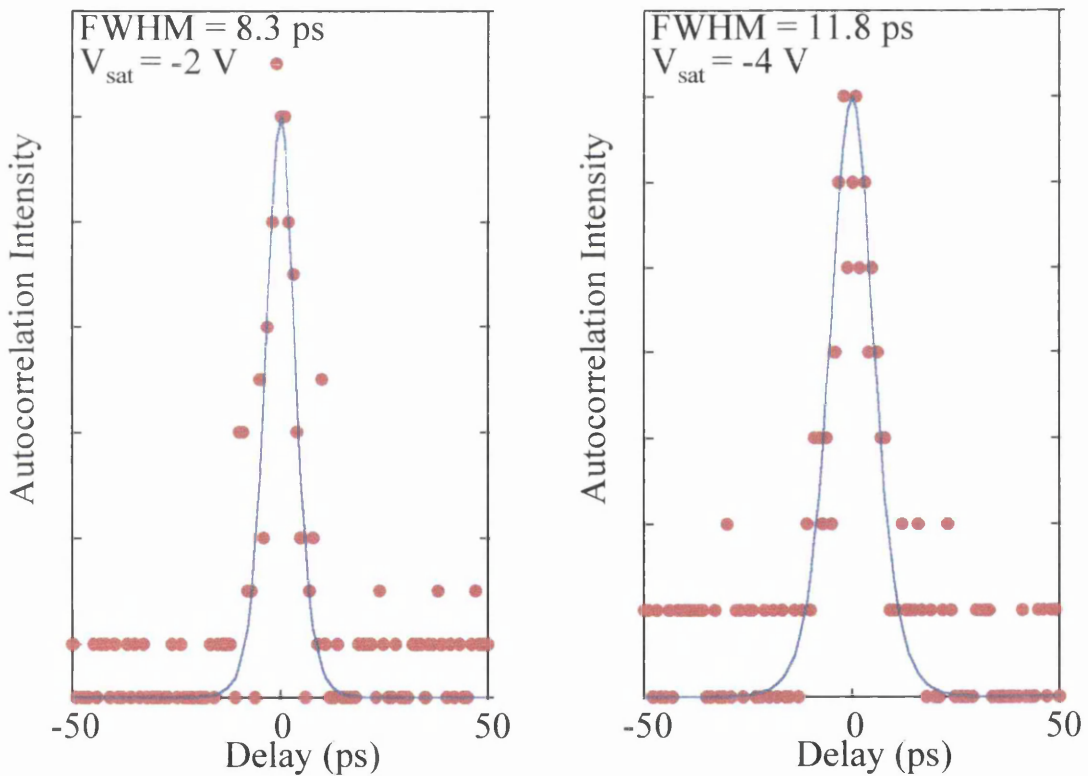


Figure 5.17: TPA autocorrelation measurements (red) and fitting curve assuming hyperbolic secant square shape of the modelocking pulse (blue) for $V_{\text{sat}} = -2 \text{ V}$ (left) and $V_{\text{sat}} = -4 \text{ V}$ (right).

²¹ D.J. Derickson, R.J. Helkey, A. Mar, J.R. Karin, J.G. Wasserbauer and J.E. Bowers, "Short pulse generation using multisegment mode-locked semiconductor lasers", *IEEE J. Quantum Electron.*, 1992, **28**, 10, pp. 2186-2202.

Performing the same calculations as in chapter 4, summarised in the Table 5.1, and taking into account that the spectral width of the modelocking pulses was also around 2 nm, the true FWHM of the modelocking pulses was found to be 3.5 and 6.4 ps for the cases when the saturable absorber voltage was -2 and -4 V respectively.

V_{sat} (V)	Autocorrelation FWHM (ps)	Sech ² FWHM (ps)	True FWHM (ps)
-2	8.3	5.3	3.5
-4	11.8	7.6	6.4

Table 5.1: Calculation of the true pulse width from the autocorrelation trace.

As expected, the ECL configuration generates mode-locked pulses much shorter than those generated by the AAL configuration, which are around 2 to 3 times broader.

5.4.3 Spectral analysis.

Optical spectral analysis has been carried out with the same equipment as in chapter 4. The intermode spacing for a 4 mm long laser, given by Eq.(4.9), is around 0.023 nm. Again, the spectrum analyser measures the envelope of the longitudinal modes as it cannot resolve the intermode wavelength spacing.

Figure 5.24 shows the evolution of the optical spectrum of a ECL operating under pulsed excitation with an injected peak current of 80 mA versus the saturable absorber voltage. When the saturable absorber was left floating, the spectral width was around 0.2 nm and the wavelength peak was at around 856 nm (marked with * in Figure 5.18). When the saturable absorber was connected, due to the high injected current, the ECL mode-locked even with a saturable absorber voltage of 0 V. As it happened with the AAL, the optical spectral suffered a shift of more than 2 nm to longer wavelengths when the laser was mode-locked. The modelocking spectra were also very asymmetric as with the AAL configuration, but the multi-shouldered structure seen in the AAL optical spectrum did not appear in the ECL optical spectrum. Obviously, the chirp of pulses from the ECL is more linear than from the AAL, a very important fact because pulses that are linearly chirped lend

themselves well to pulse compression techniques²².

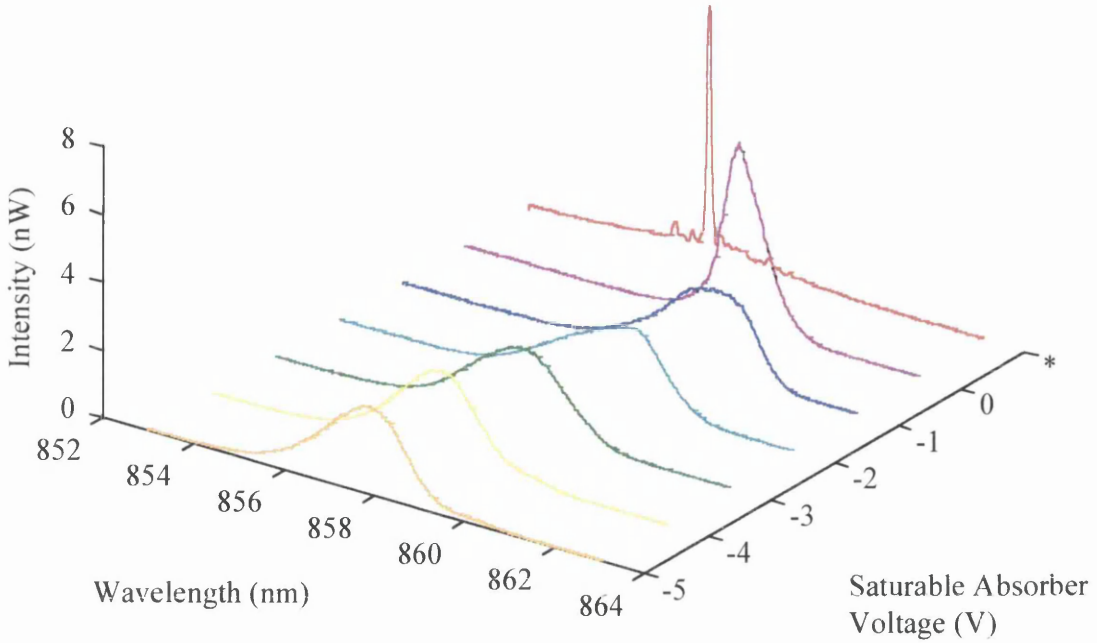


Figure 5.18: *Optical spectrum evolution with the increase of the saturable absorber voltage magnitude.*

It can be seen that the spectral width had a maximum, of around 2 nm, when the saturable absorber voltage was -2 V, which corresponded to the shortest pulses measured. The time-bandwidth product, as calculated in chapter 4, was around 2.5, much lower than that of the AAL configuration which was around 7. Still, this value was around 8 times bigger than the transform-limited value for sech^2 pulses, which indicates the high amount of chirp present in the pulse train. In any case, this value is superior to that previously reported using an ECL fabricated using regrowth techniques³, where due to the high reflections present at the active/passive waveguide interface (which in our case are practically non-existent) the time-bandwidth product was more than twice than that of our ECL.

The evolution of the modelocking optical spectrum peak was also studied under CW operation and Figure 5.19 shows these results, which were taken under the same biasing conditions as in Figure 5.15. As before, the group refractive index variations are the causes as they affect the local optical frequency in the laser and therefore changes in the wavelength emission peak.

²² J.M. Xie, S. Bouchoule, J.M. Lourtioz, E. Brun and D. Lesterlin, "Chirp compensation in mode-locked DFB laser diodes with extended cavity", *J. Lightwave Technol.*, 1996, **14**, 2, pp. 179-187.

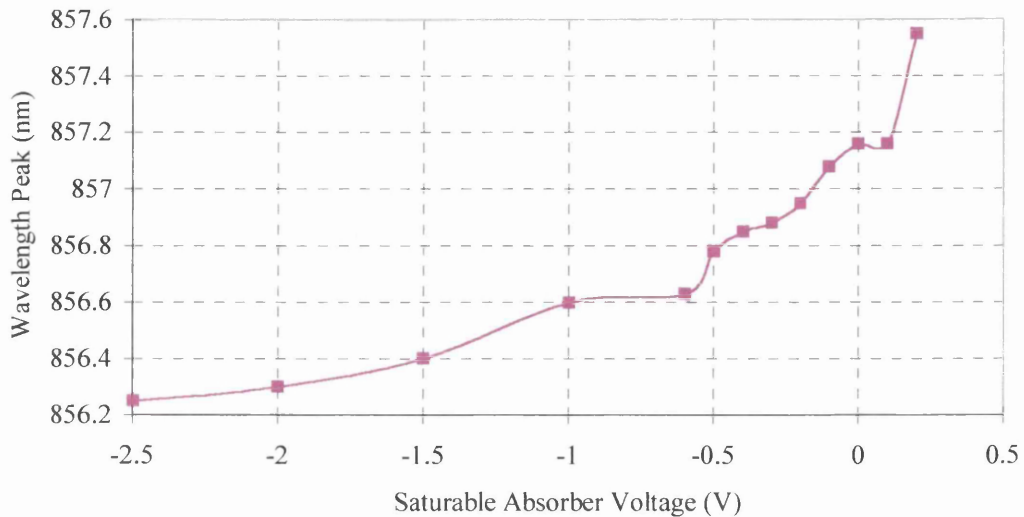


Figure 5.19: Peak wavelength variation with the saturable absorber voltage.

5.4.4 Timing jitter.

As in the previous chapter, pulse to pulse measurements were taken in order to assess the jitter levels present in the ECL pulse train, under pulsed excitation, and these are shown in Figure 5.20. As before, the distances between pulses were measured from a 5 ns long streak camera image profile, containing in this case 46 pulses. The pulse to pulse timing standard deviation was found to be 2 ps, a substantially lower value than that measured for the AAL.

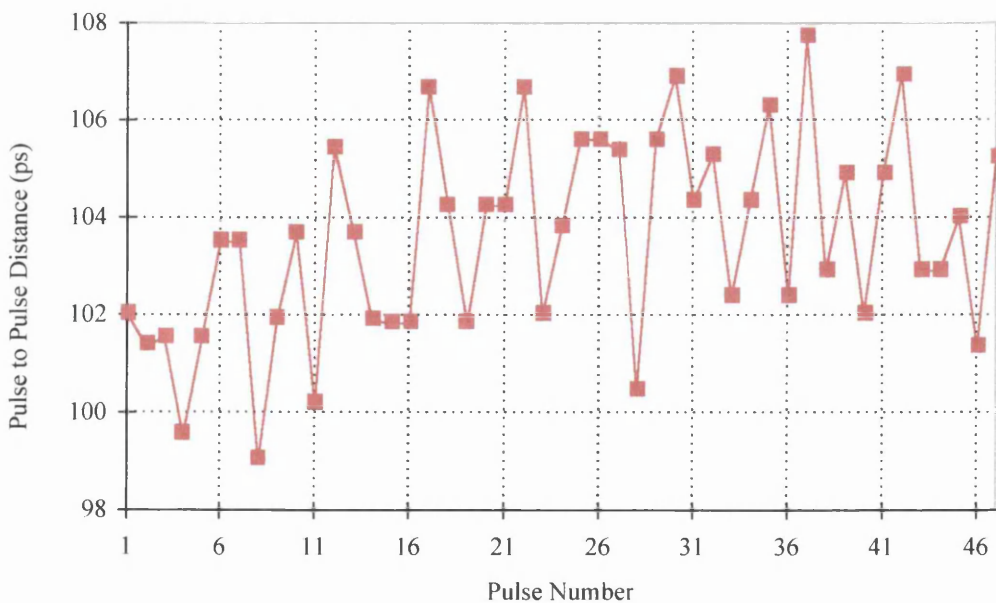


Figure 5.20: Pulse to pulse distance measurements from a 5 ns long streak image.

A systematic investigation of the noise in a mode-locked laser, however, requires measurements of the microwave spectrum of the intensity of the laser under test when it is operated in CW²³. Different types of noise, such as fluctuations of the pulse energy, pulse repetition time and pulse duration, can be recognised, and individually characterised in a quantitative way, even if they occur simultaneously.

The optical intensity from a *perfectly mode-locked laser* is a train of pulses that can be written as

$$I_0(t) = \sum_n f(t + nT_{ML}) = f(t) * \sum_n \delta(t + nT_{ML}) \quad (5.8)$$

where $f(t)$ is the temporal intensity profile of the individual pulses in the train, T_{ML} is the mode-locked pulses period and n is an integer that runs from minus to plus infinity.

The Fourier transform of the intensity from the *perfectly mode-locked laser* is given by

$$\tilde{I}_0(\omega) = \tilde{f}(\omega) \left[\frac{2\pi}{T_{ML}} \sum_n \delta(\omega - \frac{2\pi}{T_{ML}} n) \right] \quad (5.9)$$

where \tilde{I}_0 and \tilde{f} are Fourier transforms of I_0 and f . From appendix III, the power spectrum of the laser intensity is given by

$$S_{I_0} = \left(\frac{2\pi}{T_{ML}^2} \right) \left| \tilde{f}(\omega) \right|^2 \sum_n \delta(\omega - \frac{2\pi}{T_{ML}} n) \quad (5.10)$$

An *imperfectly mode-locked laser* exhibits a certain amount of fluctuation, considered small compared with $I_0(t)$. In the analysis that follows, the output fluctuations are considered slowly varying in comparison with the pulse intensity $f(t)$, that is, the amplitude and the repetition time exhibit random fluctuations, but the pulse shape remains constant. The laser intensity of the *imperfectly mode-locked laser* can be written as

$$I(t) = (1 + N(t)) \sum_n f(t + nT_{ML} + J(t)) \quad (5.11)$$

where $N(t)$ is the relative pulse intensity variation from the average pulse intensity and $J(t)$ is the repetition time variation from the average pulse repetition time.

²³ D. von der Linde, "Characterisation of the noise in continuously operating mode-locked lasers", *Appl. Phys. B*, 1986, **39**, pp. 201-217.

A pulse train with small variations of the repetition time compared with the average repetition time can be approximated by a Taylor expansion up to the first order as

$$f(t + nT + \delta T) = f(t + nT) + \frac{df(t + nT)}{dt} \delta T \quad (5.12)$$

When Eq.(5.12) is introduced into Eq.(5.11) one directly obtains

$$I(t) = I_0(t)[1 + N(t)] + \dot{I}_0(t) J(t) \quad (5.13)$$

where $\dot{I}_0(t)$ denotes the time derivative of the laser intensity in the absence of noise. Eq.(5.13) represents the optical intensity of the *imperfectly mode-locked laser* where the first term is the optical intensity of the *perfectly mode-locked laser*, the second term represents the pulse intensity variations and the third term represents the timing fluctuations of the pulse train.

Because of the random nature of the fluctuations in Eq.(5.13), these noise signals are uncorrelated with the mode-locked pulse train, and the intensity autocorrelation function of $I(t)$ can be expressed in terms of the autocorrelation functions of $I_0(t)$, $N(t)$, $J(t)$ and $\dot{I}_0(t)$ as follows

$$G_I(t) = G_{I_0}(t)[1 + G_N(t)] + G_{\dot{I}_0}(t)G_J(t) \quad (5.14)$$

where G denotes autocorrelation, and is defined in Eq.(AIII.5).

Using Eq.(5.14) the power spectrum can be written as

$$S_I(\omega) = S_{I_0}(\omega) * [\delta(\omega) + S_N(\omega)] + [\omega^2 S_{I_0}(\omega)] * S_J(\omega) \quad (5.15)$$

where the fact that the autocorrelation function of the time derivative $G_{\dot{I}_0}$ is given by

$\omega^2 S_{I_0}$ has been used. Introducing Eq.(5.10) in Eq.(5.15)

$$S_I(\omega) = \left(\frac{2\pi}{T_{ML}^2} \right) \left| \tilde{f}(\omega) \right|^2 \sum_n \left[\delta(\omega_n) + S_N(\omega_n) + (\omega_{ML} n)^2 S_J(\omega_n) \right] \quad (5.16)$$

where $\omega_n = \omega - 2\pi n/T_{ML}$.

Figure 5.21 shows the normalised power spectrum of the *imperfectly mode-locked laser* where the different sum terms from Eq.(5.16) can be recognised:

- a) the δ -function contribution, the first term in the sum of Eq.(5.16), which corresponds to the noise-free pulse train,
- b) the frequency shifted power spectrum of the amplitude noise, second term in the sum of Eq.(5.16), whose maxima are indicated by the horizontal dashed line.
- c) the power spectrum of the timing jitter, third term in the sum of Eq.(5.16), which is proportional to n^2 .

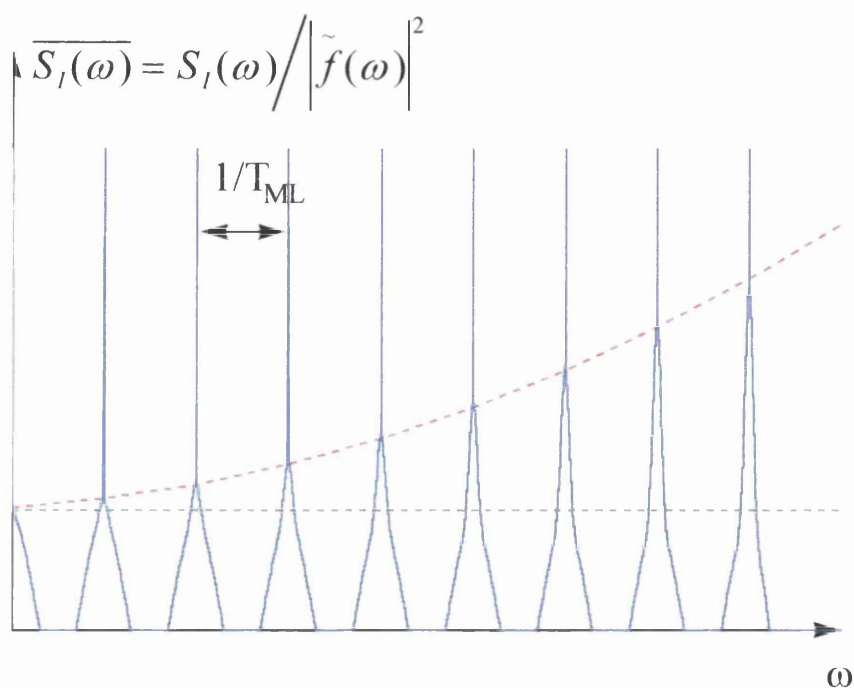


Figure 5.21: Normalised power spectrum $S_I(\omega)$ of a pulse train with fluctuations in the pulse amplitude and repetition time.

It is important to notice this dependence of the jitter with harmonic number n because this allows the two different types of noise to be distinguished and therefore allows us to determine both $S_N(\omega)$ and $S_I(\omega)$. At harmonics of sufficiently low order, the amplitude-noise sidebands predominate and $S_N(\omega)$ can be measured, while the phase-noise sidebands dominate for harmonics of high order and $S_I(\omega)$ can be measured.

Using Parseval's theorem, derived in appendix III, the rms deviation of a noisy quantity can be calculated by integrating the area of the noise spectrum. Thus, the rms

amplitude and jitter fluctuations, σ_N and σ_J are given by

$$\sigma_N^2 = \langle N^2(t) \rangle = \frac{1}{2\pi} \int_{-\infty}^{+\infty} S_N(\omega) d\omega \quad (5.17)$$

$$\sigma_J^2 = \langle J^2(t) \rangle = \frac{1}{2\pi} \int_{-\infty}^{+\infty} S_J(\omega) d\omega \quad (5.18)$$

In measurements, σ_N and σ_J are determined in a finite bandwidth $[\omega_{low}, \omega_{high}]$, and the integration in Eq.(5.17) and Eq.(5.18) runs only over this frequency range.

As defined in the previous chapter, the single-sideband phase noise spectrum of the laser n th harmonic is

$$L_n(\omega) = n^2 \omega_{ML}^2 S_J(\omega) \quad (5.19)$$

and introducing Eq.(5.19) in Eq.(5.18), and accounting for both sidebands, the following relationship is obtained,

$$\sigma_J = \frac{1}{2\pi n f_{ML}} \sqrt{2 \int_{f_{low}}^{f_{high}} L_n(f) df} \quad (5.20)$$

meaning that the rms timing jitter can be calculated by integrating the noise spectrum against offset frequency of the phase noise sideband.

Figure 5.22 shows the first and second harmonics of the power spectrum from a mode-locked ECL operating at 9.32 GHz (note the difference in frequency span). In both cases, the noise sidebands due to the amplitude and phase noise are clearly seen.

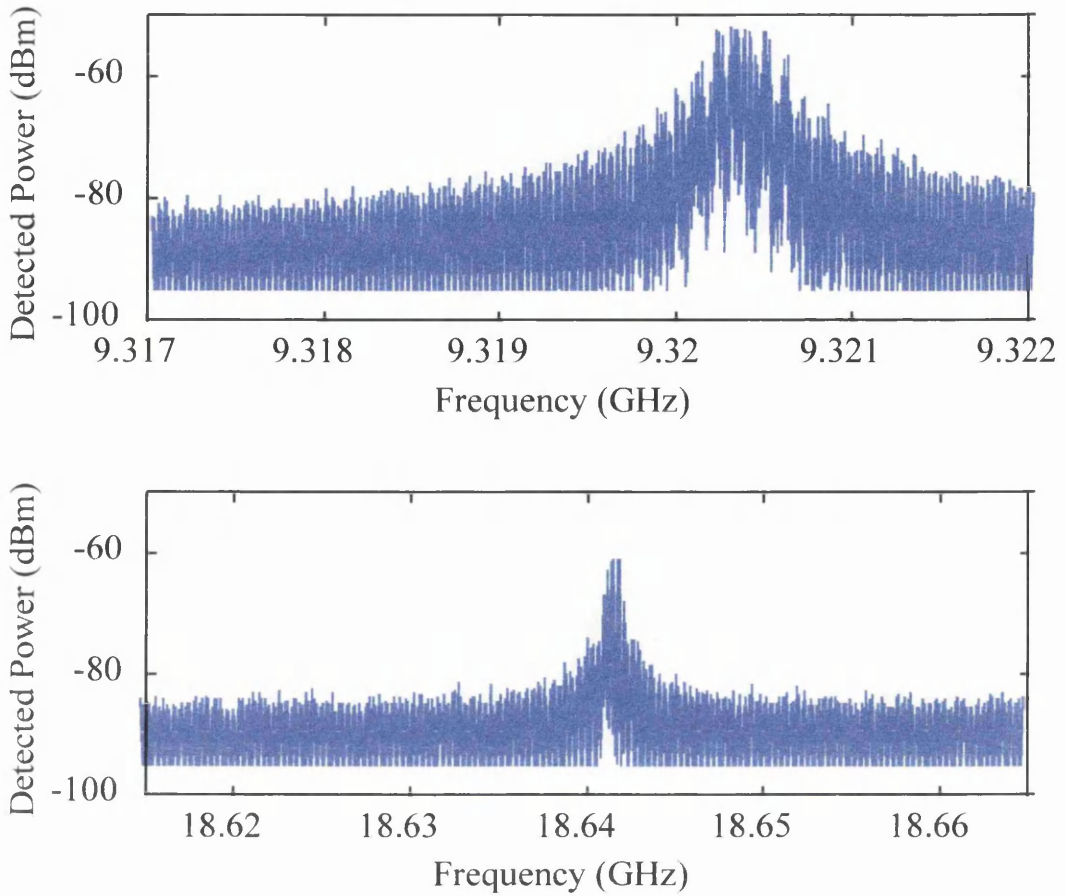


Figure 5.22: *First and second harmonic of the passively mode-locked ECL (note the difference in frequency span).*

The noise sideband from a harmonic n of the power spectrum $P(f)$ displayed by the spectrum analyser is calculated as the ratio of the power in one sideband, in a 1 Hz measurement bandwidth, to the power of the modelocking frequency harmonic being measured P_c , which is the reason why the noise is measured in dBc or dB under the carrier power. The spectrum analyser shows the spectral power $P(f)$ integrated over the resolution bandwidth B , so it is normalised dividing $P(f)$ by B . From the above considerations the noise sideband is calculated as

$$L_n(f) = \frac{P(f)}{B P_c} \quad (5.21)$$

and the rms jitter as

$$\sigma_J = \frac{1}{2\pi n f_{ML}} \sqrt{2 \int_{nf_{ML}+f_{low}}^{nf_{ML}+f_{high}} L_n(f) df} \quad (5.22)$$

A typical spectrum measurement has some errors caused by the instrumentation, mainly due to the differences between the filter shape of the resolution bandwidth filters compared with ideal filters. These errors must also be taken into account when calculating the noise sideband of the different harmonics of the modelocking signal. In our case, the HP 85671A phase noise utility was used to measure noise sidebands, which minimises all the instrumentation errors.

The single sideband noise of the first and second harmonics from the power spectrum of a passively mode-locked ECL are shown in Figure 5.23. It can be seen that the noise above 2 kHz is phase noise in nature as it increases in 6 dB in the second harmonic noise sideband. Below this frequency the noise is mainly due to amplitude fluctuations and does not increase from the first to the second harmonic.

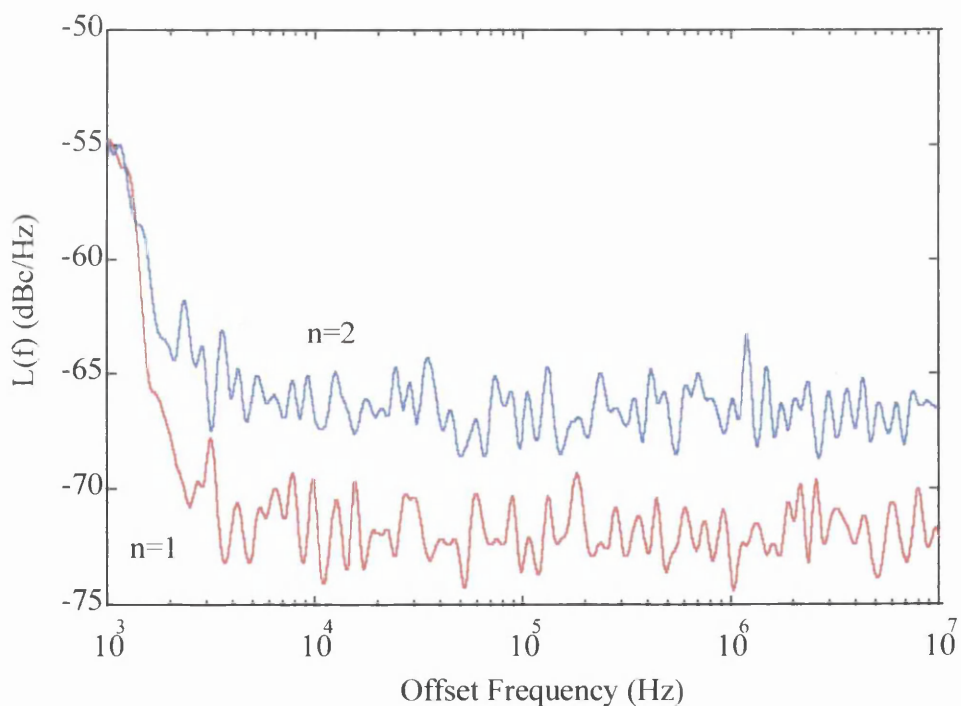


Figure 5.23: Single-sideband total noise power for the first, $L_1(f)$, and second, $L_2(f)$, harmonic.

Usually, the rms jitter is calculated by measuring the phase noise spectrum from a high harmonic, where it is dominant due to its dependence of n^2 . In our case, due to the impossibility of measuring harmonics higher than the second because of the photodetector bandwidth, a different approach was used. Taking into account that the

first and second harmonic noise side bands are related to the amplitude and jitter noise spectra as

$$NSB_1(f) = S_N(f) + (2\pi f_{ML})^2 S_J(f) \quad (5.23)$$

$$NSB_2(f) = S_N(f) + (4\pi f_{ML})^2 S_J(f) \quad (5.24)$$

and using Eq.(5.23) and Eq.(5.24) into Eq.(5.19)

$$L_2(f) = \frac{4}{3}(NSB_2 - NSB_1) \quad (5.25)$$

with is the relation used to calculate the rms timing jitter.

The calculated timing jitter (1 kHz-10MHz) for different saturable absorber voltages is summarised in Table 5.2.

V_{sat} (V)	0	-0.5	-1	-1.5	-2	-2.5
σ_{rms} (ps)	9.5	10.9	10.6	11.6	10.3	9.3

Table 5.2: *Timing jitter (1 kHz - 10 MHz) variation with the saturable absorber voltage.*

As was commented in chapter 4, a stabilising mechanism may be necessary, due to the large rms jitter. One way to do this is to inject an RF signal, at the modelocking frequency or at sub-harmonic²⁴, that is, to use *hybrid modelocking* instead of *passive modelocking*, as will be shown in chapter 7.

5.4.5 Development of passive modelocking.

Using the same set-up as in the previous chapter, the modelocking build-up time was quantified by performing a short-term Fourier transform of the optical output power, with a window length of 500 ps. Figure 5.24 shows the time evolution of the optical power at the fundamental modelocking frequency of 9.3 GHz, fitted to an exponential function of the form $1 - e^{-t/\tau}$. As explained in chapter 4, the reason the x-axis of this figure begins at 1.5 ns is because there is a further delay from the moment when the

²⁴ T. Hoshida, H.F. Liu, M. Tsuchiya, Y. Ogawa and T. Kamiya, "Locking characteristics of a subharmonically hybrid mode-locked multisection semiconductor laser", *IEEE Photonics Technol. Lett.*, 1996, **8**, 12, pp. 1600-1602.

current pulse reaches the gain section to when the modelocking pulse train begins to build up. The estimated modelocking development time is 2.8 ns, around 26 round trips, again in good agreement with the results of AuYeung *et al*²⁵.

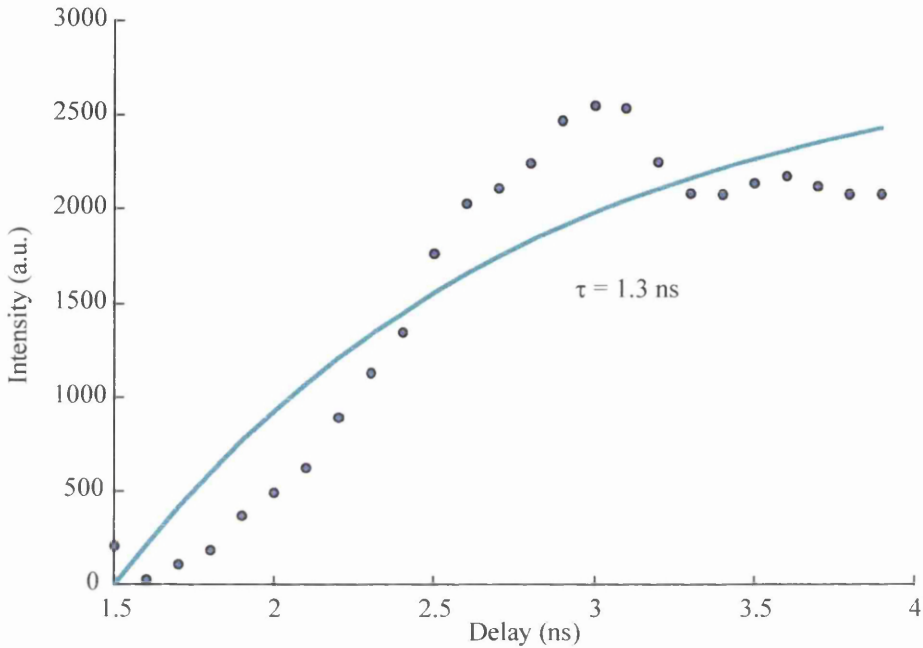


Figure 5.24: Time evolution of the optical power at the fundamental modelocking frequency.

Figure 5.25 shows the passive modelocking development under different saturable absorber voltages. It can be seen that, even though the modelocking pulse build-up time seems to be independent of the saturable absorber voltage, the relaxation oscillations that accompany the pulses build-up are stronger the lower the saturable absorber voltage.

²⁵J. C. AuYeung, L. A. Bergman and A. R. Johnston, “Transient behaviour of an actively mode-locked semiconductor laser diode”, *Appl. Phys. Lett.*, 1982, **41**, 2, pp. 124-126.

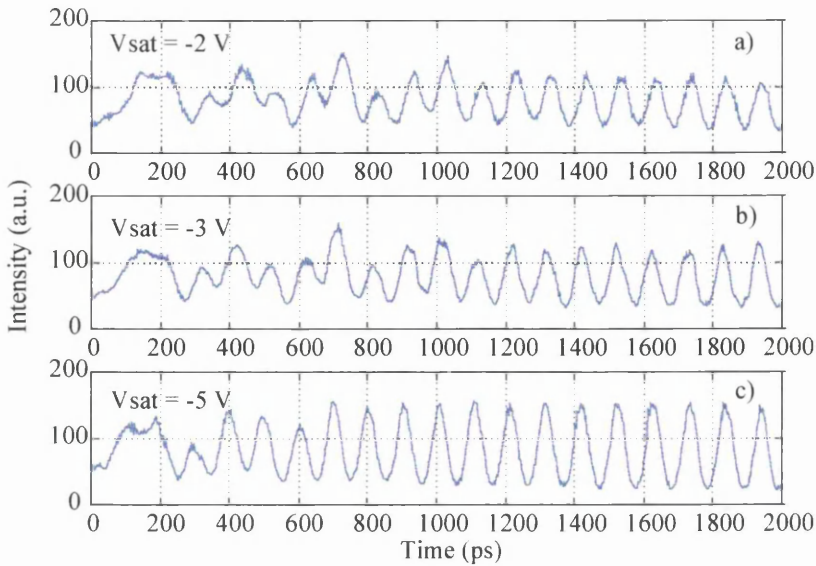


Figure 5.25: *Modelocking development under different saturable absorber voltages.*

5.5 Numerical simulations.

To assist construction optimisation, the same numerical model used in chapter 4 to analyse the experimental results obtained from the AAL configuration was used in the case of the ECL configuration. For the experiments a $50 \mu\text{m}$ saturable absorber was used as simulations predicted that ECL lasers with shorter absorber sections ($30 \mu\text{m}$) may not reach complete ML, whereas longer absorber sections ($70 \mu\text{m}$) lead to very strong self-pulsing modulation up to currents 2.5-3 times above threshold. Therefore, the most important agreement between these theoretical and experimental results is the absence of combined self-pulsation accompanying the modelocking pulse train which can be reproduced using the model.

A comparison between optical spectra obtained experimental and theoretically is presented in Figure 5.26. In Figure 5.26.(a) the voltage applied to the saturable absorber of the ECL was -3 V and the device was mode-locked. As already mentioned, when the device was mode-locked the optical spectrum suffered a shift of more than 2 nm to longer wavelengths, became very asymmetric and the spectral width changed from 0.2 nm at zero absorber bias to almost 2 nm when the saturable absorber was reverse biased. Figure 5.26.(b) is the simulated spectra for the same construction and bias conditions. Both the asymmetry and the shift of the spectra (the zero frequency of the simulated spectra was aligned to the experimental CW lasing wavelength) are readily reproduced by the theory.

The modelling thus shows that both effects may be explained almost entirely by the self-phase modulation (SPM) in the gain section.

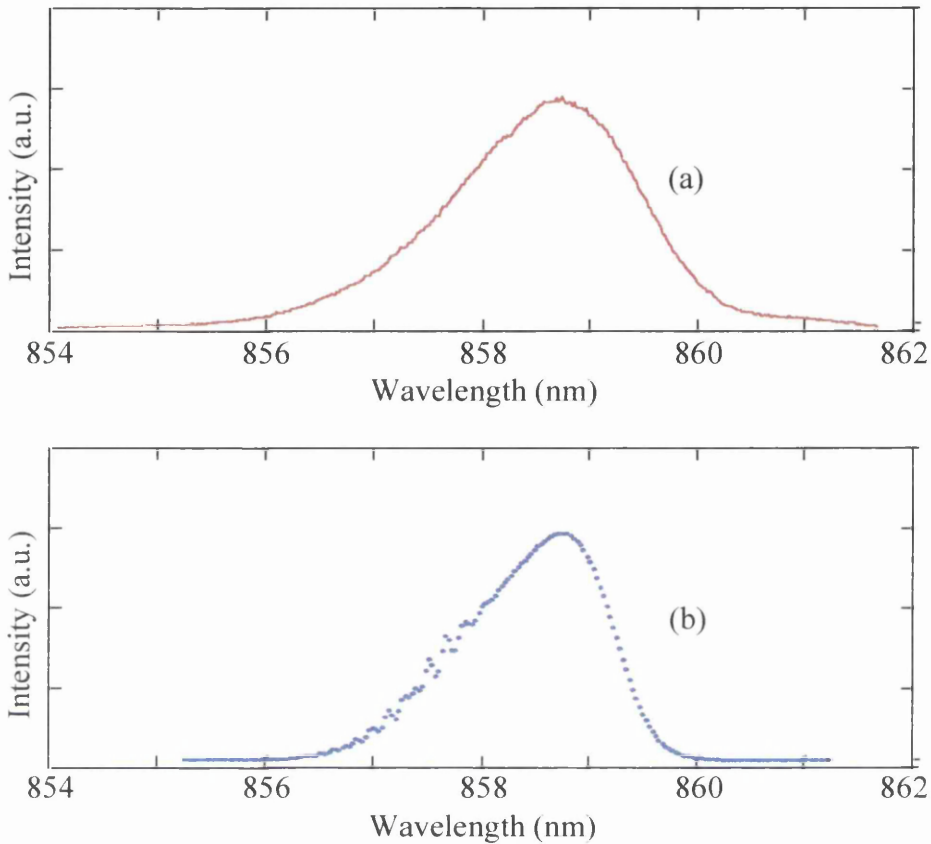


Figure 5.26: *Optical spectra: (a) measured from the ECL at $I/I_{th}=2.9$; (b) simulated at the same bias.*

5.6 Conclusions.

It has been shown that the ECL is a very efficient configuration as a short pulse generator in terms of narrow pulse width, low timing jitter levels and linear chirp. A very important factor is also the absence of self-pulsing modulation in the pulse train envelope, which could degrade the quality of the pulses.

Even though this configuration is not as straightforward to fabricate as the AAL configuration, as the passive waveguide must be created, the IFVD process is very reliable using SiO_2 and P:SiO_2 which makes this type of laser one of the most promising types of passively mode-locked semiconductor laser.

Fabricating the integrated passive waveguides using IFVD, instead of other reported methods, allow us to achieve negligible reflections at the interface between the active and passive sections and therefore to obtain mode-locked lasers with better characteristics than those reported earlier.

This structure with the integrated passive waveguide is also very flexible and a very wide range of ECLs for different modelocking frequencies can be fabricated with hardly any difference in the threshold currents.

It has also been shown that the numerical model agrees very well with the experimental results, confirming the model is a useful tool for laser applications analysis.

Chapter Six ***EXTERNAL CAVITY MODE-LOCKED LASERS.***

An external cavity laser (XCL) consists of a semiconductor laser coupled to an external cavity that can be either air, ended by a mirror or a grating, or an optical fibre with a grating written on or in it. The use of an external cavity for modelocking offers the advantages of widely variable repetition rates and tunability of wavelength. Modelocking frequencies as low as hundreds of MHz can be achieved using XCL, but the maximum frequency is limited by the finite length of the external cavity optical elements.

Though a versatile tunable laser for the laboratory, these XCLs suffer from sensitivity to vibration, and they are also larger in size and more difficult to work with than their monolithic counterparts analysed in previous chapters. In our case, due to these instability problems, realignment of the external cavity was often required, probably due to vibrations from the departmental mechanical workshop place opposite our laboratory.

To fabricate an XCL, the reflectivity of one of the semiconductor laser's facets must be reduced, usually either by anti-reflection (AR) coatings, by orienting the waveguide at some angle with respect to the direction normal to the facet, or by using both of these techniques. The light is then coupled into an external optical cavity and reflected back into the laser with a mirror or diffraction grating. It is worth noting that the facets reflectivity, throughout this chapter, is defined as intensity reflectivity, not field reflectivity.

6.1 Laser configurations.

Figure 6.1 depicts the different external cavity laser configurations analysed. Figure 6.1(a) and Figure 6.1(c) show the semiconductor laser coupled to a fibre grating, which forms the external cavity, the former using an AR coating and the latter using a bent waveguide laser as methods for the reduction of the laser's facet reflectivity. In Figure 6.1(b) and Figure 6.1(d) the light is focused with a lens onto a high reflectivity

(HR) dielectric mirror, the external cavity being air, and again the former is an AR coated laser and the second is a bent waveguide laser.

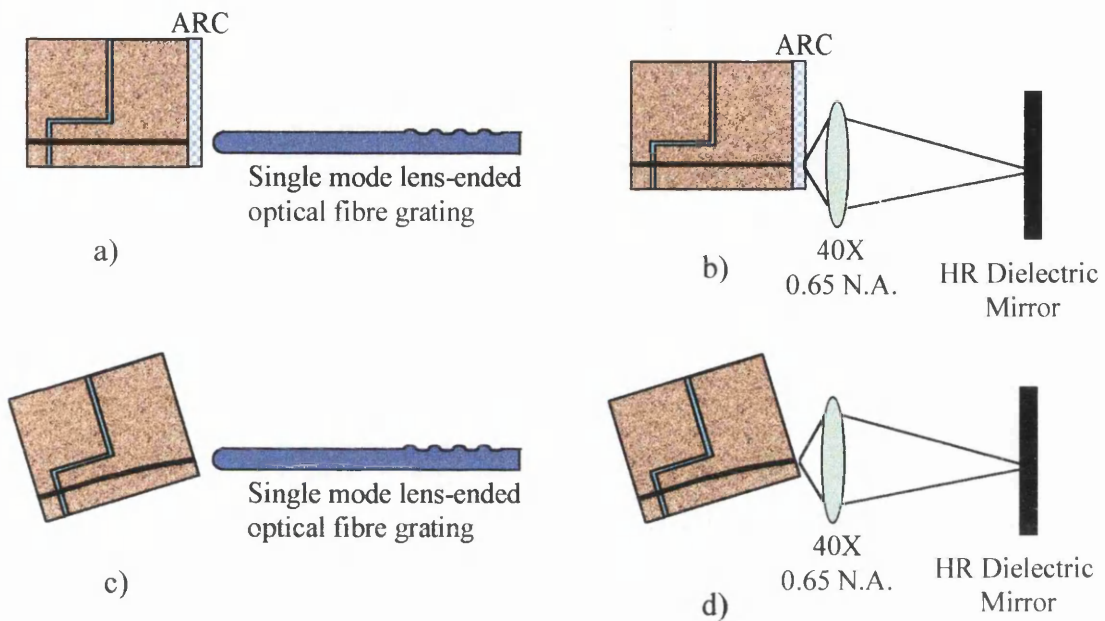


Figure 6.1: *External cavity laser configurations: a) AR coated laser with fibre grating, b) AR coated laser with external mirror, c) bent waveguide laser with fibre grating and d) bent waveguide laser with external mirror.*

It is possible to obtain wavelength tunability with the configurations shown in Figure 6.1(c) and 6.1(d) by changing the HR mirror for an external diffraction grating.

6.2 External cavities.

As has already been shown, two different types of external cavity can be used for the XCL. The first one, *air*, is the easiest to make, but it also is the one with larger instabilities. The light is either collimated or focused onto an external mirror or diffractive grating and reflected back to the semiconductor device^{1,2}. This type of device has been widely studied for active and hybrid modelocking.

¹ A. Mar, D. Derickson, R. Helkey, J. Bowers, R.T. Huang and D. Wolf, “Actively mode-locked external cavity semiconductor lasers with transform-limited single-pulse output”, *Optics Lett.*, 1992, **17**, 12, pp. 868-870.

² R. Ludwig and A. Ehrhardt, “Turn-key-ready wavelength-, repetition rate- and pulsewidth-tunable femtosecond hybrid mode-locked semiconductor laser”, *Electronics Lett.*, 1995, **31**, pp. 1165-1167.

The second type of external cavity contains an optical fibre with a Bragg grating written on or in it^{3,4}. This type of external cavity is more robust than air, but the coupling efficiencies between the semiconductor device and the external cavity are usually poorer than using air as the external cavity. For a better understanding of this type of laser, the properties of the fibre grating will now be discussed further.

6.2.1 Fibre gratings.

Photorefractive fibre Bragg gratings have many applications in telecommunications and sensor systems due to their compatibility with the transmission medium and relative ease of fabrication^{5,6,7,8}.

There are many ways in which gratings can be written into the optical fibre, but the fibre gratings used in our case were written using the phase mask technique. The output from a frequency doubled argon-ion laser, operating at 244 nm, was focused through a phase mask onto the optical fibre, which had been further sensitised by a short period of high pressure hydrogen loading, as can be seen in Figure 6.2⁵. The grating is photoinduced as a spatial modulation of the core refractive index with a period determined by the angle between the two writing beams.

³ P.P. Iannone, G. Raybon, U. Koren and P.R. Prucnal, "Robust electrically tunable 1.5 μm mode-locked fiber-external-cavity laser", *Appl. Phys. Lett.*, 1992, **61**, 13, pp. 1496-1498.

⁴ J. Yu, D. Huhse, M. Schell, M. Schulze, D. Bimberg, J.A.R. Williams, L. Zhang and I. Bennion, "Fourier-transform limited 2.5 ps light pulses with electrically tunable wavelength (15 nm) by hybridly modelocking a semiconductor laser in a chirped Bragg grating fibre external cavity", *Electronics Lett.*, 1995, **31**, 23, pp. 2008-2009.

⁵ I. Bennion, J.A.R. Williams, L. Zhang, K. Sugden and N.J. Doran, "UV-written in-fibre Bragg gratings", *Optical and Quantum Electron.*, 1996, **28**, pp. 93-135.

⁶ K.C. Byron, K. Sugden, T. Bricheno and I. Bennion, "Fabrication of chirped Bragg gratings in photosensitive fibre", *Electronics Lett.*, 1993, **29**, 18, pp. 1659-1660.

⁷ K.C. Byron and H.N. Rourke, "Fabrication of chirped fibre gratings by novel stretch and write technique", *Electronics Lett.*, 1995, **31**, 1, pp. 60-61.

⁸ D.Z. Anderson, V. Mizrahi, T. Erdogan and A.E. White, "Production of in-fibre gratings using a diffractive optical element.", *Electronics Lett.*, 1993, **29**, 6, pp. 566-568.

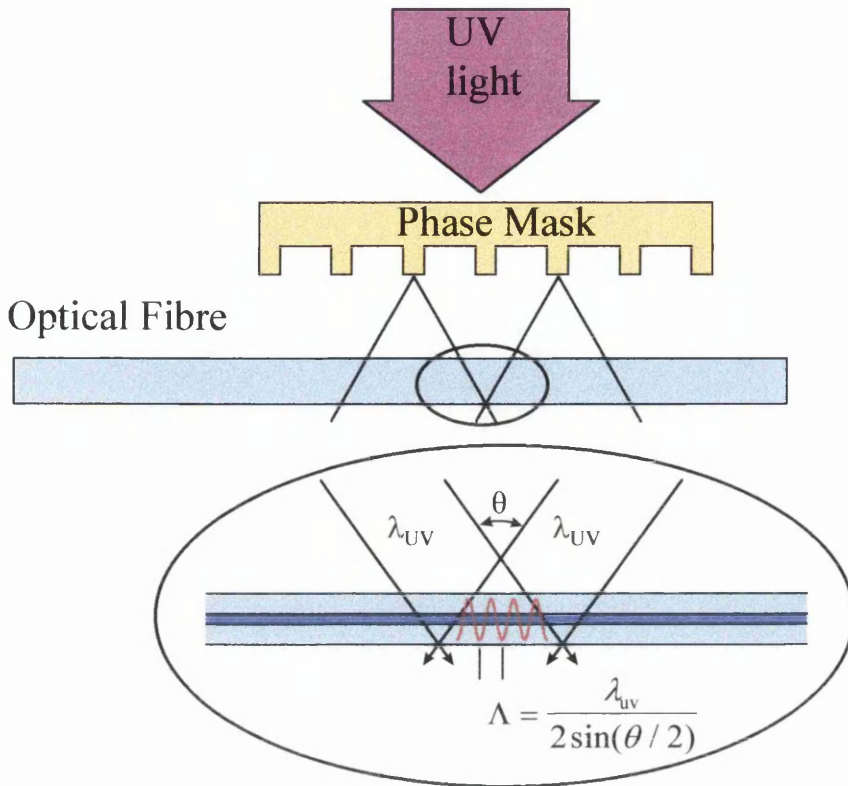


Figure 6.2: *Phase mask technique. Inset shows the inscription of a periodic grating in the core of a photosensitive fibre by two interfering UV beams.*

The characteristic response of the grating can be tailored to suit any application by using a combination of length, chirp, shading and exposure time (refractive index variation). The fibre grating characteristics are as follows⁹

- Reflectivities up to 100%.
- Linewidths from tens of nm down to 0.01 nm.
- Wavelength range: U.V. - I.R.
- Very long lifetime, a reflectivity of 75% will just drop by 3% over a period of 25 years.
- Stable up to 500 °C.
- Simple packaging.

The fibre gratings used in this work were written in Aston University. In Figure 6.3, the transmission spectrum of a fibre grating can be seen. It shows a reflectivity peak

⁹ K.C. Byron, Private communication.

close to 60%, with the wavelength peak being at 859.8 nm and the linewidth being around 0.17.nm.

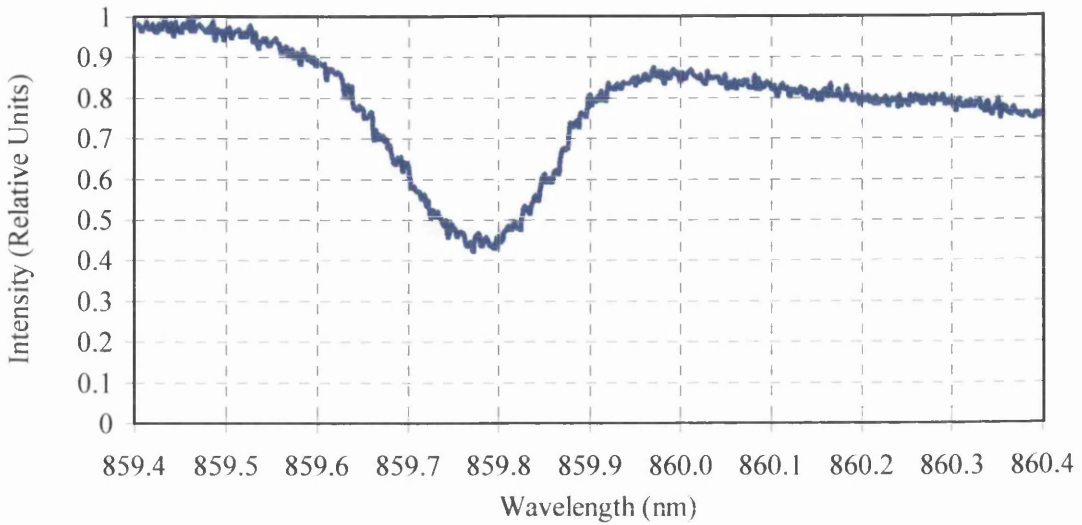


Figure 6.3: *Transmission spectrum of a fibre grating.*

6.3 Reduction of the reflectivity from a laser facet.

The reduction of the reflectivity of one of the laser facets, i.e. that coupled to the external cavity, is the most important issue when designing an XCL. The reflectivity of a semiconductor device can be reduced by means of a highly efficient AR mechanism, either a single or multi-dielectric AR coating deposited on the cleaved facet, or by using a structure where the waveguide is not normal to the cleaved facet.

6.3.1 Antireflection coatings.

Coating technology for facets of semiconductor lasers has been widely studied mainly for controlling facet reflectivity^{10,11}. In particular, antireflection (AR) coatings are indispensable for high power lasers, semiconductor optical amplifiers and external cavity lasers. In an AR coating, as the one shown in Figure 6.4, precise control of the

¹⁰ K. Shigihara, T. Aoyagi, S. Kakimoto, M. Aiga, M. Ostubo and K. Ikeda, "Antireflection coating for laser diodes", *Electronics Lett.*, 1995, **31**, 18, pp. 1574-1576.

¹¹ I.P. Kaminow, G. Eisenstein and L.W. Stulz, "Measurement of the modal reflectivity of an antireflection coating on a superluminescent diode", *IEEE J. Quantum Electron.*, 1983, **19**, 4, pp. 493-495.

refractive index and thickness of the single or multiple layers is indispensable, but the refractive index of the coating materials is always very difficult to control. In any case, reducing the facet reflectivity to below 0.1%, the value required for efficient operation of an XCL, requires a very high degree of control over both the refractive index and the thickness of the coating.

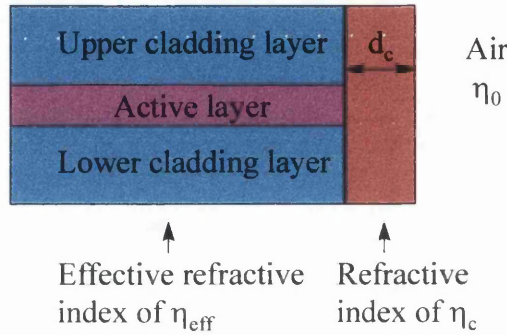


Figure 6.4: Antireflection coating layers.

A plane wave with normal incidence at the interface between the semiconductor and the coating has a reflectivity given by¹²

$$R = \frac{\eta_c^2 (\eta_{eff} - \eta_0)^2 \cos^2 k_c d_c + (\eta_0 \eta_{eff} - \eta_c^2)^2 \sin^2 k_c d_c}{\eta_c^2 (\eta_{eff} + \eta_0)^2 \cos^2 k_c d_c + (\eta_0 \eta_{eff} + \eta_c^2)^2 \sin^2 k_c d_c} \quad (6.1)$$

where k_c is the light propagation constant in the coating layer, given by $k_c = 2\pi \eta_c / \lambda$. Eq.(6.1) becomes particularly simple when $k_c d_c = (2n + 1)\pi/2$, which is equivalent to saying that the thickness of the coating film is an odd multiple of $\lambda/4\eta_c$. In this case

$$R = \frac{(\eta_0 \eta_{eff} - \eta_c^2)^2}{(\eta_0 \eta_{eff} + \eta_c^2)^2} \quad (6.2)$$

Therefore, a perfect single layer AR coating, for a plane wave, can be realised if the refractive index of the coating layer, η_c , and the coating thickness, d_c , fulfil the following relationships

$$\eta_c = \sqrt{\eta_{eff}} \quad (6.3)$$

$$d_c = \frac{\lambda}{4\eta_c} \quad (6.4)$$

¹² E. Hecht, "Optics", Addison -Wesley, 1987.

where η_{eff} is the effective refractive index of the semiconductor laser and λ is the lasing wavelength. This perfect single layer AR coating is called *the ideal quarter wavelength AR coating*. For a GaAs/AlGaAs laser, with an effective refractive index around 3.3 and a lasing wavelength peak around 860 nm, the coating material needed must have a refractive index of 1.82 and a thickness of 118 nm. The material that best fits this refractive index requirement is aluminium oxide (Al_2O_3) which has a refractive index around 1.69. Due to the fact that the refractive index of Al_2O_3 is not exactly the square root of the effective refractive index of the semiconductor laser, the minimum reflectivity that can be obtained using a quarter wavelength coating is around 0.5%, calculated by introducing the adequate values in Eq.(6.2).

Figure 6.5 shows the apparatus designed to measure the residual reflectivity of AR coatings deposited on GaAs substrates. It can be seen that the output light from the monochromator was unpolarised, which is represented by the two little arrows. The light was passed through a polariser and then, being linearly polarised, through a polarising beam splitter. After passing through the quarter-wave plate the light was circularly polarised, and was used to illuminate the sample under test. After reflection, the light was again passed through the quarter-wave plate, which polarised it linearly, but rotated through 90° in comparison with before. When the light reached the polarising beam splitter, because of this 90° change in polarisation, it was directed towards the detector.

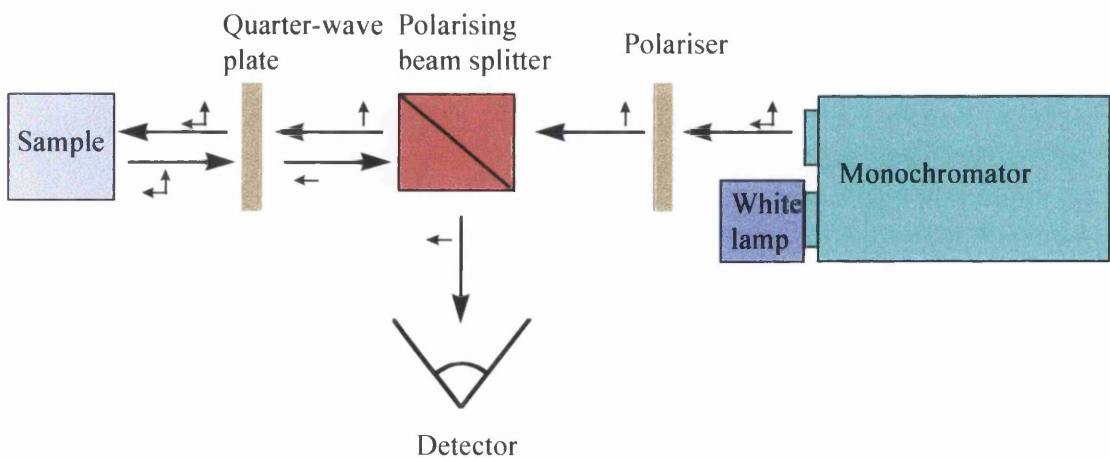


Figure 6.5: Reflectivity measurements set-up.

Figure 6.6 shows a comparison between the theoretical and measured values of the reflectivity of a GaAs sample, with an estimated effective refractive index equal to 3.3, with 125 nm of Al_2O_3 on top of it. It can be seen how sensitive the AR coatings are, because the difference between the two graphs was probably due to a slight variation in the Al_2O_3 refractive index and the coating thickness, e.g. a coating film with a refractive index of 1.8 and thickness of 140 nm would give a theoretical reflectivity very similar to the one measured.

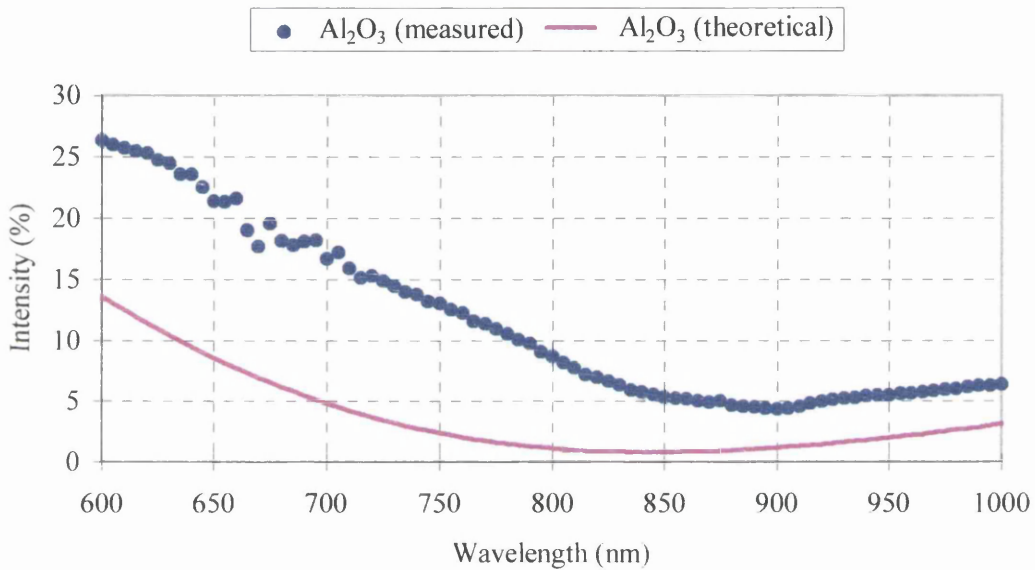


Figure 6.6: Theoretical (line) and experimental (dots) reflectivity from a single layer AR coating using Al_2O_3 .

To confirm the operation of the AR coating, the I-L characteristics of lasers with one facet AR coated were measured. The AR coating was a layer of Al_2O_3 125 nm thick. The lasers were cleaved to length of 650 μm . The threshold current of devices of the same length but without AR coating was found to be around 17-18 mA. Figure 6.7(a) shows the I-L curve from the AR coated facet, whilst Figure 6.7(b) was taken from the uncoated one. The first thing we notice is that the threshold current increased from 17-18 mA to 22 mA, because of the reduction in the reflectivity of one of the facets.

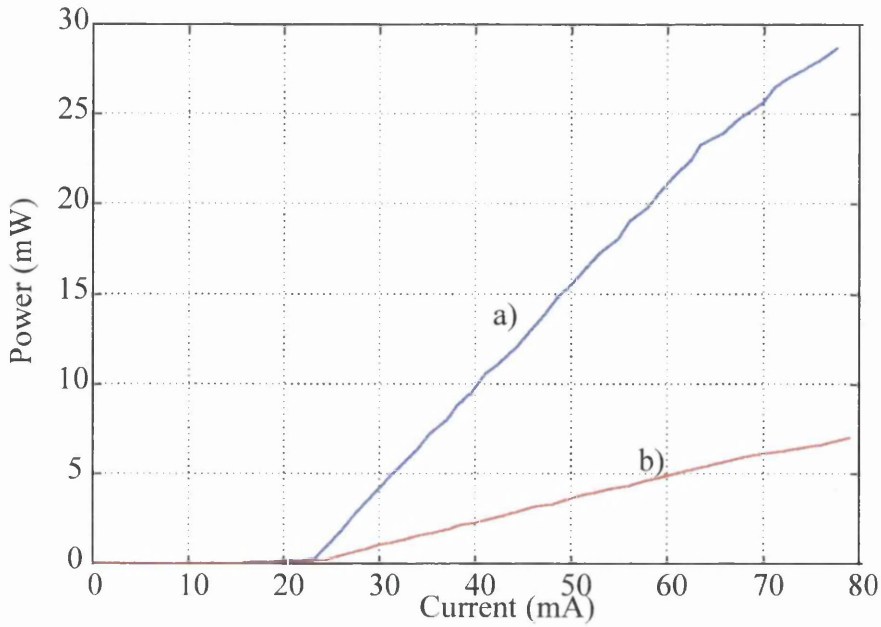


Figure 6.7: *I-L curve of a AR coated laser: a) coated facet and b) uncoated facet.*

When the end-faces of the lasers are not symmetrical and the facets' reflectivities are different, the output P_1 from one of the ends is no longer equal to the output P_2 from the other end¹³. The ratio is given by

$$\frac{P_1}{P_2} = \frac{R_1^{-1/2} - R_1^{1/2}}{R_2^{-1/2} - R_2^{1/2}} \quad (6.5)$$

From Figure 6.7 it can be seen that, for a current of 60 mA, the output from the uncoated facet P_1 was 5 mW, while from the coated facet P_2 was 21 mW. Assuming a reflectivity of 32% for the uncoated facet, from Eq.(6.5) the AR coated facet reflectivity was calculated to be around 3.5%, in close agreement with the value found from the surface reflectivity measurements.

It has therefore been shown that a single layer AR coating is not a precise method to reduce the reflectivity of the laser's facet to a value below 0.5%, because we cannot find a material with a refractive index exactly equal to the square root of the effective refractive index of the semiconductor device. For this the reason, multiple layer AR coatings are usually used. A three layer AR coating, with the refractive index and

¹³ G.H. Thompson, "Physics of semiconductor laser devices", *John Wiley & Sons*.

thickness of the third layer equal to those of the first layer, can give reflectivities as low as 0.08%¹⁰, but in our case it was not possible to deposit this type of AR coating.

6.3.2 *Bent waveguide lasers.*

Reduction of the reflectivity of one of the laser's facets by AR coating to below 0.1% requires a very high degree of control of the refractive index and the thickness of the coating film. The fabrication of lasers with the waveguide bent at some angle with respect to the direction normal to the facet provides a simple way to overcome the need for a tightly controlled AR coated facet, when reflectivities below 0.1% are required, as in our case^{14,15,16}. This method is particularly attractive because it requires no more processing steps than fabricating conventional laser diodes. The use of angled facets to reduce the reflectivity is straightforward if the device supports only the fundamental mode because the reflectivity of the mode, at the angled facet, is inversely proportional to the angle with respect to the direction normal to the facet. However, when higher modes can propagate, the reflection from the angled facet can excite them and cause laser oscillation, or spectral modulation of the output light.

Figure 6.8 shows a diagram of the bent waveguide laser design. This device design has been widely used as a superluminescent diode¹⁷ but, to the best of our knowledge, has not been used as an active device for external cavity mode-locked lasers. The ridge waveguide was 5 μm wide, with a straight section of length 150 μm , a bent section of length 300 μm and a radius of curvature of 2145 μm , and another straight section of length 50 μm , the total length of the laser being 500 μm . The waveguide formed an angle of 8° with the normal to the cleaved facet, which reduced the reflectivity of the

¹⁴ G.A. Alphonse and M. Toda, "Mode coupling in angled facet semiconductor optical amplifiers and superluminescent diodes", *IEEE J. Lightwave Technol.*, 1992, **10**, 2, pp. 215-219.

¹⁵ A.J. Collar, G.D. Henshall, J. Farre, B. Mikkelsen, Z. Wang, L. Eskildsen, D.S. Olesen and K.E. Stubkjaer, "Low residual reflectivity of angled-facet semiconductor laser amplifiers", *IEEE Photonics Technol. Lett.*, 1990, **2**, 8, pp. 553-555.

¹⁶ C. Vassallo, "Gain ripple minimisation and higher-order modes in semiconductor optical amplifiers", *Electronics Lett.*, 1989, **25**, 12, pp. 789-791.

¹⁷ C.F. Lin and C.S. Juang, "Superluminescent diodes with bent waveguide", *IEEE Photonics Technol. Lett.*, 1996, **8**, 2, pp. 206-208.

first four modes to less than 0.01%¹⁴. The bending losses for a device very similar to ours were calculated by C.F. Lin *et al*¹⁷ to be 10.8 dB. As can be seen, the laser was divided in two sections, the saturable absorber which was 50 μm long, and the gain section, which was 450 μm long.

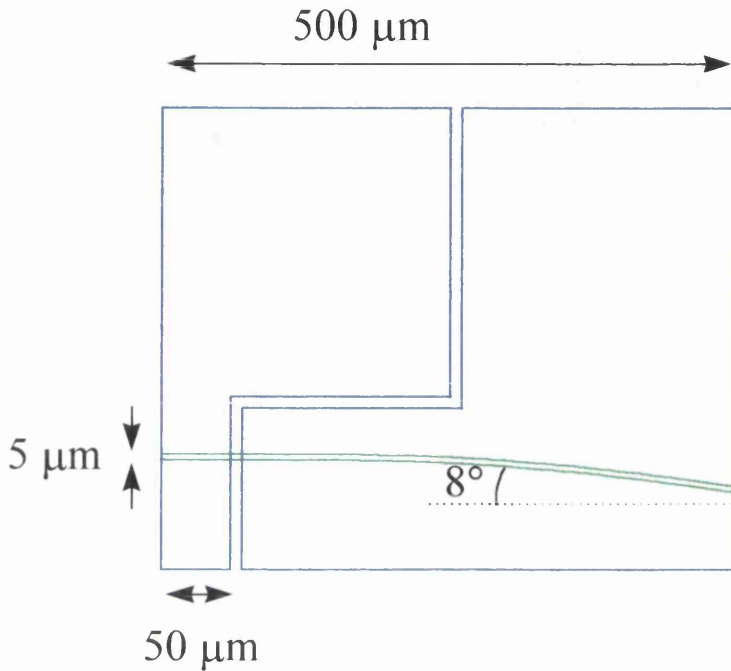


Figure 6.8: *Bent waveguide laser design.*

Before fabrication, the guiding characteristics of the device were analysed using a 3-D finite difference beam propagation method (BPM) simulation program. Figure 6.9 shows the field propagation through the bent waveguide. It shows that most of the light is perfectly guided through the laser, but the output mode is very asymmetric. It can also be seen that some of the light is radiated, due to the finite radius of curvature of the bent waveguide.

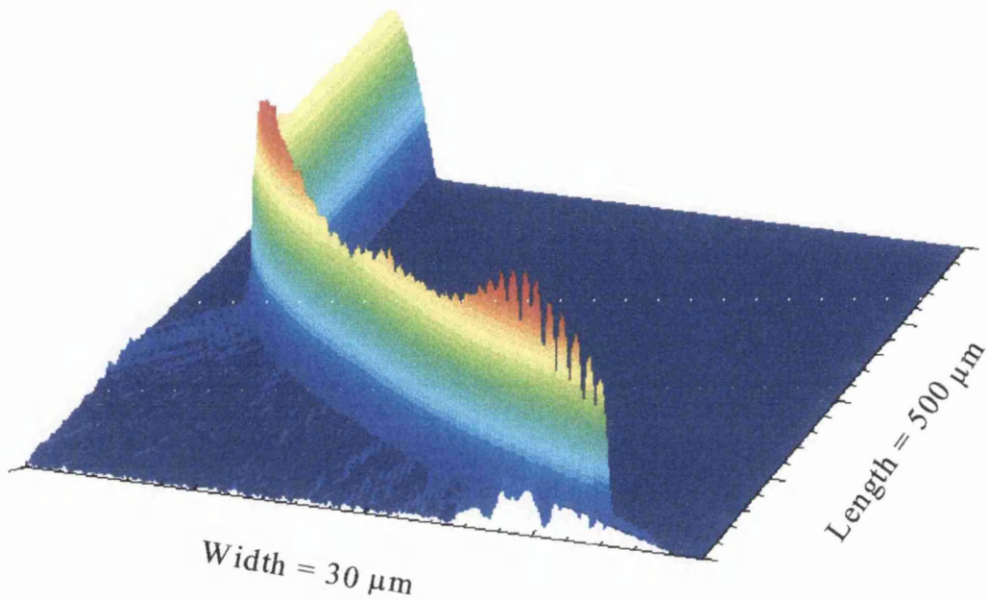


Figure 6.9: BPM simulation of the bent waveguide. (Note the vertical axis represents $36 \mu\text{m}$ and the horizontal axis $500 \mu\text{m}$).

Some methods have been suggested to reduce the radiated light, such as placing a trench outside the curved waveguide^{18,19}, and this method will be used in a future variant of this device design.

To analyse the asymmetry of the output mode and the radiation of light, the near-field of a solitary device was studied by focusing the output light from the tilted facet into the streak camera. Figure 6.10 shows a streak image of the device's near-field, where the asymmetry of the output mode can be seen in the form of a longer tail at the left of the field maximum. The radiated light can also be seen at the right of the figure.

¹⁸ M.L. Wu, P.L. Fan, J.M. Hsu and C.T. Lee, "Design of ideal structures for lossless bends in optical waveguides by conformal mapping", *J. Lightwave Technol.*, 1996, **14**, 11, pp. 2604-2614.

¹⁹ C. Seo and J.C. Chen, "Low transition losses in bent rib waveguides", *J. Lightwave Technol.*, 1996, **14**, 10, pp. 2255-2259.

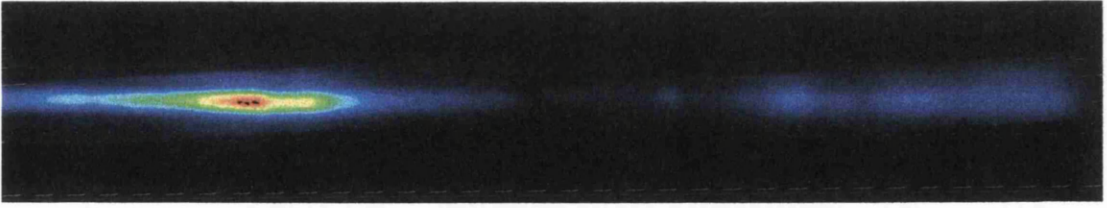


Figure 6.10: *Near-field image from the tilted facet of the bent waveguide device.*

The I-L curves and optical spectra of the bent waveguide laser were also measured. The threshold current for this type of lasers was found to be around 350 mA. Considering that the threshold current for a straight laser of the same length is around 10-15 mA, it is possible to be confident that the reflectivity of the tilted facet was very low.

Measuring the output power from both laser facets showed that the emitted power from the tilted facet was more than an order of magnitude bigger than the power emitted from the normal facet. Figure 6.11 shows the optical spectrum from the bent waveguide laser when the injected current was 50 mA CW. The output power from the tilted facet was close to 2 mW. From this figure, it can be seen that the spectral width (FWHM) was around 20 nm.

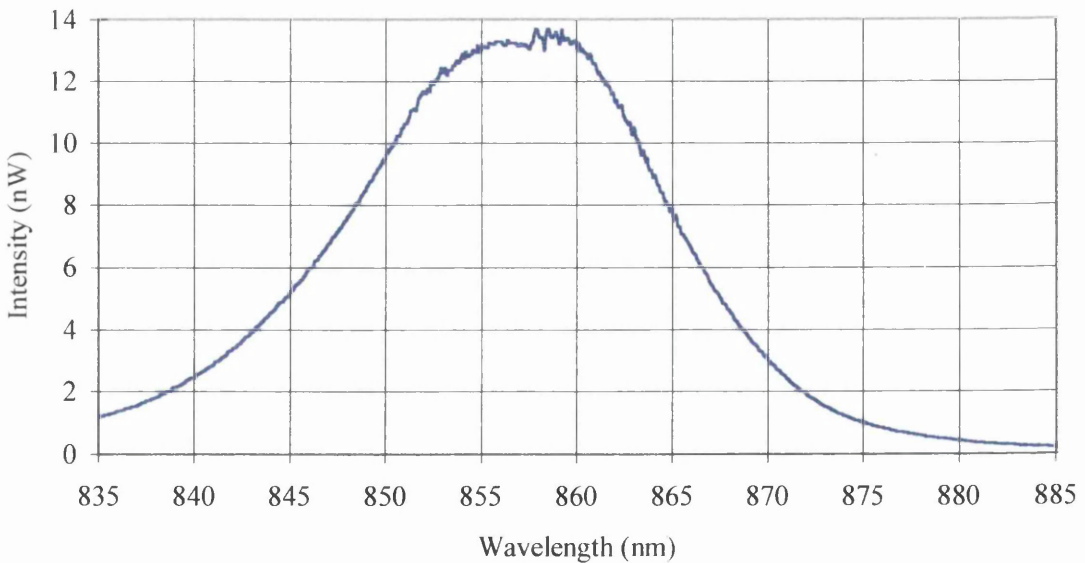


Figure 6.11: *Bent waveguide laser optical spectrum.*

6.4 Experimental results.

A single layer AR coating was not sufficient to prohibit laser oscillation when the AR coated semiconductor device was not coupled to the external cavity, therefore external cavity lasers experiments were only performed using bent waveguide devices.

6.4.1 XCL with a fibre grating.

Figure 6.12 shows the optical spectrum of a bent waveguide device, measured from the normal facet, (a) when it was operating as a solitary device and (b) when it was coupled to a fibre grating.

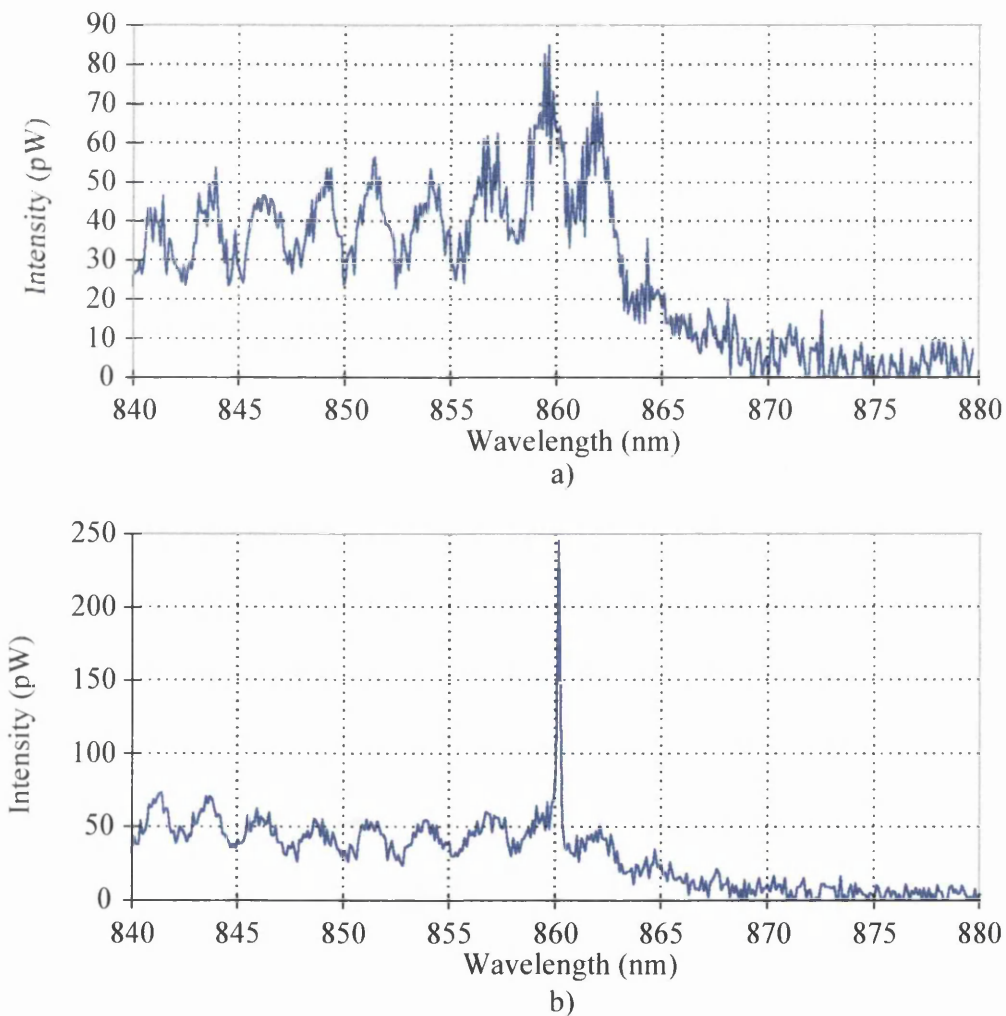


Figure 6.12: *Optical spectrum of a bent waveguide device: (a) solitary device and (b) coupled to a fibre grating.*

The fibre grating used to obtain Figure 6.12 was the same as that whose transmission spectrum was shown in section 6.2.1. The measurements were taken under pulsed excitation, with pulses 100 ns long, a duty cycle of 0.1% and a peak current of 150 mA. Without the fibre grating, the device did not lase, the output power was just due to spontaneous emission, and a modulation of the optical spectrum can be seen due to the residual reflectivity of the tilted facet. When the device was coupled to the fibre grating, lasing oscillation was achieved and a sharp peak centred at 859.8 nm and with a spectral width of 0.17 nm, equal to the fibre grating linewidth, can be seen.

The threshold current for the above XCL was found to be around 120 mA. This high value is most probably due to poor coupling between the fibre grating and the bent waveguide device. Passive modelocking was not achieved with the above XCL, probably because the fibre grating linewidth was too narrow and most of the longitudinal modes were filtered out.

6.4.2 XCL with an external mirror.

Figure 6.13 shows the experimental set-up used for the XCL with an external mirror. The semiconductor device was mounted on a moveable track which allowed the cavity length to be varied, and therefore the fundamental cavity mode could be tuned between 1 and 3 GHz. The output from the normal facet was coupled to a lensed single mode optical fibre.

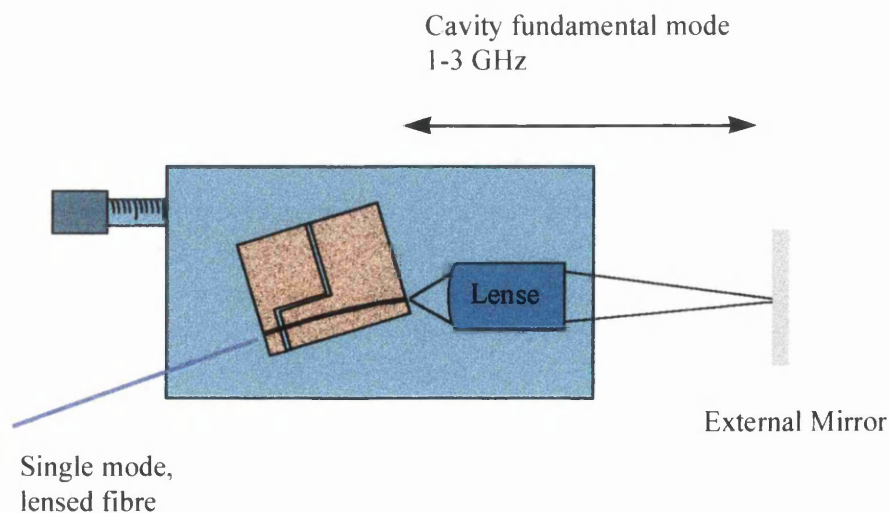


Figure 6.13: Frequency tunable, XCL mode-locked laser.

Figure 6.14 shows the optical spectrum of a bent waveguide device coupled to an external mirror when, (a) it was operating as a solitary device, and (b) it was coupled to a mirror. The external mirror had an HR broadband (700-1000 nm) dielectric coating. These measurements were taken under CW operation with an injected current of 50 mA. The XCL threshold current was found to be around 40 mA, lower than when using external fibre grating because the coupling between the semiconductor device and the external cavity was better than before. The spectral width in this case was wider than for that with the external grating, as a broadband reflector was used and many longitudinal modes were oscillating.

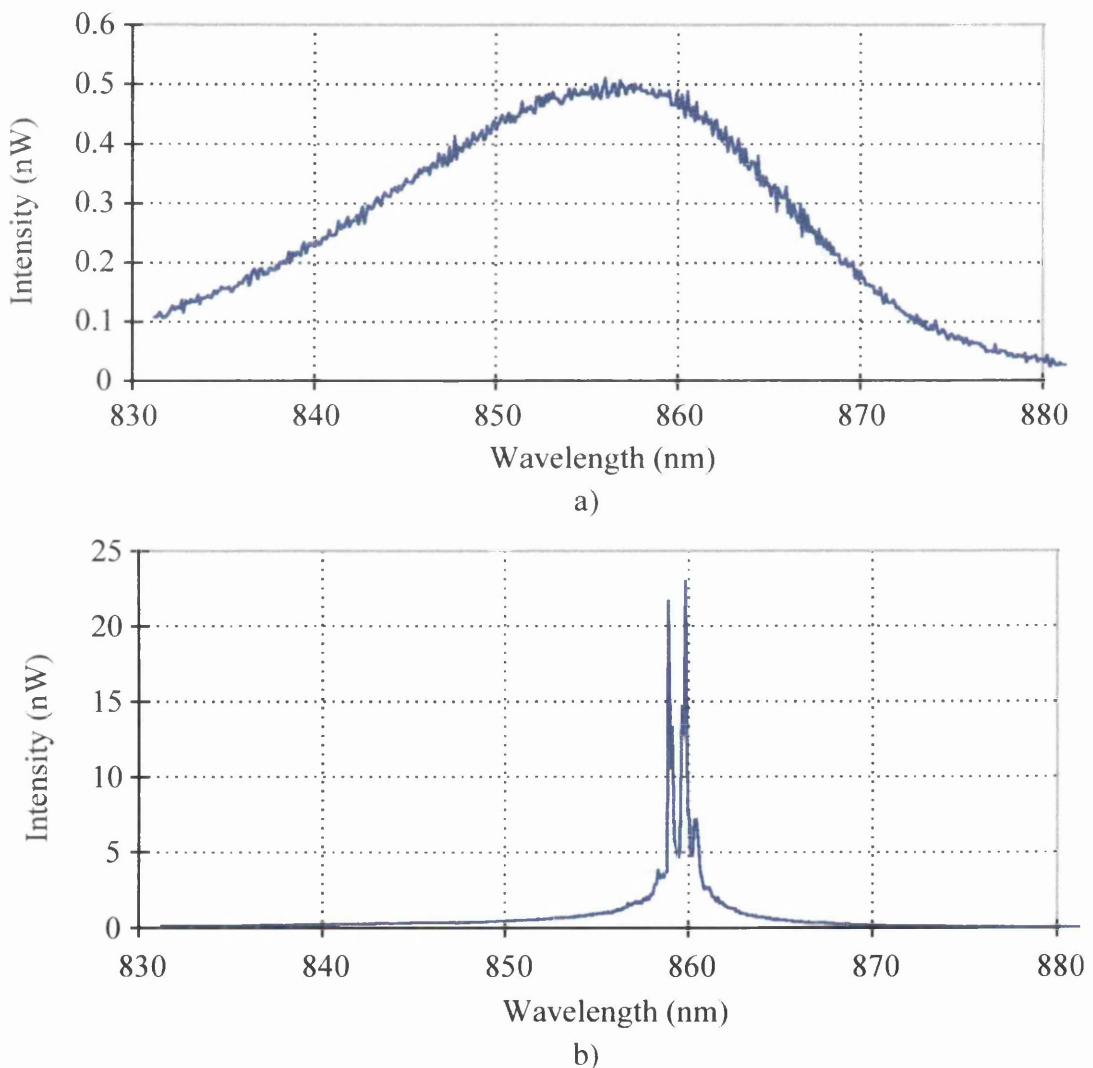


Figure 6.14: Optical spectrum of an bent waveguide device: (a) solitary device and (b) coupled to an external mirror.

The distance between the laser and the mirror was approximately 11.8 cm, which gave a fundamental cavity mode of around 1.25 GHz. The temporal response of the above XCL, operating under pulsed excitation, was analysed using the streak camera. Passive modelocking was achieved by injecting a current of 65 mA and by reverse biasing the saturable absorber section at -1.5 V. Figure 6.15 shows the streak image and profile of a passively mode-locked pulse train. The distance between the pulses was around 800 ps, which gave a modelocking frequency of 1.25 GHz. It can be seen that the pulse width was very wide, around 150 ps FWHM, probably due to modal reflections at the tilted facet.

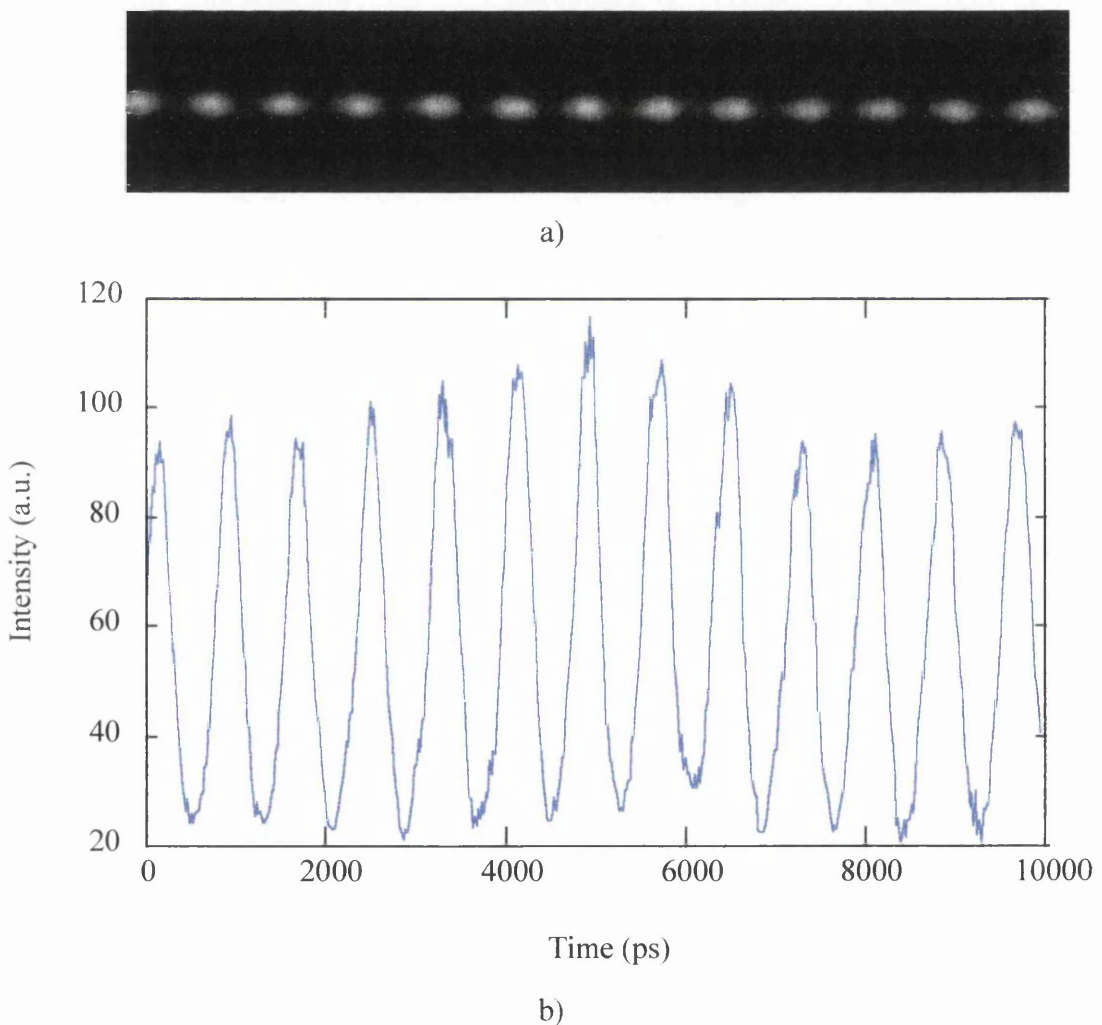


Figure 6.15: *Streak image (a) and profile (b) of a passively mode-locked XCL with an external mirror at the fundamental cavity mode.*

The same XCL was also analysed under hybrid modelocking operation. A microwave generator was connected to the saturable absorber section of the bent waveguide device and a signal of 13 dBm was applied. The hybrid modelocking operation was analysed at frequencies equal to the first, second and third harmonic of the fundamental cavity mode. Figure 6.16 shows the streak camera image and profile of the XCL operating at the second harmonic of the cavity length, i.e. 2.5 GHz. The reduction in the pulse width is noticeable when the microwave signal was applied to the XCL (below 50 ps FWHM).

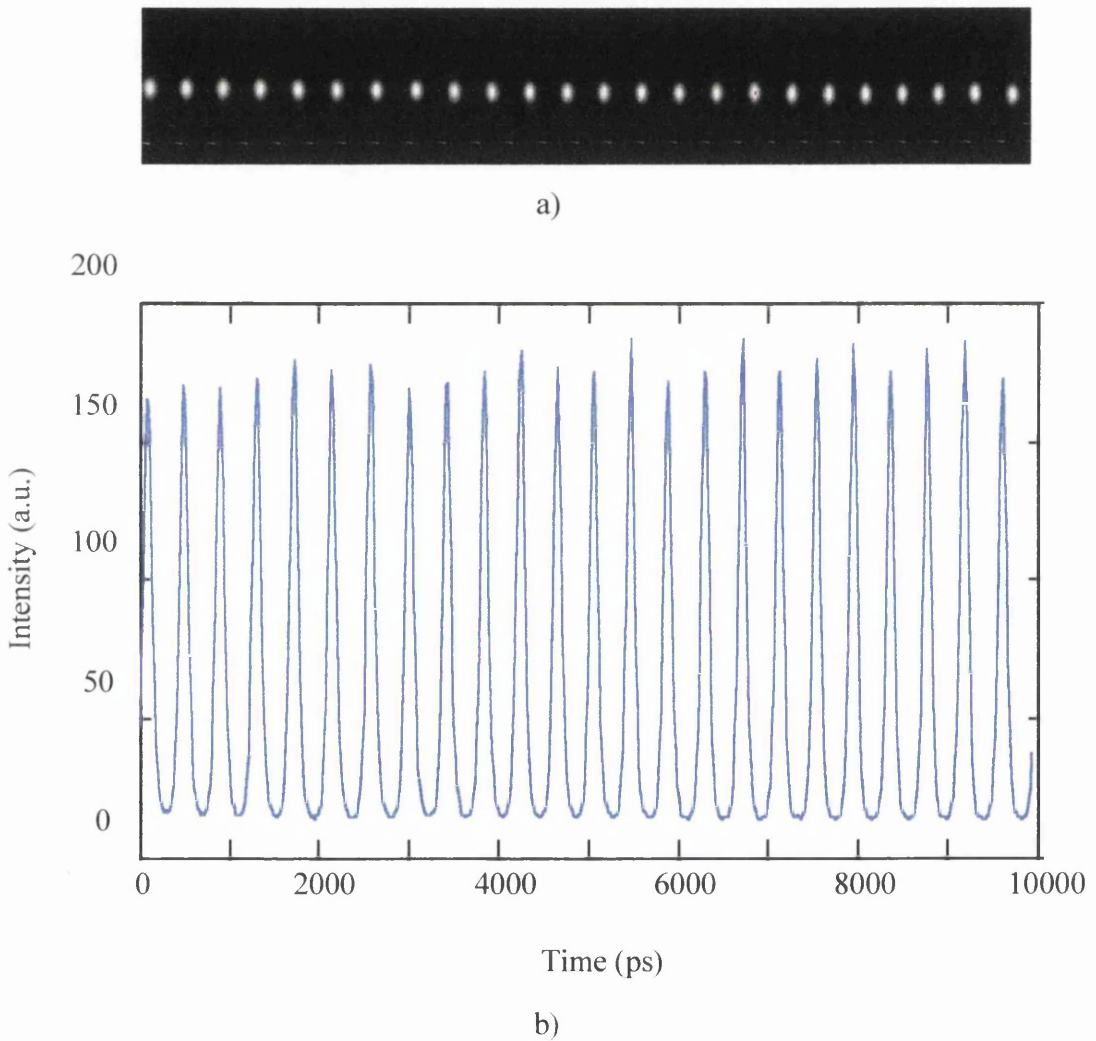


Figure 6.16: *Streak image (a) and profile (b) of a hybrid mode-locked XCL with an external mirror at the second cavity mode.*

To explain this behaviour a new concept of modelocking is introduced: when a laser is driven at some multiple N of its oscillating frequency *harmonic modelocking*²⁰ can be achieved. When a laser is harmonic mode-locked, sidebands, which are spaced by N longitudinal-mode intervals apart, couple together. This can lead to the production of up to N individual pulses circulating simultaneously around the laser cavity, separated by equal time intervals of T_{ML}/N , T_{ML} being the round-trip period.

Passively mode-locked lasers can also oscillate with several distinct pulses circulating within the cavity depending on the biasing conditions^{21,22}. In this situation the pulses do not have to be equally spaced, since each pulse can burn its way, more or less independently, through the saturable absorber.

The temporal response of the XCL was also analysed under different biasing conditions. As before, the fundamental modelocking frequency was around 1.25 GHz. Depending on the current injected and on the voltage applied to the saturable absorber, the laser mode-locked at the fundamental, second or third harmonic of the laser cavity. Figure 6.17 shows mode-locked pulse trains for three different biasing conditions. In Figure 6.17(a) the current peak was 75 mA and the saturable absorber voltage was -2.8 V. It can be seen that the pulses at the fundamental modelocking frequency developed a secondary pulse. When the saturable absorber bias was increased to -2.1 V, as seen in Figure 6.17(b), the pulse train was more regular at a modelocking frequency equal to 2.5 GHz, the second harmonic of the cavity length. When the injected current was increased to 85 mA and with a saturable absorber voltage of 0 V, Figure 6.17(c), the pulse separation was around 265 ps, which gave a modelocking frequency of 3.75 GHz, the third harmonic of the XCL modelocking frequency. It is believed that the observation of passive harmonic modelocking, instead of

²⁰ A.E. Siegman, "Lasers", *University Science Books*.

²¹ M. Kuznetsov, D.Z. Tsang, J.N. Walpole, Z.L. Liao and E.P. Ippen, "Multistable mode locking of InGaAsP semiconductor lasers", *Appl. Phys. Lett.*, 1987, **51**, 12, pp. 895-897.

²² S. Sanders, A. Yariv, J. Paslaski, J.E. Ungar and H.A. Zarem, "Passive modelocking of a two-section multiple quantum well laser at harmonics of the cavity round-trip frequency", *Appl. Phys. Lett.*, 1991, **58**, 7, pp. 681-683.

modelocking at the cavity fundamental frequency, was due to reflections at the tilted facet of the semiconductor device.

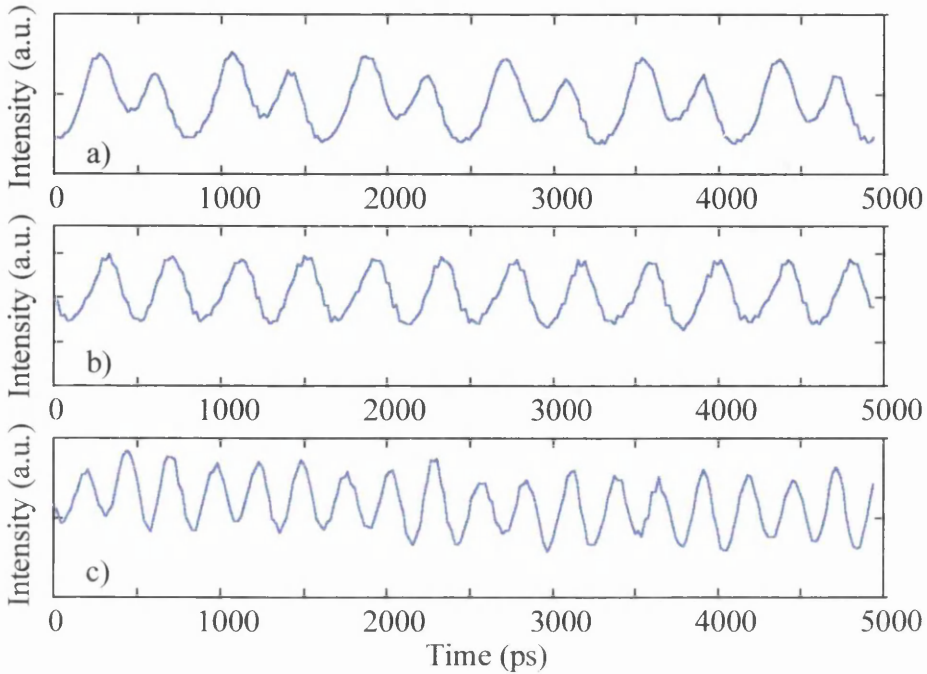


Figure 6.17: *Streak camera profiles of the output from an XCL with different modelocking frequencies.*

6.5 Conclusions.

It has been shown that the XCL configuration is a very versatile approach to short pulse generation, when frequencies from hundreds of MHz up to some GHz are required. For this range of frequencies, a monolithic device would have to be very long (> 1 cm), and would be difficult to fabricate.

The problems of mechanical instabilities can be solved by using a pigtailed fibre grating, but a further study of fibre grating with a wider reflection barrel and also of chirped Bragg gratings is required.

It is also possible to achieve harmonic modelocking in these devices, giving several circulating pulses in the external cavity, and this could have some advantages in applications such as clock-recovery, where clock-recovery elements *with memory* can

be achieved. In clock recovery applications, the mode-locked laser synchronises to an incoming digital data stream, containing 1's and 0's, that operates at the frequency of the mode-locked laser. However, it is possible to lose the locking between the data stream and the mode-locked laser when some consecutive 0's (missing pulses) are received. Using a harmonically mode-locked XCL it is more difficult to lose this synchronisation as the pulse period of the external data stream is *remembered* by the period between the several pulses that circulate inside the laser cavity.

Chapter Seven SYNCHRONISATION OF MODE-LOCKED SEMICONDUCTOR LASERS WITH EXTERNAL SIGNALS.

In this chapter two different issues are analysed, both of them being related to the synchronisation of a passively mode-locked laser to an external signal: the first is the reduction of the noise, i.e. the timing jitter, in a passively mode-locked laser and the second is the locking of a passively mode-locked laser with an optical signal in order to perform clock recovery.

Thus, this chapter describes the experimental results obtained by synchronising passively mode-locked laser configurations with external signals. Due to the poor mechanical stability of the XCL configuration, these experiments were only performed with the AAL and ECL configurations, but the results for the XCL should be very similar to those of the ECL.

7.1 Introduction.

Injecting an external signal into a more powerful free-running oscillator can produce interesting locking effects. When the frequency of the external signal is within a narrow range of the resonance frequency of the oscillator, the injected signal can then capture or *lock* the oscillator, so that it is more or less completely controlled by the injected signal.

The application of the external signal to a mode-locked laser may result in various types of dynamical behaviour, depending on the power of this external signal and the detuning between the resonance frequency of the mode-locked oscillator and the frequency of the external signal¹. Figure 7.1 shows the theoretical map of the possible

¹ E.A. Avrutin, J.M. Arnold and J.H. Marsh, "Analysis of dynamics of monolithic passively mode-locked laser diodes under external periodic excitation", *IEE Proc. Pt.J Optoelectronics*, 1996, **143**, pp. 81-88.

dynamical regimes, depending on the detuning range and amplitude of the external signal:

- When the detuning range is relatively small, the mode-locked laser emission is locked to the external signal. This tuning range depends on the amplitude of the external signal, and increases monotonically with it until it saturates. It is also noticeable that the locking range is found to be, both experimentally² and theoretically^{3,1}, asymmetric, with a wider locking range when the injected signal frequency is lower than the free-running frequency.

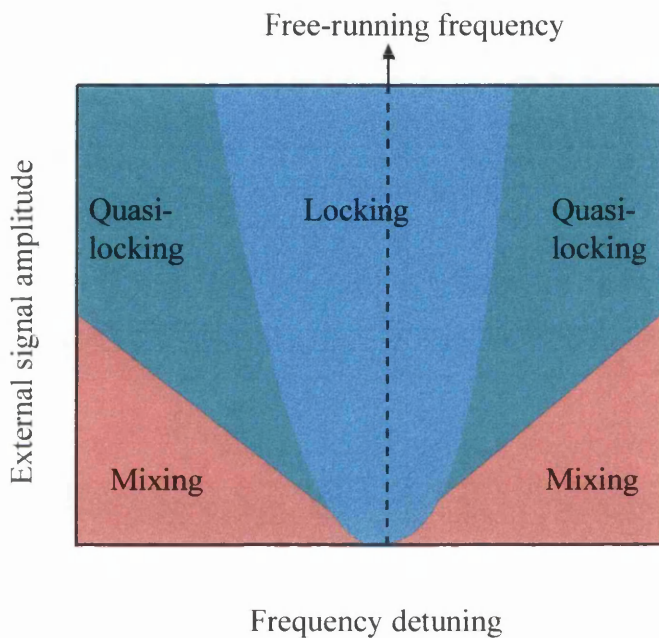


Figure 7.1: Schematic map of possible regimes of operation for an externally excited mode-locked laser.

- When the frequency of the injected signal is detuned by large amount from the free-running frequency, the mixing regime shown in Figure 7.1, the mode-locked laser operates at the free-running frequency and the amplitude of the pulse train is

² X. Wang, H. Yokoyama and T. Shimizu, "Synchronized harmonic frequency mode-locking with laser diodes through optical pulse train injection", *IEEE Photonics Technol. Lett.*, 1996, **8**, 5, pp. 617-619.

³ Z. Ahmed, H.F. Liu, Y. Ogawa, M.D. Pelusi and D.Y. Kim, "Locking characteristics of a passively mode-locked monolithic DBR laser stabilised by optical injection", *IEEE Photonics Technol. Lett.*, 1996, **8**, 1, pp. 37-39.

modulated due to parametric mixing between the signal frequency and the frequency of the free-running laser.

- Between these regimes there is an area of more complicated dynamics, the chaotic or quasi-chaotic locking areas shown in Figure 7.1.

In the experimental work reported in this chapter, the interest is centred only on the locking dynamics.

7.2 Noise reduction in passively mode-locked semiconductor lasers.

As was mentioned in previous chapters, a passively mode-locked semiconductor laser is a noisy optical pulse generator, with variations of the pulse to pulse timing of 10% or more of the average value. Obviously, to use these pulse generators in real applications, the jitter must be reduced, and the pulse generation stabilised. There are two immediate techniques that could be implemented; a) using a controllable electrical signal to modulate the laser at the round trip frequency, that is *hybrid modelocking techniques*, and b) using a controllable optical signal to synchronise the passive modelocking laser with it, that is *injection-locking modelocking techniques*.

a) *Electrical Locking*. When a passively mode-locked semiconductor laser is locked to an external RF electrical signal, the situation is called *hybrid modelocking* (hybrid between active and passive modelocking). Frequency locking occurs within a certain detuning range, known as locking-range, and can be maximised by increasing the RF power, with locking ranges up to 0.8% being reported experimentally⁴. Hybrid modelocking of the semiconductor laser reduces the timing jitter levels of the device from tens of picoseconds to sub-picosecond levels⁵. However, hybrid modelocking techniques at high frequencies

⁴ Z. Wang, J.M. Nielsen, S.D. Brorson, B. Christensen, T. Franck, N.G. Jensen, A.M. Larsen, J. Norregaard and E. Bodtker, "15.8 Gbit/s system transmission experiment using 5.2 mm long monolithic colliding-pulse-modelocked quantum well laser diode", *Electronics Lett.*, 1995, **31**, 4, pp. 272-274.

⁵ D.J. Derickson, P.A. Morton, J.E. Bowers and R.L. Thornton, "Comparison of timing jitter in external and monolithic cavity mode-locked semiconductor lasers", *Appl. Phys. Lett.*, 1991, **59**, 26, pp. 3372-3374.

are often limited by the electronic response speed of the laser and, in this case, the locking range is usually very small, as most of the RF power is rejected.

b) *Optical Locking*. The second way to stabilise a passively mode-locked laser is through *optical injection locking*. With optical injection, the problem of injecting a high frequency RF electrical signal is avoided. Again, depending on the power of the incoming pulse train, the locking-range can be maximised up to 0.2-0.5% of the round trip time^{1,3}. As will be shown later in this chapter, synchronisation of a passively mode-locked semiconductor laser to an external signal by optical injection locking could be used for clock extraction in communications systems

Neither of the previous solutions are suitable when the modelocking repetition frequency is very high, because a) it is very difficult to inject the electrical signal into the laser and b) it is difficult to obtain a very stable optical signal to synchronise the laser. The solution for this problem is to synchronise the passively mode-locked laser to an optical signal that is a subharmonic of the cavity round trip, or *subharmonic injection modelocking*^{6,2}. The idea is to use a very stable optical pulse train at low repetition rate from the *master laser*, stabilised through electrical injection, to stabilise a passively mode-locked pulse train at high repetition rate from the *slave laser*, where the low frequency of the master laser is a subharmonic of the modelocking frequency of the slave device, as shown in Figure 7.2.

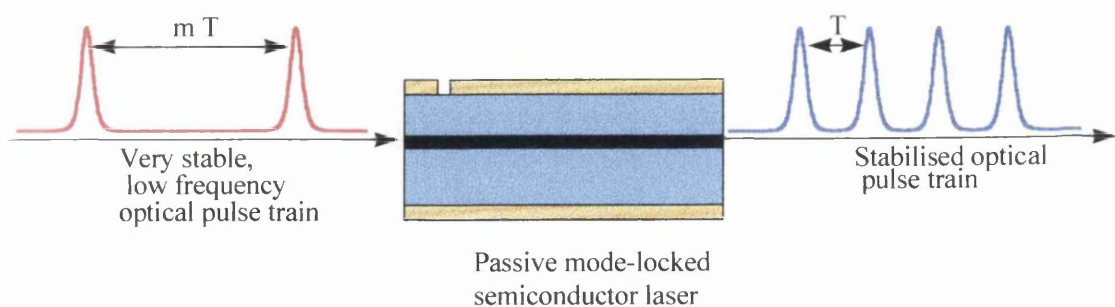


Figure 7.2: Schematic diagram of subharmonic locking.

⁶ S. Arahira and Y. Ogawa, "Synchronous mode-locking in passively mode-locked semiconductor laser diodes using optical short pulses repeated at subharmonics of the cavity round-trip frequency", *IEEE Photonics Technol. Lett.*, 1996, **8**, 2, pp. 191-193.

7.2.1 Hybrid modelocking experiments.

In this section the experimental results obtained when locking passively mode-locked lasers to an RF generator are presented.

a) All Active Cavity Lasers.

As mentioned in chapter 4, due to the high threshold current of the AAL and the difficulty of providing efficient heat sinking for the devices, it was not possible to drive the AAL configuration under continuous-wave (CW) operation. However, to electrically lock the device operating under pulsed excitation, synchronisation must be maintained between the injected current pulse and the RF electrical signal. There are two obvious ways to do so, either to lock the RF generator to the pulse generator or vice versa. The first way was impossible in our case, as the RF generator could not be externally synchronised, but it did provide a sinusoidal reference signal at 10 MHz. The signal generator could be externally synchronised, but the maximum repetition rate of the current pulses was 10 kHz. The solution was therefore to build a frequency divider, as shown in Figure 7.3. The reference sinusoidal signal from the RF generator was converted into a square wave by an Schmitt-trigger. This signal was then used as the clock for three cascaded decade counters and, therefore, the initial signal was divided by 1000, giving at the output a square wave at 10 kHz.

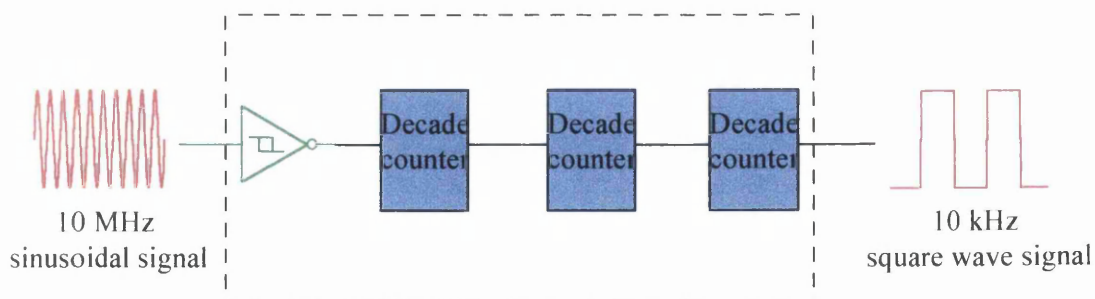


Figure 7.3: Schematic diagram of the frequency divider.

Figure 7.4 shows the schematic diagram of the set-up used for the AAL electrical locking experiment. As can be seen, the reference synchronisation signal from the RF generator was divided down to 10 kHz square wave signal to trigger the pulse generator, and the pulse generator trigger out signal was used to trigger the streak camera.

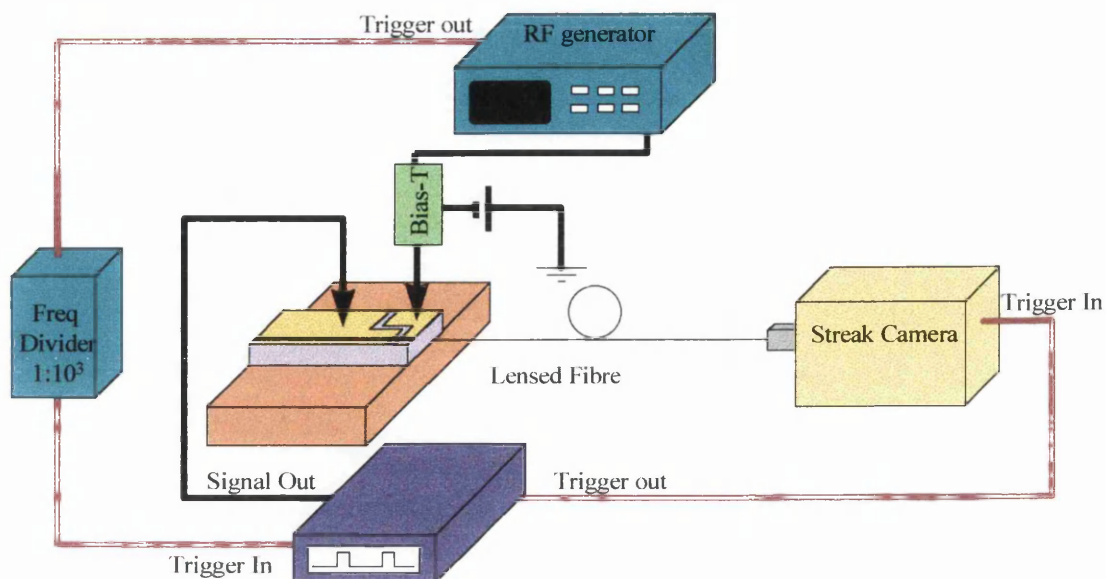


Figure 7.4: Schematic diagram of the experimental set-up for the electrical synchronisation of the AAL.

A 5 mm long AAL with a threshold current of 130 mA was used. The gain section was driven under pulsed excitation with 100 ns wide pulses, at a duty cycle of 1:1000 and a peak current of 200 mA. When a reverse voltage of 3.6 V was applied to the saturable absorber, the device passively mode-locked. The average pulse separation of a streak camera profile was around 129 ps, which gave an operating frequency of about 7.7 GHz. A 16 dBm RF signal at 7.7 GHz was then applied to the saturable absorber and the device hybridly mode-locked. No apparent reduction in the pulse widths was observed but, as has been mentioned the streak camera did not resolve the true pulse width of the mode-locked pulse train.

Due to the fact that the AAL was running under pulsed excitation, the measurement of the jitter reduction was carried out in the time domain, because the frequency domain technique described in chapter 5 required the laser to run CW. As in chapter 4, pulse to pulse timing measurements were taken in order to assess the jitter levels. Figure 7.5 shows the pulse to pulse distance measurements, over a 5 ns long streak profile, for the passively mode-locked and for the hybridly mode-locked situations.

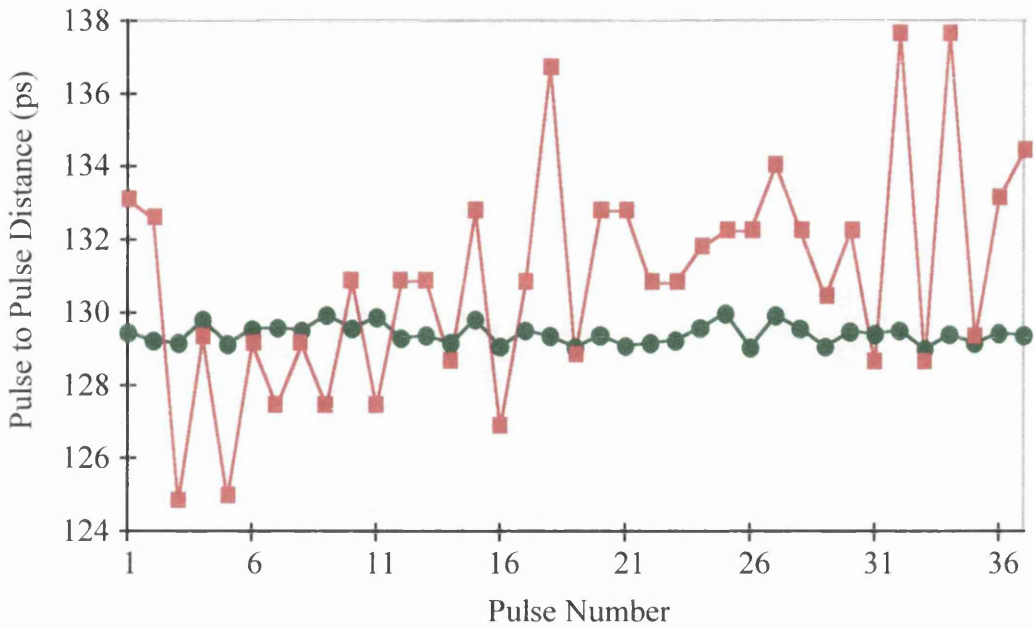


Figure 7.5: Comparison between the pulse to pulse variations of the passively (red squares) and the hybridly mode-locked pulse train (green dots).

From these measurements, the pulse to pulse timing standard deviation was found to be around 0.3 ps for the hybridly mode-locked pulse train, in comparison with the 3 ps of the passively mode-locked pulse train.

Due to the difficulty of measuring very narrow frequency variations, and the fact that the above method for determining the timing jitter is very poor as it does not account for jitter components with frequencies under 50 MHz (chapter 4), a measurement of the electrical locking range was not performed in this case.

b) Extended Cavity Lasers.

The synchronisation characteristics of the ECL configuration were measured under CW operation and, therefore, no synchronisation was required between the injected current and the RF signal. A 4 mm long ECL was used for the experiments carried out in this section. The gain section was driven with an injected current of 45 mA. When a reverse voltage of 0.5 V was applied to the saturable absorber, the device passively mode-locked at a frequency slightly over 9.32 GHz, as can be seen in Figure 7.6(a). An RF signal at 9.32 GHz of 16 dBm was then applied to the saturable absorber and the

device hybridly mode-locked, as seen in Figure 7.6(b). The stabilisation of the mode-locked pulse train can be clearly seen, as the sidebands observed in the case of passive modelocking virtually disappear in the case of hybrid modelocking.

In these cases, the reduction of the timing jitter was estimated by the frequency domain technique described in chapter 5. For the passively mode-locked case, shown in Figure 7.6(a), the timing jitter was estimated to be around 10 ps (1 kHz-10MHz), while for the hybridly mode-locked case, shown in Figure 7.6(b), the timing jitter was estimated to be less than 0.5 ps (1 kHz-10MHz), a factor of 20 times lower.

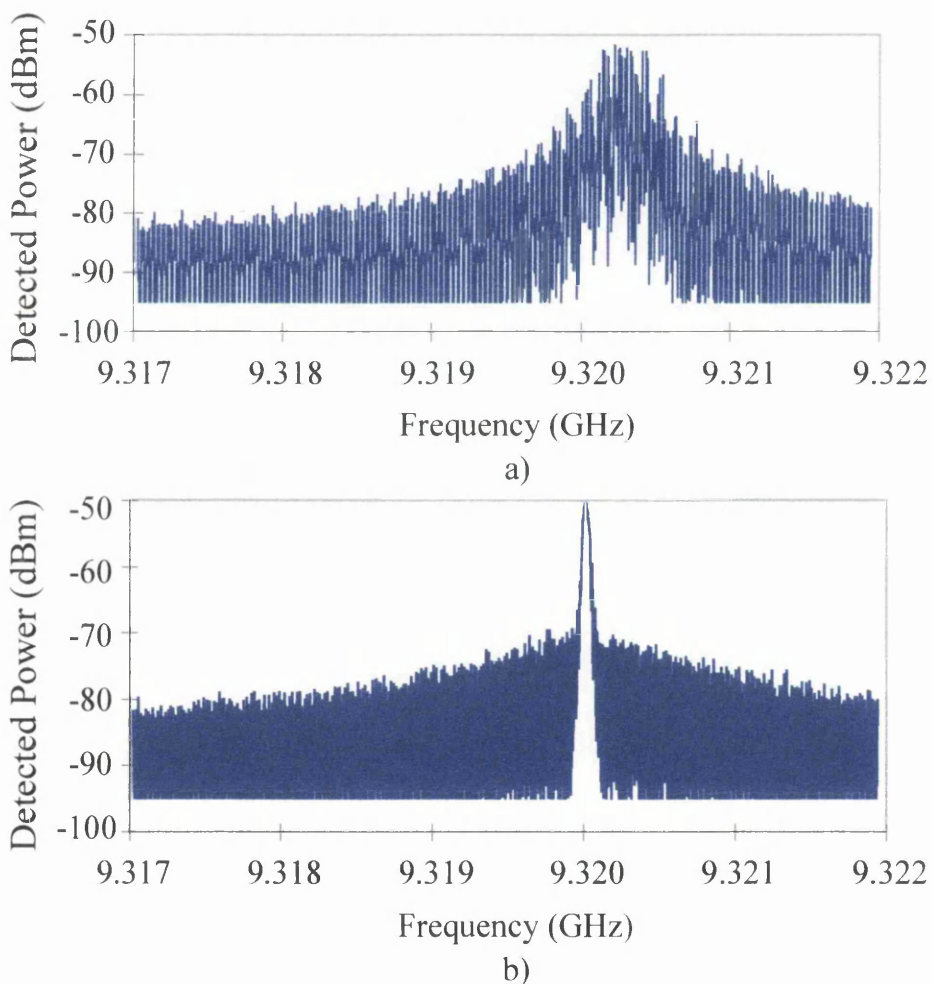


Figure 7.6: Comparison between RF spectra of the a) passively and b) hybridly mode-locked ECL.

To assess the locking characteristics of the ECL to the electrical signal, RF signals at different frequencies were injected into the ECL, as can be seen in Figure 7.7. In Figure 7.7(a) the frequency of the injected RF signal was 9.3214 GHz. As the driving frequency was greatly detuned from the cavity round-trip frequency, the ECL did not lock to the RF signal. Due to this, the RF spectrum shows two different peaks, at the driving frequency and at the modelocking frequency. In Figure 7.7(b) the driving frequency was 9.322 GHz. In this figure, just one peak appears but the device was not completely locked to the driving signal as can be deduced for the large sidebands around the main peak. In Figure 7.7(c) the driving frequency was 9.3225 GHz, and it can be seen that the ECL was perfectly locked to the driving signal. In Figure 7.7(d) the RF signal was 9.323 GHz. It can be seen that again two peaks appear in the spectrum, as the ECL no longer could lock to the detuned driving signal.

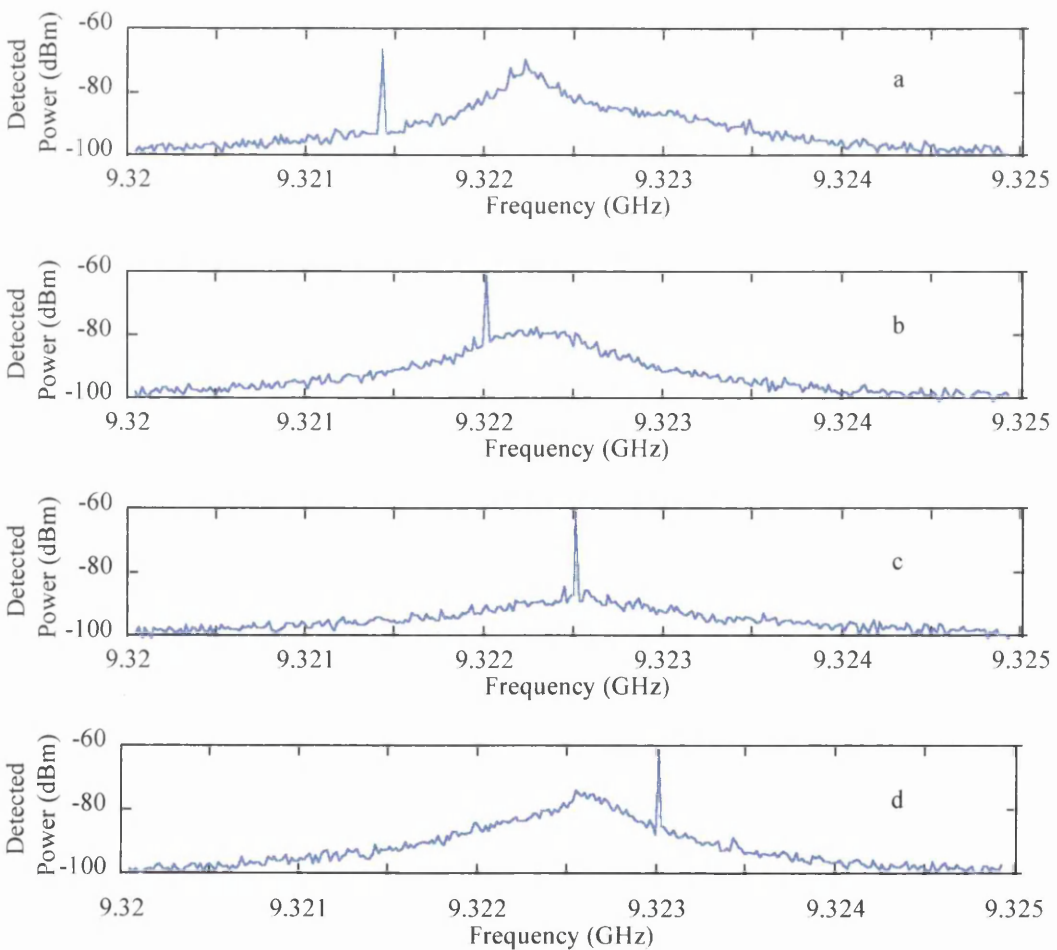


Figure 7.7: *RF spectra observed by varying the RF modulation frequency. The RF frequencies were: a) 9.3214, b) 9.322, c) 9.3225 and d) 9.323 GHz.*

To determine the locking range of the ECL, the single sideband phase noise of the RF spectra under different driving frequencies was measured. Figure 7.8 shows the single sideband noise for the cases shown in Figure 7.7. It is clearly seen that in only some cases did the single sideband noise stay below -80 dBc/Hz at 1 MHz offset. This is the way we define the locking range⁷, as the range over which the phase noise level stays below -80 dBc/Hz.

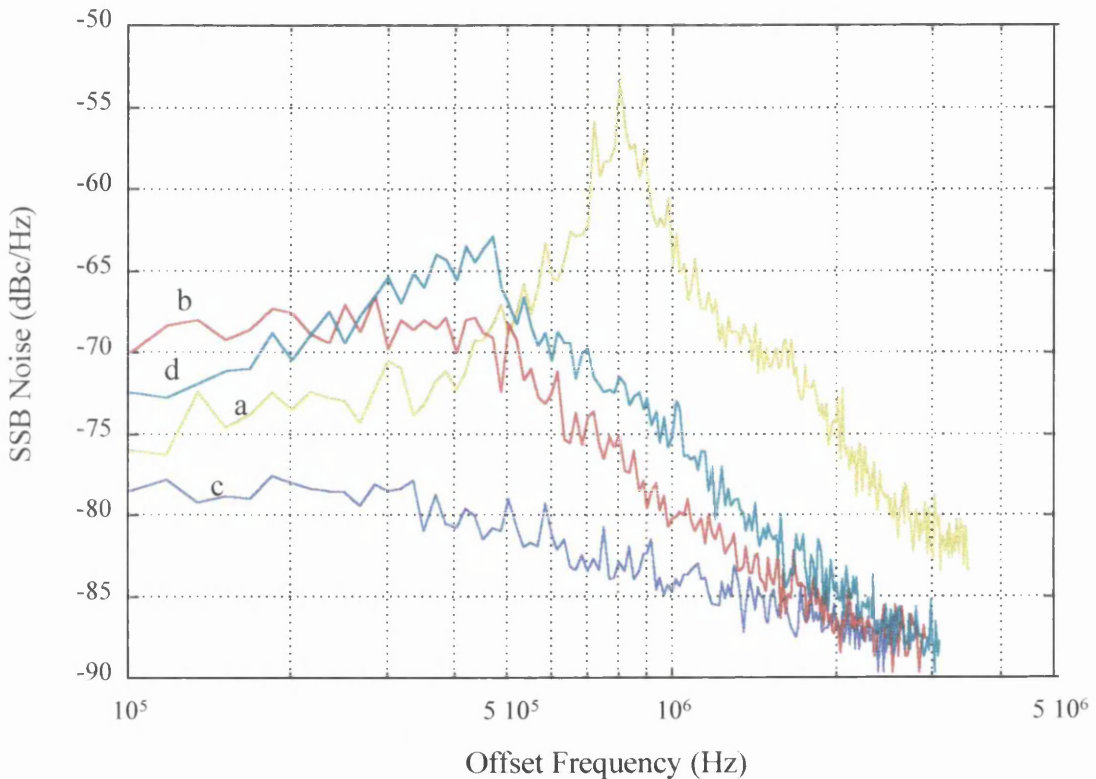


Figure 7.8: *Single sideband noise for the cases when the driving frequency was a) 9.3214, b) 9.322, c) 9.3225 and d) 9.323 GHz.*

Considering the zero detuning frequency to be the frequency where the phase noise, and therefore the timing jitter, is minimised, Figure 7.9 shows the tuning range for the ECL under electrical modulation. It can be seen that for the biasing conditions used this locking range is around 0.8 MHz, nearly 0.01% of the modelocking frequency. It

⁷ T. Hoshida, H.F. Liu, M Tsuchiya, Y. Ogawa and T. Kamiya, “Locking characteristics of a subharmonically hybrid mode-locked multisection semiconductor laser”, *IEEE Photonics Technol. Lett.*, 1996, **8**, 12, pp. 1600-1602.

is also noticeable, as mentioned in section 7.1, that the locking range was asymmetric, with a wider locking range when the driving signal frequency was below zero detuning.

This small locking range, compared with other reported locking ranges of nearly 1%⁴, arises due to two reasons. First of all, the locking range depends strongly on the RF injected power. In our case, it is believed that most of the RF injected power was rejected due to impedance mismatching between the semiconductor laser and the RF generator. Secondly, previously reported values used all-active cavity lasers, where the locking range is larger due to longer dispersive media. Introducing longer active cavities or dispersive elements such as distributed Bragg reflectors (DBRs) can significantly increase the locking range of a mode-locked laser^{8,9}.

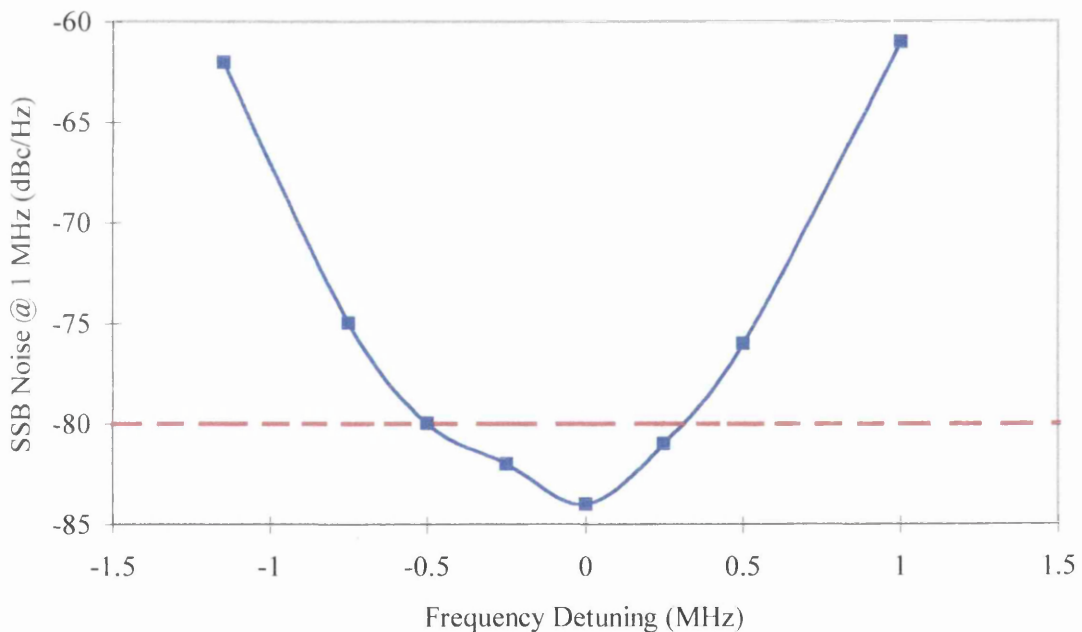


Figure 7.9: *Measured single side-band noise at 1 MHz offset as function of frequency detuning.*

⁸ M. Schell, D. Bimberg and T. Kamiya, “On the locking range of hybridly mode-locked semiconductor lasers”, *IEEE Photonics Technol. Lett.*, 1996, **8**, 8, pp. 1004-1006.

⁹ E.A. Avrutin, J.H. Marsh and E.L. Portnoi, “Mode-locked diode lasers for microwave optoelectronics applications”, to be published in *International J. High Speed Electronics & Systems*.

7.2.2 Subharmonic optical locking experiments.

For the subharmonic locking experiments, a stable frequency tunable optical pulse train generated from the *master laser* is needed, as shown in Figure 7.2. In our case a Q-switching semiconductor laser, similar to that used by E. Pornoi *et al*¹⁰, was used as the master laser. The Q-switching laser configuration is essentially the same as that of the AAL, but with a gain section 470 μm long, and a saturable absorber 20 μm long.

The threshold current of the Q-switching lasers used in our experiments varied between 15 and 20 mA. The operating frequency of the Q-switching laser could be tuned approximately between 1 and 3 GHz by varying the gain section current and the saturable absorber voltage. Figure 7.10 shows the dependence of the Q-switching frequency on the biasing conditions. It can be seen that the operating frequency increases with the injected current and decreases with the magnitude of the saturable absorber voltage.

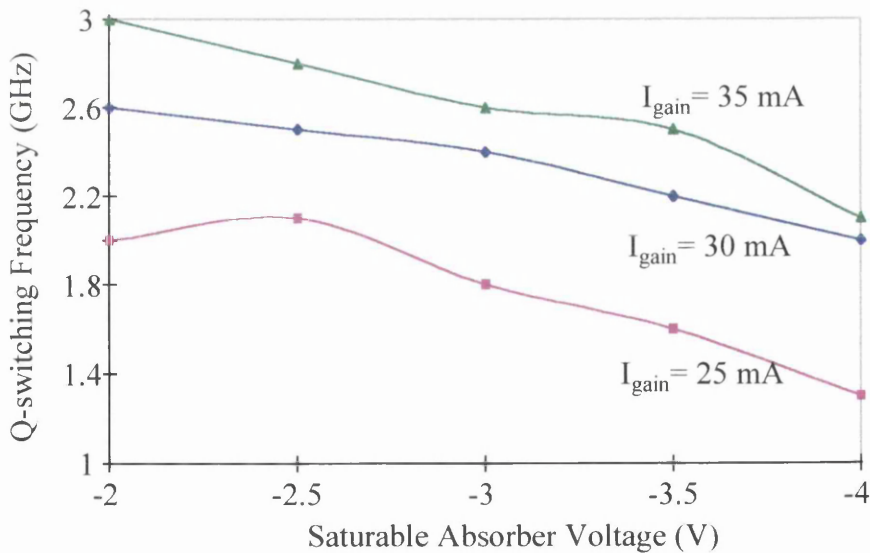


Figure 7.10: *Q-switching frequency variation with the saturable absorber voltage and gain section current.*

¹⁰ E.L. Portnoi, V.B Gorfinkel, D.A. Barrow, I.G. Thayne, E.A. Avrutin and J.H. Marsh, "Semiconductor lasers as integrated optoelectronic up/down-converters", *Electronics Lett.*, 1995, **31**, 4, pp. 289-290.

As mentioned above, a very stable pulse train is required to perform the subharmonic locking experiments, but a passive Q-switching pulse train is usually very noisy, much noisier than the mode-locked laser that we want to stabilise¹¹. Therefore, to produce a very stable optical pulse train, the Q-switching laser was locked to an RF generator, i.e. hybrid Q-switching. Figure 7.11 shows the RF spectra of the passive and hybrid Q-switching device. It can be seen that the sidebands in the case of passive Q-switching were very broad, but they are virtually completely suppressed when the device was hybrid Q-switching. Using the frequency domain technique described previously, the timing jitter of the hybridly Q-switched device was calculated to be 0.2 ps, less than 0.025% of the pulse period average.

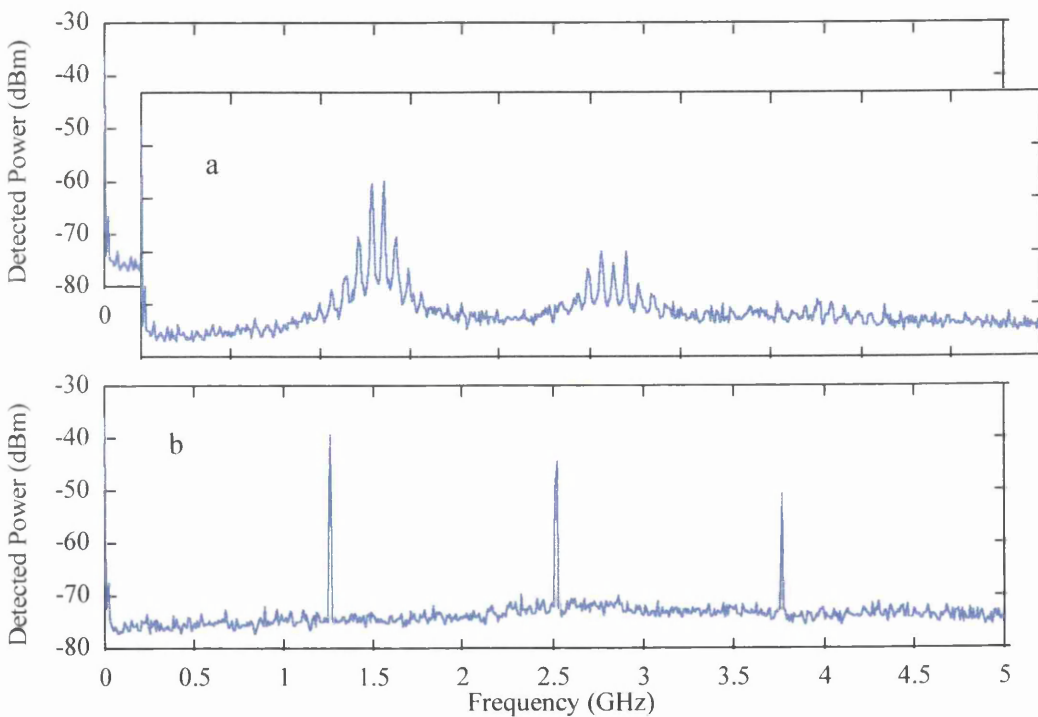


Figure 7.11: RF spectra of the a) passively Q-switched laser and b) hybridly Q-switched device.

For a fixed gain current and saturable absorber voltage, the Q-switching frequency could be tuned by around 10% of the free running value by applying a RF signal with a power of 13 dBm to the saturable absorber.

¹¹ D.J. Derickson, R.J. Helkey, A. Mar, J.R. Karin, J.G. Wasserbauer and J.E. Bowers, "Short pulse generation using multisegment mode-locked semiconductor lasers", *IEEE J. Quantum Electron.*, 1992, **28**, 10, pp. 2186-2202.

The average pulse width of the passive Q-switching semiconductor laser varied from around 100 to 150 ps, measured with the streak camera, depending on the biasing conditions. The application of an RF signal to the saturable absorber of the Q-switching laser also reduced the width of the emitted pulses. Figure 7.12 shows a 2 ns long streak camera profile of the Q-switching pulse train when the device was free running and when it was electrically locked to the RF generator. When the Q-switching laser was hybridly operated, the width of the pulses decreased from around 150 ps to 60 ps, and the peak power nearly doubled, up to around 50 mW. To inject the Q-switching pulses into the mode-locked laser, two lensed fibres were used with estimated coupling losses of 6 dB, which means that the injected power into the saturable absorber of the mode-locked laser was around 3 mW.

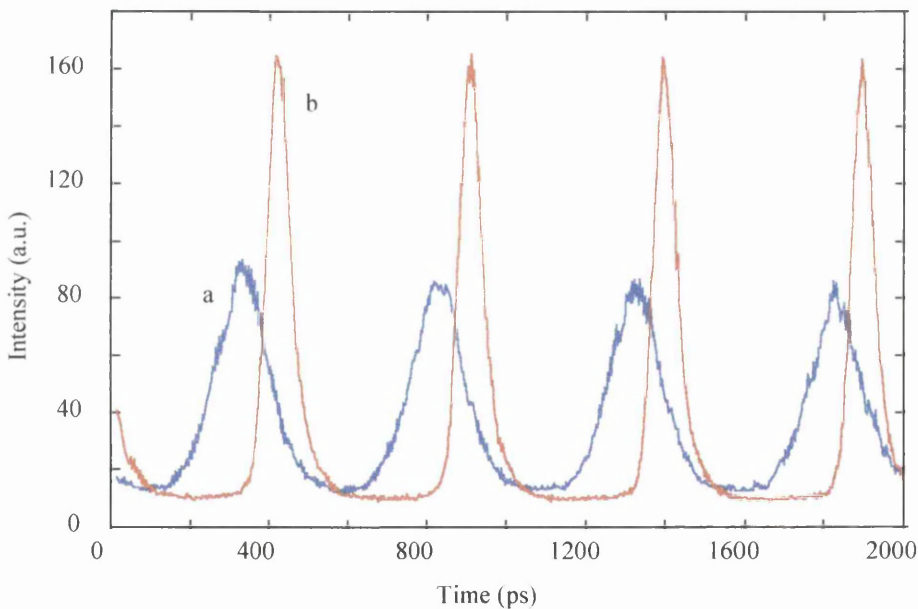


Figure 7.12: *Q-switching pulse train when a) the laser was free running and b) when it was locked to an RF generator.*

a) All Active Cavity Lasers.

As in the hybrid modelocking experiment with an AAL, this experiment was achieved under pulsed excitation. Again, synchronisation between all the signal generators was required, i.e. the RF generator, the Q-switching device pulsed current generator and the mode-locked laser pulsed current generator. As before, the frequency divider described in section 7.2.1 was used to trigger the current signal generator of the Q-switching device by dividing the reference signal from the RF generator.

Synchronisation between both lasers was also required, and therefore the current signal generator used for the mode-locked laser was triggered by the current signal generator used for the Q-switching laser. Figure 7.13 shows the experimental configuration used to perform the subharmonic locking experiment.

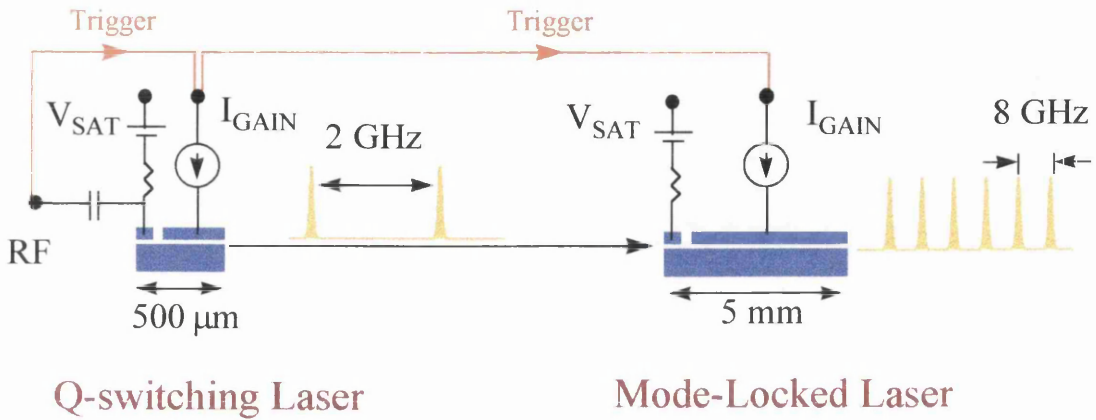


Figure 7.13: Subharmonic locking diagram.

Figure 7.14 shows a comparison between the pulse trains from the Q-switching laser and the mode-locked laser.

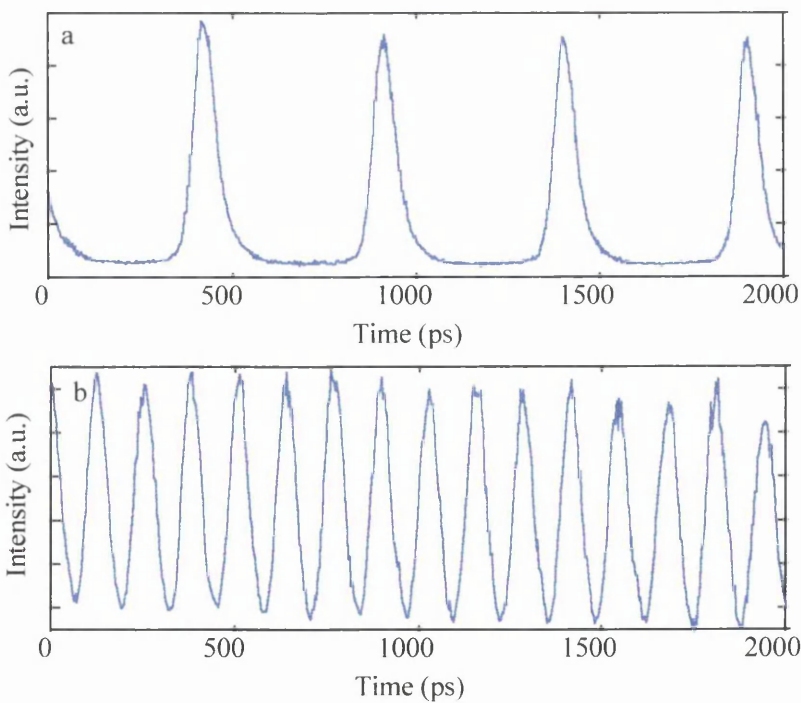


Figure 7.14: Comparison between a) the master pulse train from the Q-switching laser and b) the slave pulse train from the AAL.

As mentioned, the pulse width of the Q-switching pulses was 60 ps. The mode-locked pulse width, measured with the streak camera, was around 40 ps, but as was shown in chapter 4, the true pulse width was around 10 ps.

Successful synchronisation between the mode-locked and the Q-switching devices was achieved. With the Q-switching laser working at 1.95 GHz, from temporal measurements taken with the streak camera, it was observed that the modelocking frequency decreased by around 0.15% of the free-running value, i.e. by 12 MHz, to perfectly match the fourth harmonic frequency of the incoming optical signal.

Figure 7.15 shows 1 ns long streak profiles of the mode-locked pulse train when the laser was free running (Figure 7.15(a)) and when the laser was subharmonically locked (Figure 7.15(b)). It is seen that the mode-locked pulses were slightly broader when the mode-locked laser was locked to the Q-switching pulse train, an effect that was also observed by other workers². A slight modulation at the frequency of the Q-switching incoming signal, i.e. the fourth subharmonic of the modelocking one, can also be observed in this figure.

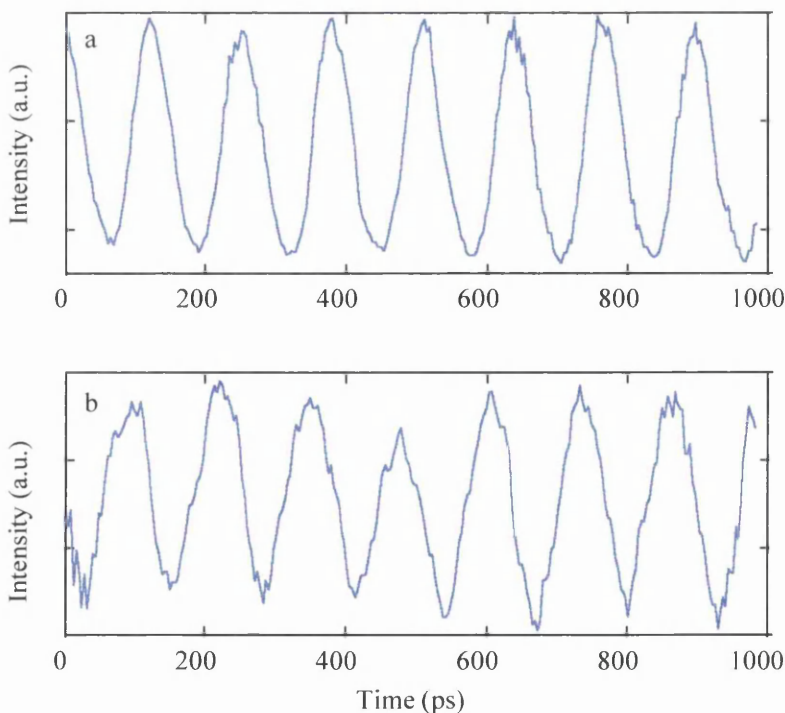


Figure 7.15: Comparison between a) the free-running AAL pulse train and b) the subharmonically locked AAL pulse train.

Figure 7.16 shows the optical spectra for a) when the mode-locked laser was free running and b) when the mode-locked laser was subharmonically locked. The first case shows a typical spectrum for the all-active cavity mode-locked laser, with a multi-peak structure due to self-phase modulation in the laser cavity. The optical spectrum for the second case does not show such a distinctive superstructure, and only the main emission peak is prominent.

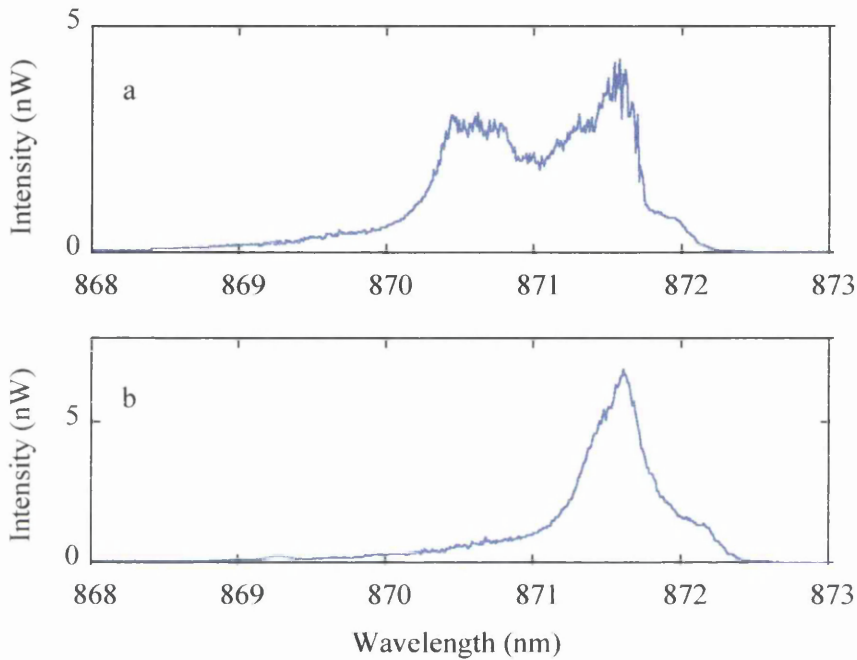


Figure 7.16: Comparison between a) the free-running and b) the subharmonically locked AAL mode-locked optical spectrum.

Taking into account this reduction in the spectral width, from 2 nm to less than 0.5 nm, and considering that the pulse width increased slightly, it is concluded that the time-bandwidth product for the mode-locked pulsed train decreased from around 7 to less than 2. This reduction in the time-bandwidth product means that the amount of chirp in the pulse train from the subharmonically locked laser was much less than the pulse chirp from the free-running mode-locked laser.

Pulse to pulse timing measurements were taken in order to assess the jitter levels of both the free running and the subharmonic locked mode-locked pulse trains, and also

to estimate the locking time for the mode-locked laser to synchronise with the Q-switched laser.

To quantify the locking time for the mode-locked laser, the pulse to pulse distance from this laser was measured from the moment when the Q-switching pulses started. Figure 7.17 shows that modelocking takes a few ns to build-up, while Q-switching starts virtually instantaneously. Therefore, to have a good estimation of the time that the mode-locked laser takes to lock to the external signal, modelocking must be allowed to build-up completely before the external signal is injected into the mode-locked laser. For this reason, a delay of around 4 ns between the injected current pulses of the Q-switching laser and the mode-locked laser was used.

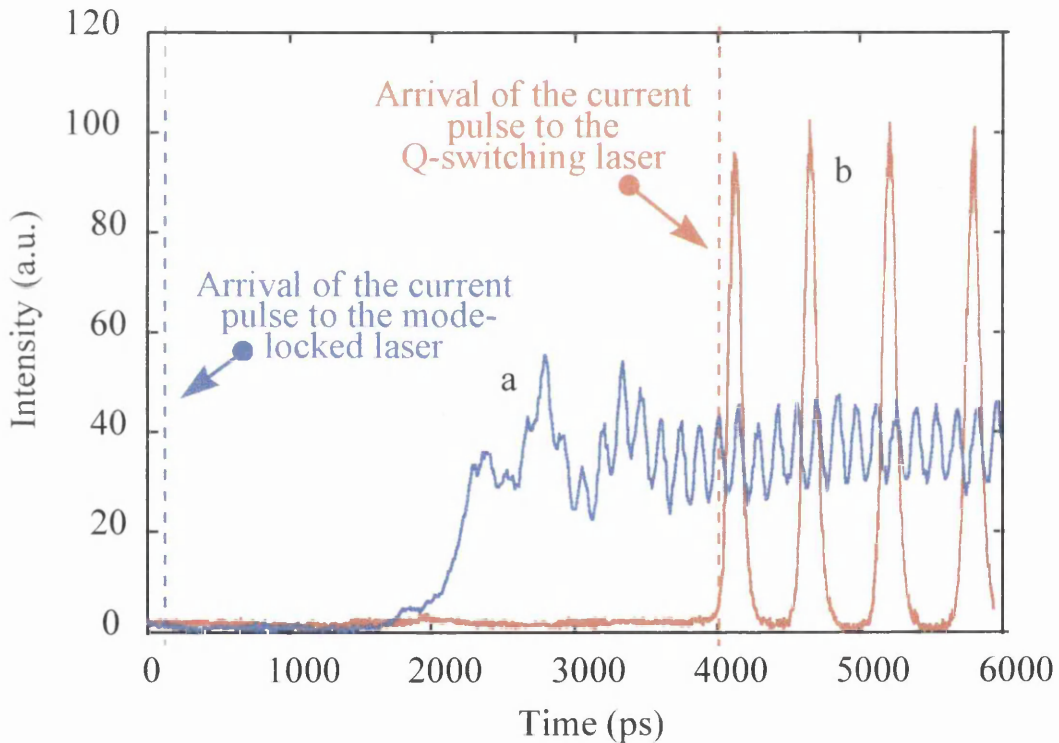


Figure 7.17: Comparison between the development times of Q-switching and modelocking.

Figure 7.18 shows the pulse to pulse distance measured when the mode-locked laser was free-running and when it was subharmonically locked to the external signal. The pulse to pulse distance, for the subharmonic locking case, was measured 1 ns after the QS pulses started, which is represented by the upper x-axis.

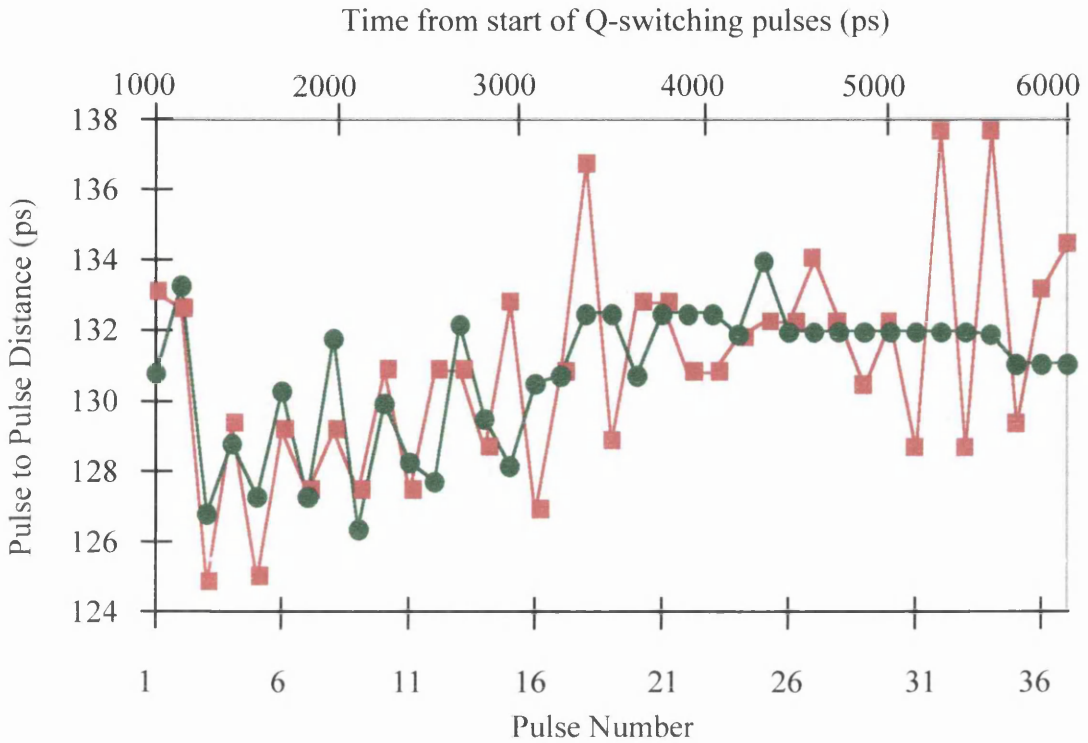


Figure 7.18: Comparison between the pulse to pulse variations of the free-running (red squares) and the subharmonically locked mode-locked pulse train (green dots).

The free-running train, the same which was analysed in section 7.2.1, had a standard deviation of around 3 ps. The pulse to pulse distance of the subharmonic locked train seems to become perfectly stabilised after 16 pulses. Taking into account that the external pulse train began around 1 ns before the first pulse in the picture, it means that the mode-locked laser took around 3 ns to lock onto the incoming pulse train.

For the subharmonic locked train, once the mode-locked laser is locked, the pulse to pulse timing standard deviation was found to be around 0.8 ps, in comparison with the 3 ps of the free-running pulse train.

As in section 7.2.1, the locking range of the AAL was not measured because the device was not operated CW, a requirement to perform noise analysis by the frequency domain technique (chapter 5). However, it has been mentioned that the mode-locked

pulse train can change its oscillating frequency by about 0.15% of the free-running value, so the locking range of the AAL was expected to be *at least* 0.15%.

b) Extended Cavity Lasers.

As in section 7.2.1, the subharmonic locking characteristics of the ECL were measured under CW operation, and the timing jitter reduction was estimated by the frequency domain technique.

In this case, the Q-switching laser was operating at around 1.55 GHz, the sixth subharmonic of the mode-locked laser.

The free-running frequency of the ECL under test was around 9.349 GHz, as can be seen in Figure 7.19(a). When an optical pulse train at 1.558 GHz, the sixth subharmonic of the modelocking frequency, was injected into the saturable absorber of the ECL, the device locked to the external signal. This can be seen in Figure 7.19(b) as a reduction in the modelocking frequency sidebands of the RF spectrum.

To determine the locking range of the ECL, the operating frequency of the Q-switching pulse train was varied, and the RF spectra of the mode-locked pulse train were inspected. In Figure 7.19(c) the operating frequency of the external signal was 1.5577 GHz, 300 kHz lower than before. As can be seen, ECLs locked to the external signal and changed its modelocking frequency in order to follow the variation in the Q-switching pulse train. When the Q-switching pulse frequency was decreased even further, the ECL could no longer follow the incoming signal, and the RF spectrum of the mode-locked pulse train was something similar to that shown in Figure 7.19(a), but with wider sidebands. In Figure 7.19(d) the operating frequency of the Q-switching laser was 1.5583 GHz, this time increased by 300 kHz. In this case the operating frequency of the ECL did not completely follow the variation of the external signal, as the modelocking frequency should have increased by 1.8 MHz, but actually increased by just 1.2 MHz. It is believed that the ECL could have been operating in some kind of quasi-chaotic dynamic regime as the power at the modelocking frequency decreased by more than 6 dB with respect to the other two subharmonic locking cases.

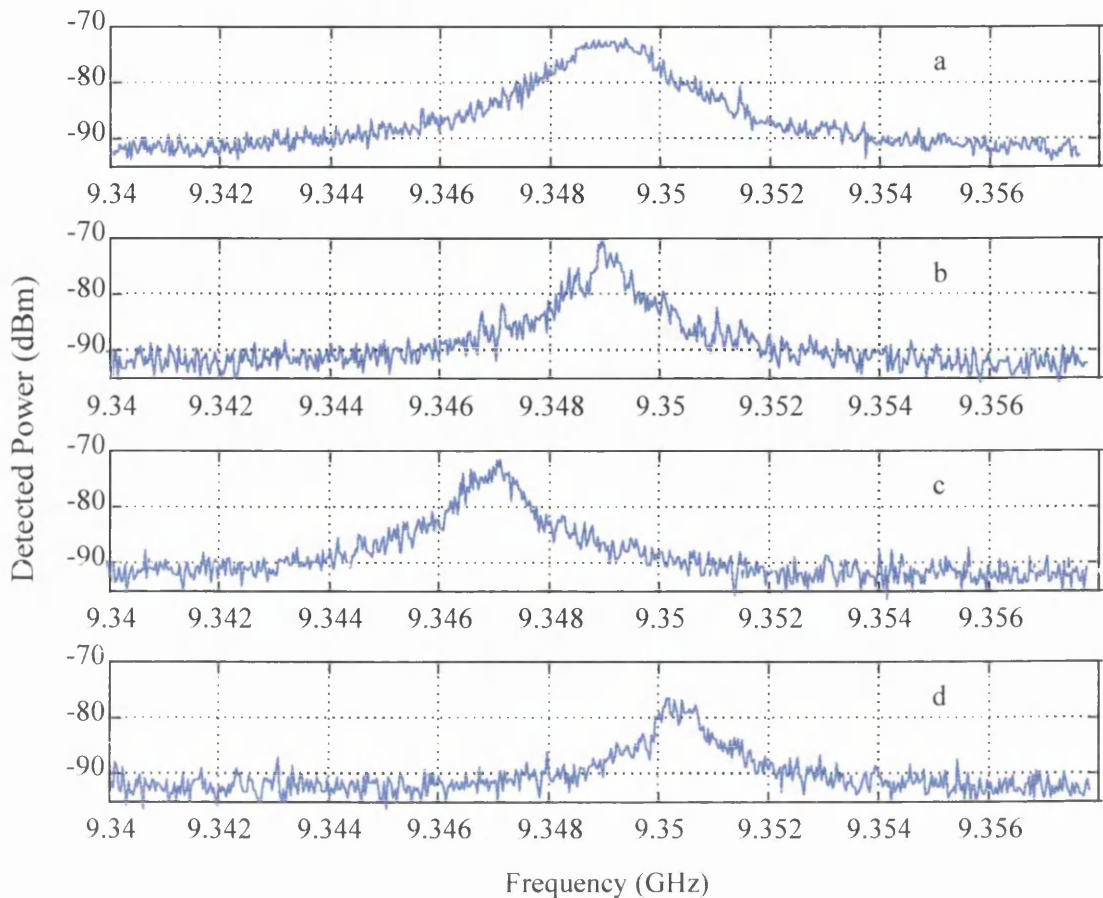


Figure 7.19: *ECL RF spectra for the cases when it was a) free-running, b) subharmonically locked to a 1.558 GHz signal, c) subharmonically locked to a 1.5577 GHz signal and d) subharmonically locked to a 1.5583 GHz signal.*

Again, to analyse the locking range of the ECL, the single sideband phase noise was measured under different driving frequencies of the external signal. Figure 7.20 shows the single sideband noise for the cases shown in Figure 7.19. It can be seen that, when the frequency of the external signal was exactly the sixth subharmonic of the free-running frequency of the ECL, the single sideband noise (Figure 7.20(b)) was greatly reduced in comparison with the free-running single sideband noise (Figure 7.20(a)). It can also be seen that there are some cases where the single sideband noise stayed below -80 dBc/Hz, which again is the way the locking range is defined.

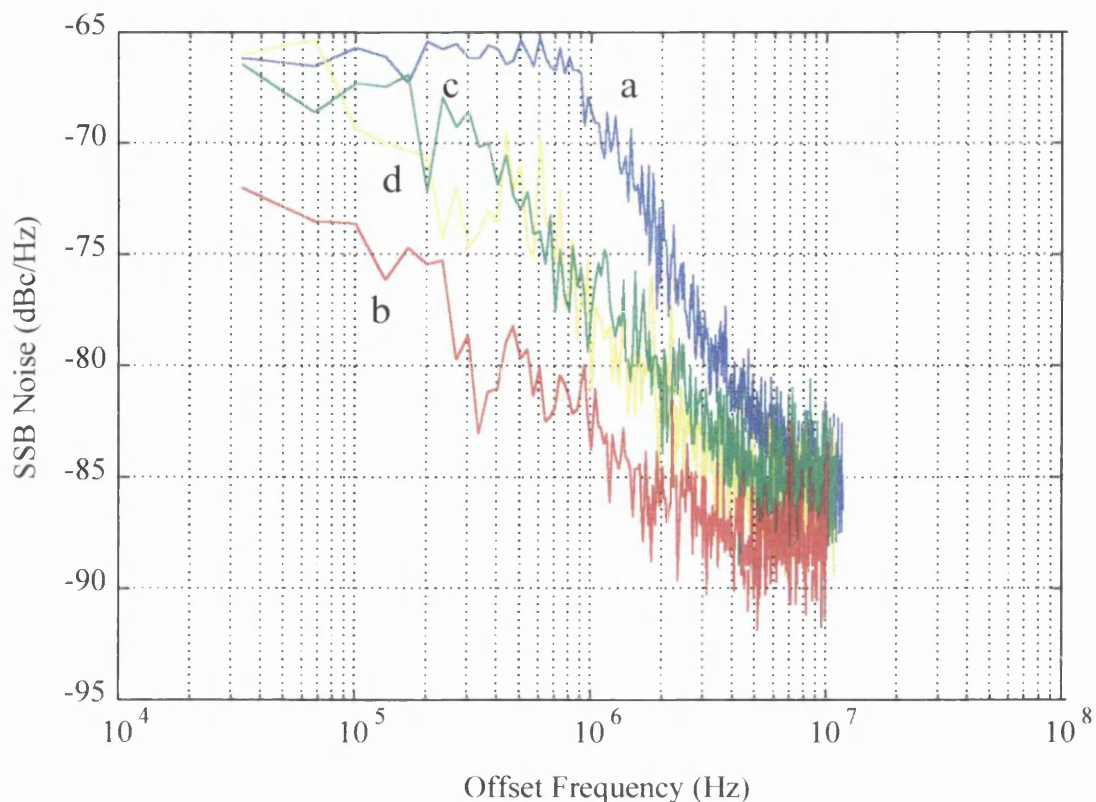


Figure 7.20: *Single sideband noise for the cases when a) no external signal was applied and when the Q-switching pulse train frequency was b) 1.558 GHz, c) 1.5577 GHz and d) 1.5583 GHz.*

Considering the zero detuning frequency to be the frequency that minimises the phase noise, Figure 7.21 shows the single side band noise at 1 MHz for the three measured cases. It can be seen that, under the conditions investigated, the locking range was narrower than 3.5 MHz, around 0.035% of the modelocking frequency.

As for electrical locking, the optical locking range for the ECL was much narrower than in previously reported cases, where locking ranges of more than 2.3% of the modelocking frequency have been measured^{2,6}. Again, it is believed that this is the consequence of the short active cavity in the ECL in comparison with these previously reported cases, where the whole cavity (~5 mm) was active.

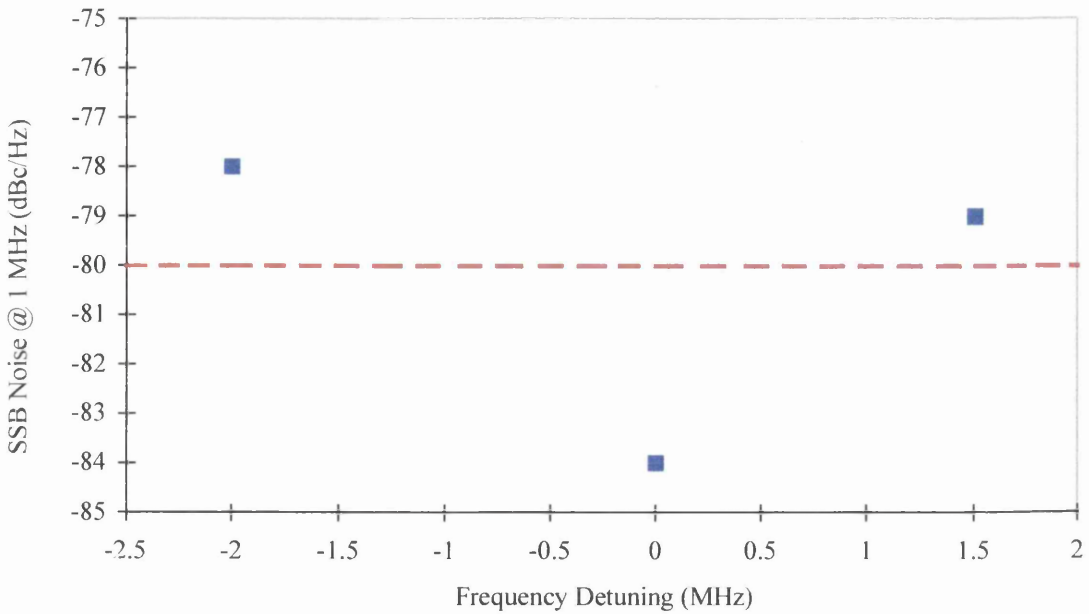


Figure 7.21: *Measured single side-band noise at 1 MHz offset as function of frequency detuning.*

7.3 All-optical clock recovery using semiconductor mode-locked lasers.

The basic idea of clock recovery was described in chapter 1. In this section, the possibility of using any of the semiconductor mode-locked laser configurations analysed throughout this work is studied.

The demonstration of subharmonic locking, provides strong proof that all-optical clock recovery using semiconductor mode-locked lasers is perfectly possible. As our devices locked to an external optical pulse train operating at the fourth or sixth subharmonic, it means that they could also locked to an amplitude modulated digital signal with up to 3 or 5 consecutive zeros.

Even though our experimental results showed successful locking to the fourth and sixth subharmonic of the modelocking frequency of a mode-locked laser, it is believed, and has also been demonstrated by other workers², that locking at much lower subharmonics is perfectly possible, which would correspond to a much larger number of consecutive zeros in the digital signal before the locking is lost. In any case, a

transmission code that only allows a maximum number of consecutive zeros is perfectly realizable¹².

One of the main problems in all-optical clock recovery is that of variations of the free-running frequency of the clock recovery element due to temperature fluctuations. A semiconductor laser used as a clock recovery element should be able to lock to the transmission data frequency, without frequency fluctuations which would cause transmission errors. For this the reason a wide locking range of the mode-locked laser is required.

The properties as clock recovery elements of the different semiconductor mode-locked laser configurations are as follows:

- a) *All active cavity mode-locked laser.* The locking subharmonic range of this kind of devices was not studied, but it was demonstrated that the modelocking frequency can vary by at least 0.15% of the free-running value. Obviously, the possibility of having a locking range wider than 0.15% makes this configuration especially desirable for the all-optical clock recovery even if, as it was mentioned in chapter 4, it is not the best configuration for generating short optical pulses.
- b) *Extended cavity mode-locked laser.* Having a very narrow locking range makes this configuration less effective as a clock recovery element. A significant increase in the locking range of this configuration could be achieved by introducing a distributed Bragg reflector (DBR)⁸, which would make this configuration ideal as a clock recovery element.
- c) *External cavity mode-locked laser.* Even though optical locking was not demonstrated with this configuration, it is believed that its locking range is similar to that of the ECL configuration. This configuration would be useful for clock recovery at low frequencies. It also has the possibility of harmonic modelocking, where several pulses are in the laser cavity at the same time. This could allow the mode-locked device to have ‘memory’, as even when the external data signal is a zero (missing pulse) the pulse period of the external data stream is ‘remembered’ by the period between the other pulses inside of the laser cavity.

¹² F.G. Stremmler, “Introduction to communication systems”, Addison Wesley, 1990.

7.4 Numerical simulations.

The numerical model analysed in chapter 4 was also used to study the performance of the AAL and ECL mode-locked configurations under external excitation. In the simulations, the locking range for the AAL was 0.6% of the free-running modelocking frequency, and 0.1% of the modelocking frequency for the ECL configuration. Even though the absolute values of the locking range are not similar (probably because the locking range depends on the power of the injected signal, which was not maximised in our experiments), the ratio between the AAL and ECL locking ranges agree reasonably well, being 6 in the simulation results and around 5 in the experimental results.

Figure 7.22 shows the simulated temporal behaviour of an all active cavity laser in colliding pulse modelocking configuration, i.e. the saturable absorber in the middle of the cavity, under subharmonic locking. The laser, operating at 20 GHz, was locked to an optical pulse train at 5 GHz, the fourth subharmonic of the modelocking laser frequency. As in the experimental result, the amplitude of the mode-locked pulses were slightly modulated at the frequency of the external signal, i.e. 5 GHz.

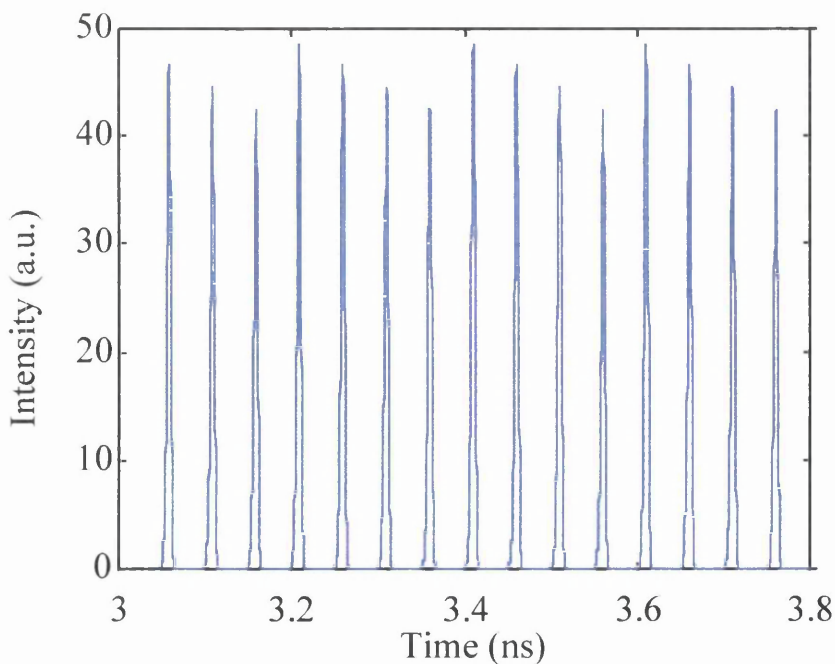


Figure 7.22: *Calculated temporal profile of a AAL operating at 20 GHz locked to a 5 GHz optical pulse train.*

7.5 Conclusions.

The fact that the locking range for the ECL was around three times wider under subharmonic locking than under electrical injection confirms that it is much easier to inject high frequency signals optically than electrically and that a subharmonic locking techniques is the only solution to stabilise a mode-locked laser when much higher frequencies (> 10 GHz) are in use.

Even though the locking range of the AAL configuration was not measured, due to the difficulties commented on above, it was found that its modelocking frequency can be changed by larger margins than that of the ECL, a change of 0.15% of the free-running frequency being measured in the AAL while the maximum locking range for the ECL was narrower than 0.035% of the free-running modelocking frequency. This is due to the longer active cavity in the AAL than in the ECL (ten times longer). For this the reason, the AAL might be considered a good solution for use as a clock recovery element, but we must bear in mind that the high current required for this device configuration rule it out in many applications.

Clock recovery using a semiconductor mode-locked laser was not demonstrated in this work, but it was proven, through the subharmonic optical locking, that it is a possible solution for future all-optical networks.

In this thesis a wide range of semiconductor mode-locked laser configurations has been reported, all of which are specifically designed to generate short optical pulses at frequencies lower than 20 GHz. The diversity in the advantages and drawbacks of these configurations offer a broad scope of possible operational fields, such as telecommunications systems or optoelectronic integrated circuit (OEIC) applications. The measured modelocking parameters of our AAL (chapter 4) and ECL (chapter 5) are summarised in Table 8.1, along with the best previously reported values.

	AAL ¹	XCL ¹	ECL ²	Our AAL	Our ECL
Active section (mm)	6.1	0.5	0.65	5	0.5
ML Frequency (GHz)	5.5	5	8.6	7.6	9.3
Threshold current (mA)	116	13	50	105	18
Pulse FWHM (ps)	10	2.5	5.5	10	3.5
Time-bandwidth product	4	1.8	7	7	2.5
Pulse peak power (mW)	200	25		10	15
Timing jitter (ps)	12.5	12.2		22	9
	(150 kHz-50 MHz)	(1.5 kHz-50 MHz)		(1 kHz-10 MHz)	(1 kHz-10 MHz)
Wavelength (μm)	0.85	0.85	1.55	0.86	0.86

Table 8.1: Comparison between previously reported mode-locking parameters and the ones reported in this thesis.

¹ D.J. Derickson, R.J. Helkey, A. Mar, J.R. Karin, J.G. Wasserbauer and J.E. Bowers, "Short pulse generation using multisegment mode-locked semiconductor lasers", *IEEE J. Quantum Electron.*, 1992, **28**, 10, pp. 2186-2202.

² P.B. Hansen, G. Raybon, U. Koren, P.P. Iannone, B.I. Miller, G.M. Young, M.A. Newkirk and C.A. Burrus, "InGaAsP monolithic extended-cavity lasers with integrated saturable absorbers for active, passive and hybrid mode locking at 8.6 GHz", *Appl. Phys. Lett.*, 1993, **62**, 13, pp. 1445-1447.

It can be seen that the performance of our IFVD ECL is better than that of previously reported monolithically integrated Fabry-Perot constructions. Only external cavity constructions have shown better modelocking parameters, however external cavity constructions have major disadvantages, such as mechanical instabilities and difficulties in eliminating secondary pulses.

The AAL configuration is not of much use if it cannot be operated CW. Some attempts were made with AALs under CW operation but, due to the high injected current (around 200 mA), the heat generated in the ridge waveguide was too high, with the result that the lasers did not last for more than 5 minutes. One way to provide efficient heat sinking is to bond the devices p-side down with the ridge waveguide in direct contact with the heatsink holder (when the device is p-side up the heat must propagate through 200 μm of substrate). However, when a two-contact device is used this technique is not feasible because the standard heatsink holders are made of copper and both laser sections would be short circuited. A new technique for thermal management of optoelectronics components is being studied in the department, using chemical vapour deposited (CVD) diamond. Diamond has a thermal conductivity 5 times larger than that of the copper, but it is electrically insulating. Thus, diamond deposited on top of a heatsink holder will allow us to bond our devices p-side down and, therefore, minimise our thermal problems.

The mechanical instabilities of the XCL configuration make it a unusable mode-locked device, apart for laboratory research. One way to solve this problem is to use pigtailed grating fibres, which would eliminate the mechanical instabilities. There is ongoing research in the department to investigate micromachined silicon holders with CVD diamond for mounting lasers and optical fibres. This type of holders will provide an easy solution for laser/fibre alignment and heat management.

The ECL configuration is a very good short optical pulse generator, but suffers for a very poor locking range. A way to increase the locking range of the ECL would be the introduction of a unchirped or chirped (when a very wide locking range is required) grating reflector or distributed Bragg reflector (DBR). The schematic diagram of such configuration is shown in Figure 8.1.

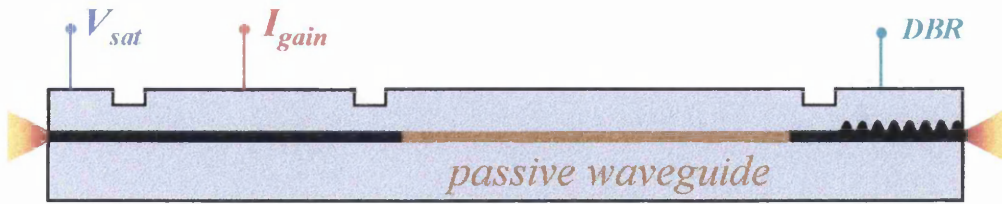


Figure 8.1: Schematic diagram of the proposed extended cavity DBR semiconductor mode-locked laser.

The mode-locked pulse train from such a configuration would be somehow more noisy and, therefore, with higher jitter levels than the ECL configuration, but it would offer a wide locking range and also the advantage of a very stable operating wavelength.

A different way to increase the locking range of the ECL configuration would be using electronic feedback. As analysed in chapter 5, the modelocking frequency of the ECL can vary around 1% of the free-running value depending on the biasing conditions (gain section current and saturable absorber voltage). Figure 8.2 shows the proposed circuit to provide electronic feedback to the ECL in a clock recovery circuitry. The frequency detector would give a signal proportional to the difference between the frequencies of the data signal and the optical clock. If this difference were too high for the ECL to remain locked to the external signal, the logic circuit would alter the ECL biasing conditions to bring the modelocking frequency in close range with the data signal frequency.

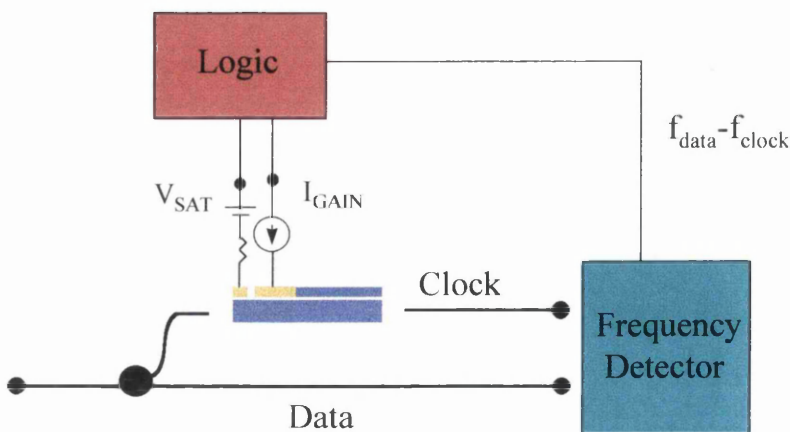


Figure 8.2: Schematic of an ECL with electronic feedback to increase the locking range.

We would like to highlight the importance of the integration process, the IFVD technique described in chapter 5, which enables the fabrication of both active and passive areas in the same device. This is a very important technique, because integration of passive and active elements onto the same chip will OEICs to be realised simply, one of the most important issues in the optoelectronic research world. Comparing other integration techniques with IFVD, our technique is a much simpler, one step fabrication process which offers lower cost and better results than the rest of the techniques described in chapter 5. IFVD has already been used to fabricate laser with reduced linewidth or with integrated electro-optic modulators, but this thesis is the first report of the use of IFVD in mode-locked semiconductor lasers.

The detection of short optical pulses using the TPA waveguide autocorrelator instead of the most usual technique using a SHG crystal and the *in fibre* interferometer instead of the usual bulk optics interferometer are also novel features reported in this thesis. The *in fibre* interferometer provides very easy alignment, compared with the more standard technique, but its performance can be greatly improved by using polarisation maintaining fibre, which would make the measurements much easier to take. The TPA autocorrelation measurement technique is at least as sensitive as those using SHG, but as the detection element is a semiconductor waveguide it is much easier to use, and it could be even possible to integrate the interferometer and the TPA autocorrelator waveguide onto the same chip.

Even though we have demonstrated the possibility of all-optical clock recovery using semiconductor mode-locked lasers, we would also comment that more research in this field would be necessary before a practical clock extraction circuit is fabricated. Real digital signals must be used to lock the semiconductor device, and the bit error ratio (BER) of the detected signal must be measured.

Another interesting area for future research is to study the configurations analysed in this thesis in a longer wavelength semiconductor material. The devices analysed in this work were fabricated in the GaAs/AlGaAs system, with an operating wavelength around 860 nm but, for long range telecommunications purposes, the generation of short pulses at 1.55 μm is required. As, in principle, these laser configurations should

operate in the same way at long wavelength, the results obtained in this thesis will be very useful for the design and fabrication of long wavelength semiconductor mode-locked lasers.

Appendix I THE TWO PHOTON ABSORPTION WAVEGUIDE AUTOCORRELATOR.

Two-photon absorption (TPA)¹ is a nonresonant, nonlinear optical process which occurs for photons with energy $h\nu$ such that

$$\frac{E_g}{2} < h\nu < E_g \quad (\text{AI.1})$$

where E_g is the energy bandgap of the semiconductor material used for the TPA detection. For this photon energy, there is very small absorption of single photons, but a significant carrier population can be created by means of two-photon absorption, where an electron can be excited from the valence band to the conduction band by the absorption of two photons.

Because the carrier density generated by the TPA is a quadratic function of the light intensity, it can be used as the nonlinear process for autocorrelation measurements. Using a photodiode in a waveguide geometry to perform the TPA has a number of advantages over conventional second-harmonic generation (SHG) techniques such as²:

- a) TPA has a much broader wavelength response than SHG.
- b) In a TPA waveguide autocorrelator the detection and nonlinear response functions are integrated into a single device while, for SHG, a SHG crystal and photomultiplier tube are required.
- c) The TPA waveguide autocorrelator is suitable for integration.

To perform the autocorrelation of an optical pulse, the optical beam is divided into two beams orthogonally polarised to reduce interference effects within the waveguide. As the time delay t_d between the beams is altered, the photocurrent generated by TPA also changes.

¹ F.R. Laughton, J.H. Marsh, D.A. Barrow and E.L. Portnoi, "The two-photon absorption semiconductor waveguide autocorrelator", *IEEE J. Quantum Electron.*, 1994, **30**, 3, 838-845.

² M.M. Karkhanehchi, J.H. Marsh and D.C. Hutchings, "The polarisation dependence of two-photon absorption coefficient in an AlGaAs waveguide", *Conference on Lasers and Electro-Optics CLEO'97*, 1997, **11**, pp.488-489.

To calculate the theoretical TPA photocurrent, as a function of the time delay between the beams, consider two orthogonally polarised pulses travelling along the waveguide. A gaussian pulse shape of the pulse to be measured is assumed. The intensity profile of the pulse is given by

$$I(t) = I_0 e^{-t^2/2\tau_p^2} \quad (\text{AI.2})$$

where I_0 is the pulse peak intensity and τ_p is related with the FWHM of the gaussian pulse as $\tau_{FWHM} = \sqrt{8 \text{Ln } 2} \tau_p \approx 2.35 \tau_p$. The average intensity of a gaussian pulse train with a pulse period of T is given by

$$I_{\text{ave}} = \frac{1}{T} \int_{-\infty}^{\infty} I(t) dt = \sqrt{2\pi} I_0 \frac{\tau_p}{T} \quad (\text{AI.3})$$

The instantaneous intensity in the waveguide, due to both pulses, is given by

$$I(t) = I_0 e^{-t^2/2\tau_p^2} + I_0 e^{-(t-t_d)^2/2\tau_p^2} \quad (\text{AI.4})$$

where t_d is the delay between both beams. Because the pulses are orthogonally polarised, there are no interference effects between them, as can be seen in Eq.(AI.4).

The average carrier photogeneration in the waveguide is given by

$$\left(\frac{dN}{dt} \right)_{\text{ave}} = \frac{1}{T} \int_{-\infty}^{\infty} \left(\frac{\alpha}{h\nu} I(t) + \frac{\beta}{2h\nu} I^2(t) \right) dt \quad (\text{AI.5})$$

where $h\nu$ is the photon energy, β is the two-photon absorption coefficient and α is the single-photon absorption coefficient.

Considering the waveguide to be sufficiently short that the intensity, and hence the carrier generation, remains constant throughout the length of the waveguide, the average photocurrent as function of the time delay between the pulses is

$$I_{ph}(t_d) = e V \left[\frac{2\alpha}{h\nu} I_{\text{ave}} + \frac{\beta}{2\sqrt{\pi} h\nu \tau_p} T I_{\text{ave}}^2 \left(1 + e^{-t_d^2/4\tau_p^2} \right) \right] \quad (\text{AI.6})$$

where e is the electron charge and V is the volume in which the carriers are generated.

As can be seen from Eq.(AI.6), the average photocurrent for the TPA waveguide autocorrelator has the same gaussian dependence on the time delay between the two

beams as the conventional SHG autocorrelator, so that the width of the autocorrelation trace must be divided by $\sqrt{2}$ to obtain the true pulse width.

Photoluminescence (PL) provides a non-destructive technique for the determination of certain impurities in semiconductors. The technique is also a valuable tool for QW characterisation and QWI investigation since it allows accurate energy bandgap measurements.

The main operation concepts of PL are now discussed briefly. The sample to be measured must be cooled to minimise thermally-activated non-radiative recombination processes which could reduce the resolution of the bandgap measurements. It is then excited with an optical source, typically a laser, with photon energies larger than the energy bandgap of the material. When the sample is illuminated, electron-hole pairs are generated which then emit photons assuming recombination is radiative. There are several recombination mechanisms, including band-to-band recombination which dominates at room temperature and excitonic recombination which is most commonly observed at low temperatures¹.

The PL experimental set-up used for bandgap measurements is shown in Figure AII.1. An argon ion laser, operating at 514.5 nm, was used to excite the sample, which was placed in liquid nitrogen to cool it to 77 K. Excitonic luminescence from the QWs was therefore observed. The reflected and excited light were guided to a monochromator, where the luminescence was separated spectrally and detected using a germanium detector, also cooled by liquid nitrogen. The laser beam was modulated by an optical chopper and the detected signal from the Ge-detector was amplified by an lock-in amplifier. The whole process, including data acquisition and analysis, was computer controlled.

¹ D. K. Schroder, "Semiconductor material and device characterisation", *John Wiley & Sons*, 1990.

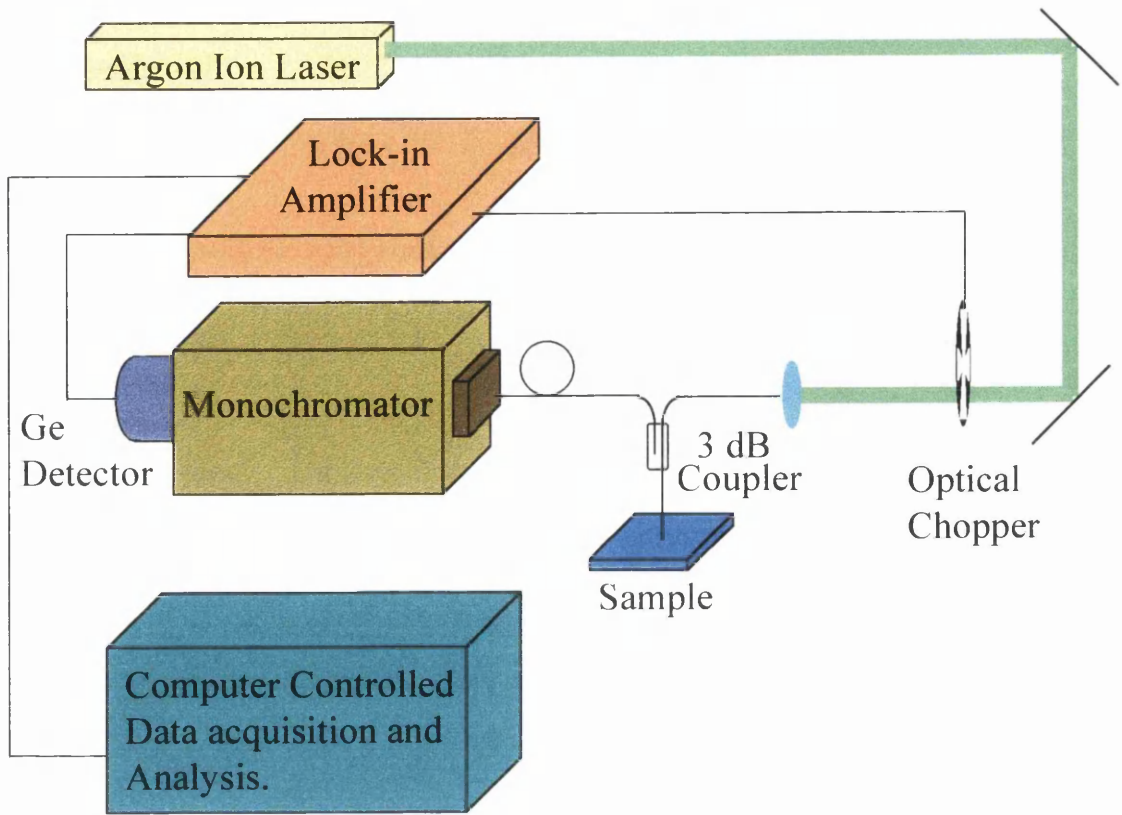


Figure AII.1: PL experimental set-up.

**Appendix III THE FOURIER TRANSFORM:
NOTATIONS AND CONVENTIONS.**

The Fourier transform and inverse Fourier transform of a real function $X(t)$ are written¹

$$\tilde{X}(\omega) = \int_{-\infty}^{+\infty} X(t) e^{-j\omega t} dt \quad (\text{AIII.1})$$

$$X(t) = \frac{1}{2\pi} \int_{-\infty}^{+\infty} \tilde{X}(\omega) e^{j\omega t} d\omega \quad (\text{AIII.2})$$

where the ‘tilde’ symbol is used to denote the Fourier transformed function. Taking into account that the energy of a signal must be the same in either the time domain or the frequency domain, *Parseval’s theorem* is obtained

$$\int_{-\infty}^{+\infty} |X(t)|^2 dt = \frac{1}{2\pi} \int_{-\infty}^{+\infty} |\tilde{X}(\omega)|^2 d\omega \quad (\text{AIII.3})$$

The power spectral density of the real function $X(t)$, which describes the distribution of power versus frequency, measured over a period of time T is written as

$$S_X(\omega) = \lim_{T \rightarrow \infty} \frac{|\tilde{X}(\omega)|^2}{T} \quad (\text{AIII.4})$$

The autocorrelation function of the real function $X(t)$ is written as

$$G_X(\tau) = \langle X(t + \tau) X(t) \rangle \quad (\text{AIII.5})$$

where the operator $\langle \rangle$ denotes time average, and is defined as

$$\langle X(t) \rangle = \lim_{T \rightarrow \infty} \frac{1}{T} \int_{-T/2}^{+T/2} X(t) dt \quad (\text{AIII.6})$$

The power spectral density of the laser intensity is also given by the Fourier transform of the autocorrelation function as

$$S_X(\omega) = \int_{-\infty}^{+\infty} G_X(t) e^{-j\omega t} dt \quad (\text{AIII.7})$$

¹ F.G. Stremler, “Introduction to communication systems”, *Addison Wesley*, 1990.

Conference:

- F. Camacho, D.A. Barrow, E.A. Avrutin, A.C. Bryce and J.H. Marsh, “Two-contact semiconductor mode-locked lasers”, *The first Canterbury workshop on microwave and millimetric-wave optoelectronics*, Canterbury, March 1996, pp 4-7.
- F. Camacho, E.A. Avrutin, A.C. Bryce and J.H. Marsh, “High frequency, stable optical pulse generation using two-section passively mode-locked semiconductor diode lasers”, *High performance electron devices for microwave and optoelectronic applications workshop EDMO'97*, Leeds, November 1996, pp. 85-90.
- F. Camacho, E.A. Avrutin, A.C. Bryce and J.H. Marsh, “Comparison between all-active and extended cavity semiconductor mode-locked lasers”, *Semiconductor and integrated optoelectronics SIOE'97*, Cardiff, April 1997, paper 74.
- F. Camacho, E.A. Avrutin, A.C. Bryce and J.H. Marsh, “Stable optical pulse generation by subharmonically locking a two-section passive mode-locked semiconductor laser”, *Conference on lasers and electro-optics CLEO'97*, Baltimore (USA), May 1997, pp.243-244.
- F. Camacho, E.A. Avrutin, A.C. Bryce and J.H. Marsh, “Monolithically Integrated Passive Waveguides Made By Impurity-Free Vacancy Disorder: An Improvement In Mode-Locked Semiconductor Lasers”, *International Topical Meeting on Microwave Photonics MWP'97*, Germany, September 1997.
- F. Camacho, E.A. Avrutin, A.C. Bryce and J.H. Marsh, “Noise Reduction In Passive Mode-Locked Semiconductor Lasers By Subharmoning Locking”, *International Topical Meeting on Microwave Photonics MWP'97*, Germany, September 1997.

Journal:

- F. Camacho, D.A. Barrow, E.A. Avrutin, A.C. Bryce and J.H. Marsh, “Two-contact semiconductor mode-locked lasers”, *International Journal of Optoelectronics*, 1995, **10**, 6, pp. 433-437.

- F. Camacho, E.A. Avrutin, P. Cusumano, A. Saher Helmy, A.C. Bryce and J.H. Marsh, "Improvements in mode-locked semiconductor lasers by using monolithically integrated passive waveguides made by quantum well intermixing", *IEEE Photonics Technology Letters*, 1997, **9**, 9.
- F. Camacho, E.A. Avrutin, A.C. Bryce and J.H. Marsh, "Passive modelocking in semiconductor lasers with monolithically integrated passive waveguides", submitted to *IEE Proceedings, Special Issue on Semiconductor Lasers*, 1997.
- A.C. Bryce, F. Camacho, P. Cusumano and J.H. Marsh, "CW and mode-locked integrated extended cavity lasers fabricated using impurity free vacancy disordering" (Invited Paper), to be published in *IEEE Special Topics in Quantum Electronics*, 1997.

